FABRICATION OF III-NITRIDE BASED ENERGY EFFICIENT ULTRAVIOLET PHOTODETECTOR

Thesis submitted to the Delhi Technological University
For the Award of Degree of

DOCTOR OF PHILOSOPHY
IN
ELECTRONICS AND COMMUNICATION ENGINEERING

By

LALIT GOSWAMI

(Enrolment No.: 2K15/PHD/EC/02)

Under the supervision & co-supervision of

PROF. RAJESHWARI PANDEY (DTU) &
PROF. GOVIND GUPTA (CSIR-NPL)

DEPARTMENT OF ELECTRONICS & COMMUNICATION ENGINEERING
DELHI TECHNOLOGICAL UNIVERSITY
(FORMERLY DELHI COLLEGE OF ENGINEERING)
DELHI-110042, INDIA

SEPTEMBER 2020

Dedicated to My Ancestors

CANDIDATE'S DECLARATION

I hereby declare that the thesis entitled "**Fabrication of III-Nitride based Energy Efficient Ultraviolet Photodetector"** is an original work carried out by me under the supervision of Dr. Rajeshwari Pandey, Professor, Department of Electronics and Communication Engineering, Delhi Technological University, Delhi and co-supervision of Dr. Govind Gupta, Sr. Principal Scientist CSIR-National Physical Laboratory, New Delhi and Professor, Academy of Scientific & Innovative Research (AcSIR). This thesis has been prepared in conformity with the rules and regulations of the Delhi Technological University, Delhi. The research work reported and results presented in the thesis has not been submitted either in part or full to any other university or institute for the award of any other degree or diploma.

(Lalit Goswami)
Research Scholar
Enrolment No.: 2K15/PhD/EC/02
Department of Electronics &
Communication Engineering
Delhi Technological University
Delhi-110042

Date: September 2020
Place: New Delhi

DELHI TECHNOLOGICAL UNIVERSITY
FORMERLY DELHI COLLEGE OF ENGINEERING
(UNDER DELHI ACT 6 OF 2009, GOVT. OF NCT OF DELHI)

CERTIFICATE

This is to certify that the Ph.D. thesis entitled "**Fabrication of III-Nitride based Energy Efficient Ultraviolet Photodetector"** submitted to the Delhi Technological University, Delhi for the award of **DOCTOR OF PHILOSOPHY** is based on the original research work carried out by **Lalit Goswami (2K15/PhD/EC/02)** under the supervision of Dr. Rajeshwari Pandey, Professor, Department of Electronics and Communication Engineering, Delhi Technological University, Delhi and co-supervision of Dr. Govind Gupta Sr. Principal Scientist CSIR-National Physical Laboratory, New Delhi and Professor, Academy of Scientific & Innovative Research (AcSIR). It is further certified that this work has not been submitted to any other Institute or University for the award of any other diploma or degree.

(Lalit Goswami)
Candidate
(Enrolment No.: 2K15/Ph.D./EC/02)

This is to certify that the above statement made by the candidate is correct to the best of our knowledge.

(Dr. Govind Gupta)
(Co-Supervisor)
Sr. Principal Scientist & Professor (AcSIR)
CSIR-National Physical Laboratory
Dr. K.S Krishnan Marg, New Delhi-110012

(Dr. Rajeshwari Pandey)
(Supervisor)
Professor, Department of ECE
Delhi Technological University
Bawana Road, Delhi- 110042

Prof. N.S. Raghava
Head of the Department,
Department of Electronics & Communication Engineering,
Delhi Technological University, Bawana Road, Delhi-110042

ACKNOWLEDGMENT

First and foremost, praises and thanks to God, the Almighty, for the showers of blessings throughout my research work to complete the research successfully.

It is my pleasure to express a deep sense of gratitude and indebtedness to my learned supervisor Dr. Rajeshwari Pandey, Professor, Delhi Technological University, New Delhi (India) for her invaluable guidance towards high quality research work, vision, encouragement and patient review. Her continuous inspiration has made me complete this thesis. I am delighted to be associated with her. I found myself so blessed to have such a motivating, focused, kind-hearted, soft-spoken, helpful and resourceful person as my supervisor.

I want to express my deep and sincere gratitude to my co-supervisor, Dr. Govind Gupta, Professor, AcSIR & Sr. Principal Scientist, CSIR-National Physical Laboratory, New Delhi (India) for allowing me to do research and providing invaluable guidance throughout this research. His dynamism, vision, sincerity, and motivation have deeply inspired me. He has taught me the methodology to carry out the research and to present the research works as clearly as possible. It was a great privilege and honour to work and study under his guidance. I am incredibly grateful for what he has offered me. His enthusiasm and his mission for providing high-quality work have made a deep impression on me.

I sincerely thank Prof. N.S. Raghava, Head, Department of ECE, Prof. S. Indu, for providing all the necessary facilities for the completion of my work. I am also grateful to Prof. Yogesh Singh, Vice-Chancellor, DTU, Delhi, for providing the research environment in the university. I would also like to express my deep sense of gratitude to Dr. D.K Aswal, Director, and Dr. Ramesh C. Budhani, Ex-Director, CSIR-National Physical Laboratory for providing world-class state-of-the-art & highly sophisticated facilities to carry out the experiments for growth & characterizations which has solely increased the quality of the work. I would also like to express my gratitude to Dr. Amish G. Joshi, Dr. Suresh Chand and Dr. S.T. Lakshmikumar for their timely support & encourgement.

I have grown all the GaN samples on the state of the art facility called Plasma Assisted Molecular Beam Epitaxy. Thus, I would like to thanks my nitride activity team and my lab mates, i.e., Dr. Neha Aggarwal, Dr. Shibin Krishna TC, Dr. Monu Mishra, Dr. Subhendra Kumar Jain, Mr. Abhiram Gundimeda, Mr. Saket Vihari, Dr. Amit Kumar Chauhan and newly joined member Mr. Pargam Vashishtha for their dedication, cooperation, support, and hard work. Among them, I would like to owe special mention to Dr. Neha Aggarwal, who helped me a lot during my Ph.D. journey. I am feeling very grateful for having such a talented, helpful, and scientific expert of a similar domain. She has actively contributed to the research work carried out in this thesis, which helps me to increase scientific understanding, whose impact is reflected as high-quality SCI publications. Besides, I would also like to give my special thanks to Mr. Saket Vihari for sharing my workload at some extent on workplace for accomplishing my research work. I want to acknowledge and register my sincere gratitude to Dr. Surinder Pal Singh, Dr. Shailesh Narayan Sharma, Dr. Manjri Singh, Dr. Rajni Verma and Dr. Swati Bishnoi for helping me for providing Gold Nanoparticles, ZnO-nanorods, Graphene Quantum Dots Synthesis and characterizations in CSIR-NPL.

I sincerely mark my gratitude to several scientists and technical officers for their support in accomplishing various characterizations in CSIR-NPL such as Dr. Nita Dilawar, Dr. Sudhir Husale, Dr. Nidhi Singh, Mr. Jasveer Singh, Dr. Jai Tawale. Dr. Mandeep Kaur and Mr. Biplab Bhattacharya.

Last but not least, I would like to dedicate this work to my family, especially my parents and my wife Dr. Vandana Goswami, for her continuous encouragement, motivation, fighting spirit towards hard time, everlasting support, and shared family responsibilities mainly our two beautiful children Utsav and Bhavanshi.

Finally, I thank my God for letting me through all the difficulties. You are the one who let me finish. Thank you, Lord. Finally, I would like to share a very motivational quote “God has a reason for allowing things to happen. We may never understand his wisdom, but we simply have to trust his will”.

Date:

(Lalit Goswami)

LIST OF PUBLICATIONS

(Included in the Thesis)

1. **Lalit Goswami,** Rajeshwari Pandey, and Govind Gupta, "Epitaxial growth of GaN nanostructure by PA-MBE for UV detection application", **Applied Surface Science 449, 186-192 (2018), Impact Factor: 6.182.**
2. **Lalit Goswami,** Rajeshwari Pandey, Govind Gupta, "Ultra-thin GaN nanostructures based self-powered ultraviolet photodetector via non-homogeneous Au-GaN interfaces", **Optical Materials 102, 109820 (2020), Impact Factor: 2.779.**
3. **Lalit Goswami,** Neha Aggarwal, Shibin Krishna, Manjri Singh, Pargam Vashishtha, Surinder Pal Singh, Sudhir Husale, Rajeshwari Pandey, Govind Gupta, "Au Nanoplasmonics Mediated Surface Plasmon Enhanced GaN Nanostructured UV Photodetectors", **ACS Omega 5, 24, 14535–14542 (2020), Impact Factor: 2.87.**
4. **Lalit Goswami,** Neha Aggarwal, Pargam Vashishtha, Shubhendra K. Jain, Shruti Nirantar, Rajeshwari Pandey, Govind Gupta, "Fabrication of High Aspect Ratio GaN Nano-Towers for Efficient UV Photodetection", **(Under Review: Materials Advances, 2020).**
5. **Lalit Goswami,** Neha Aggarwal, Manjri Singh, Rajni Verma, Pargam Vashishtha, Shubhendra K. Jain, Jai Tawale, Rajeshwari Pandey and Govind Gupta, "A Gigantic Photoresponse from ZnO Nanorods Hybridized GaN Nanotowers based UV Photodetector integrated with Au Nanoparticle's Nanoplasmonics", **ACS Applied Nano Materials. 3, 8, 8104–811 (2020).**
6. **Lalit Goswami,** Neha Aggarwal, Rajni Verma, Swati Bishnoi, Pargam Vashishtha, Sudhir Husale, Rajeshwari Pandey and Govind Gupta, "Graphene quantum dots functionalized ZnO-Nanorods / GaN-Nanotowers heterostructure based high-performance UV Photodetector" **(Accepted: ACS Applied Materials & Interfaces, 2020), Impact Factor: 8.758.**

PUBLICATIONS OTHER THAN THESIS WORK

1. Shubhendra Kumar Jain, Rishi Ranjan Kumar, Neha Aggarwal, Pargam Vashishtha, **Lalit Goswami,** Sruthi Kuriakose, Akhilesh Pandey, Madhu Bhaskaran, Sumeet Walia, and Govind Gupta, "Current Transport and Band Alignment Study of MoS_2/GaN and MoS_2/AlGaN Heterointerfaces for Broadband Photodetection Application", **ACS Applied Electronic Materials 2, 3 (2020).**

2. Shibin Krishna, Neha Aggarwal, **Lalit Goswami,** Govind Gupta, "Growth Dynamics of Epitaxial Gallium Nitride Films grown on c-Sapphire Substrates", book entitled as **Advances in Thin Film Research, edited by S. Kumar and D. K. Aswal, Springerlink publisher page 75-101, 2020.**

3. Neha Aggarwal, Shibin Krishna, Shubhendra K. Jain, Arzoo Arora, **Lalit Goswami**, Alka Sharma, Sudhir Husale, Abhiram Gundimeda, and Govind Gupta, "Impact on Photon-Assisted Charge Carrier Transport by Engineering Electrodes of GaN-based UV Photodetectors", **Journal of Alloys and Compounds, 785, 883 (2019).**

4. Neha Aggarwal, Shibin Krishna, **Lalit Goswami,** and Govind, "Inclination of Screw Dislocations on the Performance of Homoepitaxial GaN-based UV Photodetectors", **Under Review: Material Science & Engineering: B (2020).**

5. Neha Aggarwal, **Lalit Goswami**, Shubhendra K. Jain, Bhasker Gahtori, Sandeep Singh, Jasveer Singh, Nita Dilawar, and Govind Gupta, "Impact of AlN buffer layer on the growth & fabrication of AlGaN/AlN heterostructure based photodetectors", **Under Review: Journal of Alloys & Compounds (2020).**

6. Monu Mishra, Abhiram Gundimeda, Shibin Krishna, Neha Aggarwal, **Lalit Goswami,** Bhasker Gahtori, Biplab Bhattacharyya, Sudhir Husale and Govind Gupta, "Surface-engineered nanostructure-based efficient non-polar GaN ultraviolet photodetectors", **ACS Omega, 3 2304−2311 (2018).**

7. Neha Aggarwal, Shibin Krishna, Alka Sharma, **Lalit Goswami**, Dinesh Kumar, Sudhir Husale, and Govind Gupta. "A Highly Responsive Self-Driven UV

Photodetector Using GaN Nanoflowers," **Advanced Electronic Materials, 3, 1700036 (2017)**.

8. Neha Aggarwal, Shibin Krishna, **Lalit Goswami**, Monu Mishra, Govind Gupta, K.K. Maurya, Sandeep Singh, Nita Dilawar, and Mandeep Kaur. "Extenuation of stress and defects in GaN films grown on MOCVD-GaN/c-sapphire substrate by PAMBE," **Crystal Growth & Design, 15, 2144−2150 (2015).**

9. Shibin Krishna, Neha Aggarwal, Anurag Reddy, Palak Dugar, Monu Mishra, **Lalit Goswami,** Nita Dilawar, Mahesh Kumar, K. K. Maurya, and Govind Gupta, "Probing the correlation between structure, carrier dynamics and defect states of epitaxial GaN film on (11-20) sapphire grown by rf-molecular beam epitaxy", **RSC Advances, 5, 73261 (2015)**

10. Monu Mishra, Shibin Krishna, Prachi Rastogi, Neha Aggarwal, Amit Kumar Singh Chauhan, **Lalit Goswami,** and Govind Gupta, "New Approach to Clean GaN Surfaces", **Materials Focus 3, 218-223 (2014**).

11. Shibin Krishna TC, Rahul Deshmukh, Amit Kumar Singh Chauhan, **Lalit Goswami**, and Govind, "Influence of temperature on the controlled growth kinetics and superstructural phase formation of indium on a reconstructed Si (113) 3 × 2 surfaces", **Materials Research Express, 1, 1 (2014).**

LIST OF PAPER PRESENTED IN NATIONAL/ INTERNATIONAL CONFERENCES

1. **Lalit Goswami,** Rajeshwari Pandey, Govind Gupta. Growth Kinetics of Gallium Nitride Nanostructures on Si (111) Substrate for Harmful UV Detection Application, 4^{th} International Conference on Nanoscience and Nanotechnology, 9^{th} -11^{th} August 2017, SRM University, Chennai. **(Poster Presentation)**

2. **Lalit Goswami,** Neha Aggarwal, Shibin Krishna, Biplab Bhattacharyya, Sudhir Husale, Rajeshwari Pandey, and Govind Gupta. Gallium Nitride Nanostructure Based Self Powered MSM UV Photodetector, 19th International conferences on The Physics of Semiconductor Devices, 12^{th} -15^{th} Dec. 2017 held in **IIT Delhi. (Poster Presentation)**

3. **Lalit Goswami,** Temperature driven Gallium Nitride Nanoclusters on Stepped Si (113) surface International Conference on Material Science (ICMS-2017), 16^{th}-18^{th} Feb. 2017, **Deptt. Of Physics Tripura University, Tripura (Poster Presentation)**

4. **Lalit Goswami,** Rajeshwari Pandey, Shibin Krishna, Neha Aggarwal, Monu Mishra, Mandeep Kaur, Govind Gupta, Growth of GaN Nanostructures on Silicon (111) Surface International Conference on Material Science & Technology 2016, **Delhi University (Oral Presentation)**

5. **Lalit Goswami,** Shibin Krishna, Neha Aggarwal, Monu Mishra, S. Singh, K.K Maurya, Mandeep Kaur, Rajeshwari Pandey, Govind Gupta, Epitaxial growth of GaN nanostructures on Si_3N_4/Si(111) substrate by PAMBE system National Conference on Semiconductor materials and devices, 4^{th}-6^{th} March 2016, **IIT Jodhpur**, Rajasthan. **(Poster Presentation)**

6. **Lalit Goswami,** Rajeshwari Pandey, and Govind Gupta, Fabrication of GaN Nanostructure equipped UV Detector for handheld devices, National Scholar Day (Shodharth 2016) Symposia at **NIT Delhi** on 15^{th} Oct. 2016 **(Oral Presentation)**

7. **Lalit Goswami,** Rajeshwari Pandey, Neha Aggarwal, Shibin Krishna, Alka Sharma, Sudhir Husale, and Govind Gupta, Realization of low voltage operable UV-Detectors using GaN Nanostructures by PA-MBE 3rd International Conference on Young Researchers on Advanced Materials, 11th - 15th Dec. 2016, **IISc Bangalore**. **(Poster Presentation)**

8. **Lalit Goswami,** Rajeshwari Pandey, Neha Aggarwal, Shibin Krishna, Alka Sharma, Sudhir Husale and Govind Gupta, Gallium Nitride nanostructures equipped UV-Detector by PA-MBE International conference on advances in nanomaterials and nanotechnology, 4th-5th Nov. 2016, **Jamia Millia Islamia, Delhi (Poster Presentation)**

AWARDS /RECOGNITION

1. **Commendable Research Award** in Delhi Technological University, New Delhi (India), 18 March 2019. "Epitaxial growth of GaN nanostructure by PA-MBE for UV detection application" by **Lalit Goswami**, Rajeshwari Pandey and Govind Gupta.

ABSTRACT

III-Nitride semiconductor devices reserve their utmost place in the ubiquitous class of technology due to its applicability in a wide range of applications, which include solar cells, light-emitting diodes (LEDs), laser diodes (LDs), photodetectors (PDs), etc. Consequently, the extensive range of applications and projected gigantic market size generates continuous demand for more efficient, durable, and quality device products. The researchers have world-wide taken up this challenge of the never-ending requirement of technological improvisation and devoting their rigorous efforts to achieve better materials quality and device design. Among numerous domestic, commercial, and defence applications of III-nitride semiconductor-based devices, the detection of harmful ultraviolet (UV) radiation (<400 nm) found to be an extreme necessity. Universally, technologist finds potential needs to detect UV for plume detection, flame detection, chemical as well as biological analyses, secure space to space communications, environmental monitoring, astronomical research, and anti-missile technology. Thus, the recommended ideal photodetector (PD) device should be adverse environment friendly with excellent sensitivity, high responsivity, high signal to noise ratio, and high spectral selectivity. Henceforth, as compared to conventional Si-based UV PD devices, III-nitride is proven to be a promising candidate due to their remarkable credentials such as wide-direct bandgap, high thermal conductivity, superb radiation hardness, which makes them operable in harsh environmental conditions. Besides, the detectors with Si-based technology severely loses signal to noise ratio as well as efficiency as a function of increasing dark current with elevated temperature. The solution to these problems has been provided by usage of the bulky cooling arrangement, expensive optical filters, and their operational instrumentation setups. Therefore, the movement of the semiconductor market from the Si-based to III-nitride based can be well understood. However, a key challenge is the presence of a large density of defects and dislocations due to lack of suitable lattice-matched substrates, and low resistance Ohmic contacts. Thus, particularly in the case of energy-efficient UV PD fabrication, the curiosity to grow good quality epitaxial III-nitride films has been mainly directed towards the study on GaN nanostructures (NSs). Thereby, the

growth of high surface to volume ratio based GaN NSs increases the incident photon absorption sites without sacrificing the device nano dimensionality. Besides, the possibility of integration of GaN with existing Si-based device technology leads us towards growth & fabrication on Si (111) substrates. Till date, numerous methodologies have been adopted to grow and optimize stress relaxed, higher aspect ratio, high crystalline quality as well as an excellent opto-electrical transport based GaN NSs by using plasma-assisted molecular beam epitaxy (PAMBE). Despite improvisation in crystalline quality, grown NSs as well as device geometry, recent advancement for enhancing the performance of PD devices emphasized on other exciting and potential approaches such as hybridization of III-nitride materials with other UV sensitive semiconductors, functionalization by novel metal nanoparticle's nanoplasmonics and sensitization by highly conductive quantum dots.

Thus, the thesis aims to explore and meticulously investigate the precise control epitaxial growth of high surface to volume ratio oriented GaN NSs on Si (111) substrate using the PAMBE system and their utilization as energy-efficient UV PDs. Besides, the effort made in this work excavates and execute the new prospects for emerging next-generation highly efficient photodetectors via. ZnO/GaN heterojunction hybridization, Au-NPs functionalization, and GQDs sensitization.

The thesis consists of seven chapters, briefly described below:

Chapter 1 gives a brief overview of the photodetection devices which are sensitive towards the UV range. Further, the significant contribution of III-nitrides in the fabrication of energy-efficient and durable UV PDs has been discussed. Moreover, the introduction of III-nitrides semiconductor's inherent physical, chemical, optical properties with their bandgap engineering has been elaborated, which were found responsible for the fabrication of narrow to broadband PDs for harsh environment. Additionally, to enhance the performance of existing III-nitride UV PD technology, other potential approaches such as nitride's surface functionalization, hybridization and sensitization have also been suggested.

Chapter 2 describes the detailed mechanism of the technique used for the growth of III-nitride semiconductors along with various in-situ as well as ex-situ analytical tools

and methods utilized for probing the structural, morphological, optical and electrical properties of the grown structures. This chapter illustrates a brief description of the steps involved in devices fabrication process and evaluation of their performance parameters as well.

Chapter 3 elucidates the growth of nanoisland shaped, lower stress, and strain facilitated GaN-NS on Si (111) substrate via PAMBE and fabrication of GaN-NS based UV photodetection device even with NS's tiny dimensionality. The three-dimension (3D) growth of GaN-NS in real-time was observed by the in-situ RHEED technique, which displays transformation from streaky to the spotty pattern. A micro-Raman technique has been employed to elaborate on NS's crystallinity and lower stress value, which is found to be in good agreement with related lower strain as evaluated by HR-XRD spectra. An observed sharp near band edge emission at 363.2 nm by room temperature photoluminescence measurement signifies the presence of GaN. After that, the as-grown ultra-thin GaN NSs were utilized to fabricate energy-efficient self-powered UV PD, wherein non-homogeneous GaN nanoislands were perceived on the Si surface with a thickness of ~30 nm and an average distribution density of 2×10^{10} cm^{-2}. Despite nano dimensional GaN NSs film, the capability of UV detection of fabricated PD added novelty to this work, where performance parameters such as photosensitivity ($\sim 10^2$), detectivity ($\sim 10^9$ Jones), responsivity (1.76 mA/W) and NEP: noise equivalent power (3.5×10^{-11} $WHz^{-1/2}$) under self-powered mode were observed. The transient photo-response measurement revealed a rapid rise and decay time constants of ~18 ms and ~27 ms, respectively. Under varying optical power (1 mW to 13 mW), the GaN PD displayed significant enhancement in photocurrent with increasing optical power. The performance of the fabricated detector has also been analyzed under the photoconductive mode of operation, where it revealed significantly enhanced responsivity (23 fold) and detectivity (~1000 fold). Such nanostructured self-powered GaN-based UV PD paves the way towards the fabrication of energy-efficient optoelectronic devices.

Chapter 4 presented the nanoplasmonic impact of chemically synthesized Au nanoparticles (NPs) on the performance of GaN NS based UV PD is analyzed. The devices with uniformly distributed Au NPs on GaN NSs (nanoislands) prominently

respond toward UV illumination (325 nm) in both self-powered as well as photoconductive modes of operation and have shown fast and stable time-correlated response with significant enhancement in the performance parameters. A comprehensive analysis of the device design, laser power, and bias-dependent responsivity and response time is presented. The fabricated Au NP/GaN nanoisland-based device yields the highest responsivity of ~ 216 mA/W, detectivity of ~ 10^9 jones, reduced NEP of ~ 1.8×10^{-12} W $Hz^{-1/2}$, External quantum efficiency (EQE) of ~ 82%, and fast response/recovery time of ~ 40 ms. Moreover, the study also illustrates the mechanism where light interacts with the chemically synthesized NPs guided by the surface plasmon to enhance the device performance effectively. Further, the decoration of low dimensional Au NPs on GaN NSs acts as a detection enhancer with fast recovery time. It paves the way toward the realization of energy-efficient optoelectronic device applications.

Chapter 5 elaborates on the fabrication of GaN-Nanotowers (GaN-NTs) based on highly efficient UV PD with distinct AlN buffer layer thickness and NTs lengths. The unique nanotower (tapered ended) morphology of an epitaxially grown hexagonal stacked nanocolumnar structure with truncated strain and high surface-to-volume ratio contributes to the significantly enhanced performance of the fabricated detector towards UV illumination. The fabricated GaN-NT UV PDs displays very low dark current (~12nA) & very high I_{Light}/I_{Dark} ratio (>10^4) along with the highest responsivity of 485 A/W. The device exhibits very high EQE ~10^5 %, fast time-correlated transient response (~430 µs), very low NEP (~10^{-13} $WHz^{-1/2}$), and excellent UV/Vis rejection ratio. Therefore, the utilization of such GaN-NT structures can be advantageous towards the fabrication of energy-efficient ultraviolet photodetector.

Chapter 6 introduce the concept of performance augmentation of existing III-nitride (GaN) UV PDs technology employing hybridization using UV sensitive & compatible semiconductors (ZnO), surface functionalization by novel metal Gold (Au) NPs and sensitization by highly conductive graphene quantum dots (GQDs). Thereby, as grown (as discussed in chapter 5) vertically aligned longer GaN NTs with higher AlN thickness oriented highly responsive UV demonstrated fast response with excellent stability when functionalized with Au Nanoparticles, GQDs, and ZnO Nanorods.

Initially, GaN-NTs structure is hybridized by ZnO Nanorods (ZnO NRs), wherein, to capture maximum incident photons, a strategically formulated model of NSs over NSs has been proposed as an enhanced device active surface area. Consequently, the fabricated GaN-NTs based device with ZnO NRs hybridization, GQDs sensitization, and Au NPs functionalization significantly accelerate the performance of the device where a prominent three order reduction in dark current is observed along with gigantic R, lower NEP and enormously enhanced EQE of 7042 A/W, 1.84×10^{-14} $W.Hz^{-1/2}$ and 2.7×10^{6} % respectively. Mechanism elaborating the enhanced device performance with an appropriate energy band diagram has been discussed in detail. The fabricated highly sensitive device can lead a path towards future optoelectronic applications of integrated III-Nitride technology.

Chapter 7 enlightens the major conclusions derived from the thesis work and the scope of future work.

CONTENTS

LIST OF FIGURES

LIST OF TABLES

1.1 Introduction to UV Photodetection

In 1801, J.W. Ritter discovered that upon exposure to radiation with a shorter wavelength than violet, some specific chemical reactions could be catalysed, which first specified ultraviolet (UV) radiation. Later, the efforts of many other researchers together with this observation established that similar to the visible ranges of emission, UV emissions were also manifestations of the electromagnetic (EM) radiation, while the only difference lies in their energy and wavelengths. Hence, these are extremely ionizing radiation, which can trigger many chemical processes. The principal origination of UV rays is the sun. However, the stratospheric ozone layer inhibits radiation having wavelengths shorter than 280 nm from entering the Earth's surface. It was found that nearly 9% of the total energy received from the Sun at higher layers of the atmosphere is in the UV range [1]. Previously, it is widely established that the UV region of the EM spectrum covers a wavelength range between 10 nm to 400 nm [2]. The classification of UV radiation (Figure 1.1) based on their effects is broadly divided into four sections as given below:

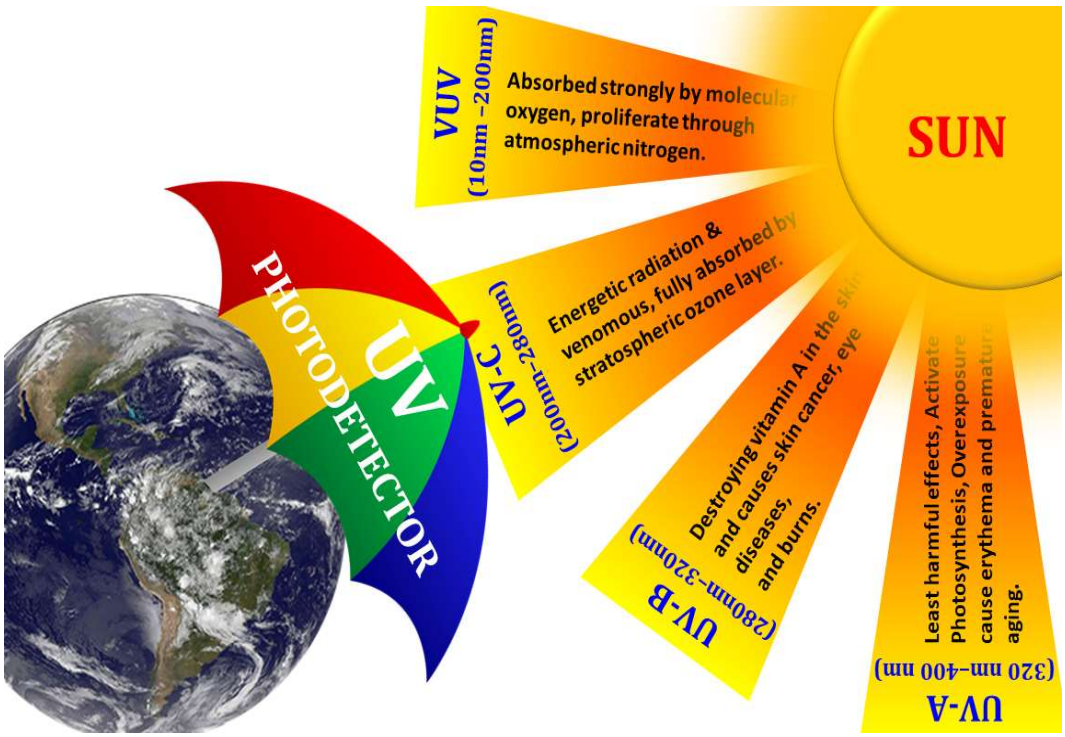

Figure 1.1: An elaborated UV regime.

I. ***UV-A (400–320 nm) region*** - This spectral region has the least harmful effects as it is in the lowest energy range. Although it can activate the photosynthesis process. However, Overexposure may cause erythema and premature ageing.

II. ***UV-B (320–280 nm) region*** – However, this spectral region is moderately absorbed by the ozone layer itself, but still, 10% of the total UV radiation reaches the surface of the Earth. Though exposure to this region also provides some beneficial properties, like activation of vitamin D. While, extensive exposure to UV-B radiation can be hazardous for human life by destroying vitamin A in the skin and causes various health-related issues like skin cancer, eye diseases, and burns).

III. ***UV-C (280–200 nm) region*** – This is the most energetic radiation range, which is venomous. Practically, the UV-C region is fully absorbed by the stratospheric ozone layer and, thus, does not enter Earth's surface.

IV. ***VUV (200-10 nm) region*** – Vacuum UV radiation is absorbed strongly by molecular oxygen in the atmosphere, though few wavelengths in the larger limit side (*i.e.*, 150–200 nm) can proliferate through atmospheric nitrogen.

The growing demand for sensing UV radiation compels the fabrication of optoelectronic devices to be operable in adverse environmental conditions. An optoelectronic device that converts the optical signal into electrical impulses is called a photodetector (PD). In recent times, the necessity to detect UV radiation (being the highly harmful and energetic radiation) have stimulated up much interest in the field of research and development of UV PDs as it offers a diversified range of applications, such as biological and chemical sensing, medical imaging, flame detection (which includes fire alarming system, missile warning, and combustion monitoring), secure communications (predominantly, space-to-space communications at wavelengths less than 280 nm) and astronomical studies. Researches, including environmental and biological sensing applications as well as industries such as aerospace, automotive and military, have upheld the advancement of UV PDs to be operable at high temperatures and inimical environments. Thus, several attempts have been made to develop photodetection devices to be operable in a UV region being blind towards the visible wavelengths.

1.1.1 Background of a Photodetector

Generally, the principle of operation for all-solid-state photosensitive devices is the photoelectric effect. Figure 1.2 demonstrates a band-diagram schematic illustrating the basic principle of a PD along with all the favourable transitions activated by incident photon energy. Transition I represents the basic principle where a photon with energy larger or equal to the energy of bandgap interacts with the semiconducting material and electrons present in the valence band gains sufficient energy from incoming photons to cross the bandgap and conquer an energy state in conduction band thereby, creating electron-hole (e-h) pairs. These photogenerated e-h pairs are then collected by their respective metal electrodes to produce photoelectric current conduction or photocurrent. Eventually, if the generated e-h pairs are not collected quickly within a specific time of interval then, they recombine and release the extra energy in the form of photons as depicted in transition II of Figure 1.2. This characteristic time scale is called the recombination lifetime, τ_r. In Transition III, the excited electron may jump from the valence band to a trap state existing within the bandgap (E_T).

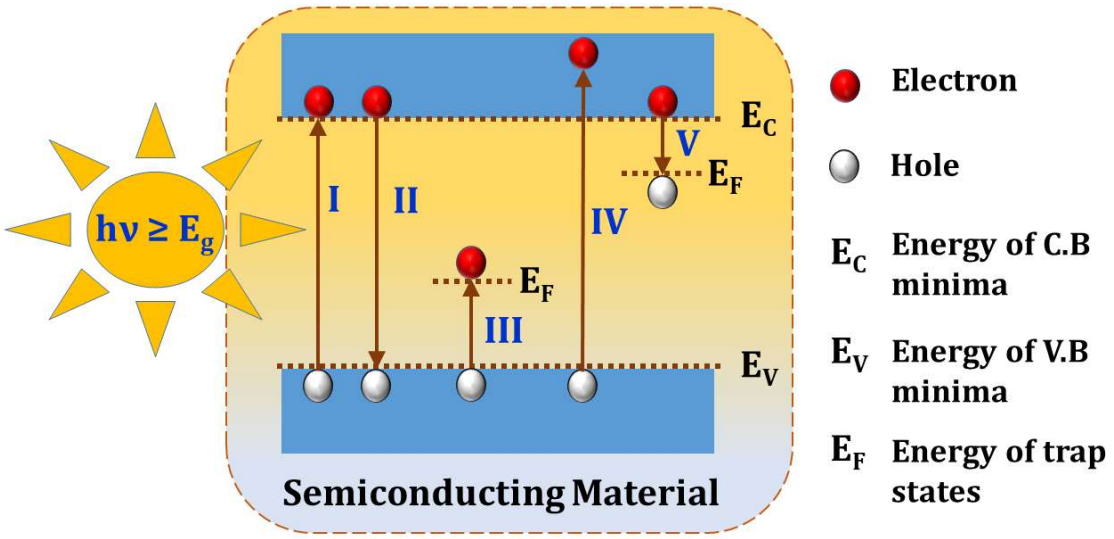

Figure 1.2: A schematic band-diagram is illustrating the operating principle of a PD along with the related possible transitions.

Further, if a photon with much higher energy than the bandgap energy enters the semiconducting material, electrons may reach to a high energy state in the conduction band which then relaxes by thermalization process in which it releases energy in the form of phonons and reaches to the bottom of the conduction band (Transition IV).

Transition V depicts trapping of the electron in trap state during a recombination process.

The photon stimulated e-h pairs (as per the transition-I) generation, and their collection by respective electrodes, *i.e.*, photocurrent is called primary parameter to understand the quality as well as the efficiency of the fabricated photodetector. Besides, many other vital parametersto decide the performance of a photodetection device. These are described as follows:

I. ***Responsivity (R)*** - is defined as the ratio of photocurrent to the incident optical power.

II. ***Quantum efficiency (η)*** - is defined as the ratio of a fractional number of electron-hole pairs generated that contributes to overall photocurrent per incident photon flux.

III. ***Response time (τ)*** – is a measure of time taken by a PD to respond to the specified optical signal. Specifically, it is the time taken by the light signal to rise or decay to a specific value. The rise time (τ_r) is defined as the time within which photocurrent increases from 10% to 90% of its maximum value when the device is exposed to the optical signal [3]. And decay time (τ_d) is defined as the time in which the photocurrent drops from 90% to 10% of its maximum value when the light is turned off [3]. However, the response time of a PD depends upon three vital factors:

   (1) time constant, RC (R is load resistance and C is the capacitance of photodiode),

   (2) diffusion time of charge carriers generated outside the depletion region and,

   (3) drift time is taken by the charge carriers to cross the depletion region.

Usually, drifting of generated carriers through the depletion region is quite fast due to the presence of a built-in electric field near the junction. By applying external bias, drift velocity can be further incremented until it reaches saturation. In contrast, the diffusion of carriers is relatively slow as it is impelled by the recombination time (or the lifetime of carriers).

I. ***Bandwidth (BW)*** - is defined as the frequency when photocurrent is 3 dB lesser than the low-frequency response.

II. ***Noise equivalent power (NEP)*** - is defined as the minimum optical input power required for producing a signal-to-noise ratio equal to one in a one-hertz output bandwidth. It is basically a measure of the sensitivity of a PD.

III. ***Detectivity (D)*** - is defined as the inverse of noise equivalent power, and it is generally normalized for *BW* and active area of the detector.

An ideal PD must possess high sensitivity, fast response, minimum noise, high detectivity, insensitive to temperature variations, long operating lifetime, high spectral selectivity, high radiation hardness, and low cost. However, the growing necessity of reliable and miniaturized UV detection devices for portable applications guided a path towards the development of semiconductor-based UV PDs. Previously; narrow bandgap semiconducting materials were first considered to perform UV detection, such as silicon and some III-V compounds. Soon, the Si technology, despite being well established in device applications, was exposed to have some limitations to be operable in the UV region because they require optical filters to block the low energy photons (from VIS and infrared regime) and highly energized UV photons induces significant degradation on the device (shortens the device lifetime). Later, SiC-based photodiodes discovered, but they have a relatively narrow range of sensitivity, and then, the GaP photodiodes emerge, which have a good signal to noise ratio, but still, it is impossible to create solar-blind and visible-blind devices without using optical filters. To avoid the use of optical filters and achieve better device performance, UV detectors based on wide bandgap (WBG) semiconductors have been vastly explored during the last decade. Thus, one of the versatile WBG semiconductor,*i.e.*, first GaN-based UV detector fabricated from as-deposited single-crystal GaN films was demonstrated in 1992 [4].

1.1.2 A Roadmap of Semiconductors employed as UV PDs

Traditionally, UV detection was first achieved by photomultiplier tubes (PMTs), secondly, thermal detectors, and then, the narrow bandgap semiconductor-based photodiodes or charge-coupled devices (CCDs) emerge. Among them, only PMTs display low noise, high gain, and also reasonably visible-blind detection. However,

device based on these materials requires high power supplies and synchronized instrumentation for proper cooling arrangement. Thermal detectors (such as bolometers and pyrometers) are generally used for calibration in the UV range. Even though beneficial as radiometric standards, the response of these detectors is slow and wavelength-independent. Alternatively, semiconductor-based photodiodes and CCDs provide the assets of solid-state devices that require only moderate bias for functioning. Semiconductor based PDs are miniscule, low cost, lightweight as well as insensitive to magnetic fields. The good sensitivity as well a high-speed operation capability makes them an exquisite material for UV detection. Lately, silicon photodiodes are the most common devices for UV photodetection due to their well-established technology[5]. In Si-based p–n junction UV photodiodes, the devices are coated with a thin oxide layer (SiO_2), which fulfils the role of surface passivation as well as an anti-reflective coating. Since, surface recombination is predominantly detrimental for UV photodetection, particularly for the case of VUV photodiodes. Using this approach, Korde *et al.*[6] realized internal quantum efficiency, η_i equal to 1 in 350–600 nm spectral range while wavelengths (λ) larger than 600 nm, η_i decreases due to the higher penetration of the light, so that the carriers are photogenerated too deeply that it is difficult to reach the p–n junction. Conversely, η_i is larger than unity for $\lambda < 350$ nm, due to the impact ionization process, and decreases sharply for $\lambda < 200$ nm, due to the absorption in the top oxide layer. Therefore, the control of the Si/SiO_2 interface is one of the critical technological processes in such devices.

Regrettably, the operation and feasibility of these UV detectors deterioratewith the time duration it is exposed to UV radiation since continuous exposure can cause damage to the top oxide layer. Conclusively, Si-based UV photodiodes exhibit some limitations that are inherent in silicon technology. The core drawback in these narrow-bandgap semiconductor-based detectors is device ageing, because of the exposure to radiation of energy, which is much higher than the semiconductor bandgap energy. An additional limitation of these devices includes their sensitivity towards low energy photons so that expensive optical filters are essentially employed to block photonsfrom visible and infrared ranges, ensuing a substantial loss of effective area of the instrumentation as well as making them bulky and costly. Lastly, for high-

sensitivity applications, the active area of a detector needs to be cooled to diminish the dark current. Certain evaluations of commercial Si PDs have been studied, which reports the restrictions of this technology [7].

Use of WBG semiconductors (like SiC, some II–V compounds, and III-Nitride compounds) for UV photodetection conquers many of the difficulties listed above. A comparison of material properties of various WBG semiconductors with conventional narrow-bandgap semiconductors is tabularized in Table 1.1. The wide bandgap is itself a significant advantage for PDs, as it offers intrinsic visible-blindness and facilitates room-temperature operation. It is also perceived from Table 1.1 that WBG materials pertain significantly higher thermal conductivity than silicon, which makes them an appropriate material for high-temperature as well as high-power applications. Though the hole and electron mobilities are comparatively lower for WBG semiconductors, still, the electron velocity is typically much larger at higher electric fields. Another advantage is their bond strength, which enhances the radiation hardness. Furthermore, the WBG materials do not require passivation, thereby, enhances the responsivity and stability even at shorter wavelengths. An exciting feature of WBG semiconducting material is negative electron affinity, which usually appears in the materials having a bandgap larger than 5.4 eV (like AlGaN and AlN) and offers efficient visible-blind UV Photodetection.

Table 1.1: Basic parameters comparing various semiconductors used in UV Photodetection.

Property	Si	SiC	GaP	GaN	AlN
Bandgap(eV)	1.12	2.4 – 3.1	2.27	3.4	6.2
Thermal Conductivity(W cm^{-1} K^{-1})	1.5	3.2-4.9	1.1	2.1	3.2
Electron saturation velocity (10^7 cm s^{-1})	1	2	1.25	2.5	1.4
Electron mobility(cm^2 V^{-1} s^{-1})	1400	400-1000	350	1000	135
Hole mobility(cm^2 V^{-1} s^{-1})	600	50-120	100	30	14
Breakdown field(10^5 V cm^{-1})	3	20-24	10	26	20

1.1.2.1 Challenges of using Wide-Bandgap Semiconductors as UV PDs

Irrespective of all the encouraging characteristics, there are still a lot of hindrances that need to be exploited for availing the complete advantage of WBG semiconductors.

a. Mismatch in semiconductor--substrate lattice parameters and high dislocation density even after implementation of hetero-epitaxy as a solution towards the high crystalline quality, found to be a prominent challenge to fabricate defect-free and efficient devices.

b. The obligation of high activation energy to match the threshold level of incorporated dopant materials and severe reduction in carrier mobility due to the presence of unwanted impurities of dopant having the direct impact on electrical transport of the device.

c. Fabrication of devices with highly conductive metal contacts to extract the all possible generated e-h pairs is found to be another challenge.

d. Notwithstanding these difficulties, WBG PDs based on SiC, diamond, and III-Nitrides were already commercialized. A list showing the performance of several commercialized WBG devices is provided in Table 1.2.

Table 1.2: Performance of some commercially available WBG based GaN UV PDs [8].

	CENTRONICPD 1.4	**SVT-GaN0.8D**	**APA OPTICS GaN**
Material	Diamond	GaN	GaN
Spectral range (nm)	130-225	250-360	200-365
Responsivity ($A.W^{-1}$)	0.15 at 200 nm	0.1 at 360 nm	>=0.1 at 325 nm
Dark current	< 1nA	-	<=1-100 nA at -0.5 V
Effective area (mm^2)	1.4	0.50	0.2-20

1.1.3 Nitride based Photodetection Devices: An introduction

III-Nitrides (including, InN, GaN, AlN, as well as their ternary and quaternary alloys) are found to be a premeditated technology for developing highly efficient UV PDs, especially in the late 20th century. They have several benefits, which include ideal spectral selectivity, high thermal stability, radiation hardness, and high

responsivity[9].The direct bandgap of nitride semiconductors is the supreme asset for optoelectronic device applications. Additionally, the wide bandgap of these materials results in low intrinsic carrier density that consecutively leads to low dark current, which is essentially crucial for PDs and high-temperature electronics. Adding to the list, it is also known that III-Nitrides are very robust materials having strong mechanical strength and high melting points. Thus, their ability to resist radiation damage yields a material technology suitable for high-power along with high-temperature applications. Besides, III-Nitride semiconductors, GaN (3.42 eV), and $Al_xGa_{1-x}N$ (3.42 eV - 6.2 eV with x varying between 0 to 1) offer the detection of a complete UV region [10, 11]. Subsequently, there is a simple rule for optimizing best device performance, *i.e.*, the excellent devices come from high-quality epitaxial device layers. Noticeably, the high quality here means that the epitaxial layer structure should match very well with the originally designed structure, and the imperfections should be as low as possible. Thus, an ample amount of considerable issues need to be resolved before employing these materials in establishing fruitful devices. Since the high density of dislocations and low doping probability were amongst the most challenging problems faced by researchers in this particular area. Initially, it was really tough to accept that a material with such high dislocation density (in the order of 10^8-10^{10} cm^{-2}) would become the building block of many viable next generation optoelectronic devices. Owing to the hard work of many researchers who contributed to successfully commercializing the today blue/violet light-emitting diodes (LEDs) and laser diodes (LDs) based on (Al, In, Ga)N.

The photoconductive properties of GaN material were first introduced to the world by Pankove and Berkeyheiser in 1974[12].After that, with progressive technological advancement in theIII-Nitride-based UV PDs found to be instigated in the early 1990s. However, the first GaN-based UV PD was fabricated by Khan *et al.* in 1992[13], wherein afterwards in the late 1990s, WBG GaN had been recognized as a material of the first choice for UV detection.Recently, a brief review about the GaN-based UV PD has been presented by Aggarwal *et al.*[14]Thus, the first phase was focused on state of the art GaN-based UV PDs which discussed the fundamental approach of generating the high signal to noise ratio by opting low defect density

oriented GaN samples. Thereby crystalline quality of as-grown GaN provides lower dark current and higher photocurrent, higher sensitivity, responsivity, detectivity, EQE %, and very low NEP. Moreover, the advantage offered by the direct and wide bandgap of GaN-based PD has also been discussed in detail where the requirement of bulky filters, their cooling arrangement and required instrumentation were completely eliminated. The second phase has been significantly enlightening the importance of a PD device structure where the solution to a quick collection of generated charge carriers has been provided by various structures such as p-n junction, p-π-n, p-i-n, avalanche, Schottky, and MSM PDs.

1.1.3.1 GaN-Nanostructured UV PDs

Recently, the curiosity has been diverted towards using the nanostructured semiconductors for active nanoscale electronic and photonic devices [15-17]. Boruah and Misra demonstrated that light-harvesting efficiency could be drastically incremented by using nanostructures (NSs) [18]. The NSs have played a significant role due to very low stress-strain induced electrical as well as optical defects that reciprocate its significant impact on detector performance[16, 17]. Moreover, NSs were also recognized as a structure with a high surface to volume ratio. The increased surface area in NS offers more absorption sites to incident photons for generating high density of carriers, and lower resistance path, which can cumulatively increase the detection capability of the PDs. Henceforth, growth of high surface-to-volume ratio and stress relaxed 3D GaN-NSs could play a crucial role in the development of highly efficient optoelectronic devices. A comprehensive study by Sang *et al.* discussed the semiconductor UV PDs for thin films as well as NSs [19]. Moreover, it has been also reported that GaN-nanocolumnar crystals exhibit the inherent property of wavelength tunability, low dislocation density and lower lattice related strain[20]. Due to defect-suppression property of nanocolumnar structures, [21, 22] GaN-nanocolumns (GaN-NCs) have also been utilized for efficient UV-PDs fabrication.

1.1.3.2 ZnO/GaN heterostructure based hybridized GaN UV PDs

For UV PDs fabrication, sensing materials (semiconductors) with heterojunctions have been utilized with a common strategic approach of utilizing semiconductors having

comparable bandgap energies, lesser lattice mismatch, and suppressing the interfacial photo carriers' recombination [23]. The heterojunctions with lesser lattice mismatch can achieve high photo-induced charge carrier separation efficiency as well as their efficient opto-electrical transport [24]. The impact of these heterojunction hybridized structures has been realized as increased photodetection, higher responsivity, as well as external quantum efficiency[25-27]. So far, numerous heterojunction based UV PDs such as p-NiO/n-ZnO [28], TiO_2/SnO_2[29], TiO_2/NiO [30], Se/ZnO [31], ZnO/SnO_2[32] and ZnO/GaN [23, 33-43] *etc*. have been fabricated. Among them, ZnO/GaN heterojunction based hybridized UV PDs have attracted considerable attention due to their similar properties as of the epilayer (*i.e.*, GaN) such as analogous crystalline wurtzite structure, better interface [minimum lattice mismatch (1.8%)], wide and direct bandgap [E_{gGaN} (3.4eV), E_{gZnO} (3.3eV)], high thermal coefficient, high carrier mobility, high chemical stability and higher resistance towards electric breakdown field, *etc*. [44]. Su *et al.*[35] and Huang *et al.*[38] demonstrated n-ZnO film /p-GaN film heterojunction UV PDs and displayed responsivity of 0.68 mA/W and 1.5 mA/W, respectively. Recently, nanostructured (ZnO-nanostructures/GaN-film) UV PDs has also received considerable attention due to their high surface to volume ratio which leads to higher photon absorption and correspondingly higher photo-stimulated charge carriers which enhance photo as well as electrical conductivities in the device [39-42]. Vikas *et al.* has fabricated n-ZnO-NRs/p-GaN heterostructure based UV detector has demonstrated responsivity 11 A/W and response time of < ms[42]. Consequently, numerous ZnO-NRs/GaN film nanostructures based UV PDs have been fabricated wherein, highest responsivity value of 437A/W has been demonstrated by Chen *et al.*[43] using n-ZnO/i-ZnO-NRs/p-GaN film heterojunctions UV PDs. Despite major enhancement in opto-electrical properties using the ZnO/GaN heterojunction, the device is still lacking to achieve low dark current, high switching speed and most importantly peak responsivity in the desired UV detection range. Hence, one-dimensional (1D) ZnO-nanostructures such as nanorods (NRs) and nanowires were explored due to high susceptibility to UV-light, high density of surface trap states and enhanced surface-to-volume ratio[44, 45].

1.1.3.3 Au-NPs FunctionalizedZnO/GaN based UV PDs

Functionalization is the process of increasing the functionality of the mother structure materials (GaN and ZnO here) by incorporating additional features, properties, and capabilities by means of changing the surface chemistry. It is a fundamental approach widely accepted universally in chemistry, biological and material science engineering, and nanotechnology. Particularly in the case of PDs development, these functionalizing agent works as opto and electrical catalysts which enhance the detection capability of the detector. Henceforth, the involvement of nanoplasmonics in nitride materials has been gaining substantial attention in the field of PD research due to metal nanoparticle-induced localized surface plasmon resonance (LSPR) effect[46-49]. The LSPR generated from the light-induced collective oscillation of free conduction band electrons at the interface between metal nanoparticles (NPs) and dielectrics[50], leading to strong absorption, scattering, damping, relaxation, dissipation, and local field enhancement as shown in Figure 1.3.

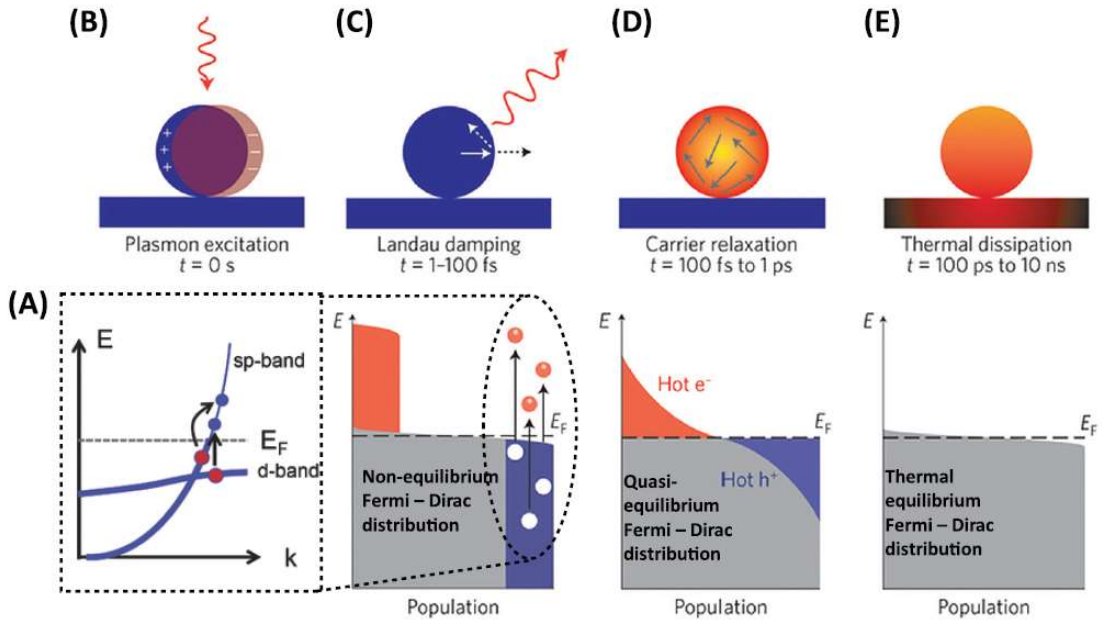

Figure 1.3: (A) Electron–hole pairs (EHPs) generation in Au intraband, (B) local surface plasmon excitation by incident photons, (C) thermal distribution of EHPs (in 1–100 fs) radiatively (through Landau damping) and generation of hot resonant carriers (non-radiatively), (D) Hot carriers energy redistribution (relaxation) by electrons scattering (in 100 fs to 1 ps),(E) Thermal dissipation by electron-phonon scattering (in ps) and from the NP to mother material (in ps to ns). Adopted from Brongersma *et al.*[51]

These LSPR or NP's nanoplasmonic characteristics are very sensitive to size, the shape of NPs, plasmon energy, plasmon mode symmetry, the density of state of material and electronic structure[52]. Thus, these novel metal NP's nanoplasmonic property has been explored for enhancing PD performance[46, 53]. The reports suggest that the defect emission energy of ZnO, as well as GaN, matches very well with the LSPR excitation energy. Therefore, the NP's LSPR effect excited by these semiconductor defect band emissions generates hot resonance electrons, which will be combined with the already existing electrons of the conduction band of ZnO[54] and GaN[55, 56]. This increases the density of carriers in the conduction band of the heterojunction device and is reflected as improved photocurrent as well as the enhanced performance of the developed UV detection device.Some previous reports also found in coherence with the fact that the use of NP's nanoplasmonics such as platinum (Pt) NPs[47], aluminium (Al) NPs[48], silver (Ag)[46]and gold (Au) NPs[49] have been realized as a solution for the carrier enhancement seeker GaN-based UV-PDs. Among them, the utilization of Au-NPs has proven to be noteworthy in LSPR due to advantageous inherent physical properties like high physio-chemical stability, non-linear optics, magneto-plasmonic, optically active,[57] and ease of surface functionalization with plasmon oriented multitude of optical properties [58, 59]. Similarly, Au-NPs decorated ZnO nanostructures based UV detectors result in improved performance by reducing the dark current via the LSPR effect[56, 60].

1.1.3.4 GQDs Sensitized ZnO/GaN-NSs UV PDs

The fabricated ZnO and GaN nanostructure-based UV PDs have shown remarkable enhancement in their performance by integrating with semiconductor quantum dots (CdS, CdSe, PbS, CdTe and graphene quantum dots(GQDs),*etc*.). The presence of these quantum dots in the photodetection devices was appreciated by enhanced photoconductivity and suppressed carrier recombination [61-66]. Among these quantum dots, the latest addition of nanocarbon materials family,*i.e.*, graphene quantum dots (GQDs) are getting more attention due to their unique merits such as excellent dispersibility, better tunability in chemico-physical properties, abundant active sites, catalytic ability and bandgap opening due to quantum confinement[67]. GQDs have progressed as a novel carbon-based nanomaterial with zero dimension

(0D), comprising 2 to 10 monolayer graphene (size ~30 nm). These GQDs were also known for the unique opto-electrical properties, which helps them to find their suitability in an extensive range of applications such as electroluminescence, photocatalysis, solar cells, bioimaging, LEDs, and photodetector devices. Moreover, GQDs are also known for their semiconductor behaviour,[68] higher mobility at lesser bias voltage [69] and nano-dimensionality (<100 nm), which allow them the ease of settle down on the surface of detector fabrication mother material (ZnO, GaN,*etc*.) structure. The impact of GQDs sensitization on GaN-film and ZnO-NRs on UV PD's performance has been realized by Lin *et al.*,[64], Dhar *et al.*[70]and Rahimi *et al.*[65], respectively, wherein, photo-induced extra charge carriers by GQDs has guided towards enhanced photodetection. Moreover, the presence of GQDs also helps in faster collection of the photogenerated charge carrier leading to reduce response time. Lately, Liu *et al.* have reported GQDs sensitized ZnO-NRs/ GaN-film (MOCVD) heterostructure based UV PD. However, the reported responsivity of the detector is very low (~34mA/W) even at very high applied bias voltage of 10V [66].

1.2 III-Nitride Semiconductors: An Emerging Technology

The evolving advancements in technologies have become an essential part of our lives in countless ways. So far, the technology of silicon semiconductor materials for the development of devices, which include transistors, diodes, integrated chips, and microprocessorunits, has indirectly affected human life in every aspect. Correspondingly, III-Nitride semiconductors are dignified to change our lives profoundly. There are several pivotal developments, which held accountablefor setting the technical framework, which paved the way for remarkable commercial and research curiosity in III-Nitrides. The importance of III-Nitride semiconductor technology has rapidly gained attention in the last few years due to a substantialamount of commercial and defence applications. III-Nitride semiconductors with binary, ternary, and quaternary compounds established themselves for the fabrication of device having operability in the diverse range from 0.7eV to 6.2eV. The rapid progress in the development of nitride materials empowers the fast commercialization of semiconductor devices having new capabilities and

brings about the reinvention of existing technologies.The interest in III-Nitride based semiconductor devices has been the focus of research mainly because of their enormous potential in optoelectronic applications, which include light-emitting diodes (LEDs), laser diodes (LDs), solar cells, photodetectors (PDs), *etc*. [15, 71-75]Such applications necessitateenhanced material quality and superior device design, which is possible only by acquiring a good knowledge of nitride material's growth and fabrication parameters to meet our growing hi-tech needs.Among nitrides, GaN has become a remarkable semiconducting material in the industry of optoelectronic devices due to its magnificent properties such as wide direct bandgap, good thermal stability, strong piezoelectricity, and high thermal conductivity[76].Mainly, the crystal structures for GaNare classified as cubic zincblende and hexagonal wurtzite. Both can co-exist simultaneously under various conditionsdepending upon the crystal growth[77]. The cubic structure is thermodynamically metastable while, the wurtzite structure is thermodynamically stable.

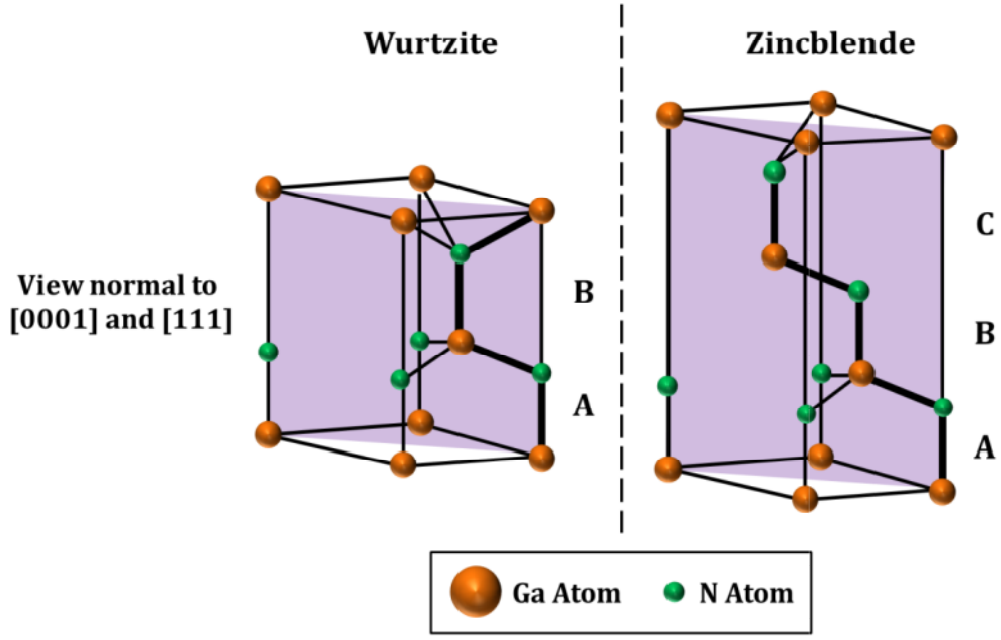

Figure 1.4: The wurtzite and zincblende crystal structures of Gallium Nitride in stick-and-ball stacking model representation**.**

The wurtzite structure found to be ordered with an ABAB stacking sequences along the *c*-direction andthe lattice points in hexagonal wurtzite structures are indexed by four indices *h*, *k*, *i*, *l*, where $i = -(h+k)$. The first three indices correspond to the

equivalent *a*-direction vector in the basal plane, and the last index corresponds to the *c*-direction vector. Figure 1.4 shows the fundamental lattice vectors of the basal plane in the hexagonal wurtzite structure. For negative vectors, a bar is used over-index.In general, indices surrounded by square brackets "[ ]" or angled brackets "<>" are applied to describe a direction and a family of direction, respectively. Indices surrounded by parentheses "( )" are used to describe a plane and a family of planes, respectively. It is necessary to point out that [*h k i l*] direction is not normal to (*h k i l*) plane in real space unless l =0 or $h = k$ =0. Besides, various planes of GaN are represented in Figure 1.5. In GaN wurtzite hexagonal system, the c-plane is on the top of the hexagonal unit. This plane is called the polar oriented plane where the termination is either Ga or N ions, so there is always a net charge on this plane. The m- and a- plane (yellow and blue colour planes Figure 1.5) are at the side wall of the hexagonal system, they belongs to non-polar oriented planes.

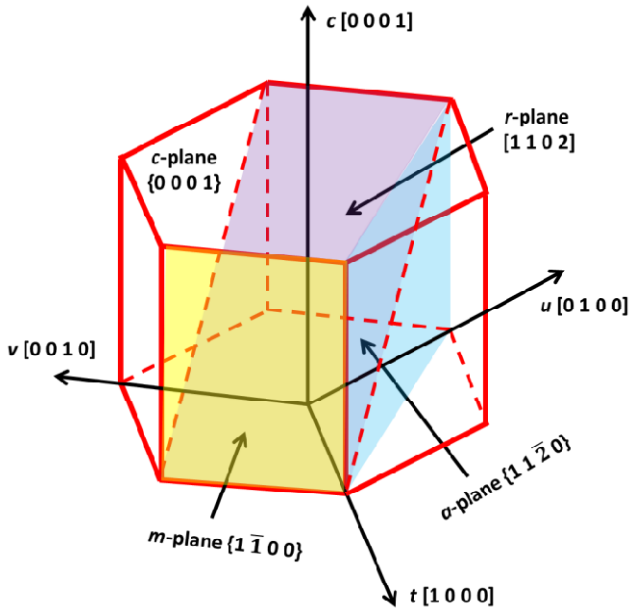

Figure 1.5: Schematic representation of different planes (c-, a-, r- and m-planes) of GaN.

Here, the termination is both by Ga and N ions so that the net charge will be neutralized. While r-plane (the violet colour plane in Figure 1.5) is a semi-polar oriented surface where the termination is dominated either by Ga or N ions leading to semi-polarity on the surface. Moreover, it is vital to mention that in the Ga-polar (0001) and N-polar (000$\bar{1}$) surfaces of the wurtzite structure are not equivalent, and

they exhibit dissimilar chemical properties. The (0001) and (000$\bar{1}$) polarity depends on whether Ga atoms or N atoms terminate at the top of (0002) bilayer as represented in Figure 1.6. Usually, the Ga-polar GaN iscomparatively more chemically stable and smooth surface than N-polar GaN. Some basic physical properties for group III-Nitride semiconducting materials are listed in Table 1.3.

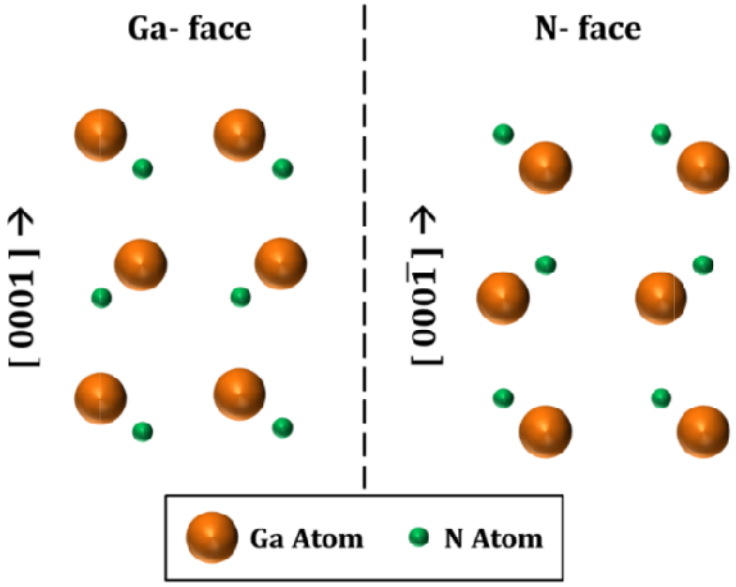

Figure 1.6: The wurtzite GaN in Ga- and N- Polarity.

Table 1.3: Basic properties of group III-Nitride semiconductors[8].

Physical Property	**AlN**	**GaN**	**InN**
E_g (eV)	6.2	3.44	0.7
Thermal Expansion coefficient (300 K)			
a (x 10^{-6} K^{-1})	4.2	5.59	5.59
c (x 10^{-6} K^{-1})	5.3	3.17	3.7
Lattice constant (300 K)			
a (Å)	3.112	3.189	3.545
c (Å)	4.982	5.185	5.703
Bond Length (Å)	1.89	1.94	2.15
Cohesive Energy per Bond (eV)	2.88	2.24	1.93
Melting point (°C)	>3000	>2500	>1100
Density (g/cm^3)	3.26	6.10	6.99

Besides, the direct growth of GaN on Si substrate may lead to a high amount of defects and cracks due to lattice-mismatch (17%) and thermal expansion coefficient mismatch between the substrate and the epitaxial film. Consequently, these defects states instigate degradations in structural, morphological, and optical properties. Thus, the introduction of a buffer layer is extremely necessary as it plays a crucial role in improving the crystalline quality and reducing the defect states in epitaxial GaN films. Though, the effect of the AlN buffer layer has been studiedon the properties of GaN films [78]. However, the impact of these AlN buffer layers on the performance of UV PD devices is not yet explored much in detail. Thus, the development in nitride device technology has transformed the material requirements for efficacious growth as well as device fabrication processes. The growth kinetics involved in synthesizing various III-Nitrides as well as growth techniques utilized for it will be elaborated in the next sections.

1.3 Growth Dynamics of III-Nitrides

The growth process is affected by a variety of factors, including substrate material, impinging flux of adatoms, the growth parameters, and surface interaction with the adatoms. The growth mechanism can be explained by adatoms residing on the surface of a substrate, which involvesthe existence of several surface phenomena. These are presented in Figure 1.7, which includes adatom adsorption on the surface, desorption from the surface, surface diffusion, and diffusion towards nucleation site having the lowest surface free energy. The surface free energy quantifies the disturbance in intermolecular bonds when any surface is formed. Since the adatoms have a tendency to acquire the site with the lowest surface free energy. The adatom diffusion occurs towards the nucleation site, which was created by defects/dislocations in the lattice and exhibit low surface free energy.The general growth kinetics is based on surface diffusion, which is explained as follows. When adatom arrived at the target surface (substrate), the incident atoms generally lose their momentum perpendicular to the surface, while receiving kinetic energy from the substrate for their in-plane diffusive motions, and the energy depends on the substrate temperature.

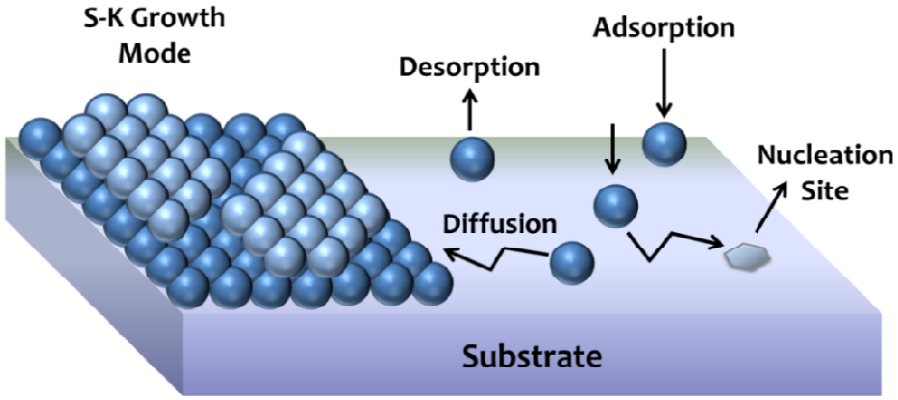

Figure 1.7: A schematic representation of various microscopic kinetic processes during growth.

Such diffusionmay be described by a two-dimensional (2-D) "random-walk" model on the surface by "hopping" from one site to another. While the free random-walk of the adatoms will stop due to some other kinetic effects on the surface, such as nucleation, adatom attachment, desorption from the substrate, *etc*. which are illustrated in Figure 1.7[79]. The mobility of such diffusing adatoms can be given by:

$$r_s = a \exp\left(\frac{E_{des} - E_{sd}}{2k_B T}\right) \quad (1.1)$$

Where r_s is the "mean displacement" of the diffusion, and $T$is substrate temperature.E_{des}, E_{sd} are the activation energies of the surface desorption and diffusion, respectively. The k_B is the Boltzmann constant, while 'a' is the adsorption site spacing, which is determined by the lattice of the surface. This suggests that a proper substrate temperature maintains sufficient diffusion on the surface leads to an improvement in the surface morphology.

Over the past few years, numerousefforts have been made to grow high-quality III-Nitride epitaxial films using variousgrowth techniques on selective substrate-types and different orientations.Progressively, researchers have successfully exploited the advantagesof metal-organic vapour phase epitaxy (MOVPE), hydride vapour phase epitaxy (HVPE), and plasma-assisted molecular beam epitaxy (PAMBE) techniques, which ensures significantly enhanced film quality.As the technology of thin-film growth advances, each new emerging growth technique has beentested for the nitride problem, and several different substrates were also explored, which will be discussed in the next section of this chapter.

1.3.1 Choice of Substrates

A wide variety of materials have been used as a substrate for growing the nitride epitaxial layers[8].However, the choice of substrate for GaN epitaxy is very crucial as the quality of grown layers depends intensely on the properties of the substrates - both the innate properties like lattice mismatch and thermal expansion coefficient mismatch, and the growth process affected properties such as stress generation, defect formation, and surface roughness[8].When the GaN growth is carried out on GaN templates itself, it is known as homoepitaxial growth, and it offers the benefit of better control over the crystalline quality with reduced defects and dislocations in the grown layers so as to fabricate a device with enhanced performance. These defects and dislocations are the foremost origins of stress or strain in the grown films. But, III-Nitride materials are usually heteroepitaxial grown on foreign substrate since bulk GaN crystal are not commonly available and very expensive. Extensive effortshave been carried outto overcome the challenges exist due to lack of suitable substrate material which is lattice matched and thermally compatible with GaN. Amongst, the lattice constant mismatch is a primary concern for determining the appropriate substrate material for GaN epitaxy. Lattice mismatch is defined as the difference between the lattice constant of two crystals with different lattice planes. Lattice mismatch usually prevents growth of a defect-free epitaxial film. If a film grows coherently on a thick substrate, a uniform stress will build up due to lattice mismatch. The stress state of heteroepitaxial layers depends on whether the in-plane lattice space of the epitaxial film is smaller or larger than that of the substrate. Figure 1.8 illustrates two cases of strain: compressive ($a_{film}>a_{substrate}$) and tensile ($a_{film}<a_{substrate}$).

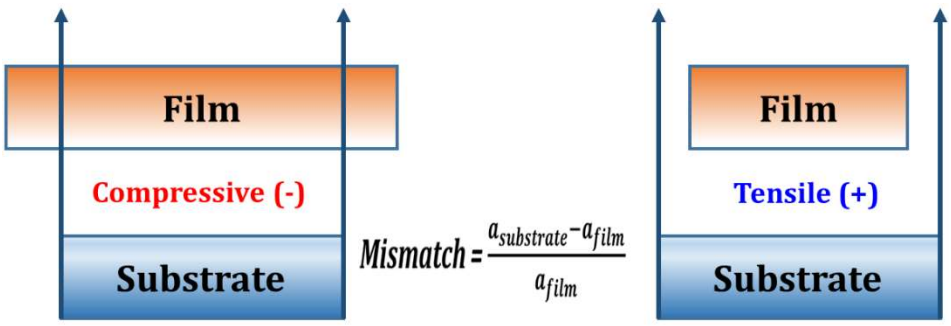

Figure 1.8: Schematic diagrams are showing a compressive strain state (when $a_{substrate}<a_{film}$) and tensile strain (when $a_{substrate}>a_{film}$).

However, other material properties such asthe crystal structure, surface morphology, strain, and composition, chemical, thermal, optical,and electrical properties also play an essential role in determining a suitable substrate for growing an epitaxial layer. As the substrate properties eventually define whether the device will be able to yield optimal performance or not. Thusresearchers extended their efforts of growth on foreign substrates, which is known as hetero-epitaxy, for better growth quality anddevice fabrication. Due to the lack of an ideal substrate, sapphire has been primarily utilized for GaN growth, most commonly the (0001) orientation. The sapphire substrates were endorsed due to their wide availability, the hexagonal structure, which is similar to GaN, and ease of handling and pre-growth cleaning process. Additionally, sapphire is stable even at higher temperatures (1000°C), which is required for epitaxial nitride growth using various commonly employed growth techniques. Afterestablishing that, the crystal structure of epitaxial GaN is strongly inclinedon the substrate material and its orientation, it has become necessary for researchers to dedicateextra attention to improving the growth quality of nitrides on different substrates. A wide range of substrates was explored for the GaN epitaxy, including SiC, sapphire, silicon, *etc*. Due to the adverse consequence of heteroepitaxial growth, nitride films are bound by some degree of strain, which could be introduced during the post-growth cooling process. Due to the thermal mismatch between epitaxial GaN and various different substrate materials, a number of adverse effects have been witnessedby the researchers. For instance, Chu's group [80] observed cracking of SiC substrates on which GaN was grown, and Grimeiss and Monemar[81] noticed the same for sapphire substrates.Since GaN is a strong and robust material, and a sufficiently thick film may generate cracks in the substrate.In this thesis, the growth of the III-Nitride binary compound, *i.e.*, GaN on Si (111) substrate, has been discussed.

1.3.2 Growth Technique: Molecular Beam Epitaxy

The growth of high-quality III-Nitride films is the prerequisite for highly-efficient III-Nitride based devices. Among various techniques employed for the growth of nitrides such as HVPE, MOVPE, MOCVD and MBE, molecular beam epitaxy (MBE) is considered as one of the most promising and successful methods because it offers

precise control over the growth parameters, deep understanding of each growth step, in situ growth monitoring, and successful repeatability of growth [82]. The term "molecular beam epitaxy" was first used in the 1970s, but the concept of MBE originated even before that. MBE distinctly differs from other evaporation systems due to their precise flux control. For example, modern MBE systems can grow with layer thickness control of the order of a half monolayer. It is proven to be an effective approach for growing epitaxial thin films. Elemental sources in the ultra-pure gas form are directed towards a heated substrate under ultra-high vacuum (UHV), typically in the range of 10^{-5}to10^{-11}torr. A radio-frequency (RF) plasma system is employed to form atomic nitrogen species by breaking the chemical bonds of the nitrogen gas molecules. The RF-plasma system contains a gas source inlet, a matching-unit, a plasma generator, and a cooling water system. The growth temperature of III-Nitrides is usually in the range of 500-850°C. A higher growth temperature will result in a lower growth rate because the forward and reverse reactions happen at the same time with different rates. Along with the impinging flux from the group-III and N source, the substrate temperature is one of the key parameters which can control the growth of materials. The substrate temperature can either raise or lower the adatom mobility of impinging material, with higher temperatures leading to higher mobility. A great deal of research has been done to optimize the growth of GaN and other III-Nitride materials grown by PAMBE. One standard method to optimize growth is to adjust the ratio of impinging Ga to N (or III/V ratio) as well as substrate temperature and determine the effect on the ensuing material. By growing samples under different combinations of substrate temperature and III/V flux ratio,Koblmüller *et al.*have established different regions of GaN growth, and summarized them into surface growth phase diagrams[83-85]. Such growth phase diagram (shown in Figure1.9)is extremely helpful forthe growth of nitrides via MBE because they can use it to target certain parameters for their own thin-film growths. Also, a higher V/III ratio will prevent the dissociation of GaN. A low growth rate of less than 1μm/hr enables layer-by-layer growth. The epilayers exhibit extremelysharp interfaces. The UHV environment allows real-time monitoring of growth rate, film thickness, alloy composition, and atomic reconstruction via *in-situ* reflection high-energy electron diffraction (RHEED) technique[86].

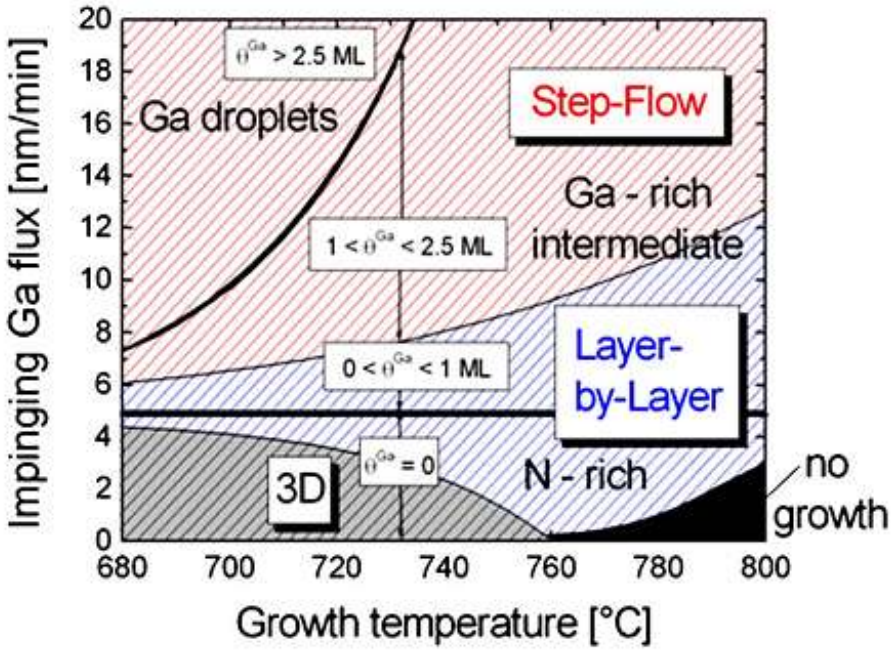

Figure 1.9: A phase diagram for GaN growth by PAMBE from Koblmuller *et al.*[84]

Although, there are some disadvantages of MBE growth of III-Nitrides such as the requirement of UHV, slower growth rate, and difficulty in processing multiple wafers. Because of these drawbacks, MBE is not widely used for commercial applications. The MBE growth can be described as a crystallizing process of the incident atoms or molecules on a target substrate in a UHV system. Because the scattering by the gas molecules in the environment is effectively lowered, the source atoms can be considered to travel in straight linear paths in the growth chamber, which form the "molecular beams."Thus, MBE is proved to be an advanced method for synthesizing single-crystalline thin-film structuresthat enables the realization of highly advanced semiconductor heterostructures. The huge advancement in the control of MBE growth has transformed a sophisticated research tool into a system of commercial production of semiconductor materials, which will further be utilized for the production of highly advanced optoelectronic devices such as LEDs, solar cells, laser diodes, photodetectors, *etc*.

1.3.3 Growth of Nanostructured Nitrides: A Review

A huge curiosity has emerged in the use of semiconductor nanostructures (NSs) for active nanoscale electronic and photonic devices [16,87-89]. III-Nitride

semiconductors are recognized to be potential candidates due to tunability of bandgap, strong interatomic bonds, and sustainability in harsh environmental conditions [90]. However, its interest has been extended because of the material potential to fabricate solar cells, lasers, sensors, high-frequency electronics, *etc*[91-94]. The growth of low-dimensional structures are predicted as promising designs to be used for enhancing the device properties due to high surface-to-volume ratio[95]. Thus, to fabricate high-efficiency devices based on GaN NSs, GaN growth should be realized by following Stranski–Krastanov growth mode (as represented in Figure 1.7) [96]. Now, there exist two vapour-phase growth mechanisms of NSs,*i.e.*, vapour–solid (VS) and vapour–liquid-solid (VLS) mechanisms. In contrast to the restricted growth of NSs due to the requirement of metal catalysts in the VLS mechanism, the VS mechanism can provide more freedom in the formation of nano-flowers (NFs) like structures without the catalyst. Several studies for growing catalyst-free NSs have been reported. For example, Kumar *et al.* proposed a qualitative mechanism for the growth of self-assembled flower-like NSs of GaN using droplet epitaxy (DE) and molecular beam epitaxy (MBE) (Figure 1.10 (a))[97], similarly Aggarwal *et al.* demonstrated a self-assembled nanoflower growth on Si (111) substrate using plasma assisted MBE (Figure 1.10 (b))[74], Dhamodaran *et al.*[98] and Shin *et al.*[99]presented growth of GaN-nanoflower based nanostructures on Si as shown in Figure 1.10 (c) and 1.10 (d), respectively. Besides, a compact and nanocolumnar growth regime for the growth of GaN nano-columns has been elaborated by Fernández-Garrido *et al.* which indicates that adatom's diffusion length and Ga/N ratio are the key factors to accomplish desired growth (Figure 1.10 (e))[100],Wang *et al.* demonstrated the growth of GaN-nanotower by chemical vapor depostion route(Figure 1.10 (f))[101] and Debnath *et al.* demonstrated the catalyst free GaN nanowires growth on Si (111) substrate by PAMBE where the longer deposition time compared to nucleation stage will decrease the length of nanowires (Figure 1.10 (g))[102].Moreover, Koester *et al.* displayed self-assembled growth of GaN single crystal nanowire on sapphire substrates without any catalytic intervention using MOVPE technique (Figure 1.10 (h)),[103]and another interesting GaN nanostructure *i.e.*, single crystal GaN nanotubes were synthesized by the Lu *et al.*[104] using MOCVD technique where GaN nanotubes were perceived with and without Ga filled cores (Figure 1.10 (i)).This thesis focuses on the growth of

low (nanoisland-like) and high (nanotowar-like) aspect ratio structures as they have a range of surface-to-volume ratios and are expected to deliver corresponding higher efficiency than other NSs and also review the journey of GaN NTs from epitaxial growth to fabricating highly efficient optoelectronic devices. Till date, a wide variety of GaN NSs has been grown by various growth techniquesas shown in Figure 1.10

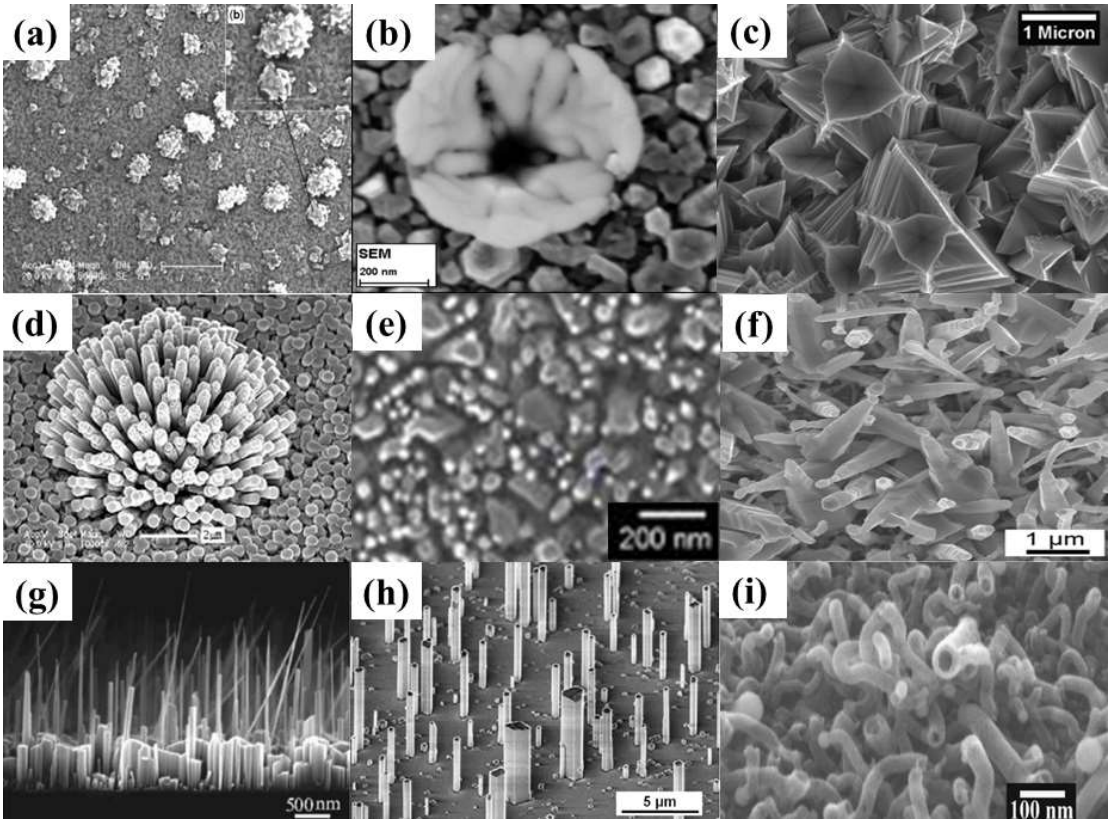

Figure 1.10: FESEM images of GaN (a-d) Nanoflower on Si (using MBE) [97], (b) Nanoflower on Si (using PAMBE technique)[74], (c) Nanoflower on Si (using CVD) [98],(d) Nanoflower on Si (using HVPE technique) [99], (e) Nanocolumns on Si (using PAMBE technique)[100], (f) Nanotower on Si (by CVD technique)[101], (g) Nanowires on Si (by PAMBE technique)[102], (h) Single crystal nanowire (using MOVPE) [103] and (i) Nanotubes (using MOCVD) [104].

Conclusively, this thesis will be focusing on the epitaxial growth of low and high surface to volume ratio oriented GaN NSs on Si (111) substrate and then discuss fabrication of state-of-the-art GaN-NS based UV photodetection devices. Besides, the effort made in this work excavates and execute the new prospects for emerging next-generation highly efficient photodetectors via.ZnO/GaN heterojunction hybridization, Au-NPs functionalization, and GQDs sensitization.

1.4 Statement of the research problem

The thesis aims to grow low and high surface to volume ratio oriented III-Nitridenanostructures on Si (111) substrate by using the PAMBE system in nitrogen-rich conditionsfollowed by the design and fabrication of photodetection devices in MSM geometry for energy-efficient photodetection applications. Furthermore, the impact of hybridization, functionalization, and sensitization on fabricated detectors towards the possibility of enhancing performance have also been meticulously studied. The thesis fundamentally targets the following objectives:

I. To study the effect of Growth conditions (temperature as well as RF-plasma power) on epitaxial GaN films grown on Si (111) substrate via PAMBE.

II. The epitaxial growth of the low aspect ratio GaN nanostructures on Si (111) substrate and find its application as Energy efficient (self-powered) Ultra-Thin GaN nanostructured UV photodetector.

III. The epitaxial growth of the high aspect ratio GaN nanostructures on Si (111) substrate and find their application in energy-efficient (self-powered) UV photodetectors.

IV. Realization of performance enhancement of fabricated GaN-based UV photodetectors by means of hybridization using compatible materials.

V. To analyse the impact of functionalization using metal nanoparticle nanoplasmonics on the performance of fabricated GaN-based UV photodetectors.

VI. To study the scope of performance enhancement of fabricated GaN-based UV photodetectors by means of sensitization using highly conductive quantum dots.

2.1 Introduction

The III-Nitride semiconducting materials have gained rapid progress in the field of technology due to the rising demand of miniaturized device assembly with an advantage of highly stable and robust device performance. Many techniques can be employed for growing these III-Nitride semiconductors such as CVD, MBE, PLD, HVPE, *etc*. In this study, the MBE technique has been utilized for growing various binary and ternary compounds of nitride semiconductors. Furthermore, nitride semiconductors possess quite interesting physical, optical, chemical, and electronic properties, which lead to the curiosity of performing a systematic study for evaluating and analyzing these properties in detail. Therefore, this chapter illustrates the detailed mechanisms involved in the growth of nitride-based semiconductors as well as characterization techniques applied to check the quality of grown layers/structures along with the technological process employed to fabricate the optoelectronic devices.

2.2 Growth Technique: Plasma Assisted Molecular Beam Epitaxy (PAMBE)

The system employed in this work is a nitrogen plasma-assisted epitaxy system for the growth of III-Nitride semiconducting materials. In epitaxial growth, there should be an ordered arrangement of atoms creating a precise crystal orientation of the film w.r.t. its substrate. For the efficient operation of an electronic device, the substrate used is a single crystal (usually Si or sapphire), and so is the epitaxial layer (epilayer). In MBE, the substrate is placed in UHV, having a range of 10^{-10} to 10^{-11}torr, and the desired source materials are evaporated on it from elemental sources. The vaporized molecules or atoms flow in the form of a beam guided by UHV to reach the surface of the substrate and get adsorbed it. Once adsorbed on the surface, these atoms experience surface diffusion until they reach a thermodynamically stable site to create bond with the substrate. Since the surface diffusion of atoms takes some specific time, thus, the quality of the grown film will be better with a slower growth rate. Typically, the growth rates of nearly 1 ML/s can provide sufficiently high-quality epilayers. The Riber Compact 21 PAMBE system installed in our lab (CSIR-NPL) shown in Figure 2.1 is used to grow high quality and extremely crystalline III-Nitride materials and provide precise control over the growth parameters. The ergonomic design, highest quality

material, and highest reliability are key criteria in the design and manufacture of the system. It consists of three UHV chambers, namely: Load-lock chamber (to load/unload the 6-platen cassette carrying wafers into the system), Buffer chamber (to store and outgas the wafers) and Growth chamber (to perform the epitaxial growth of compound semiconductor materials). Other main parts of the system include a number of pumps and gate valves (to achieve and maintain ultra-high vacuum), a lift (to move cassette vertically between load-lock and buffer chamber), and a magnetic transfer arm (to transfer the platen between buffer and growth chamber). The main growth chamber is a vertical UHV reactor equipped with standard effusion cells, (to supply ultrapure III group materials and dopants), an rf–plasma source (ADDON) to supply active nitrogen (N*) species, an RHEED gun (to real-time monitor the growth of crystalline layers during the growth processes), a residual gas analyzer (RGA), a rotating manipulator, a flux gauge, cryo-panels, a cryo pumping system and viewports.

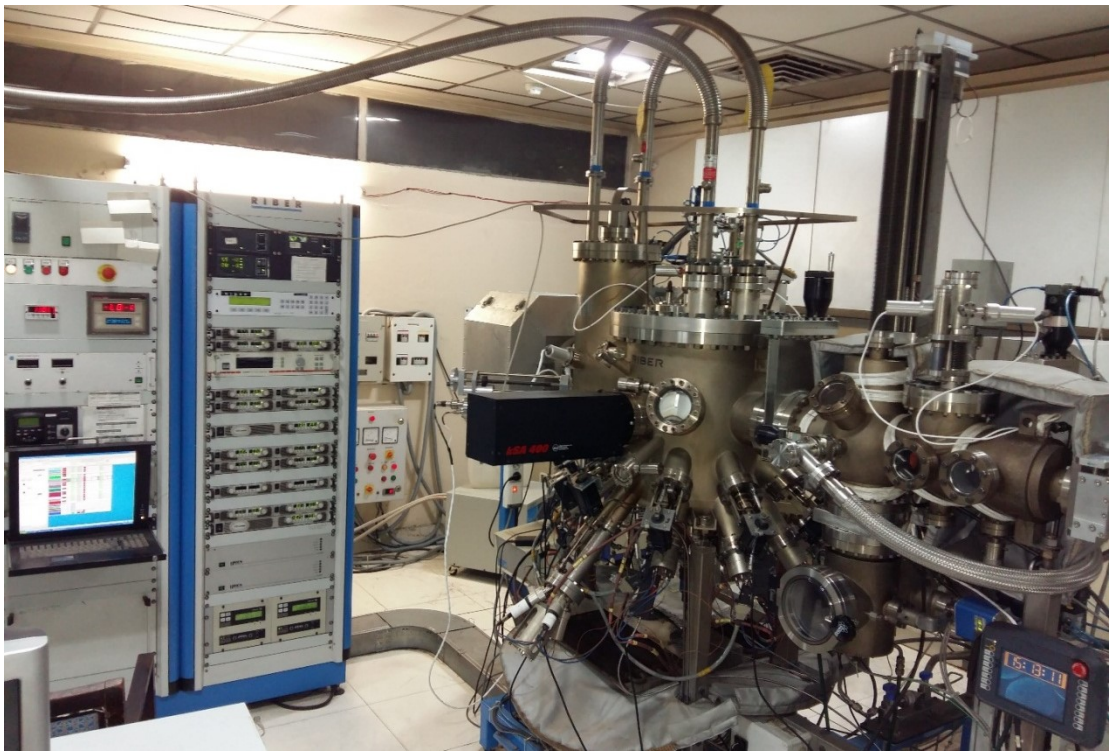

Figure2.1: Plasma - Assisted Molecular Beam Epitaxy System at CSIR-NPL, New Delhi.

Moreover, the substrate temperature in the growth chamber was monitored by an optical pyrometer and kSA bandit temperature sensor (with a resolution of 0.1 °C). The substrates used in this work were c-plane Sapphire, a-plane sapphire, and Silicon oriented

(111). The Molybdenum metal is deposited on the rough backside to promote thermal absorption in the case of the sapphire substrate as sapphire is IR transparent. In the PAMBE system, the substrate is pre-cleaned chemically and then inserted into a load-lock chamber where it is annealed up to 120 °C to remove moisture or any other water contaminants from the substrate's surface. Later, the substrate was shifted to the buffer chamber where it was annealed on a degas oven up to 600 °C to remove other contaminants, which include undesired oxide and other impurities from the substrate. Then, the substrate will be transferred to the growth chamber via a magnetically coupled transfer arm. A schematic diagram of the PAMBE growth chamber is represented in Figure 2.2. The group III-metal sources and dopant materials are introduced through an effusion cell, where a solid material is placed in a crucible, typically made of pyrolytic boron nitride (PBN) and heated until the material sublimates or evaporates.

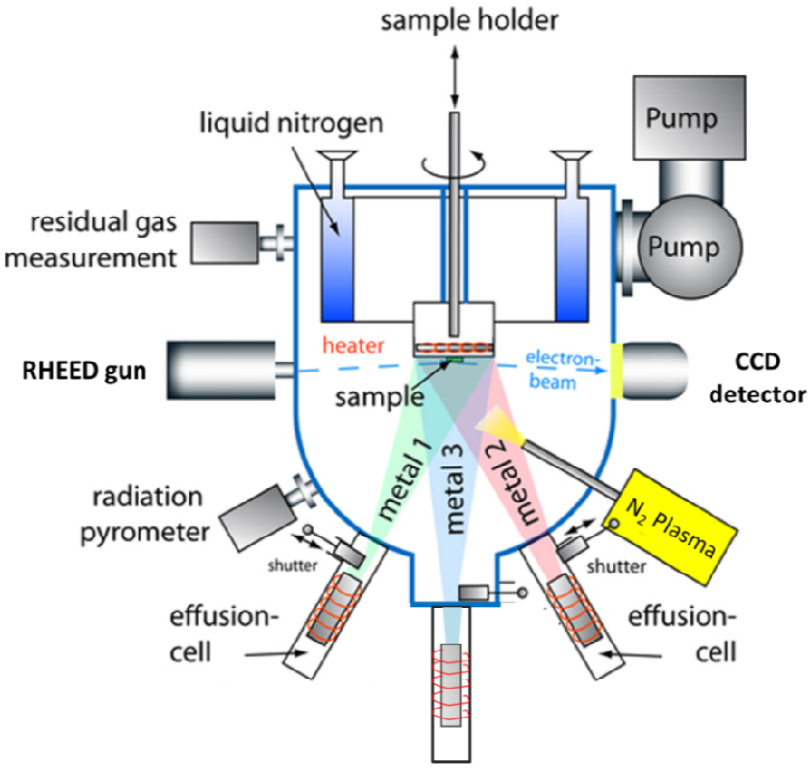

Figure 2.2: Schematics of MBE growth Chamber (Courtesy of http://en.rusnano.com).

Each effusion cell acts as a source of one individual element in the system. The effusion cell, also identified as Knudsen cell, contains the elemental form of sources with anextremely high level of purity,*i.e.*, 99.999% (Figure 2.3). The temperature of

the effusion cells is controlled by proportional-integral-derivative (PID) control parameters. For nitrogen source, the PAMBE system is incorporated with a nitrogen RF - plasma source, where highly purified N_2 is converted into a more active atomic and molecular species. The computer-controlled shutters placed in front of each effusion cell permits precise control of the thickness of each grown layer at a monolayer level. This allows the system to be able to produce different quantum well structures or even quantum dots. As such layers are an integral part of several modern technology applications, including semiconductor lasers and LEDs. The most important feature of the PAMBE system is a very low deposition rate that permits the films to grow epitaxially. These deposition rates need a proportionately higher vacuum to realize constant impurity levels as alternative deposition techniques. The absence of carrier gases along with the UHV environment in the PAMBE technique aids in achieving the growth of highly pure thin films.

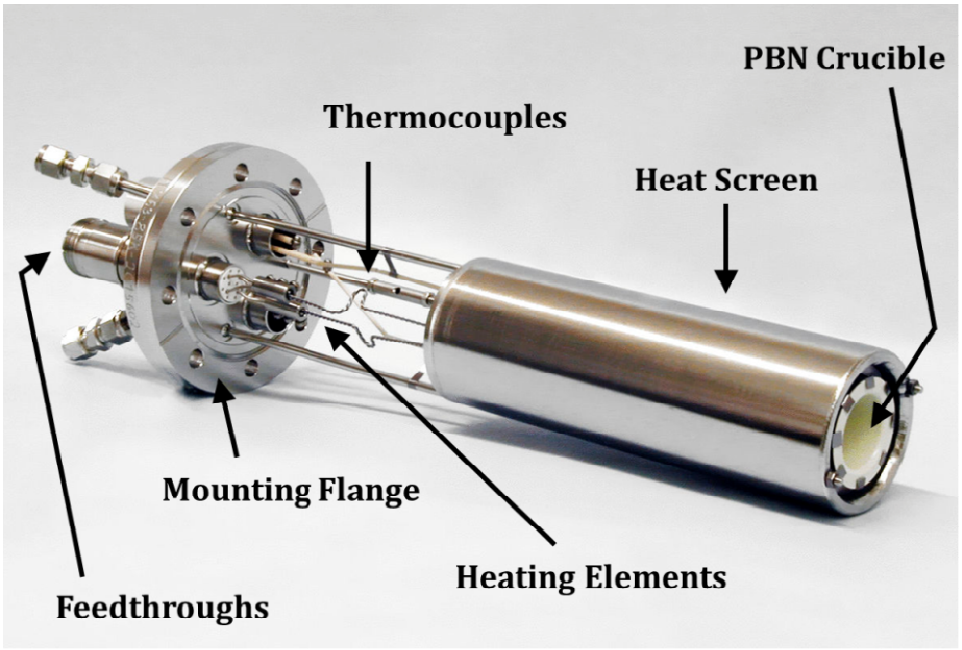

Figure 2.3: An Effusion Cell.

2.3 *In-situ* Characterization Techniques

As mentioned previously, MBE systems maintain a base pressure less than 10^{-11}torr. This base pressure allows for sophisticated *in-situ* growth analysis, such as RHEED.

2.3.1 Reflection High-Energy Electron Diffraction (RHEED)

A RHEED system (Figure 2.4) uses an electron gun (STAIB, 12 keV) that produces a beam of electrons that strikes the sample surface at a very small angle. The incident electrons which are being diffracted by the atoms present at the surface of the sample interfere constructively at definite angles to create regular patterns on a fluorescent screen, which was recorded via a charged coupled device (CCD) camera. The electrons interfere according to the position of the atoms on the sample surface, giving an indication of the growth mode. The bottom right inset of Figure 2.4 displays a typical RHEED image in which the streaky pattern governs 2D growth mode. RHEED analysis is only a surface technique. It is not able to determine the bulk quality. Oscillations of the RHEED intensity (RHEED transients) can also provide information about the time needed to grow a monolayer of material. However, RHEED transients are rarely observed on III-Nitrides, because layer by layer growth does not occur usually. During operation, RHEED is often used for *in-situ* monitoring the growth of epitaxial layers.

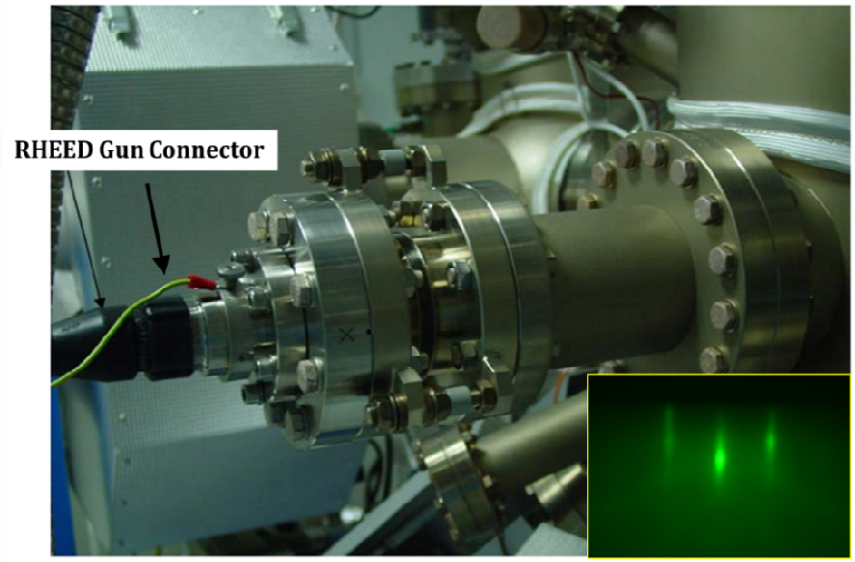

Figure 2.4: RHEED Gun on Compact 21 PAMBE system; A typical RHEED pattern (inset).

2.4 *Ex-Situ* Characterization Techniques

2.4.1 High Resolution X-Ray Diffraction (HRXRD)

HRXRD is a non-destructive technique where a crystal structure is probed with x-rays to evaluate the structural quality involving the lattice parameters, composition, strain/stress, as well as the defect densities present in the III-Nitride epitaxial layers

and their device structures. The X'Pert PRO MRD (Panalytical, Netherlands) system has been employed here, which is shown in Figure 2.5. Since most of the semiconductor device structures are epitaxially grown onto a substrate, which allows impeccably crystalline films having low dislocation density. Thus, the HRXRD technique does not determine the crystal structure, but it will investigate the deviations in it from an ideal crystal lattice, which can be induced due to defects, strain, or impurities. A crystal lattice is generally known as an ordered arrangement of atoms in space in such a way that they form a series of parallel planes separated from each other by intermolecular distance, *d*, which varies from material to material. For every crystal, each plane has its specific d-spacing and has been able to exist in a number of different orientations. When a monochromatic beam of X-ray having a wavelength '***λ***' is projected on the crystalline material at an angle '***θ,***' the diffraction happens only when the distance is covered by the rays, which are reflected from consecutive planes differs by an '***n***' number of wavelengths.

Figure 2.5: High Resolution X-ray Diffraction System.

For parallel planes of atoms (Figure 2.6), having a space d_{hkl} between the planes, constructive interference occurs only when Bragg's law is satisfied. Bragg's equation is given by,

$$n\lambda = 2d\sin\theta \tag{2.1}$$

where $1/d^2_{hkl} = (4/3) \times \{(h^2 + hk + k^2)/a^2\} + (l^2/c^2)$ for a hexagonal symmetry system, *h, k* and *l* are the Miller indices; θ is angle of diffraction. By using this equation (2.1), the lattice parameters *'a'* and *'c'* can be calculated. Further, the average size of the crystal was determined from GaN (0002) peak using the Scherrer formula,

$$t = \frac{k\lambda}{\beta cos\theta} \tag{2.2}$$

where *t* is the crystal size, *k* is a constant, $\beta$is the half-width of the peak.

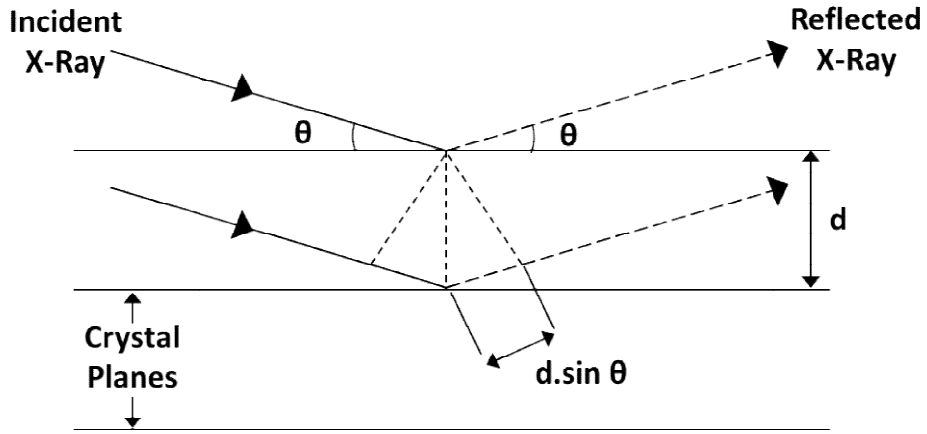

Figure 2.6: Schematic illustrating Bragg's Diffraction.

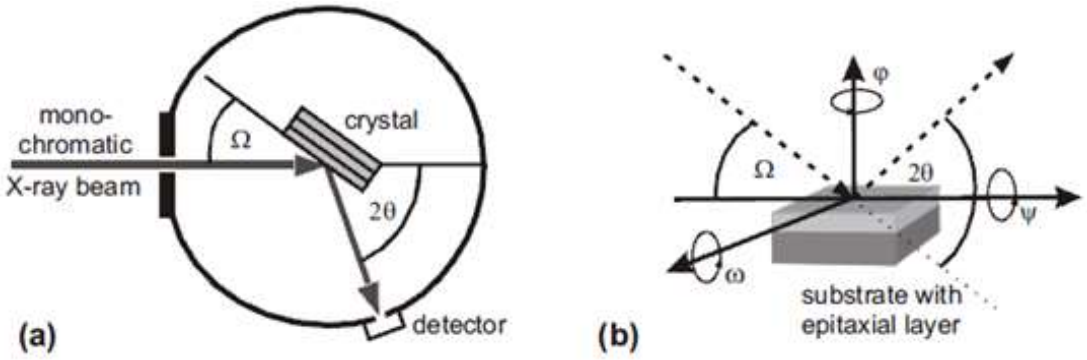

Figure 2.7: (a) HRXRD Diffraction-Meter (b) Illustration of different angles in the scan.

A typical HRXRD crystal analyzing system (Figure 2.7) consists of the following subparts:

1. An X-ray source;
2. A sample stage manipulator which is proficient to move, tilt and rotate in different directions for precise placement of sample,

3. Beam conditioners at the incident and diffracted beam side and,
4. A detector

There are 3 major types of scanning that can be done using an XRD.

1. A detector scan is a plot of scattered X-ray intensity vs. 2θ without changing ω. This type of plot is rarely used for analysis.
2. A rocking curve is a plot between diffracted x-ray intensity vs. ω.
3. Coupled Scan is a plot of scattered X-ray intensity vs 2θ, but ω also changes in a way that is linked to 2θ so that ω= ½ * 2θ + offset.

2.4.2 Field Emission Scanning Electron Microscopy (FESEM)

Although the theoretical limit to study topographical features of various organic and inorganic materials was reached in the early 1930s, still, there exists a scientific and technological inspiration to observe the fine topographical details of them. This requires a magnification > 10,000x, which cannot be achieved using light microscopes. As the traditional light microscopes are limited with a magnification of 500x or 1000x and a resolution of 0.2 μm, thus, electron microscopes need to be established in the later stages of research. Electron microscopy, a powerful technique, uses a beam of electrons instead of light to form an image, and glass lenses are replaced by electromagnetic lenses. Their much lower wavelength makes it possible to achieve a resolution, which is a thousand times better than that with a light microscope. The resolutions of electron microscopes are down to atomic resolution and make it possible to see objects having dimensions in the order of a few Å (10^{-10} m). Development in electron optics has led to tremendous changes in electron microscopy. The technique has led to the development of new materials and their use in ever increasing miniaturization of devices for different applications. An Auriga (Zeiss, Germany) FESEM system with energy dispersive X-ray analysis (EDAX) was used to probe the surface morphology of the samples, as shown in Figure 2.8. FESEM system consists of an electron gun and an aligned electromagnetic lens system to gauge the surface morphology.

Figure 2.8: AURIGA Field Emission Scanning Electron Microscopy system.

A precise electron beam falls on the specimen that leads to the emission of back-scattered electrons, secondary electrons, characteristic X-rays, *etc*. The generated electrons will be collected by a suitable detector and hence, provide information about the surface morphology of the sample under observation. Moreover, the characteristic X-rays emitted from the sample are used for identifying different elements present in the specimen via EDAX. There are various types of electrons emitting out from the sample in SEM, which gives diversified information about the sample. For instance, secondary electrons arise due to the inelastic collisions between the incident beam of electrons and loosely bound electrons in the conduction band of the specimen. Thereby, the energy transferred due to collision is adequate to overcome the work function, which binds them into a solid and, thus, ejected. These electrons are utilized for surface morphology studies; however, backscattered electrons are the outcome of the elastic collisions between the entering electrons and the nucleus of the target atom (*i.e.*, Rutherford Section). The detection of these electrons provides information onthe topography as well as composition contrast imaging to evaluate different elements present in the specimen.A complete schematic diagram of SEM is demonstrated in Figure 2.9, which shows the alignment of various lenses and arrangement of other required instrumental parts to probe a sample for surface property acquisition.

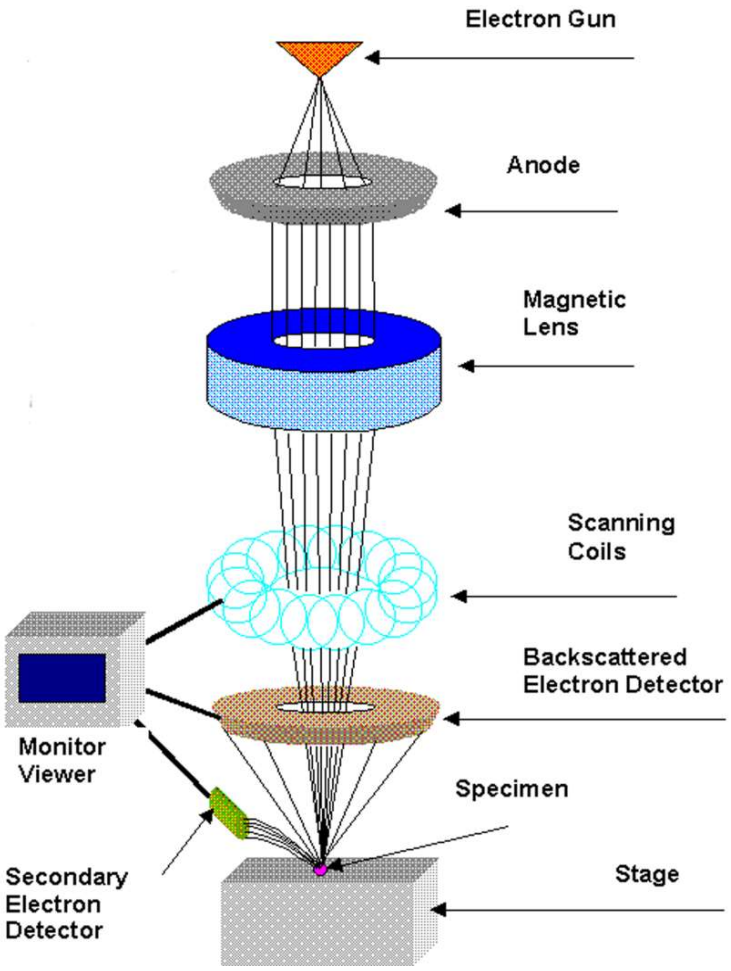

Figure 2.9: A schematic diagram of SEM.

2.4.3 High Resolution Transmission Electron Microscopy (HRTEM)

The transmission electron microscope (TEM) was the first type of electron microscope to be developed and is patterned exactly on the concept of light transmission microscope except that a focused beam of electrons is used instead of light to see through the specimen. It is a versatile microscopy technique that provides awealth of information about morphology,composition,and crystallographic properties of the studied samples.

A schematic representation of the TEM is shown in Fig. 2.10. TEM works much like a slide projector. A projector shines a beam of light through the slide, as the light transmits through, it is affected by the structures and objects on the slide. These effects result in only certain parts of the light beam being transmitted through certain parts of the slide.

This transmitted beam is then projected onto the viewing screen, forming an enlarged image of the slide. The portion which is transmitted is projected onto a phosphor screen for the user to see. The working of a typical TEM is explained as follows:

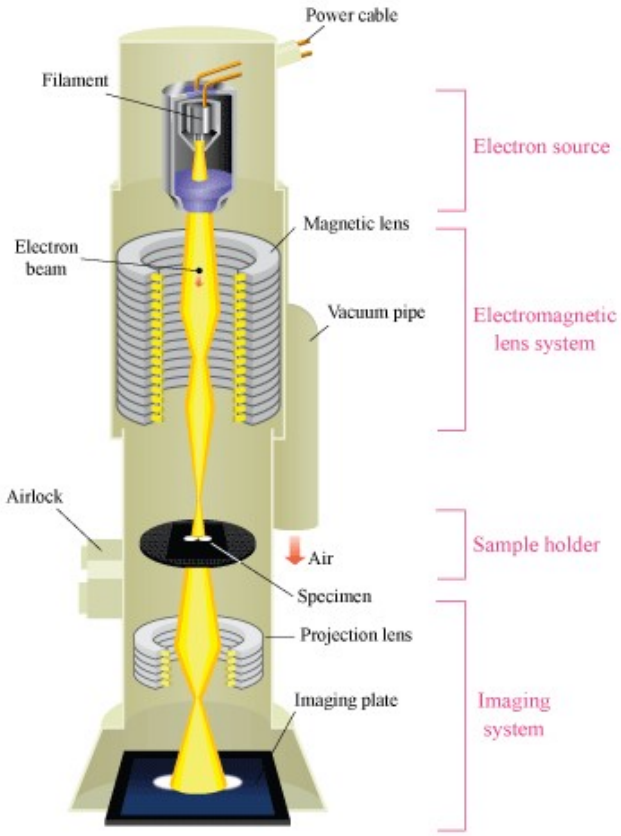

Figure 2.10: A schematic diagram of the TEM measurement setup.

The electron gun produces a stream of monochromatic electrons, which is focused onto a small, thin, coherent beam by using condenser lenses. The beam is restricted by the condenser aperture, knocking out high angle electrons. The beam strikes the specimen, and parts of it are transmitted, which is focused by the objective lens into an image. The image is passed down the column through the intermediate and projector lenses, being enlarged all the way. Then, the image strikes a phosphor screen, and light is generated, allowing the user to see the image. The darker areas of the image represent those areas of the sample that fewer electrons were transmitted through. The lighter areas of the image represent those areas of the sample that more electrons were transmitted through.

In addition to thin-sample images, electron diffraction patterns can also be formed on the final image screen by TEM. The electron rays corresponding to two modes: bright field imaging mode and diffraction mode. In bright field imaging, the image of a thin sample is formed by the electrons that pass the film without diffraction, the diffracted electrons being stopped by a diaphragm. In the corresponding dark-field imaging mode, a diffracted beam is used for imaging. Sample microstructure, *e.g.*, grain size, and lattice defects, are studied by use of the image mode, while the diffraction mode analyses the crystalline structure. Besides, the chemical composition of small volumes, for example, grain boundaries, can be obtained by the detection of x-rays emitted from the thin film samples. In case near-atomic resolution is required, film thicknesses have to be limited to a few tens of Å.

For the cross-sectional HRTEM study, the sample was cut in the pieces of ~2.2 mm X ~3.0 mm by diamond wheel saw. Stack of the film was prepared by keeping these sample pieces together like face to face and face to back using epoxy and cured at 120°C for 3-5 min. The stack was mechanically polished from corners and inserted in 2.3 mm inner diameter and 3.0 mm outer diameter hollow brass cylinder. The circular disc was cut from this brass cylinder and again mechanically polished up to 120 μm. Further, the center of the disc was dimpled to achieve 10-20 μm thickness by using a dimple grinder (GATAN 656). The dimpled disc was ion milled in two steps initially at an operating voltage of 5 kV and a beam current of 2.6 mA for 1 hr later on at an operating voltage of 1.0 kV and beam current of 1.0 mA for 3.0 hrs to achieve the final perforation at the center/region of interest. The prepared TEM specimen was examined in a TEM (FEI, Tecnai F30 G2 S-TWIN) operating at 300 kV with a point resolution of 0.205 nm and a line resolution of 0.144 nm.

2.4.4 Atomic Force Microscopy (AFM)

AFM is a high-resolution scanning probe microscopic technique, having a resolution of fractions of nm, which is more than 1000 times better than the optical diffraction limit (λ/2). It is considered to be one of the foremost techniques for imaging and measuring matter at the nanoscale level. AFM utilizes a cantilever which has a precise and sharp tip to scan above the surface of the testing sample. When the tip approaches

the sample surface, the close-range attractive force between the surface and the tip deflects the cantilever position towards the surface. Though, if the cantilever is taken extremely close to the surface such that the tip makes contact with it, then the repulsive force increases and deflects the cantilever away from the surface.

Figure 2.11: AFM Measurement Setup.

A multimode V-Veeco (Veeco, USA) AFM system has been used here, as shown in Figure 2.11. A laser beam has been utilized for detecting cantilever deflections towards or away from the surface. Every cantilever deflection causes some changes in the direction of the beam reflected by the top surface of the sample, which will be tracked by a position-sensitive photo diode (PSPD). Thus, as the AFM tip passes over crest and trough features of a surface, it results in a cantilever deflection which gets recorded by PSPD. And, a feedback loop has been used to control the distance of the tip above the surface to maintain a constant laser position. This is the mechanism behind AFM images acquiring the topographical study by perusing the cantilever over an area of interest.

2.4.5 Photoluminescence (PL) Spectroscopy

PL is a nondestructive luminescence-based technique that can be used to probe the optical characteristics of materials. In this technique, a light source (laser or a lamp) having energy greater than the band-gap energy of the material is used to excite electrons from valence band to conduction band and generate electron-hole pairs in the material. These photons driven electron-hole pairs recombine spontaneously either directly from conduction to valence band or via involving different defect and excitonic levels in the band-gap region by emitting energy in the form of photons or heat. When the emitted energy is in the form of photons, it is known as luminescence. Then, the emitted radiation is collimated and directed to the monochromator unit, which disperses the luminescence into separate wavelengths. Next, the dispersed light is recorded by a CCD camera detector to provide a plot of intensity against the wavelength on a computer screen. Here, the CCD camera detector is used as it allows simultaneous data collection for a broad spectral range in every measurement. The PL system (FLS-980, Edinburgh) employed in this experiment is shown in Figure 2.12. A continuous-wave UV excitation frequency (325 nm) He-Cd laser and a Xenon lamp (200-2200 nm) were used as the excitation sources. The optical detector has the detection range between 230-1600 nm.

Figure 2.10: Edinburgh FLS-980 Photoluminescence system.

2.4.6 Raman Spectroscopy (RS)

The Raman spectroscopy (RS) is a vibrational molecular spectroscopic technique that has been derived from an inelastic light scattering process. With this spectroscopic technique, an incident laser photon is scattered by the sample molecule and, thereby, gains (or loses) energy during the process. An energy change of the irradiating photon signifies the amount of energy transferred (lost or gained) during the scattering process, and each energy change is unique for a particular bond in a molecule. RS is the best technique for producing a precise spectral fingerprint that is distinctive to a molecule or an individual molecular structure. This technique has been used for analyzing solids as well as liquid solutions and delivers information about physical properties such as crystalline orientation, and intrinsic stress, *etc*. In the present work, Raman scattering measurements were performed using a T-64000 triple Raman spectrometer (Horiba, France) in backscattering configuration where an excitation source of argon ion laser (Ar+) was used at an operating wavelength of 514 nm with a power of 50 mW, and a charge-coupled device system with an accuracy of 0.5 cm^{-1} was used to collect the data (Figure 2.13).

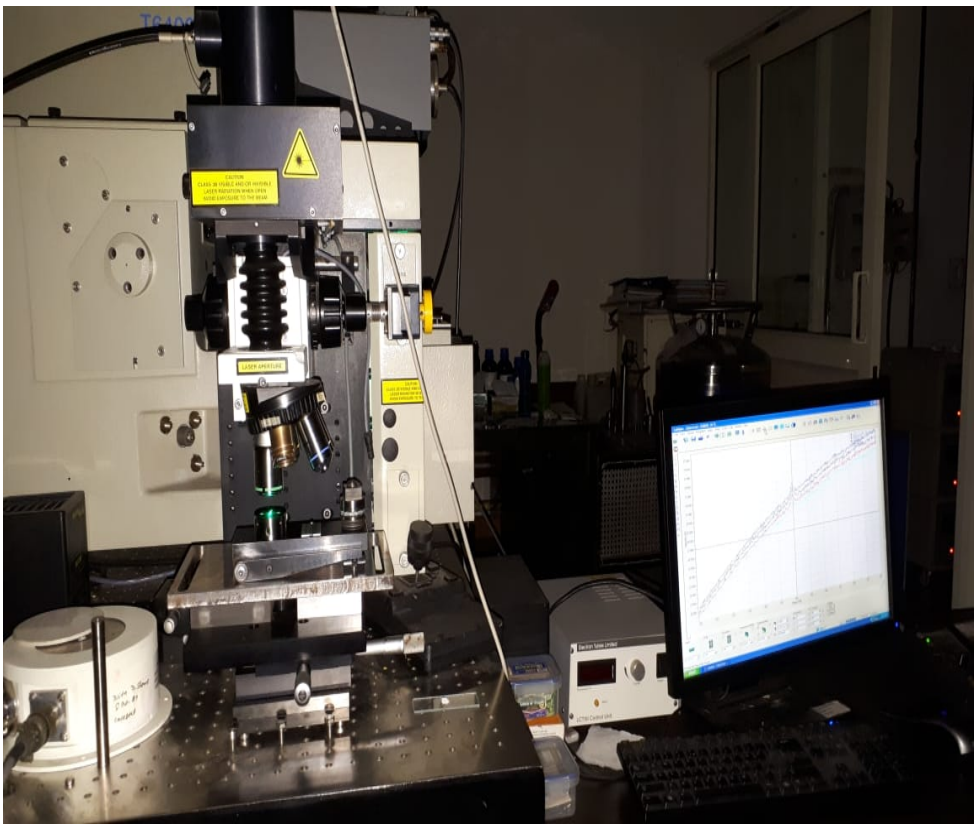

Figure 2.13: Horiba - Raman Spectroscopy system.

2.4.7 Thermal Evaporation System

The thermal evaporation system (Figure 2.14(a)) is commonly known as the Physical Vapor Deposition (PVD) method. This is basically a thin film deposition system which typically uses a resistive heating mechanism to evaporate pure source material to form a thin film under a controlled and high vacuum environment. Thereby, the source material is heated up to its vapour pressure, after that, the evaporated material traverse in the form of vapour with acquired thermal energy and deposited on the substrate. The deposited material on the substrate is also called thin-film, whose thickness range can be tunned from angstrom to microns by the precise control of applied current to the heating electrodes and optimization of film deposition time. Moreover, the system having the capability to deposit single or multiple materials in a layered structure format, wherein source materials can be pure atomic elements such as non-metals and metals, including gold, chromium, indium, copper, aluminium, silver and many more.

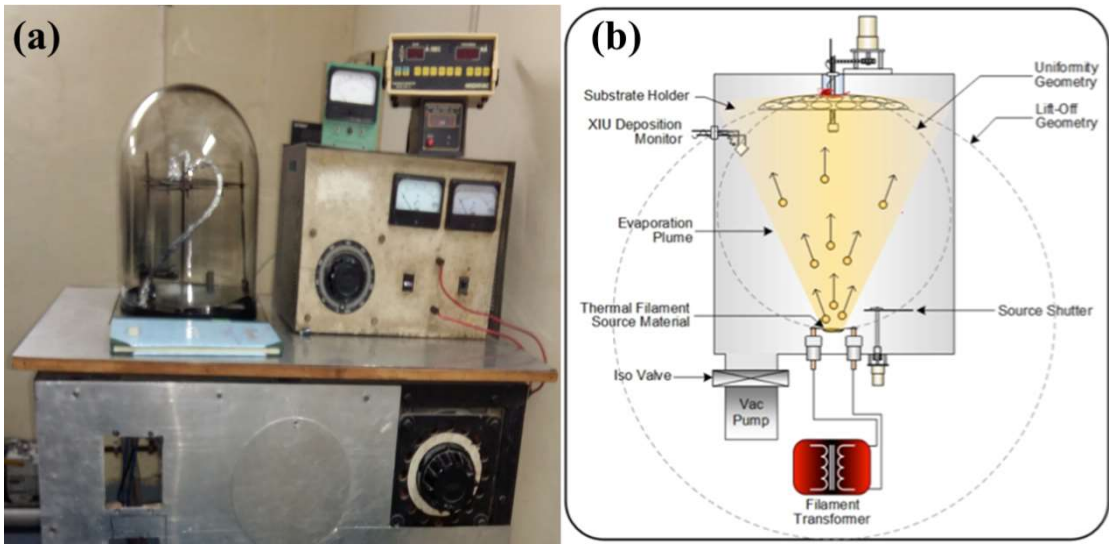

Figure 2.14: (a) Thermal Evaporation system, (b) Operational schematics

In most of the thermal evaporation system evaporated source material's vapour follow the lift of geometrical trajectory from the bottom (source material boats) to top (upside-down mounted substrate) of the vacuum chamber (shown in Figure 2.14(b)). The real-time monitoring of the deposition is precisely monitored by the quartz crystal equipped deposition monitor.

2.4.8 Photoresponse Spectrometer

The photoresponse measurements were carried out using a probe station setup, which has a shielded enclosure (Cascade Microtech EPS150TRIAX) for low signal measurements (Figure 2.15). The spectrometer is equipped with a focused laser source (λ=325 nm, illumination power, P = 1-13 mW) for UV detection. Its experimental set up is shown in Figure 2.16 which consists of a laser source to illuminate the sample, highly precise probes on the sample to minimize the noise power in the data, a source meter to measure the current flowing through the circuit upon illumination and apply bias for better charge carrier collection and finally a software to provide user-friendly output data. A block diagram of the complete experimental setup for acquiring the response from a PD device is briefly elucidated in Figure 2.17. Broadly, a PD experimental set up consists of a laser source to illuminate the sample, highly precise probes on the sample to minimize the noise power in the data, a source meter to measure the current flowing through the circuit upon illumination and apply bias for better charge carrier collection and finally a software to provide user-friendly output data on the screen.

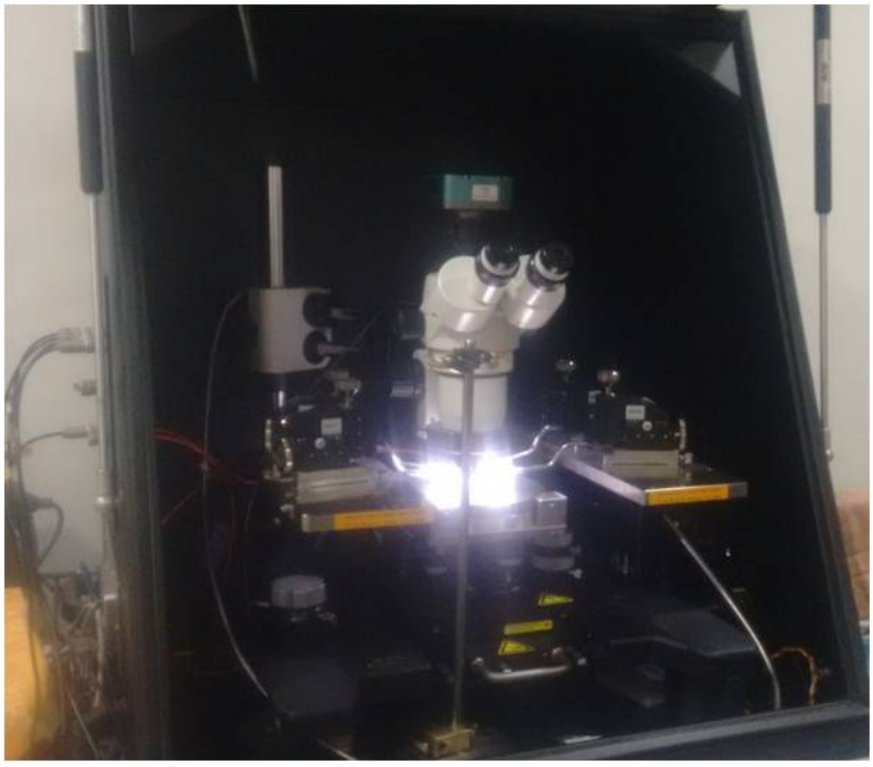

Figure 2.15: The Photoresponse measurement system.

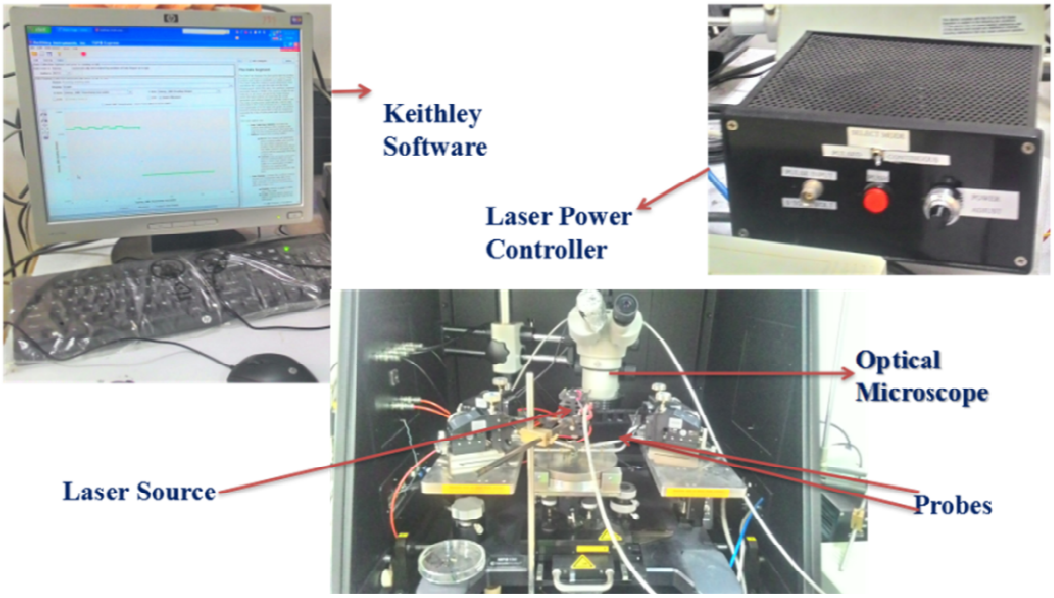

Figure 2.16: The experimental setup for Photoresponse measurements.

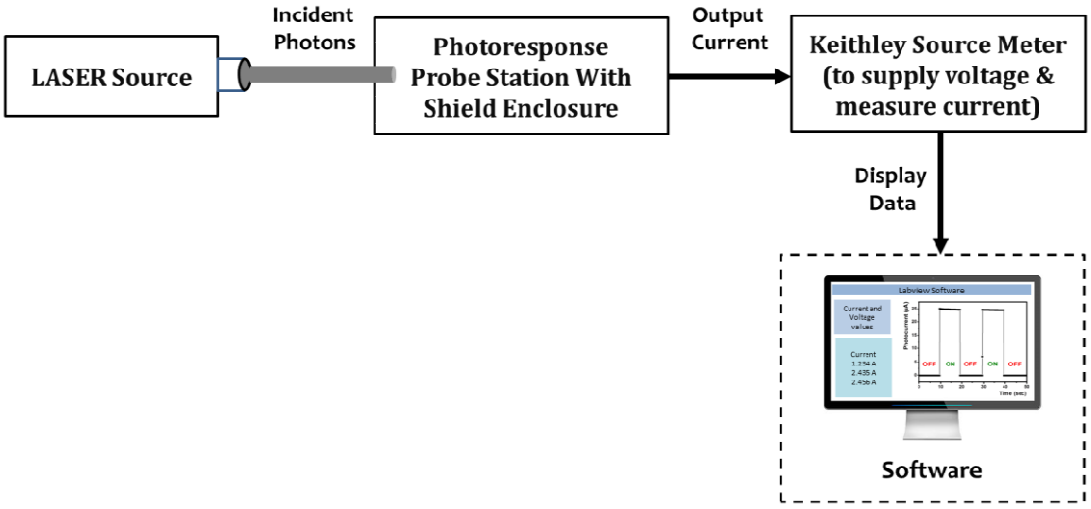

Figure2.117: A block diagram representing the experimental setup for data acquisition.

2.5 Summary

A detailed discussion on various experimental techniques used from high-quality material growth to *in-situ* and *ex-situ* characterization of III-Nitride semiconductors to complete optoelectronic device fabrication has been provided in this chapter.

3.1. Introduction

Ultraviolet photodetectors (UV-PDs) fabrication and development is the area of intense research from the last few decades, and still the ongoing research found encouraging by adding new ways to enhance the UV-detection capability of the detectors. The importance of UV-PDs is universally recognized due to their diverse range of applications, such as in anti-missile technology by plume detection, flame detection, calibration and monitoring of UV radiations, chemical as well as biological analysis, secure optical communications, environmental monitoring, and astronomical research,*etc*. [105]. For this, GaN semiconductor has demonstrated to be a potential backbone of durable device applications due to numerous advantages offered by its significant inherent properties such as wide and direct bandgap, high thermal coefficient, high carrier mobility, higher resistance towards electric breakdown field and high chemical stability [106]. The advancement in photodetection can be realized by using nanostructures (NSs), which offers additional advantages in detection applications by offering a large surface to volume ratio, which can significantly increase the UV photon absorption rate. These advancements in UV-PD can lead to good photoconductivity and enhanced electrical conductivity [16, 17]. III-Nitride NSs are more often grown on Si (111) as compared to other available substrates like Si (100), SiC, and sapphire by self- assembly process using PAMBE[20, 107, 108]. The epitaxial growth of the GaN layer on Si substrate (GaN/Si) having a large mismatch lattice constant of 17%. This large lattice mismatch and difference in thermal expansion coefficient induced large substantial elastic strains at the heterointerface. Unlike 2D thin film, the self-assemble 3D GaN NSs accommodates this lattice mismatch with the substrate and grow fully relaxed and free of extended defect (threading dislocations or basal plan stacking faults) [109, 110]. Therefore, III-Nitride NSs proved themselves, potential candidates, to develop highly efficient optoelectronic device ranging from ultraviolet-visible to infrared region. Till now, a series of studies were reported on the synthesis of high-quality GaN-NSs directly on Si by various growth techniques such as metal-organic chemical vapour deposition (MOCVD) [111], hydride vapour phase epitaxy (HVPE) [112], chemical vapour deposition (CVD) [113] and molecular beam epitaxy (MBE) [114]. In recent years,

the growth of GaN-NS via PAMBE (plasma-assisted molecular beam epitaxy) has been realized in detail by various groups under well-established nitrogen-rich conditions (III/V ratio <1) [107, 114, 115]. In this experiment, we have grown GaN-NS on Si (111) substrate via PAMBE under nitrogen-rich conditions. Subsequently, the quality of as-grown GaN-NS/ Si heterojunction is investigated in terms of its morphological, structural, optical, and opto-electrical properties. The opto-electrical property reveals that the fabricated structure confirmed its application as UV PD. This is the first study of its own kind where we have grown catalyst-free self-assemble, non-homogenously distributed, nano island-shaped GaN-NS on Si (111) substrate. These low aspect ratio GaN nano-islands, unlike high aspect ratio conventional NS such as nanorods, nanocolumn, nanoribbon, nanoflower,*etc*., have been grown with a very low material requirement which not only made the device fabrication more economical but also reduces the sample fabrication time. The present study also demonstrates the fabrication of ultra-thin non-homogeneous nano-island shaped NS oriented distinct barrier heights driven GaN-based self-powered UV-PD. The device was fabricated in the metal-semiconductor-metal (MSM) geometry by depositing Au/Cr electrodes. The MSM based photodetector does not exhibit the minority carrier charge storage effects as formed in forward bias pn-junction. Therefore, unlike ordinary pn-junction detectors, the MSM based detector performs much faster (high switching speed: ON/OFF), as in these detector flow of current is conducted by majority carriers. Moreover, due to the absence of minority carriers in the MSM detector facilitate the device to serve with very low dark current and high signal to noise ratio [116, 117]. Conclusively, due to ease of fabrication and no requirement of doping proved the Schottky barrier type MSM structure as a potential candidate for photodetection applications. Furthermore, MSM structure-based UV-PDs are getting much attention due to various offered advantages such as high UV/VIS rejection ratio, high responsivity, and fast transient reversibility of the detector [118]. Nowadays, smart and wearable sensors with wireless network interfacing technology will become a hot research area and extensively used in every corner of the world. Hence, cost-effective, sustainable, easy to carry, and maintenance-free smart UV-PD, which can harvest required energy by their own are highly desired. These smart sensor or detectors find their application in areas like submarine oil leakage monitoring, forest

fires prevention, and the wearable sensors, *etc*. Hence, unlike uneconomical and inefficient conventional detectors with batteries, high-performance self-powered UV-PDs are playing a significant role in the advancement of futuristic detector technology [119]. Self-powered PDs are attracting considerable attention as they are capable of detect light without any external bias voltage [120, 121]. Thereby, the fabricated PD has been tested under the photovoltaic (*i.e.*, 0 V) as well as the photoconductive mode of operation, where various device performance parameters such as sensitivity, detectivity, responsivity, response time and noise equivalent power were analyzed.

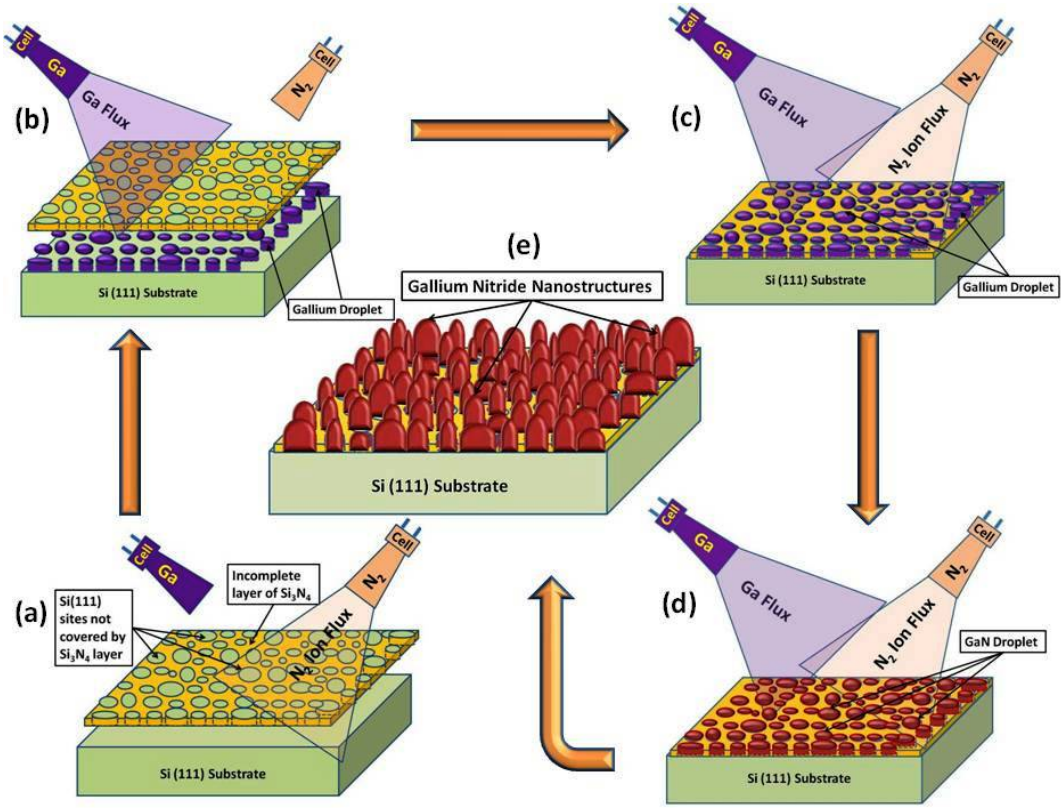

Figure 3.1: Schematic diagram of the growth process of GaN-NS on Si (111) substrate

3.2. Material Growth and Characterization

GaN-NIs were grown on Si (111) substrate using the PAMBE system (Riber Compact 21) equipped with a RF- plasma source and Knudsen cell, which provides active nitrogen species and gallium metal, respectively. The substrate was chemically pre-cleaned by ultrasonication with acetone followed by chemical cleaning in a solution of Di-H_2O: HF and blown dry with N_2 gas. The standard thermal cleaning process was adopted to clean

Si substrate [74], and the reconstructed pattern of Si (111) 7×7 was observed at a temperature of 830°C. Prior to the growth of GaN-NS, a very thin non-continuous, anti-surfactant Si_3N_4 layer (as shown in Figure 3.1(a)) was introduced, which guided the vertical growth of GaN-NIs. Si_3N_4 layer was formed by nitridation of reconstructed Si (111) 7x7 surface at 880°C using 400W plasma power (N_2 flow of 1.5sccm). After that, a self catalyzed wet layer of Gallium (Ga) was deposited for 10 sec at alow temperature of 700°C (as shown in Figure 3.1(b-c)) to proceed with the nucleation process of NIs. After the nucleation process of Ga droplets, N_2 ion active species start converting Ga droplets into GaN, as shown in Figure 3.1(d). Further, these GaN droplets follow the Stranski–Krastanov (SK) growth mode under the influence of offered substrate temperatures, applied N_2, and Ga-flux. Accordingly, high-density GaN-NIs have been grown (as shown in Figure 3.1(e)) at a substrate temperature of 770°C in the presence of N_2 plasma (1.5 sccm) and Ga beam equivalent (BEP) of 6.5×10^{-7} torr for 120min. For better understanding, a growth-time vs growth temperature diagram representing each step involved in the growth process, as shown in Figure 3.2.

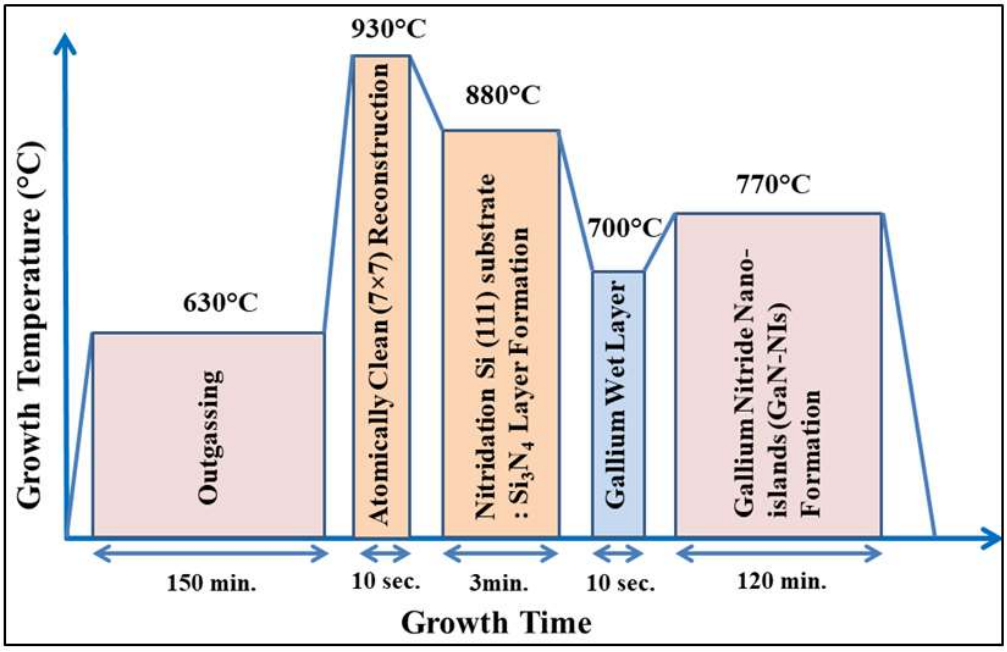

Figure 3.2: The growth-time-temperature diagram is representing the complete procedure of developing epitaxial GaN-NIs on Si (111) substrate.

The real-time monitoring of grown structural (GaN-NIs/Si (111)) has been performed by reflection high electron diffraction (RHEED) under *in-situ* using STAIB electron gun (12keV) to realize 3D growth. An infrared optical pyrometer has been deployed for real-time monitoring of growth temperature (with error value of ±5°C) calibrated with the thermocouple. The morphological, optical and structural analysis of grown GaN-NIs were characterized by Atomic force microscopy (AFM) (Multimode-V Veeco), Field emission scanning electron microscopy (FESEM) (ZEISS AURIGA), room temperature photoluminescence spectroscopy (RT-PL) (Edinburg, FLS980 D2D2) and High-Resolution X-ray diffraction (HRXRD) (PAN-Analytic), Micro-Raman Spectroscopy, respectively. The micro Raman measurement has been performed at room temperature using a triple Raman spectrometer under the backscattering mode, where an argon ion laser was used as an excitation source. The operating wavelength range is set to 514nm with an applied power of 50 mW. Besides this, for data collection, a charge-coupled device system has been used with an accuracy value of 0.5cm^{-1}.

3.3 Result and Discussion

3.3.1 Real Time Monitoring of Growth by *in-situ* RHEED Patterns

The real-time monitoring of growth has been performed with the help of the *in-situ* RHEED technique throughout the growth process. Initially, Si (111) substrate displays a streaky pattern, as shown in Figure 3.3(a), indicating the Si surface before the thermal cleaning process. Prior to the growth, the Si (111) substrate was flash heated at 830°C, which allows 7×7 reconstruction of the Si surface, as shown in Figure 3.3(b).The reconstructed Si (111) 7x7 surface is used as a template to grow Si_3N_4 layer, which was formed by the nitridation process. The formation of Si_3N_4 is observed by "(8/3×8/3)" surface reconstruction (fainted RHEED pattern, as shown in Figure 3.3(c)) due to the inadequate surface arrangement of nitrogen adatoms [122]. During the nitridation process, the Si substrates not only provide active nucleation sites but also allow the penetration of nitrogen atoms, resulting in a non-homogeneous Si_3N_4 layer. The formed Si_3N_4 layer generates localized compressive strains due to longer Si-N bond as compared to the substrate Si-Si bond has been fully relaxed in terms of extended defects free GaN-NIs [123, 124].

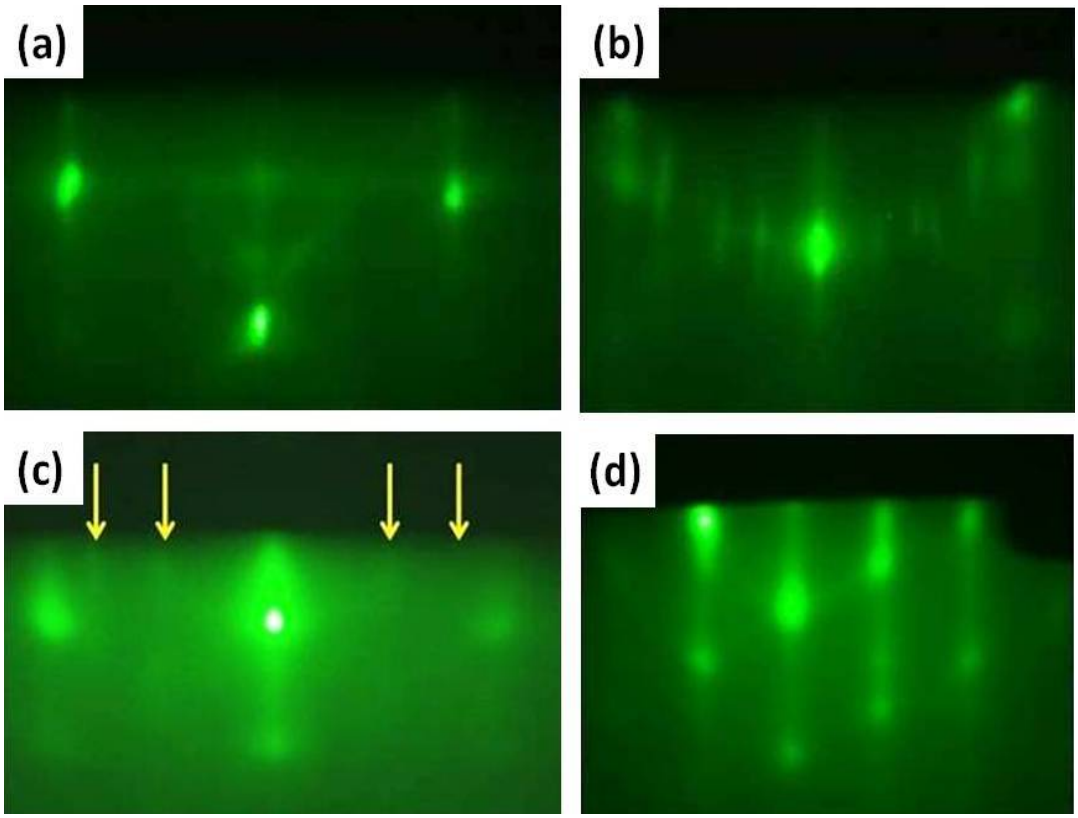

Figure 3.3: (a) RHEED reflections image of the Si (111) substrate before thermal cleaning; (b) Si (111)-7×7 surface reconstruction after annealing at 830°C; (c) arrow marks shows Si_3N_4- 8/3×8/3 surface reconstruction in-continuation after nitridation of Si (111) - 7×7 at 880°C; (d) Reflection of GaN 3D nanostructure's spotty pattern after ramping down the temperature at 770°C for 120 min.

The growth of GaN nanostructures (under nitrogen-rich conditions) can be visualized by spotty RHEED patterns (Figure 3.3(d)). This transformation from streaky to spotty pattern displays the real-time growth execution process of GaN-NIs on the Si surface. The high-temperature sustainability due to bond energies variation of Si-N (4.5eV) and Ga-N (2.2eV) [125-127] in conjunction with anti-surfactant behaviour of Si_3N_4 layer allows the growth of GaN-NIs specifically in the lateral direction [128]. The Ga atoms have high mobility on sidewall facets due to which they find their suitability to sit only vertically,*i.e.*, at the top of the droplet or island.

3.3.2 Structural, Morphological and Optical Properties

The structural properties of as-grown GaN-NIs were analyzed via HRXRD measurements. Figure 3.4(a) shows the 2θ-ω scan of the grown GaN film with 2θ

peak positioned at 34.5° displaying the wurtzite single crystalline growth along [0001] direction [129]. The peaks located at ~ 28.5 and ~ 58.5 degrees correspond to the plan of diffraction of Si (111) and Si (222) planes, respectively [130]. The peak positions in the 2θ−ω scan of GaN along (0002) was used to estimate the lattice constant (*c*) by using Bragg's law equations as follows [131]

$$\boldsymbol{d_{hkl}} = \frac{\boldsymbol{\lambda}}{\boldsymbol{2\sin(\theta_{hkl}+\Delta\theta)}} \tag{3.1}$$

Where d is lattice spacing, (hkl) are the Miller indices of the diffraction planes, λ stands for the wavelength of the X-ray source,*i.e.*, 0.154 nm (for Cu Kα radiation), θ_{hkl} is the measured angle of reflection from the (hkl) plane, and Δθ is HRXRD instrumental zero error and

$$\boldsymbol{d_{hkl}} = \frac{\boldsymbol{1}}{\sqrt{\frac{\boldsymbol{4(h^2+hk+k^2)}}{\boldsymbol{3a^2}}+\left(\frac{\boldsymbol{l}}{\boldsymbol{c}}\right)^2}} \tag{3.2}$$

for hexagonal geometry, where a and c are the lattice parameters of the grown GaN-NIs. Consequently, the strain has been calculated by using the following equation [131]

$$\boldsymbol{\varepsilon} = \frac{\boldsymbol{c-c_0}}{\boldsymbol{c_0}} \tag{3.3}$$

Where c is the lattice constant of the grown GaN film and c_o is the lattice constant of strain-free GaN (given a_o = 0.3188 nm and c_o = 0.5185 nm) [8]. The evaluated value of strain in as-grown GaN nanostructures is found to be 0.17%. Besides this, to understand the crystalline quality and dislocation density in the grown structure, HR-XRD omega scan along (0002) plan diffraction has been performed, where the large FWHM value of 3.8° attributes the screw dislocation density value,*i.e.*, 1.8×10^{11}cm^{-2}. The possible reason for such large FWHM value and corresponding dislocation density might be due to the very low thickness of the film,*i.e.*, 26nm (nano-island height).

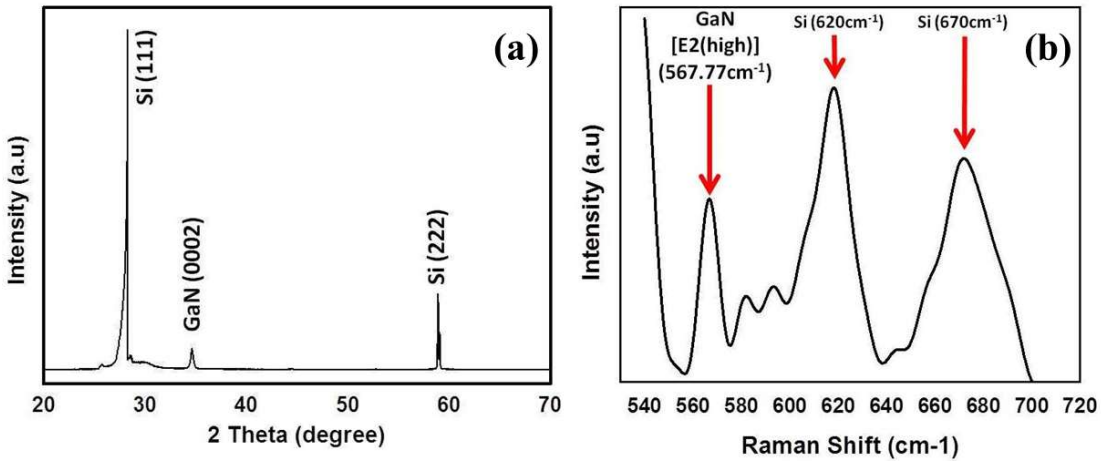

Figure 3.4: (a) HR-XRD 2θ-ω scan of GaN-NS grown on Si substrate, (b) Micro-Raman Spectra of GaN-NI/Si(111).

Raman-scattering is an important technique to investigate the crystallinity of materials and also provide the information of developed defects in the grown structure in terms of Raman peak shift (red or blue shift) guided stress values. Figure 3.4(b) shows the Raman spectra of GaN-NIs grown on Si (111) substrates. The Raman spectra show, E2-high mode of grown GaN nanostructure located at 567.77cm^{-1}. It has been observed that as compared to the standard frequency value of E2(high) phonon mode of bulk GaN (568cm^{-1}) [132], the E2(high) peak of grown GaN-NIs was shifted to lower wave-numbers (red-shift) of about 0.23cm^{-1}. The red-shift in the position of E2 (high) indicated that the GaN-NIs suffered from tensile stress. [133, 134] As studied by Aggarwal *et al.*, the stress levels of the GaN epilayer and the Raman shift are related by [131]

$$\Delta w = 4.3\sigma_{xx} \tag{3.4}$$

The biaxial stress (σ_{xx}) can be calculated from the variation in wavenumber (Δw) of E2 (high) mode. The tensile stress is estimated to be 0.053GPa for the GaN grown on Si (111) substrates. The Raman spectra indicated that the grown GaN/Si (111) exhibited the very low-stress value as compared to a high aspect ratio 3D GaN-NIs and 2D thin films, as shown in Table 3.1. This lower stress value result is in good agreement with calculated lower strain by HR-XRD analysis. The calculated lower stress value corresponds to lower strain as a consequence of reduced defects in grown GaN-NI. Another observed band marked with an asterisk at 620cm^{-1} and 670cm^{-1} related to Si substrate as it is already observed in pure Si materials earlier. [135]

Table 3.1: Various groups reported state of the art biaxial stress of GaN/Si (111).

Sample	Biaxial Stress 'σ_{xx}'(GPa)	Reference
Doped GaN/Si(111)	2.32	Velazquez *et al.*[136]
Doped GaN/ Si (111)	1.09	Zhao *et al.*[137]
GaN/3c-SiC/Si(111)	0.65	Gao *et al.*[138]
GaN-NS/n-Si(111)	0.28	Saron *et al.*[139]
GaN-NS/Si(111)	0.06	Seo *et al.*[140]
GaN-NIs/Si(111)	0.053	This Work

The morphological studies of the grown NS were performed via AFM and FESEM measurements, as represented in Figure 3.5(a-c). It was found that high-density, asymmetric, and vertically oriented GaN-NS have successfully grown over the Si (111) substrate. The histogram (shown in inset Figure 3.5(a) elucidates the distribution density of grown GaN-NIs in terms of their variation in nanoisland size with respect to their quantity (in counts) distributed on the substrate. The histogram states the average size of grown NS is 50 ± 5nm with a distribution density of $2x10^{10}$ cm^{-2} yielding an average surface roughness of 5.80nm. The grown GaN-NIs are having an average height of ~26nm concluded from a cross-sectional view of FESEM at different positions, as shown in Figure 3.5(c). The average width and height of the island are 50nm and 26nm, respectively. The calculated aspect ratio (width/height) of as-grown island-shaped GaN-NS is 1.92.

These low dimensional islands with high distribution density and increased effective surface area (optical Area) offered by NS is essential merit to increase its light absorption ability, which can be utilized for photodetector and semiconducting optoelectronic device applications. Inset in Figure 3.5(b) shows EDX spectrum measured from the as-grown GaN-NSs provide evidence of N_2, Ga and Si in as-grown GaN-NIs with respect to their corresponding weight, the atomic percentage of (10.19%, 19.58%), (9.77%, 3.77%) and (80.04%, 76.66%), respectively.

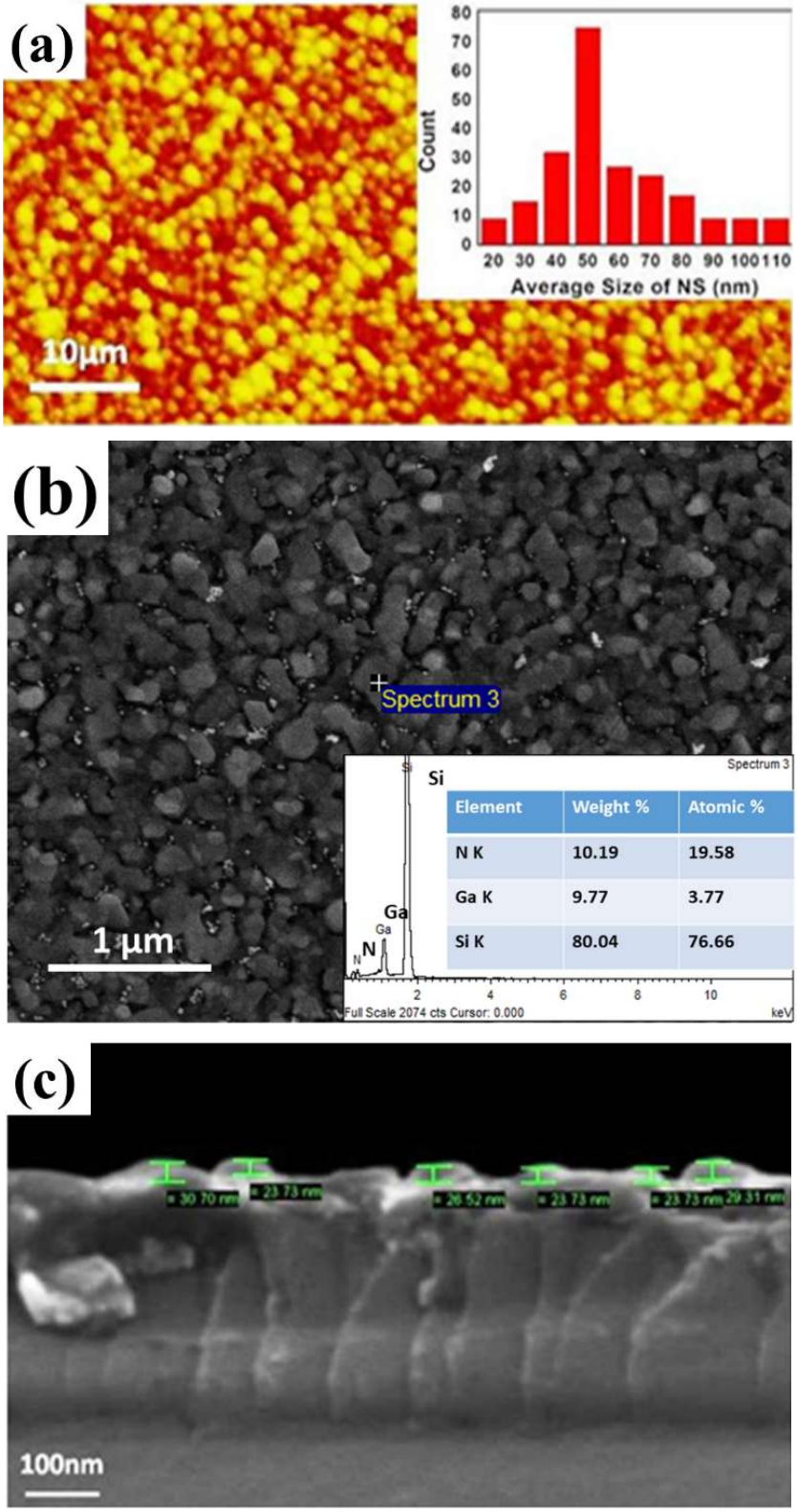

Figure 3.5: (a) AFM image of GaN-NIs; inset shows the average size distribution histogram of as-grown GaN-NIs; (b) FESEM image of high-density GaN-NIs; inset shows EDX of GaN-NIs; (c) Cross-sectional FESEM image of the tiny dimensional island-shaped GaN-NIs.

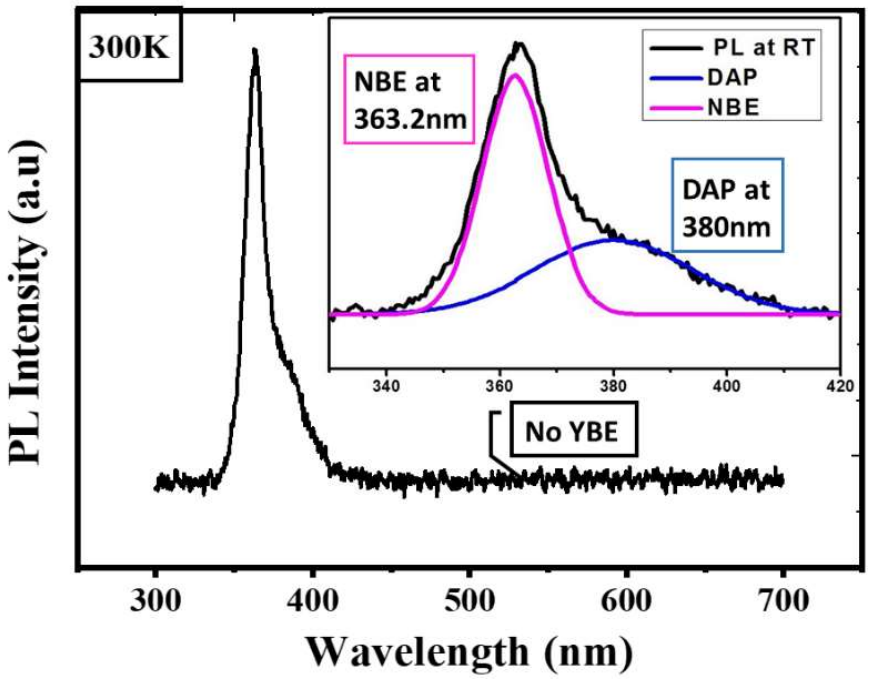

Figure 3.6: RT-PL spectra of grown GaN-NS.

Figure 3.6 shows RT-photoluminescence spectra of the grown GaN-NIs displaying a band edge emission of GaN at 363.2 nm, which is closely related to the bulk GaN (3.4eV) PL emission [132]. Inset view shows the de-convoluted PL spectra in the range of 350 to 420 nm. It was observed that besides the near band emission (NBE), an additional peak at 380 nm was also recorded. This additional peak at 380nm was attributed to the donor-acceptor pair (DAP) generated by un-intentional doping caused by the diffusion of Si in GaN [141]. High intensity of PL NBE peak shows a high level of radiative recombination though the absence of yellow band emission (YBE) indicates significantly reduced dumping zone of valuable electrons and holes offered by defects and impurities at interfaces. Such PL spectra indicate the high crystal quality of grown GaN-NIs [142]. However, the grown GaN-NIs with a high aspect ratio will result in more photons absorption sites to generate a higher number of electron-hole pairs (EHP). The high densities of photo-excited electrons sites which contribute to emitting high-intensity photoluminescence of electron-hole plasma as compared to continuous single-crystalline GaN thin films.

3.3.3 Photodetector Fabrication and Performance

The PD was fabricated in MSM geometry due to its simple fabrication process, low cost and high-speed operation. Thereby Au/Cr contacts (thickness of ~ 150 nm/20 nm) has been deposited onto the nanostructured GaN film by thermal evaporation technique. The active area of the device is calculated to be 6.75×10^{-3} cm^2 (1.5mm ×450µm). The room temperature current-voltage and photodetection measurements of GaN-NSs based UV-PD were performed on a semiconductor parameter analyzer connected to a probe station setup (Cascade Microtech EPS150TRIAX) with a shielded enclosure (EPS-ACC-SE750) for low signal measurements (current resolution in pico amperes and time resolution of 110µs). The system was equipped with a focused laser (λ = 325 nm, optical power = 1mW (power density: 0.0141 Wcm^{-2}) to 13mW (power density: 0.184 Wcm^{-2})) for UV illumination.

3.3.3.1 Photodetector Performance at Photovoltaic mode

The performance of fabricated GaN-NIs MSM structure-based UV-PD has also been analyzed at the photovoltaic mode of operation, wherein the development of built-in potential without any bias can be well understood by the device geometry and metal contact interaction. Thereby, non-homogenously distributed NIs on Si substrate, having two Au metal contacts of the same dimensions, as shown in Figure 3.7. Due to non-homogeneous GaN-NIs, a non-identical Au/GaN interface with asymmetric contact areas (A1 and A2) at the metal-semiconductor junctions were formed.

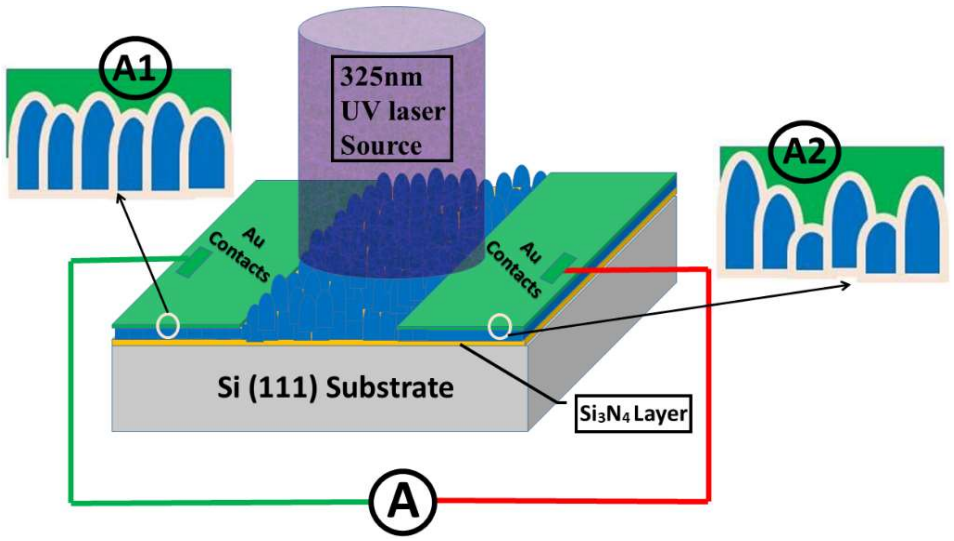

Figure 3.7: Shows a schematic diagram of the fabricated GaN-NIs PDs.

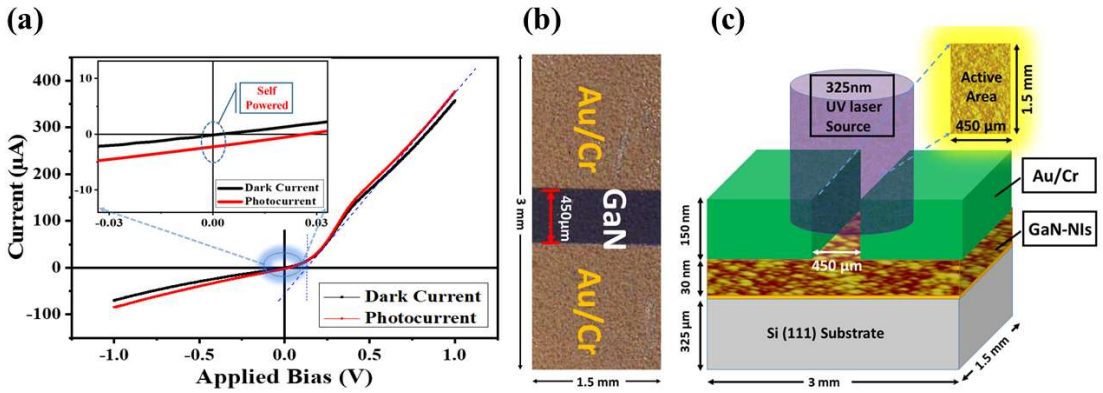

Figure 3.8: (a) I-V characteristics under dark and light condition (UV laser 325nm, 13mW optical power); inset shows a log scale I-V curve of fabricated GaN nanostructured PD under UV illumination, (b)and(c) Optical microscopic image (top view) and layout of the fabricated UV-PD.

Figure 3.8(a) depicts the I-V characteristics of fabricated GaN PD under dark and light conditions, and Figure 3.8 (b and c) display actual device top view image captured by an optical microscope and layout of the fabricated device, respectively. The I-V curves demonstrate that the fabricated detector is found to be Schottky in nature. Due to distinct Au/GaN interfaces originated different Schottky barrier heights (SBHs), provides the built-in potential to operate the fabricated detector at photovoltaic mode [without any external bias voltage (0V)]. This developed built-in potential has been utilized by the detector to channelize the very low dark current (I_d= 12nA) as well as corresponding photocurrent (I_{ph} = 2.2 μA) under UV-illumination of 13mW optical power (shown by the inset of Figure 3.8(a)). Such self-driven channelization of the photocurrent without any applied bias voltage proved the self-powered capability of the fabricated detector. Such thin GaN nanostructured film with notably low dark current value facilitates high performance from the fabricated PD. The two different Au/GaN interfaces created a difference in SBHs at the Au/GaN junctions, which deviates the device current-voltage behaviour under positive and negative bias voltage conditions. The change in Schottky barrier height (φ_b) and ideality factor (n) of the device has been calculated by the following equations [70, 139]:

$$\boldsymbol{\varphi_b = \left(\frac{nKT}{q}\right)\left(ln\frac{A_0A^*T^2}{I_s}\right)} \tag{3.5}$$

$$I = I_s \left[exp\left(\frac{qV}{nKT}\right) - 1 \right] \quad (3.6)$$

where I_s, K, T, q, A_0, and A* are reverse saturation current, Boltzmann constant, absolute room temperature in Kelvin, electronic charge, device contact area, and Richardson constant (26.8 A/cm^2K^2 for n-GaN [143]), respectively. The reverse saturation current was obtained by extrapolating the log plot of the current-voltage curve at V = 0 (Figure 3.9). Using eq. (3.5) and (3.6), the ideality factor (n_1 and n_2) and SBHs (φ_{b1} and φ_{b2}) for both asymmetric Au/GaN junctions have been calculated to be n_1 (1.43), n_2 (1.09) and φ_{b1} (0.83 eV), φ_{b2} (0.703 eV) under reverse and forward bias voltage, respectively, as demonstrated in the inset of Figure 3.9. The calculated SBHs of the Au-GaN junctions were found to be in close agreement with barrier height values reported by Noh *et al.*[144]. Thus, the fabricated GaN device revealed a self-powered mechanism due to the difference in SBHs. The charge transport mechanism in the device having an asymmetric contact area was explained via the energy band diagram [74, 118] in Figure 3.10.

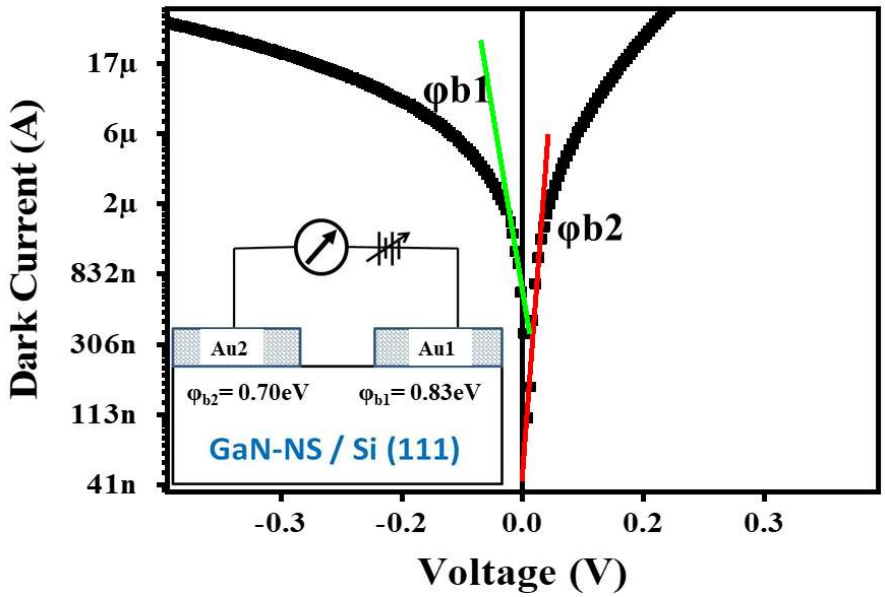

Figure 3.9: I-V curve under the dark condition to determine SBHs in negative φ_{b1} and positive region φ_{b2}. The inset demonstrates a schematic of GaN PDs with asymmetric contact areas.

The effect of asymmetric Au/GaN interface oriented metal electrodes on the built-in electric field at the metal-semiconductor junction was explained by Freeouf *et al.*

where the metal electrodes of larger contact area offer larger depletion region at the metal-semiconductor interface [145, 146]. Therefore, the asymmetric Au contact area led to a change in depletion layer width, resulting in a variation in the built-in electric field, thereby in carrier separation and transport. As a result, out of the two asymmetric contact area electrodes, the electrode of a larger interface accommodates a large number of holes as compared to the smaller ones. This higher concentration of holes at one end of the electrode producing the lowering of its barrier heights [147, 148]. These asymmetric SBHs generated built-in potential gradients inside the semiconductor, which drives the charge carriers without any applied bias voltage. Thus, an additional current (charge carriers) starts contributing to channelize the photocurrent even at zero bias voltage.

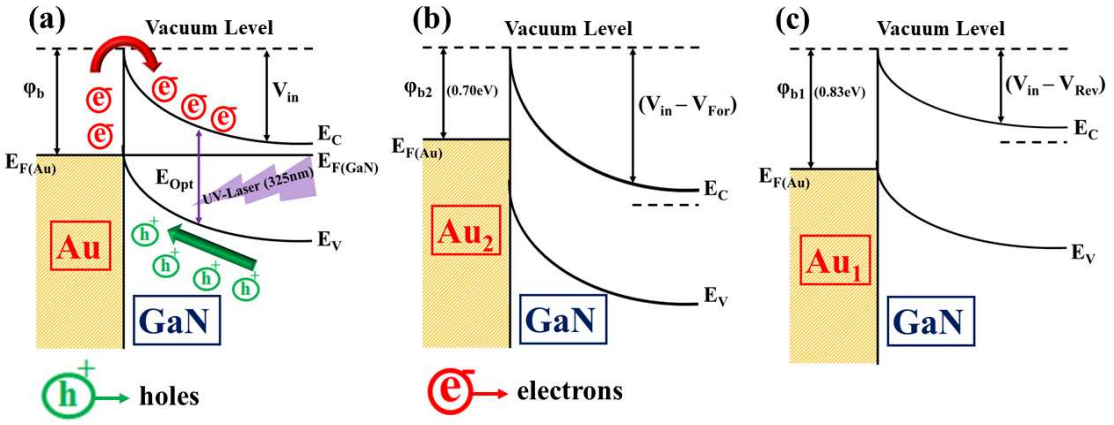

Figure 3.10: Schematic demonstration of energy band diagram at (a) equilibrium (0 V), (b) forward bias voltage, and (c) reverse bias voltage.

Figure 3.10 shows the schematic demonstration of an energy band diagram of a Schottky barrier property of the detector in equilibrium, where φ_b, E_v, E_c, $E_{F(Au)}$, $E_{F(GaN)}$ and E_{opt} stands for Schottky barrier height, valance band energy, conduction band energy, Fermi-level energy in the Au metal, Fermi-level energy in GaN-NS and optical energy band gap, respectively. Besides this, V_i, V_{For}, and V_{Rev} stand for built-in potential at 0V, applied forward bias voltage, and applied reverse bias voltage, respectively. Under the dark conditions, Au metal and GaN semiconductors were brought in contact with each other, and thermal equilibrium is reached. The fabricated detector found operational at zero-bias voltage due to the presence of developed built-in potential energy on the GaN side. The cause of the built-in potential difference is

due to the movement of the majority of generated holes of the GaN valence band tend to attract towards the Au/GaN interface under the influence of the filled Au band, and the majority of electrons moves towards the GaN side. The benefit of built-in developed potential and respective variation in SBHs has been taken up by UV illumination generated carriers at the space-charge region, *i.e.*, the Au-GaN junction, where the UV photons stimulated carriers to enhance the carrier concentration by joining the already existing dark current carriers. This enhanced carrier current cumulatively called photocurrent of the detector at 0 V bias. This self-driven channelization of current without any external bias voltage designates the detector as self-powered UV-PD, as shown in Figure 3.10(a). The fabricated detector has also been analyzed at variable bias voltage conditions were due to external bias voltage (forward or reverse) and variable SBHs offered respective lower or higher resistance path to the flow of carriers, as shown in Figure 3.10(b) and (c). The schematic diagram demonstrates the maximum enhancement in I_{ph} values have been achieved in forwarding or positive bias voltage condition where comparatively barrier height is the low and built-in potential difference is higher and vice –versa in reverse or negative bias voltage. The fabricated PD was initially tested at the self-powered mode of operation where the detector's essential performance parameters were evaluated. Figure 3.11(a) shows the optical power-dependent photoresponse of the device, and the corresponding photocurrent values were increased from 0.37 μA at 1 mW to 2.2 μA at 13 mW, which revealed a 6-fold enhancement in photocurrent. The sensitivity of the fabricated detector is determined by the following equation [149]

$$\boldsymbol{S} = \frac{\boldsymbol{I_l - I_d}}{\boldsymbol{I_d}} \tag{3.7}$$

Where I_l is the light current of the device. The sensitivity of the device was calculated to be 1.83×10^2 at 13mW at 0 V bias. Also, responsivity (R), noise equivalent power (NEP), and the detective (D) of the fabricated GaN nanostructured PD can be calculated by the following equations [75]:

$$\boldsymbol{R} = \frac{\boldsymbol{I_{ph}}}{\boldsymbol{P \times A}} \tag{3.8}$$

$$\boldsymbol{D} = \frac{\boldsymbol{R \times \sqrt{A}}}{\boldsymbol{NEP}} \tag{3.9}$$

$$\boldsymbol{NEP} = \frac{\sqrt{2e(I_d)}}{\boldsymbol{R}} \tag{3.10}$$

Where 'R' is the photo responsivity, 'A' is the device's active area. The R, D, and NEP were calculated to be 1.76 mA/W, 2.34×10^{9} Jones, and 3.5×10^{-11} $WHz^{-1/2}$, respectively at an optical power (P) of 13mW. The achieved R value is found to be higher as compared to other reported PDs, including p-n junction and MSM structures [33, 150]. Moreover, a graph of estimated external quantum efficiency (EQE %) w.r.t experimentally determined responsivity is also presented for the fixed GaN thickness, as shown in Figure 3.11(b). Interestingly, most of the devices have a film thickness ranging from 100's of nanometers to 100's of micrometers which consequently lead to reduced dislocations with increasing thickness. However, the device in this work was made with a film thickness of 30 nm, which shows the high crystalline quality of the material and comparatively better device performance.

The response and recovery time of the fabricated self-powered GaN photodetector was evaluated by periodically turning ON and OFF the ultraviolet light. The rise time constant 'τ_R' (rise time 't_r') and decay time constant 'τ_D' (decay time 't_d') were calculated to be 18 ms (t_r= 40 ms) and 28.6 ms (t_d = 63 ms), respectively, as shown in Figure 3.11(c). A comparative chart is presented in Table 3.2, which revealed the rapid reversibility of the fabricated GaN self-powered device. As far as the crystalline quality of grown GaN-NIs is a concern, the lower strain and stress values calculated by HRXRD and RAMAN analysis elucidate reduced defects in the grown film. Therefore, the fabricated detector out of this lower defect or trap states grown epitaxial GaN-NIs offered such rapid response time due to reduced channel resistance path. The statement is well supported by a report where the adverse impact of defects on electrical as well as the optical property of the GaN-based detector has been experienced, wherein a high level of defects allows a high level of trap states. These trap states consume the photon generated carriers and increase the total resistance path as well as time constant value τ =RC. [151] Therefore, the possible cause of rapid reversibility of the detector can be attributed to various factors such as built-in potential gradient, lower stress dislocation defects facilitated lower trap density, lower

optical defects [88] and the reduced dimensionality which lead to confinement of charge carrier thereby shortening the carrier transit time. [143]

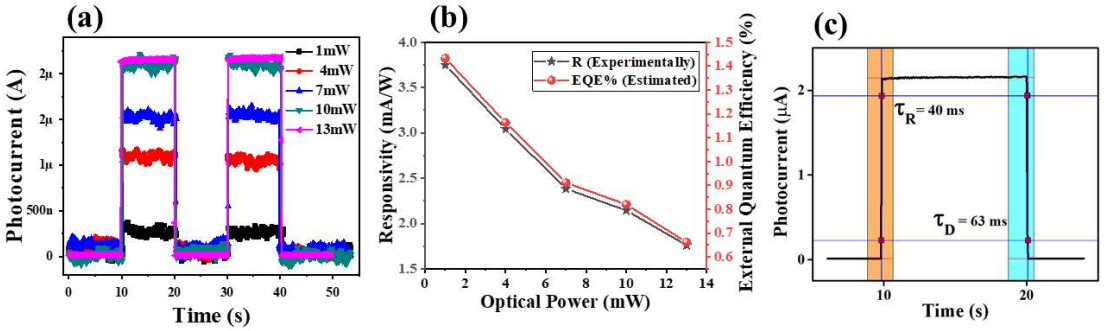

Figure 3.11: Time-dependent photoresponse of self-powered GaN PD (a) under varying optical power; estimated external quantum efficiency as per experimental responsivity; (c) rise and decay time constant fitted curves at 13 mW optical power.

Table 3.2: A comparison highlighting the rise and decay time of various ultraviolet photodetectors

Samples	Device Structure	Response Time (Reversibility)		Reference
		Rise Time (ms)	Decay Time (ms)	
GaN/Si	**MSM**	**40**	**63**	**This work**
GaN/AlN/Si	MSM	63	27	[74]
GaN Nanowire	MSM	144	256	[152]
GaN/Al2O3	MSM	280	450	[46]
Pt-NP/GaN/ Al2O3	MSM	1100	650	[47]
GaN/n-Si	pn-junction	2400	3100	[139]
GaN/n-Si	pn-junction	2800	3700	[139]
GaN/Al2O3	MSM	2900	6200	[153]
GaN/ Al2O3	MSM	17500	6200	[47]
Mesoporous GaN/Ni/Au	MSM	20000	60000	[154]

3.3.3.2 Photodetector Performance at Photoconductive mode

Furthermore, to examine the performance of the fabricated detector at the photoconductive mode of operation, a bias voltage-dependent study was performed where the applied bias voltage has been varied from -3 V to +3 V, at constant optical power of 13mW. The obtained data elaborates enhancement in photocurrent w.r.t. increasing bias voltage in both regions (negative as well as positive). The observation attributed the effect of distinctive

barrier heights and Schottky nature due to which negative bias voltage where photocurrent is lagging behind as compared to positive bias voltage which contributed enhanced photocurrent value of 43.5 µA (at 13 mW and 3V) in positive region and 37.7µA in the negative region (at 13mW, -3V) as shown in Figure 3.12. This study illustrates the role of biasing and attributed ~20 fold enhancement of photocurrent value from 2.2µA (at 0V) to 43.5 µA (+3V). Besides, to check the repeatability and reproducibility of the data, three separate detectors (S1, S2, and S3) were fabricated out of grown GaN nanostructure sample, as shown in Figure 3.13(a). The performance of the fabricated detectors was checked 5 times (M1, M2, M3, M4, and M5). Figure 3.13(b) shown variation in their respective photocurrents readings. The obtained data display reproducibility of the fabricated detector within ±0.08% error.

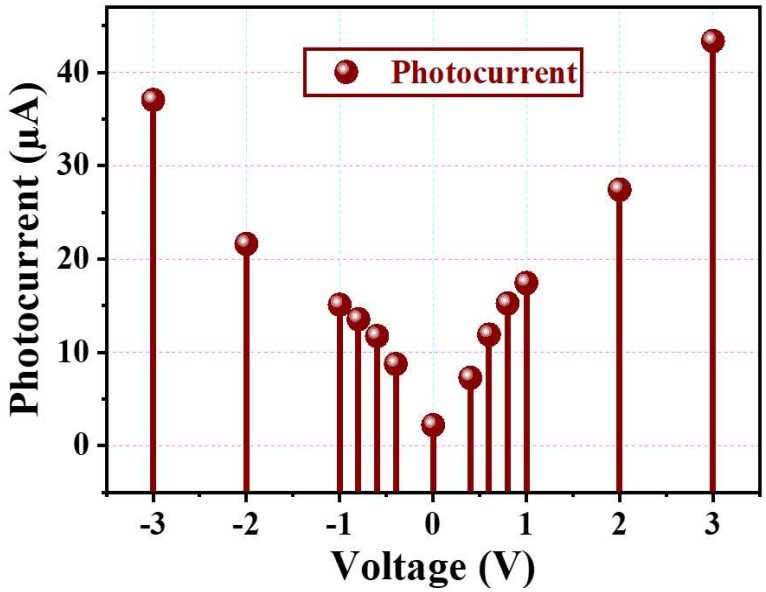

Figure 3.12: The trend showing photocurrent dependency of fabricated PD on the applied bias voltage.

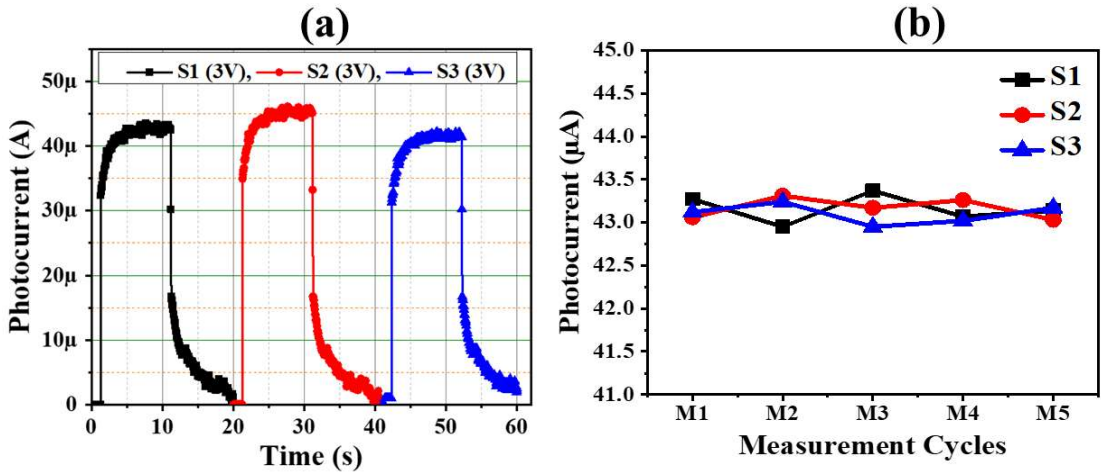

Figure 3.13: Fabricated GaN-nanostructures based UV detector's data reproducibility.

The bias voltage-dependent study (-3 V to +3 V) revealed an enhancement of photocurrent, which has a constructive effect on the performance parameters of the photodetector. Figure 3.14 shows R and D values obtained from fabricated GaN-NIs based PD by varying applied bias voltage. While applying a positive bias voltage, the R and D of the device soared to 40.3 mA/W and 5.3×10^{10} Jones, respectively. Whereas, due to the increase in negative bias voltage, the responsivity and detectivity of the device raised to 25 mA/W and 1×10^{8} Jones. A significant ~23 fold increment in R (1.76 mA/W to 40.3 mA/W) and ~10^{3} fold increment in D (7.3×10^{7} to 5.3×10^{10} Jones) is observed in the device with applied bias voltage.

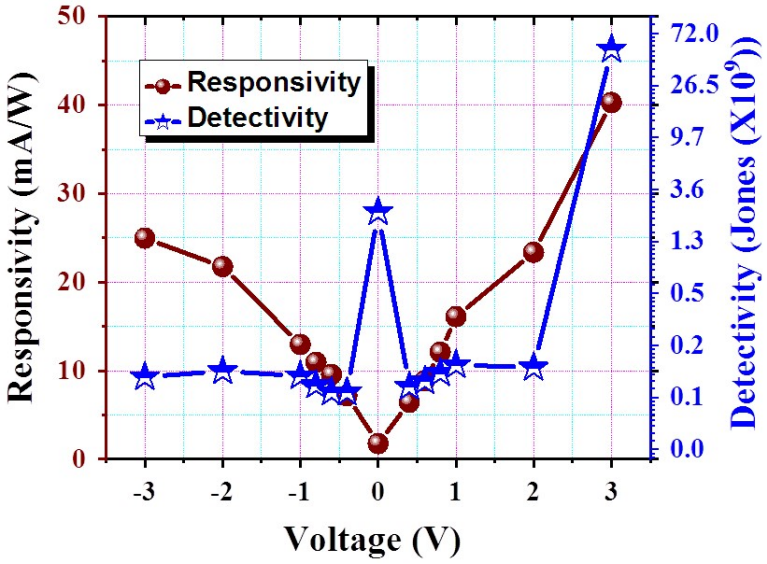

Figure 3.14: Effect of bias voltage on the responsivity and detectivity of the GaN UV photodetector.

3.4. Summery

In summery, the self-assembled GaN-NIs have been grown on Si (111) substrate with an intermediate inhomogeneous layer of Si_3N_4.The localized compressive strains fields due to bond length variation between Si-Si and Si-N, are relaxed by inhomogeneously oriented, low aspect ratio (1.92) GaN-NIs of distribution density $2\times10^{10}cm^{-2}$ and average surface roughness of 5.80 nm. Unlike conventionally available 100's of micron thin-film based detector, these tiny dimensional nano-island shaped, lower stress, and strain facilitated GaN-NIs of just 26nm height and 50nm diameter showing its dominance to detect the UV rays in MSM structure format (*i.e.*, Au/GaN/Au). The non-homogeneous GaN NS offered asymmetric interfaces leading to distinctive SBHs revealing self-powered operation of the device under photovoltaic mode. At 0V, GaN PD exhibited a detectivity, responsivity and noise equivalent power of 2.34×10^{9} jones, 1.76 mA/W and 3.52×10^{-11} $WHz^{-1/2}$, respectively. Also, the device revealed a rapid rise time constant of 18 ms. Besides, at the photoconductive mode of operation with the power-dependent study realized an increment in photocurrent which influenced PD performance parameters such as responsivity (1.76 to 40.2 mA/W) and detectivity (7.3×10^{7} to 5.3×10^{10} Jones), where a 23 fold and ~1000 fold increment was observed, respectively. The presented work is focusing on the very thin layered GaN UV-PD which can generate the interest of the researcher to develop UV detector with ease of fabrication included very low material and processing time. As far as real applications are concerned and the retrieved sensing data from the fabricated detector, the proposed detector found useful for all possible practical applications. However, the device found its limitation where response time requirement is less than a millisecond, and photocurrent requirement is extremely high to eliminate the amplifier circuitry.

4.1. Introduction

Nowadays, the revolution in the development of photodetector technology emphasising on key performance parameters such as fast switching speed, high responsivity, low noise equivalent power and high quantum efficiency [155, 156]. Hence unlike the conventional approach of improving material quality and device structure design, much attention has been paid for enhancing the performance of existing optoelectronic devices by combining the device with other more resourceful and feasible methods. Henceforth, one of the most typical representatives,*i.e.*, novel metal nanoparticle's (NP's) nanoplasmonic enhanced the performance of semiconductor devices such as solar cells, LEDs and UV-PDs [47, 49, 157]. Some previous reports articulate that, the use of nanoplasmonics behaviour of metals NPs such as silver (Ag) NPs [46], aluminium (Al) NPs [48, 157], platinum (Pt) NPs [47] and gold (Au) NPs [49] have been realized as a remedy for the carrier enhancement seeker GaN-based UV-PDs. Wherein, metal NPs stimulated hot carriers are guided by local surface plasmons resonance (LSPR) for enhancing optical detector performance. Thus, LSPR induced enhanced UV emission has been reported in Au-NPs decorated ZnO-NSs [48, 158]. The Au-NPs nowadays splendidly established their identity in LSPR due to numerous inherent advanced physical properties like non-linear optics, magneto-plasmonics, optical trapping and optical activity [57], high chemical and physical stability, ease of surface functionalization with biomolecules and plasmon oriented multitude of optical properties. [58, 59] Besides, Au-NPs is also known for access to easily polarizable hot carriers (hot resonant electrons). These polarizable conduction electrons interact with the electromagnetic field of the corresponding incident electromagnetic lightwave and generate nonlinear optical phenomena. [159] Therefore, this chapter mainly discussing the chemical synthesis of monodispersed, ~10nm sized Au-NPs, wherein, the impact of their nanoplasmonic effect on gallium nitride (GaN) nanoislands (NIs) based MSM UV-PDs (as discussed in Chapter-3) has been realised as UV detection enhancer. The study elaborates the nanoplasmonics effect which leads to trapping of incident photons by the process of localized scattering and absorption, as a consequence of incident photons and metal NP interaction which increases the light and material interaction time. This scattering

stimulated enhanced interaction allow high photons absorptions which generate more electron-hole pairs [160] which were further realised in enhancement in PD's photocurrent. This enhanced photocurrent value due to Au-NPs intervention as compared to bare GaN-NIs based UV-PD also reflected in previously discussed other corresponding performance parameters such as responsivity, detectivity, noise equivalent power, quantum efficiency and switching speed at photovoltaic as well as photoconductive mode of operation.

4.2 Au-Nanoparticles Synthesis, Deposition and Characterization

4.2.1 Synthesis of Au-Nanoparticles

Au-NPs were synthesized in the presence of trisodium citrate using Turkevich method [161] where, initially 1mM (20 mL) Gold (III) chloride hydrate ($HAuCl_4.3H_2O$) (M.W. 339.79) precursor solution (Sigma Aldrich, USA) was prepared in a flask and reflux at 90°C along with continuous stirring. Further, 40mM (2mL) Tri-sodium citrate ($C_6H_5Na_3O_7.2H_2O$) (M.W. 294.10) was added to the precursor solution (Loba Chemie, Mumbai, India). The solution changed colour from transparent to violet and finally to wine red which indicates the formation of colloidal Au-NPs (shown in Figure 4.1).

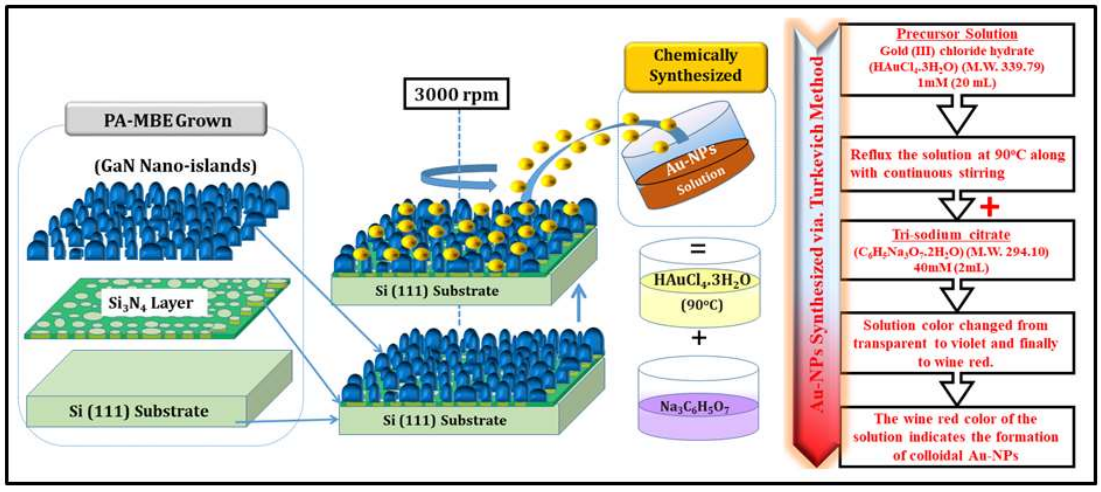

Figure 4.1: Au-NPs chemical synthesis flow chart and their deposition on PAMBE grown GaN-NIs.

These synthesized Au-NPs have been characterized by UV-Vis spectroscopy (Agilent, Cary 5000i) and high-resolution transmission electron microscopy (HRTEM) (FEI,

Tecnai F30 G2 Stwin). The HRTEM images of bare Au-NPs elucidate spherical shape with an average size ~10 nm and UV-Visible absorption spectrum shows LSPR peak position at ~520nm which also confirm the size of Au-NPs is ~10nm [162] [(Figure 4.2 (a-c)]. The broadening of UV-Visible absorption spectrum is found directly in correlation with the concentration of Au-NPs, [162]thereby lower broadening and higher absorption postulate higher concentration of Au-NPs which can contribute more LSPR generated hot carriers into the devices. The presence of LSPR stimulated hot carriers are confirmed by the room temperature (RT) photoluminescence (PL) (Edinburg, FLS980 D2D2) measurements of Au-NPs (Figure 4.2 (d)).

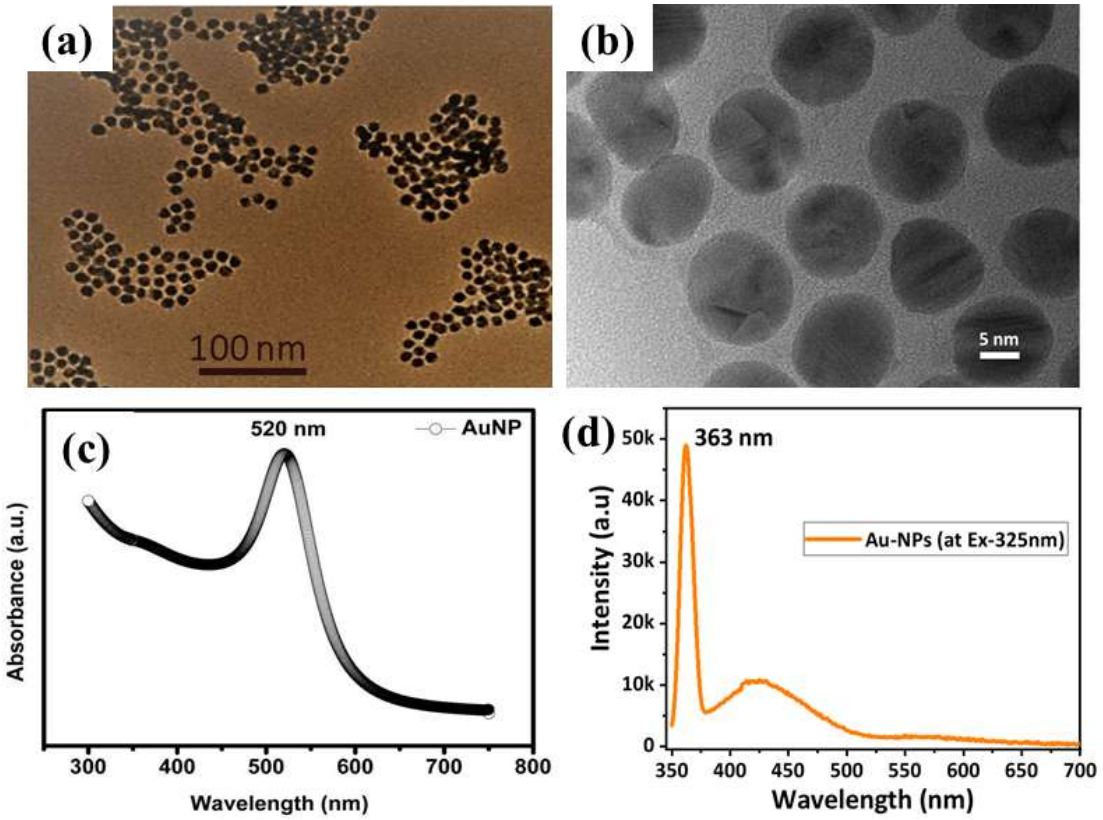

Figure 4.2: (a-b) HRTEM micrograph of NPs with 100nm and 5nm resolution (c) UV-Vis absorbance spectra of Au-NPs, (d) RT-PL spectra of Au-NP.

4.2.2 Morphological and Elemental analysis of Au-NPs decorated GaN-NIs

These chemically synthesized monodispersed ~10nm sized Au-NPs were decorated on as-grown GaN-NIs. For the uniform distribution of optimized Au-NPs, a spin coating technique was employed with a constant speed of 3000 rpm. Afterwards, the prepared Au-NPs/GaN-NIs heterostructure has been annealed up to 200°C for the better interface and

elimination of solvent chemical. The morphology and the elemental study of uniformly distributed Au-NPs decorated on GaN-NIs surfaces have been carried out using FESEM and EDS techniques (shown in Figure 4.3). Top right inset of Figure 4.3 shows EDS spectrum measured from the Au-NPs decorated GaN-NIs, provide evidence of N_2, Si, Ga and Au with respect to their corresponding weight, the atomic percentage of (10.11%, 27.23%), (44.41%, 59.68%), (12.49%, 6.76%) and (33.00%, 6.32%), respectively. An elemental mapping measurement has been performed for precise investigation of uniformly distributed Au-NPs on GaN-NIs surfaces, as shown in Fig 4.4 (a-d).

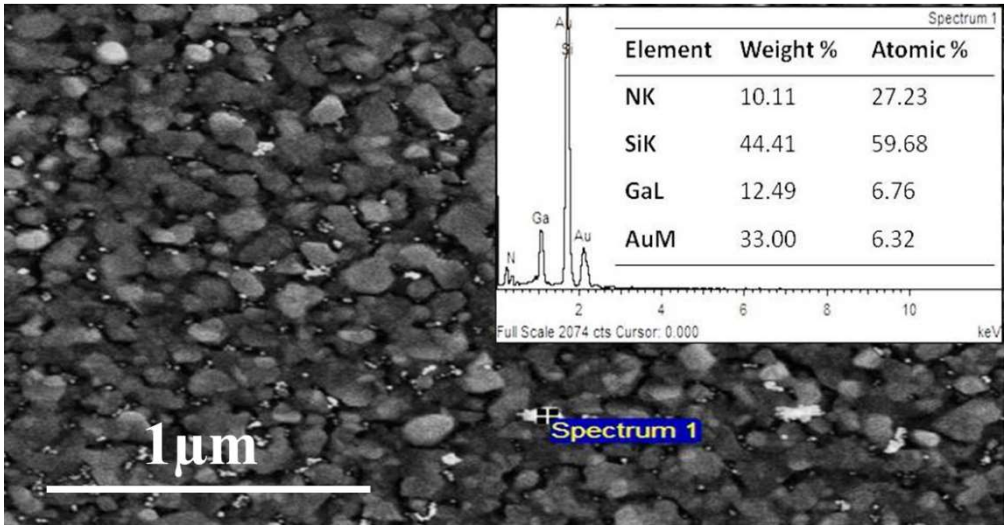

Figure 4.3: FESEM image of Au-NPs decorated GaN-NIs, top right inset shows its EDS spectra.

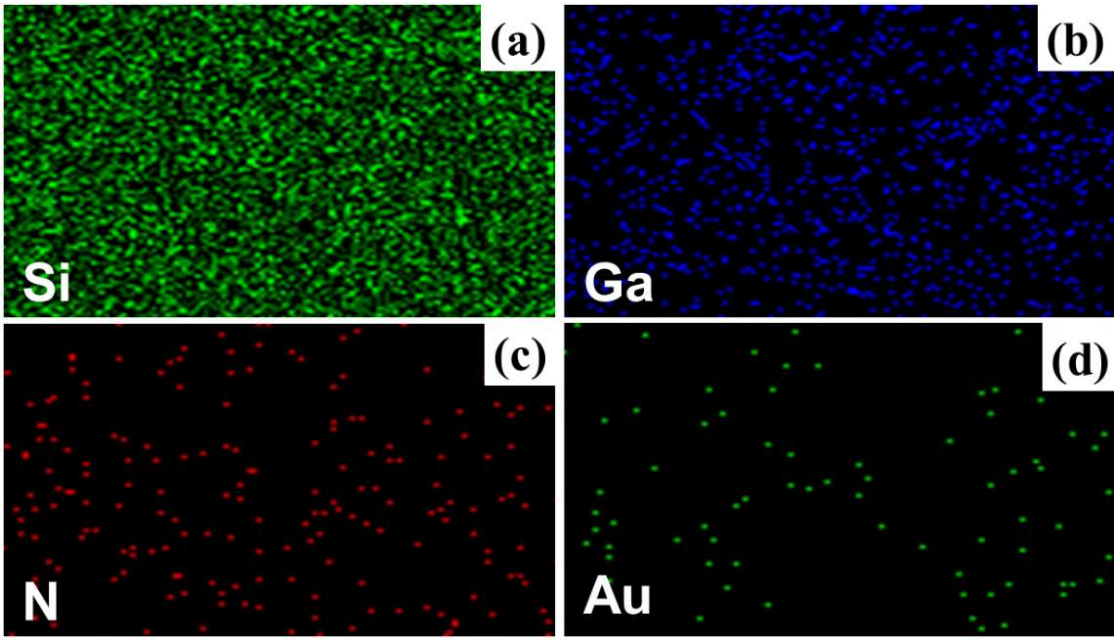

Figure 4.4: (a-d) Elemental mapping of Au-NPs/GaN-NIs/ Si (111)

4.2.3 Effect of Au-NPs on photoluminescence property of GaN-NIs

To analyze the enhancement in photon generated hot carriers from Au-NPs decorated GaN-NIs devices, the RT-PL measurements were carried out. RT-PL spectra demonstrate the UV emission at 364 nm and an additional peak of violet-blue emission for all the samples (bare GaN-NIs, and Au-NPs/ GaN-NIs) when excited by 325nm UV-laser as shown in Figure 4.5. The UV emission at 364nm resembled the near band edge emission (GaN bandgap of 3.406 eV) and recognized to the radiative recombination of excitons, although the presence of violet-blue emission (380nm to 440nm) is due to trap states related to the optical states existing in between the bandgap regime [163, 164]. The spectra clearly validate significantly enhanced UV emission for Au-NPs decorated GaN-NIs (×1.4) as compared to their bare counterpart, as shown in Figure 4.5. The coupling of Au-NP's localized surface plasmons at the interface with GaN-NIs postulates resonance interaction between electromagnetic field of the incident UV light and electron charge near the surface of Au-NPs (emission at 363nm as shown in Figure 4.2 (d)), contributes more electrons in-flow with existing GaN channel.

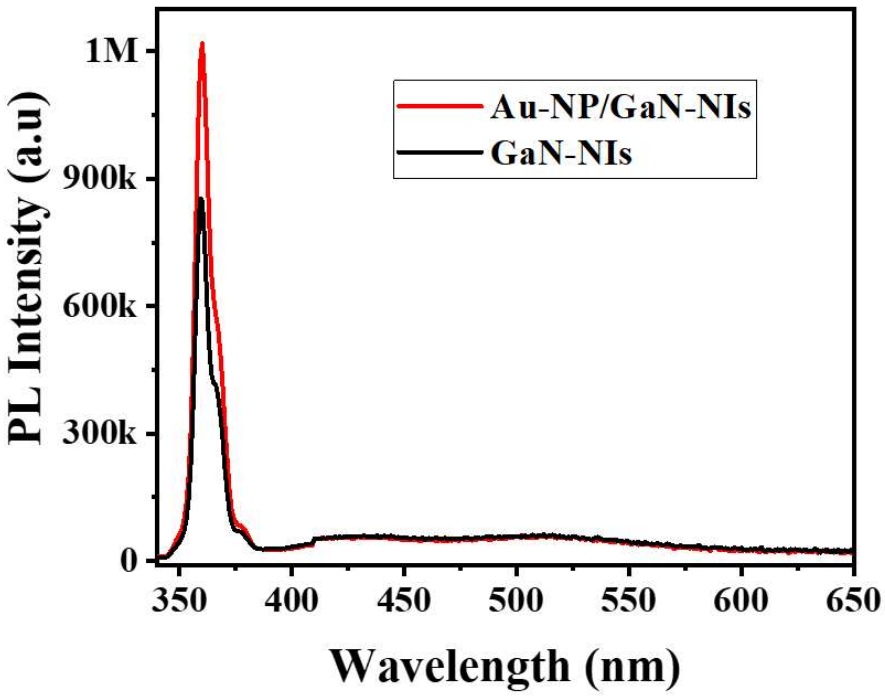

Figure 4.5: RT-PL spectra of bare GaN-NIs and Au-NP/GaN-NIs.

4.3 Device Fabrication and Opto-Electrical Measurement

For the fabrication of UV photodetectors, Au-metal electrodes (200nm thick) were deposited as MSM structure by thermal evaporation technique on bare and Au-NPs coated GaN-NIs samples, and the active area of devices is fixed to $3\times10^{-3}cm^2$. The impact of Au-NPs on the opto-electrical transport is analysed by RT current-voltage and photoresponse measurement which was carried out by using Cascade Microtech instrument (EPS150TRIAX with shield enclosure EPS-ACC-SE750) for low signal measurements (current resolution in pico amperes and time resolution of 110 μs). The system was equipped with a focused laser (λ = 325 nm, optical power = 1 mW (power density: 0.0141 Wcm^{-2}) to 13 mW (power density: 0.184 Wcm^{-2})) for UV illumination.

4.4 Au-NP's stimulated enhanced Opto-Electrical transport

To analyse the Au-NPs nanoplasmonics stimulated enhancement in the opto-electrical transport, the fabricated UV PD has been tested at the photovoltaic or self-powered (without bias) as well as at photoconductive mode of operation. Thus, I-V measurement for bare GaN NIs and Au-NPs/GaNIs based MSM UV-PD devices have been performed under dark and UV illumination (325nm) at RT, as shown in Figure 4.6. The data revealed that Au-NPs/GaN-NSs based UV-PD yield enhanced photocurrent (I_{ph}) characteristics as compared to bare GaN-NSs UV-PD devices at self-powered mode (0V bias) as well as under variable bias conditions (from -1V to +1V). At zero volt bias, the Au-NPs/GaN-NIs UV-PD display very low dark current (I_d) ~ 22nA and very high light current (I_L) ~ 25μA, however in case of bare GaN-NIs UV-PD these values are found to be ~ 12nA (I_d) and ~2.1μA (I_L) which elucidates ~ 12 folds enhancement in photocurrent ($I_{ph} = I_L - I_d$) as shown in the inset of Figure 4.6. The photovoltaic behaviour is originated from the above discussed Au/GaN Schottky junction and asymmetric Au/GaN interfaces triggered inbuilt potential gradient [165]. The analysis reveals that, due to the presence of Au-NPs, the fabricated Au-NPs/GaN-NIs device display enhanced photovoltaic characteristics as compared to their respective bare GaN-NIs based device. Further, significant variation in the

photocurrent has also been observed for these devices (bare and Au-NPs/GaN-NIs) under applied bias (-1V to +1V). The Schottky barrier height (SBH) (φ_b) and their ideality factor (n) of the Au-NPs/GaN-NIs as compared to their respective bare counterpart have been evaluated for forward as well as reverse bias by using standard thermionic emission theory [70, 139] as shown in Table 4.1.

Table 4.1: Ideality factors and SBH variations at two Au/GaN interfaces on each of four fabricated UV-PDs.

	GaN-NI(A)		**Au-NP/GaN-NI(B)**	
Au/GaN	**Interfaces**			
	1	**2**	**1**	**2**
n	n_{A1} (1.8)	n_{A2} (1.92)	n_{B1} (1.2)	n_{B2} (1.5)
φ_b(eV)	φ_{bA1} (0.75)	φ_{bA2} (0.85)	φ_{bB1} (0.703)	φ_{bB2} (0.8)

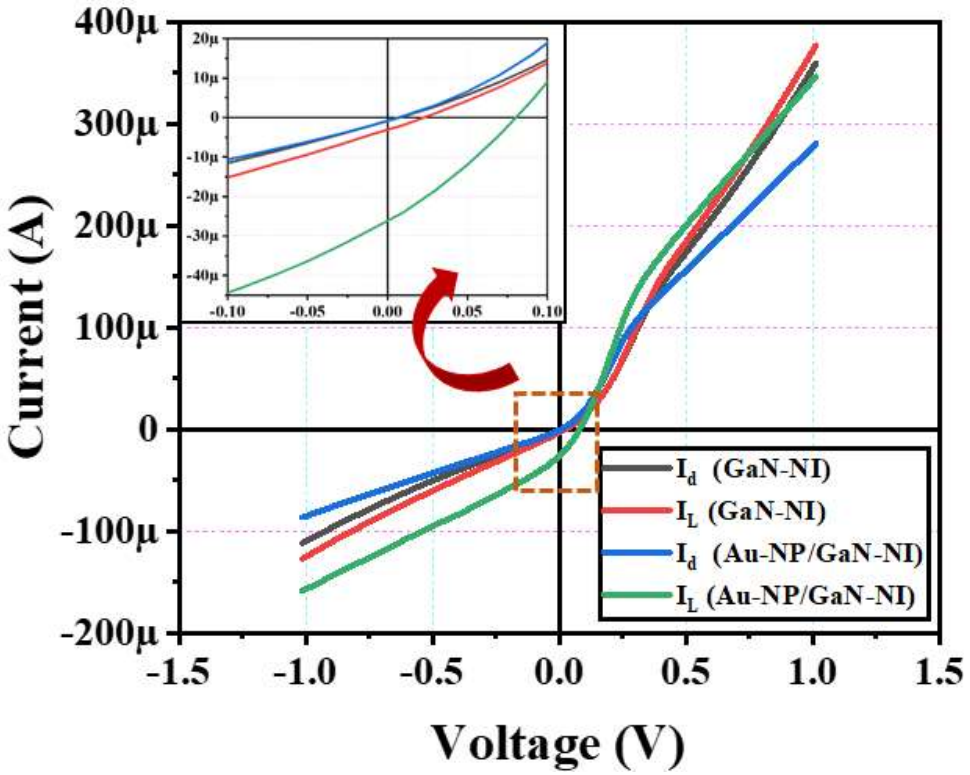

Figure 4.6: I-V characteristics of bare (GaN-NIs) and Au-NPs/GaN-NIs based devices under dark and UV illumination, top left inset shows the variation in photocurrent at 0V.

The performance parameters such as detectivity (D), responsivity (R), noise equivalent power (NEP) and quantum efficiency (η) of the fabricated UV-PDs have been calculated by using the equations 3.9, 3.8, 3.10 and 4.1.

$$\eta = \frac{R \times h \times c}{e \times \lambda} \tag{4.1}$$

Where h is the Planck's constant, c is the speed of light, e is the elementary charge, and λ is incident photon wavelength of the illuminating source. The responsivity, detectivity and NEP of all the fabricated devices is calculated for zero and applied bias between -3V to +3V. It was observed that the responsivity of the fabricated detectors in self-powered mode is enhanced by ~12× for Au-NPs decorated GaN-NIs detector as compared to their bare device, respectively. The responsivity of these devices has been analyzed at applied bias -3V to +3V where both the fabricated detectors shown gradual increment in the value of 'R' in either direction of bias polarity (Figure 4.7a). Significant enhancement in 'R' from 151.28mA/W (bare GaN-NIs) to 215.67mA/W (Au-NPs/GaN-NIs) at -3V is determined (Table 4.2).

Table 4.2: Comparative evaluation of various performance parameters of bare and Au-NPs incorporated GaN-NIs based MSM UV-PDs.

Fabricated Detectors	**R (mA/W)**		**D (10^9Jones)**		**NEP (10^{-11}WHz$^{-1/2}$)**		**Q.E (%)**	
	0V	-3V	0V	-3V	0V	-3V	0V	-3V
GaN-NIs	~4	~151	3.43	0.708	1.6	7.73	1.48	58.73
Au-NPs/GaN-NIs	~46	~216	30.5	1.22	0.18	4.49	17.6	82.4

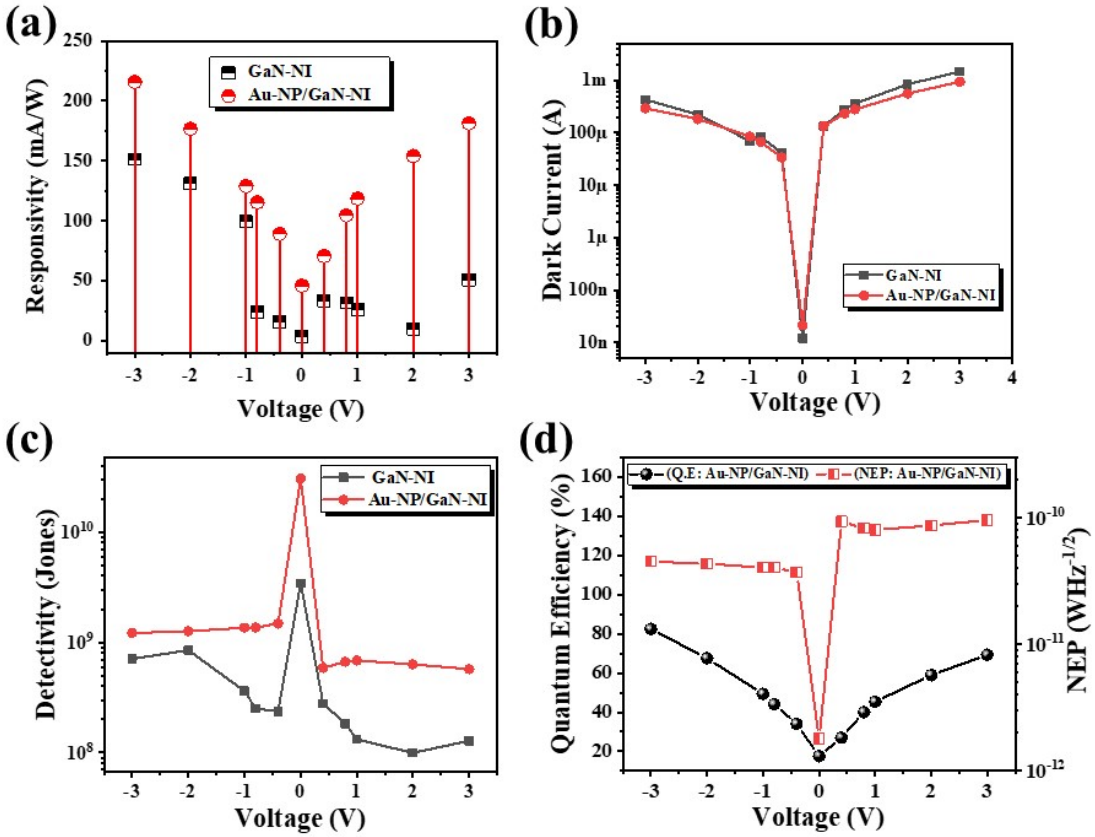

Figure 4.7: Detectors performance parameters variation w.r.t (a-d) applied bias voltages.

Furthermore, detectivity of the fabricated devices have also been analyzed at self-powered as well as at variable bias conditions (±3V). Au-NPs highly conductive behaviour accelerated reduction in the dark current (Figure 4.7(b)) and enhanced responsivity, significantly reciprocate increased D values (Figure 4.7(c) and Table 4.2),*i.e.* from 3.43×10^{9} Jones (bare GaN-NIs) to 3.05×10^{10} Jones (Au-NP/GaN-NIs) in self-powered mode. At higher applied bias, the increase in D values is limited due to high dark current. The bias dependent analysis also revealed the criticality of dark current which can directly affect detectivity as well as noise equivalent power (NEP) of the detectors as shown in Figure 4.7(c-d) and Table 4.2. The observation elucidates that unlike higher dark current values at higher bias voltage (-3V), lower dark current at self- powered mode allows the fabricated detectors to achieve higher D values and lower NEP,*i.e.*, 1.79×10^{-12} WHz$^{-1/2}$ (Au-NP/GaN/NIs) as compared to their bare counterparts (Table 4.2 and Figure 4.7(d)). The study divulges that the GaN-NI based UV-PD with Au-NPs demonstrates comparatively superior performance. The

capability of these detectors have also been investigated by applied bias voltages and realized as an increment in quantum efficiency (Q.E), where they achieved their maximum value comparatively,*i.e.*, 82.4% by Au-NP/GaN-NIs at -3V as shown in Figure 4.7(d) and Table-4.2.

The performance of both the fabricated UV-PDs with varying incident optical power 'P_{opt}' (from 1mW to 13mW) is tested which shows promising linear inclination in photocurrent (I_{ph}) values (as shown in Figure 4.8). The results demonstrate increasing I_{ph} values from 1.02µA (1mW) to 2.87 µA (13mW) revealing ~2.8× increment for bare-GaN-NIs UV-PD. The Au-NPs induced LSPR significantly enhances I_{ph} values with increasing power such as 2.46 µA (1mW) to 26.2 µA (13mW) shows ~11 fold enhancement in Au-NPs/GaN-NIs. Thus, Au-NPs hot carrier induced enhancement is evidently witnessed in the performance of the fabricated devices.

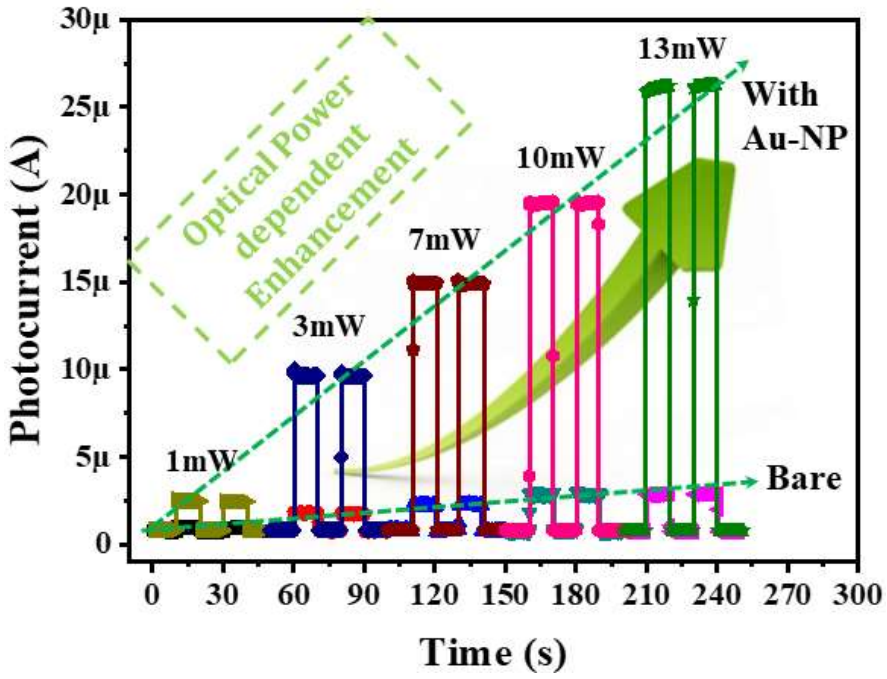

Figure 4.8: Power dependent transient response of bare and Au-NPs/GaN-NIs detectors.

Next, the switching speed of the detector, which elucidates the quality of a detector to detect illuminating photons has been evaluated. The switching speed of the fabricated UV-PD in terms of time-correlated response and recovery was estimated from its transient response by UV light illumination turning ON and turning OFF. Figure 4.9

shows the time-correlated photoresponse under self-powered mode (at 13mW optical power) of the all the fabricated UV-PDs where the rise (response) time and decay (recovery) time curves are fitted with respect to experimental data by following equations [15]:

$$\boldsymbol{I = I_0\left(1 - e^{\frac{-t}{t_r}}\right)} \tag{4.2}$$

$$\boldsymbol{I = I_0\left(e^{\frac{-t}{t_d}}\right)} \tag{4.3}$$

where I_o is the maximum saturation photocurrent value at a particular time t, t_r and t_d stand for the rise and decay time, respectively. The measured rise time from 10% to 90% of final value,*i.e.*, 't_r' under UV-illumination and decay time from 90% to 10% of final value 't_d' after switching off UV-illumination.

The observation reveals that the fabricated detectors with Au-NPs getting benefited by LSPR generated high-density charge carriers. Wherein, the highly conducting behaviour of Au-NPs plays a significant role to reduce the defects originated obstructions in the flow of charge carriers. This reduction in offered resistance to the photocurrent allows quick retardation of the photocurrent after switching OFF the UV light. Figure 4.9 shows the effect of quick retardation as quick recovery time,*i.e.*, 't_d' of GaN-NI (~63.6 ms) is reduced to Au-NP/GaN-NI (40 ms) based UV-PD. The rise and decay time measurement of the fabricated detectors is restricted <40ms due to system limitation.

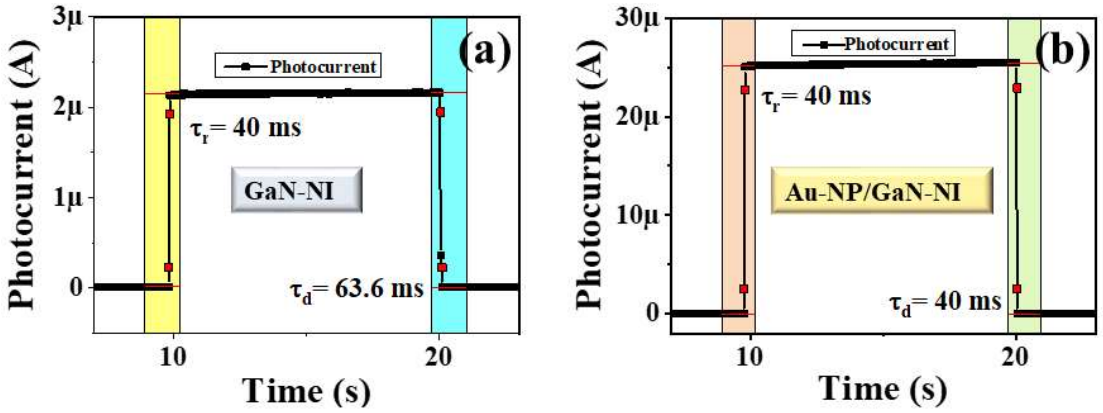

Figure 4.9: Time correlated photoresponse rise time and decay time fitted curves (a) bare GaN-NIs and (b) Au-NP/GaN-NIs MSM UV-PD under self-powered mode at 13mW.

Table 4.3: Switching speed comparison with various devices incorporating hot carrier generated by nanoplasmonics effects.

Devices	Response Time(Switching Speed)		Reference
	Rise Time (ms)	Decay Time (ms)	
Au-NPs/GaN-NF/Si(111)	40	40	**This work**
Au-NPs/GaN-NS/Si(111)	40	40	**This work**
Au-NP/Ga-polar GaN	2900	6200	[153]
Au-NP/ZnO/PET	10300	14200	[166]
Ag-NP/ZnO-NW	80	3270	[167]
Pt-NP/GaN-NS/ Al_2O_3	1100	650	[47]
ZnO-NP/Quartz	600	8000	[168]
ZnO-NP/Quartz	22000	11000	[169]
ZnO-NP/Glass	2000	12000	[170]
TiO_2-NP/SiOx	1000	900	[171]
TiO_2-nanofibers/SiO_2/Si	1500	7800	[172]

Table 4.3 shows, upon comparing with previous reports on nanoplasmonics, the fabricated GaN-NIs UV-PD with Au-NPs, herein exhibit fast rise and decay time. Such high switching speed is contributed by additional potential force due to variation in SBHs, reduced channel resistance due to the additional effect of Au-NP's higher conductivity, a better crystalline quality, which was elaborately discussed elsewhere [88] and revealed negligible defect band in PL and low stress via micro-Raman spectroscopy.

4.5 Nanoparticle's Nanoplasmonics and Hot resonance electron generation mechanism

The effect of nanoplasmonics in the opto-electrical behaviour of GaN-NIs based devices can be realized due to Au-NPs stimulated LSPR effect, which can

significantly enhance photocurrent in the fabricated device due to enhanced light absorption in the near-surface region [173, 174]. The metallic NPs had size dimensionality to the metal skin depth where the electric field of incident electromagnetic radiation of light can polarize the conduction electrons of such NPs as a consequence of ease of penetrating the metal surface [175, 176]. The LSPR with uniformly distributed Plasmon oscillation over entire nanoparticle volume where the size of NPs is much smaller (~10nm) than the incident photon wavelength (325nm) has non-propagating excitations. The generated plasmons over the NPs have two possibilities,*i.e.*, either they got absorbed or scattered. The probability of absorption or scattering can be determined by σ_{Abs} and $\sigma_{Sca,}$ respectively, which depend on the size, shape, and structure of NP's [57, 159]. The Au-NPs of size < 25nm having pure plasmon absorbers properties due to negligible scattering coefficient,*i.e.*, $\sigma_{Abs}>>>\sigma_{Sca}$[177]. These absorbed plasmons originated resonance, or electron clouds are damped (through Landau damping) by these low dimension NPs in two ways: non-radiatively and radiatively through hot electron-hole pair generation and re-emission of photons, respectively [178]. The distribution of these generated carriers depends upon factors such as particle size, plasmon energy, plasmon mode symmetry, state density of the material, and electronic structure. [52] The plasmon decay generated carriers release their energy (via. carrier relaxation) among many lower-energy electrons through their inter-scattering process,*e.g.*, Auger transition. [179]Figure 4.10 displays a complete schematic diagram (including energy band diagram) of nanoplasmonics generated LSPR excitation of Au-NPs and their damping around the medium (GaN-NIs), carrier generation, their scattering, relaxation, and distribution. These Au-NP's LSPR injected extra carriers (resonant hot electrons) in addition to existing UV photons generated carriers of GaN-NIs enhanced the cumulative photocurrent. [180]

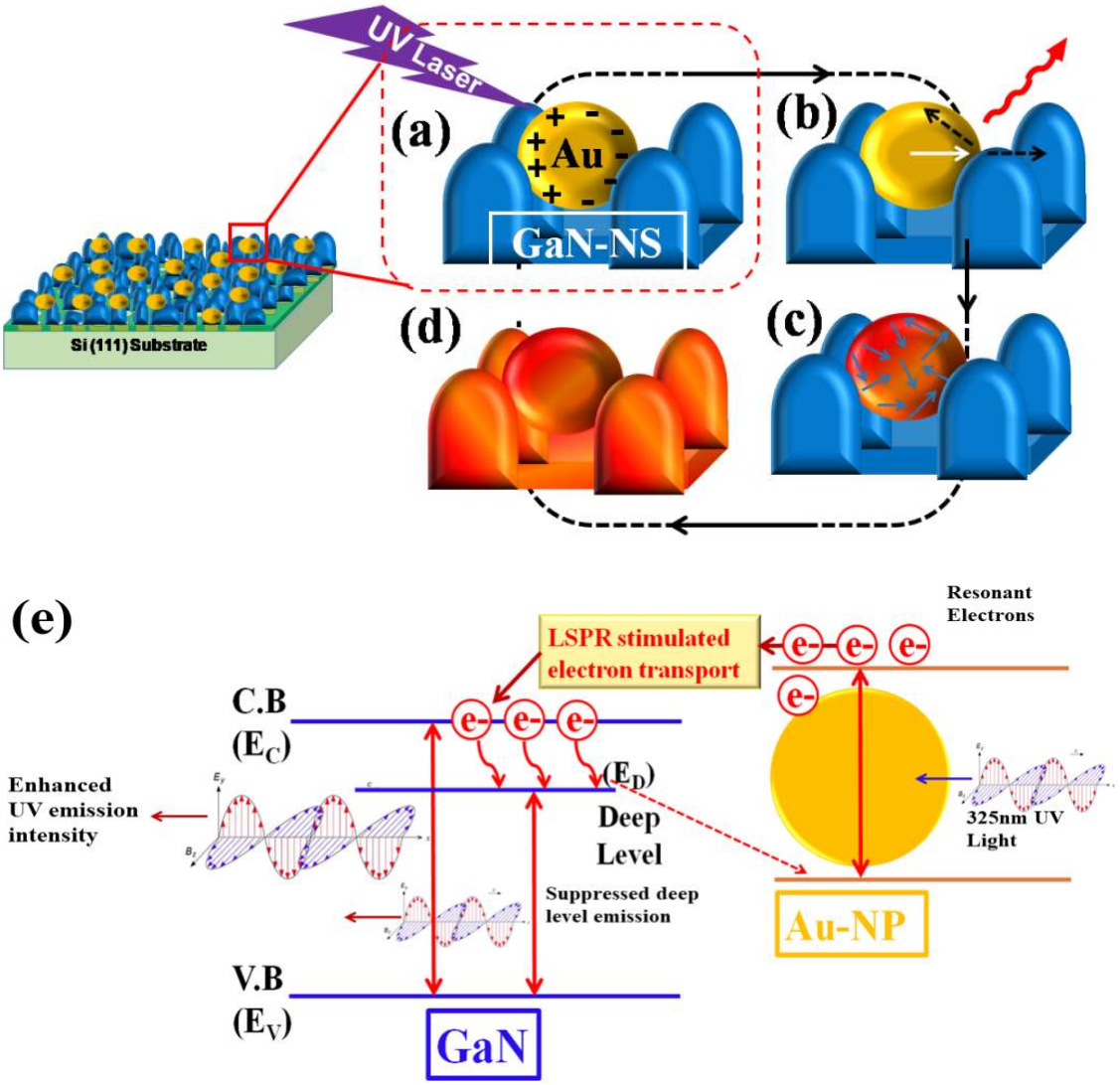

Figure 4.10 Schematic illustration of nanoplasmonics in NPs, (a) Local surface plasmons (LSPs) are excited by electromagnetic waves of UV light propagating in free space, (b) process of Landau Damping (c) Scattering and relaxation of LSPR generated hot carriers (d) Energy Dissipation. (e) Energy band diagram of GaN- NSs and Au-NPs system showing LSP coupling (325nm laser source excites GaN-NIs as well as Au-NPs). The schematic demonstrates GaN generated carriers are getting merged with Au-NPs LSP originated resonant hot electrons in the same band regime of GaN,*i.e.*, ~364nm.

4.6 Summery

Therefore to overcome the fabricated device limitation, the study adopted a significant impact of chemically synthesized, monodispersed Au-NPs (~10nm) on the performance of GaN-NIs based UV-photodetector with reduced active area geometry. GaN detectors with Au-NPs prominently respond towards UV in both self-powered as

well as photoconductive mode of operation and display fast and stable time-correlated photoresponse with significant enhancement in the performance parameters. The enhanced performance of the fabricated devices is due to nanoplasmonics induced LSPR stimulated hot resonant carriers. Moreover, the electronic transport properties affirmed the influence of Au-NPs in lowering the ideality factor and SBH at the Au/GaN interfaces due to which channel resistance of the fabricated detector is reduced. These distinctive barrier heights stimulated self-powered UV-PDs have been shown fast switching speed (rapid rise and decay time of 40 ms), maximum enhanced responsivity [(~151mA/W) → (~216mA/W)], detectivity (7.1×10^{8} jones → 1.2×10^{9} jones), quantum efficiency (58.7% → 82.4%) and reduced NEP [(7.7×10^{-11} $WHz^{-1/2}$)→ (4.5×10^{-11} $WHz^{-1/2}$)] as compared to its bare counterpart. The decoration of low dimensional Au-NP's nanoplasmonics behaviour on GaN-NIs acts as a detection enhancer with fast recovery time, paves the way towards the realization of energy-efficient optoelectronic device applications.

5.1 Introduction

Gallium nitride (GaN) ultraviolet (UV) photodetectors (PDs) attracted a lot of attention due to their versatility and ability to serve in an extreme environment. Thereby, GaN-material inherits the detectors with high carrier mobility, high saturation velocity, high-temperature sustainability, high breakdown voltages, inertness, and hardness towards chemical and radiation, respectively. Therefore with various advantageous properties, GaN UV-PDs have fixed their position in numerous important domestic, commercial as well as military applications. [105] Henceforth, the significance of durable and efficient GaN-based UV-PDs technology can be well understood by their significant contribution to mankind as well as their realized big market size. Ideally, the very low leakage or dark current and very high photo-induced charge carrier,*i.e.*, photocurrent are the prime Figure of merit for any photodetector device. For this, the reduction in dark current is an essential parameter which is broadly affected by the defect density in the grown semiconductor material. Thus, the performance of the device can directly be correlated with defects generated during the sensing material growth by the involvement of unwanted foreign elemental as well as the lattice mismatch induced stress-strain. Therefore, the growth of sensing materials with NSs morphology have played a significant role due to very low stress-strain induced electrical as well as optical defects that reciprocate its significant impact on detector performance. [16, 17] As discussed in chapter 3, the self-assemble 3D GaN NSs accommodates this lattice mismatch with the substrate and grow fully relaxed and free of extended defect (threading dislocations or basal plan stacking faults). Moreover, unlike low aspect ratio NSs, the high aspect ratio NSs were recognized as a structure with more stress relaxed and high surface to volume ratio. Besides, the increased surface area in NS offers more absorption sites to incident photons for generating high density of carriers, and lower resistance path (Resistance α 1/Area), which can cumulatively increase the detection capability of the PDs. Henceforth, growth of high surface-to-volume ratio and stress relaxed 3D GaN-NSs could play a crucial role in the development of highly efficient optoelectronic devices.

Till date, many efforts have been made to grow the one-dimensional GaN NSs such as nanorods, nanocolumns, and nanowires using different growth methods such as the

laser ablation method,[181] arc discharge method,[182] CNTs-confined reactions method,[183] metal-organic vapor phase epitaxy method (MOVPE),[103] metal-organic chemical vapor deposition method (MOCVD) [111] and plasma-assisted molecular beam epitaxy method (PAMBE).[74, 88]Among these different growth methods, the PAMBE process is found to be of particular interest due to precise control on the sensing semiconductor material growth structure by defined tuning of various growth parameters (substrate temperature, BEP of the source material, N_2 plasma power, and growth duration) that can affect the crystallinity and morphology of the grown GaN-NSs. [74, 88] It has been reported that GaN-nanocolumnar crystals exhibit the inherent property of wavelength tunability, low dislocation density, and lower lattice related strain. [20] Due to the defect-suppression property of nano-columnar structures, [21, 22]the GaN-nanocolumns (GaN-NCs) structure proven to be a strong candidate which can be utilized for the fabrication of efficient UV-PDs. Therefore, in this chapter, we have demonstrated the growth of GaN-nanocolumnar structures on Si (111) substrate under nitrogen-rich conditions. Thereafter, these GaN-NCs converted into the unique tapper ended GaN-nanotowers (GaN-NTs) structures by strategically altering the growth parameters, wherein various different GaN-NTs heights (for enhancing the active surface area) and AlN buffer layer thickness (better insulation for leakage current) samples have been grown. Furthermore, the impact of these variations in the grown samples was meticulously investigated in terms of crystalline, morphological, and optical properties. Besides this, two UV-PDs have been fabricated out of the grown samples, where the role of asymmetric Au-metal contact/GaN-NTs interfaces (provides operability at photovoltaic mode), aluminium-nitride (AlN) buffer layer thickness which is sandwiched between Si (111) substrate and sensing semiconductor material (GaN-NSs) has been very well executed as enhanced performance UV-PDs in photoconductive mode of operation.

5.2 Material Growth and Characterization

GaN-NTs structure has been epitaxially grown by Plasma assisted molecular beam epitaxy (Compact 21 Riber) on Si (111) substrates. A schematic diagram of GaN-NT growth is shown in Figure 5.1. After standard wet chemical *etc*hing and thermal

cleaning procedure [74] of Si (111) substrate (Figure 5.1(a)), for sample S1: AlN buffer layer (580nm) has been grown at 800°C with Al beam equivalent pressure (BEP) of 6.8×10^{-7} torr (shown in Figure 5.1(b)). Subsequently, a wetting layer of Gallium (Ga) has been deposited for 10 sec at a lower substrate temperature of 666°C that precedes the nucleation process of GaN growth. The growth of closely packed GaN –Nanocolumns has been performed at substrate temperature 666 °C for 220 min with Ga BEP of 2.8×10^{-6} torr and to fulfil the essential requirement growth, nitrogen-rich condition (III/V ratio <1) was maintained by adjusting N_2 flow up to 3 sccm with 400 W RF-plasma power. Afterwards, the growth conditions of closely packed GaN-NCs (shown in Figure 5.1(c)) has been altered to the tapered ended nano-tower structure by reducing the Ga-flux to 1.5×10^{-6} torr (shown in Figure 5.1(d-e)) for the next 10 min. Despite that, another sample S2 has been grown with the same the growth condition as followed by sample S1 except for two minor alterations,*i.e.*, growth of AlN buffer layer substrate temperature reduced from 800°C (for S1) to 762°C (for S2) and increased the GaN-NTs growth duration from 10 min (for S1) to 15 min (for S2). The real-time monitoring of GaN-NTs/Si (111) growth has been performed by reflection high electron diffraction (RHEED) pattern using *in-situ* STAIB electron gun (12 keV) as shown in Figure 5.2 (a-h). The morphological studies of grown GaN-NTs have been carried out using Field-emission scanning electron microscopy (FEI Verios 460L FESEM) and Atomic force microscopy (AFM) (Multimode-V Veeco). The structural quality of the grown structure was determined by High-Resolution X-ray Diffraction (HRXRD) (PANalytical X'Pert PRO MRD System) using CuKα1 radiation (λ= 1.5406 A˚). For analyzing the optical properties, room temperature (RT) photoluminescence (PL) measurement was carried out by using FLS980 D2D2 (Edinburg) system with Hd-Cd Kimmon laser (325nm) excitation source, and Raman spectroscopy was carried out in backscattering configuration, using a 514 nm argon-ion laser.

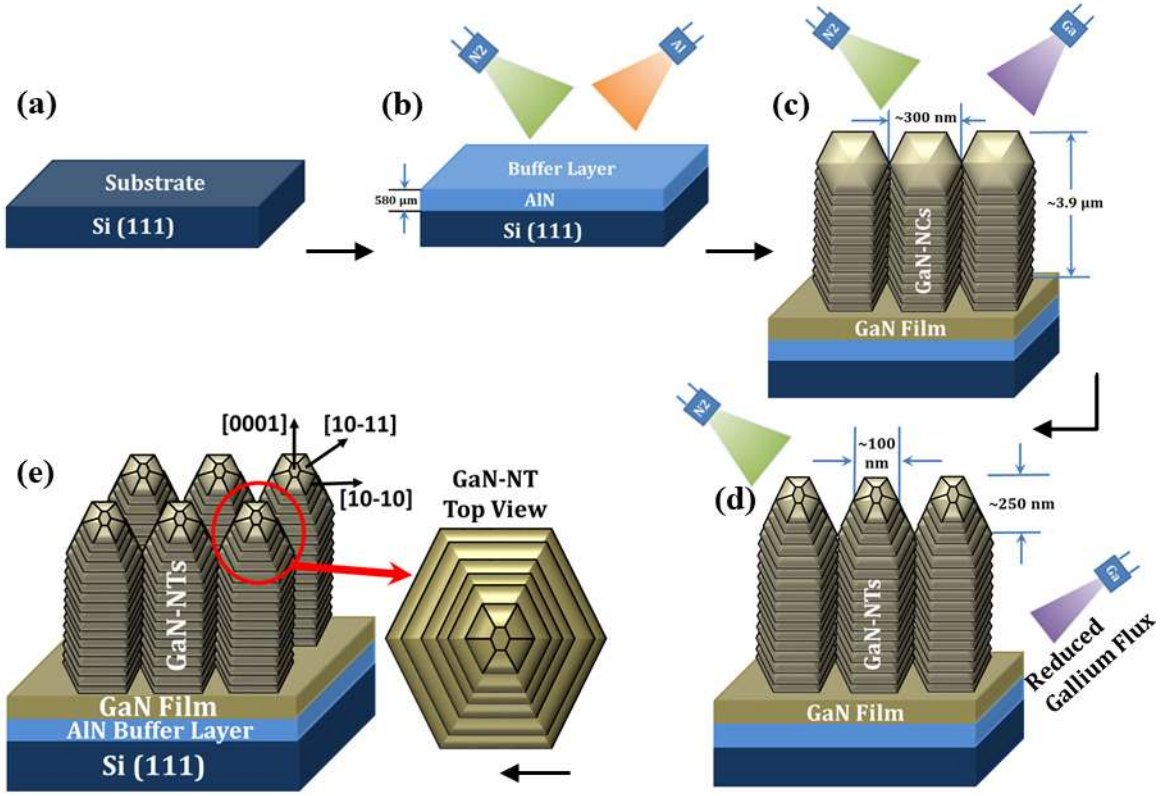

Figure 5.1: (a-e) A schematic growth diagram of grown GaN NTs on Si (111) substrate with a sandwiched AlN buffer layer in between.

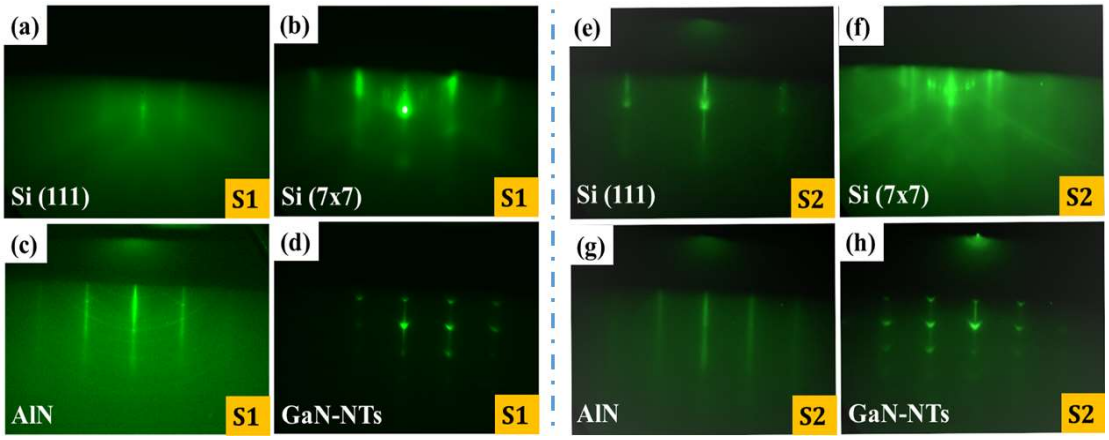

Figure 5.2: RHEED Patterns of (a, e) Si (111) substrata, (b, f) Si (111) 7 × 7 reconstruction after thermal annealing, (c, g) AlN buffer layer, (d, h) GaN-NTs.

5.3 Results and Discussion

5.3.1 Morphological, Structural and Optical Properties

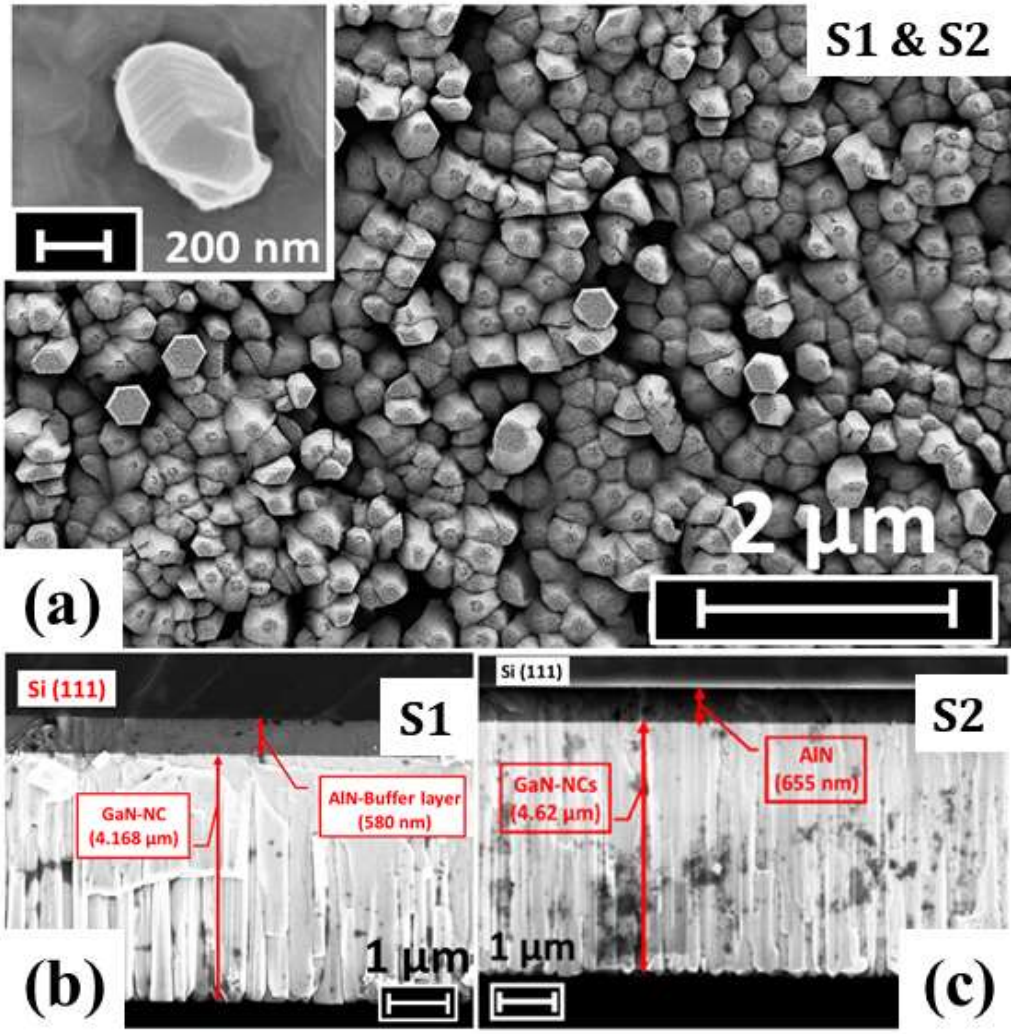

Figure 5.3: (a) Planar view FESEM image of GaN-NTs (S1 and S2), inset: shows a layer by layer stacked GaN hexagonal nanocrystal structure of a single NT); (b, c) Cross-sectional FESEM image of GaN NTs belongs to S1 and S2, respectively.

The grown GaN-NTs morphology has been probed by FESEM measurement (shown in Figure 5.3), wherein the planer view [Figure 5.3(a)] of both the samples (S1 and S2) displays high density closely packed GaN-NTs with hexagonal shapes nanocolumns with tapered ended geometry (inset shows high magnification image of layer by layer stacking of GaN hexagonal nanocrystal structure). It is noteworthy that, the variation in growth parameters of S2 such as reduced AlN buffer layer substrate temperature as well as increased GaN-NTs growth duration as compared to S1 sample

create the structural dimension difference in between them. Thereby, these novel hexagonal GaN-NTs height (H) and sandwiched as well as perpendicular grew AlN buffer layer thickness (T) of S2 found to be higher (H_{S2}= ~4.62 µm and T_{S2}= ~655 nm) as compared to S1 (H_{S1}= ~4.168 µm and T_{S1}= ~580 nm), respectively, as shown in cross-sectional FESEM image [Figure 5.3(b, c)]. Moreover, the impressive layered structure has been observed by stacking of uniform hexagonal GaN layers up to the length of ~4µm (with a very high distribution density of 3.5× 10^{10} cm^{-2}). Upon that, reduction in Ga flux in a well-defined manner resulted in a gradual decrease in the surface areas leading to the formation of NT's tip ended with total length width ~100nm. A similar structure of ZnO-NTs was grown and studied by Hu *et al.*[184]

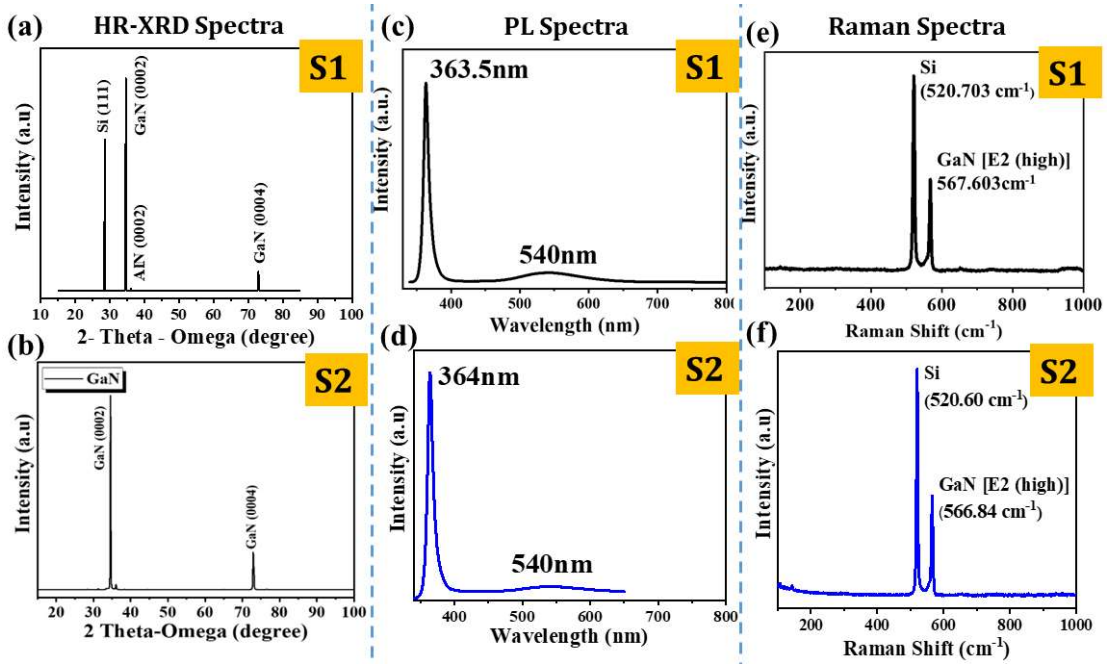

Figure 5.4: (a, b) HRXRD omega scan along (0002) plane of diffraction, (c, d) RT-PL spectra and (e, f) Raman spectra of as-grown GaN-NTs of both the samples (S1 and S2).

The crystallinity of grown GaN was evaluated by HRXRD 2θ-ω scan and its peak positions (shown in Figure 5.4 (a) for S1 and Figure 5.4 (b) for S2) along (0002) were utilized to calculate the strain via. lattice constant estimation using Bragg's law (by equation 3.1 to 3.3). [131]The estimated value of strain in GaN-NTs is realized to be 0.25% (for S1) and 0.14% (for S2), which confirms comparatively more strain relaxation in the nanostructured growth of sample S2. Moreover, to understand the level of defects in grown device structure, HRXRD omega scans along (0002) and

(10-12) plane of diffraction have also been performed. The observation reveals that FWHM values along (0002) and (10-12) were found to be 0.39° and 0.84° for S1 and 0.56° and 0.84° for S2. These FWHM values further attributed to estimate the screw and edge dislocation density of S1 (1.91×10^{9} cm^{-2} and 2.33×10^{10} cm^{-2}) and S2 (4.03×10^{9} cm^{-2} and 2.38×10^{10} cm^{-2}), respectively. Thus, the reduced strain with a reasonable dislocation density of GaN-NTs could be benefited for efficient opto-electrical application discussed later.

The grown GaN-NTs with enhanced surface area consequently allow more photon absorption sites to generate a large number of photo-excited electron-hole pairs (EHPs). These EHPs emit high-intensity photoluminescence upon recombination which was reflected by highly intense near band edge emission (NBE) peak at 363.5nm (for S1) and 364 nm (for S2) in RT-PL spectra shown in Figure 5.4(c, d). The peak is found to be in close agreement with bulk GaN PL emission (~364nm,*i.e.*, 3.406eV). [132] Henceforth, the recorded PL spectra with high-intensity NBE peak and lower FWHM value of 8.51nm (for S1) and 8.99 nm (for S2) endorse the high crystalline quality of grown GaN-NTs. [142] The observation also reveals an additional peak with reduced intensity at 540 nm in S2 as compared to S1, which is attributed to reduced yellow band emission (YBE) due to the generated reduced point defects. [185, 186] Furthermore, Raman scattering measurement was employed to quantify the stress in the grown structures as shown by the Raman spectra in Figure 5.4(e, f). The Raman spectra exhibits, E_2-high mode of grown GaN-NTs located at 567.603 cm^{-1} (for S1) and 566.84 cm^{-1} (for S2) which was found to be shifted by about 0.397 cm^{-1} and 0.26 cm^{-1} as compared to the standard frequency value of E_2 (high) phonon mode of bulk GaN. [132] The observed red-shift in the E_2 (high) position indicates that the grown GaN-NTs had tensile stress (using equation 3.4). [133, 134] The tensile stress [131] is estimated to be 0.06 GPa of S2, which is found to be lower as compared to S1,*i.e.*, 0.092 GPa (for S1). However, the estimated tensile stress of both the samples has been realised as significantly lower as compared to other available 3D GaN-NSs and 2D GaN films. [139, 187, 188] The lowest stress value in S2 is attributed to available lowest defect states in grown GaN-NTs. A recent study suggests that the presence of defects can have an adverse impact on electrical as

well as the optical property of the GaN-based UV PD, [151] where the lower level of defects attributes to lower trap states. Therefore, the grown GaN-NTs (S2) with lower defect density can significantly contribute to the fabrication of more efficient UV-PD as compared to S1.

5.3.2 Photodetector Fabrication and Performance

The grown GaN-NTs structures (S1 and S2) are utilized to fabricate UV-PDs (D1 and D2) in MSM structure by depositing metal electrodes of Au/Cr (200/10nm) using thermal evaporation system. Thereafter, the photoresponse measurements were carried out at photovoltaic as well as photoconductive mode of operation using a probe station setup (S10 Triax probe station with Keithley 2401 acquisition unit) on the fabricated detectors having 1.18×10^{-3} cm^2 active area. The spectrometer is equipped with a focused laser source (λ= 325 nm with the utilized power density of 2.5 mW/cm^2 to 184 mW/cm^2). Figure 5.5 displays RT current-voltage (I-V) characteristic of fabricated GaN-NTs (S1) based UV-PDs under dark as well as 325nm UV-laser illumination (3mW optical power or 3.2 mW/cm^2 optical power density) under photovoltaic as well as photoconductive mode of operation (applied bias voltage sweep of ±3V).

5.3.2.1 Photodetector Performance at Photovoltaic mode

The schematic image of the fabricated GaN-based UV-PD (D1) is shown in the bottom right inset of Figure 5.5. The observation reveals that due to non-identical tapper geometry of the GaN-NTs form two non-homogeneous Au /GaN interfaces between Au-metal electrodes and GaN-NTs which exhibits two Schottky natured electrodes with different barrier heights. This variation in barrier heights of two metal electrodes creates the built-in potential gradient at the GaN side, which powered the device to respond even at zero applied bias. [165] The self-channelization of light current without any applied bias voltage designates the fabricated detector as self-powered (photovoltaic mode) UV-PD revealed by I-V plots at various optical power as shown in the top-left inset of Figure 5.5.

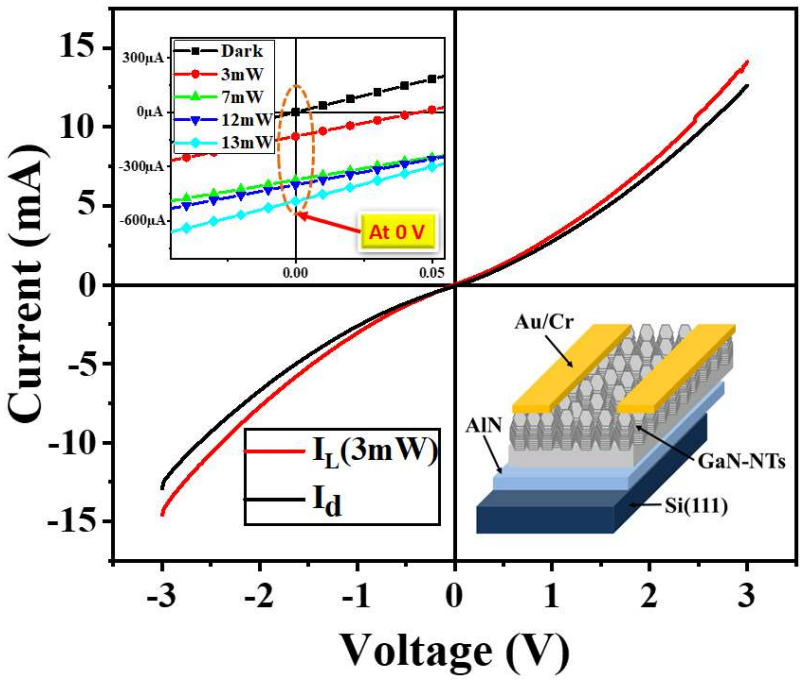

Figure 5.5: RT I-V characteristic of fabricated GaN-NTs based UV-PD under dark and 325nm UV illumination with 3mW optical power. Inset: top left indicate self-powered characteristic at various optical power and bottom right indicate schematic diagram of the fabricated device.

The transient photo-response behaviour of the fabricated detector has been realized in photovoltaic mode with the variable incident optical power (from 3mW to 13mW) as shown in Figure 5.6(a). The photo-response measurement has been performed by measuring inflow current values with periodically switching ON (I_{Light}) and OFF (I_{Dark}) the UV laser with variable optical power. The maximum value of I_{Light} / I_{Dark} ratio was recorded to be $>10^4$ under 13mWUV illumination in photovoltaic mode. The obtained results demonstrate notably the very low dark current value of ~12nA, wherein the fabricated UV-PD exhibits a stable and significant enhancement in light current value from 67.5μA to 545μA on increasing optical power from 3mW to 13mW. Further, we have explored the capability of the detector to detect low power UV photons, and their respective light current values are observed to be increased from 70.8nA (180μW) to 3.4μA (0.7mW) (shown in Figure 5.7). Conclusively, the fabricated GaN-NTs based UV-PD has shown remarkable enhancement of ~7700 fold by raising the light current value from 70.8nA (180μW) to 545 μA (13mW) in the photovoltaic mode of operation.

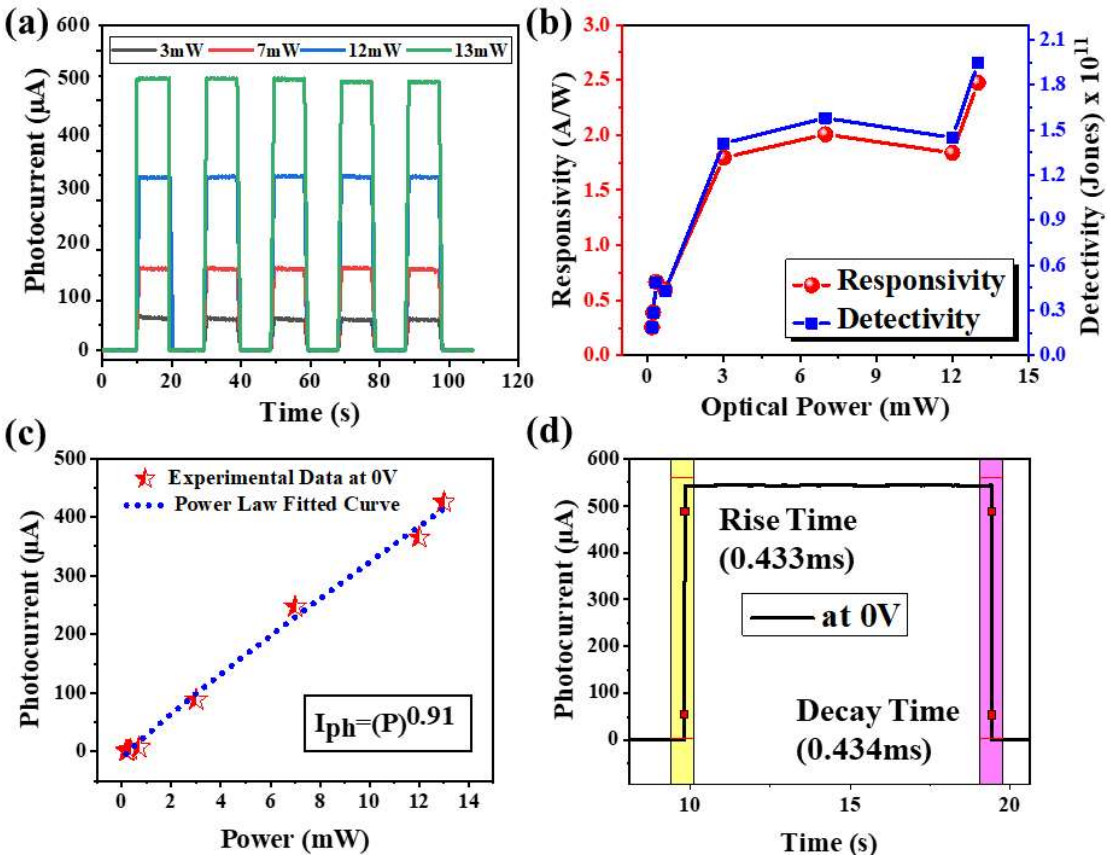

Figure 5.6: Incident optical power-dependent performance of GaN-NTs UV-PD (D1) in photovoltaic mode (a) time-correlated transient photoresponse, (b) Correlation of responsivity and detectivity with varied optical power, (c) Power-law fitted curve in the experimental data of photocurrent, (d) Reversibility (Response time) of the detector under constant 13mW optical power illumination.

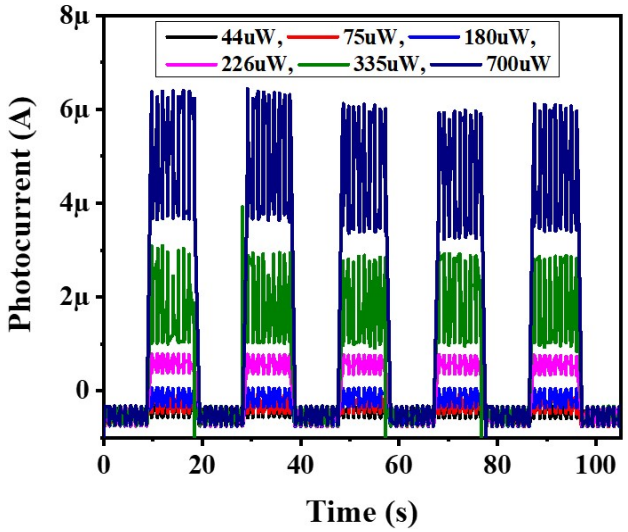

Figure 5.7: Time correlated transient photoresponse of fabricated GaN-NTs based UV-PD (D1) with applied lower optical power and fixed 325nm UV-laser at 0V.

In addition, the fabricated UV detector has also been investigated based on their well-known performance parameters like responsivity, detectivity, external quantum efficiency and reversibility of the detector. [189]Figure 5.6(b) displays that the fabricated GaN-based detector yielded a gradual increment in responsivity from 0.255 A/W to 2.47 A/W and detectivity values from 1.8×10^{10} jones to 1.95×10^{11} jones with increasing incident optical power from 180μW to 13mW. Noticeably, the evaluated responsivity and detectivity values are found to be significantly higher than the existing bare GaN-based UV-PDs at photovoltaic mode as consolidated in Table-5.1. The analysis also divulges a linear relationship between photocurrent and incident optical power, as demonstrated in Figure 5.6(c). The power law has been fitted on the experimental data, I_{Ph} α P^{θ}, where I_{Ph} is the photocurrent and θ determines the photocurrent response w.r.t optical power density. After fitting the data, the θ value is determined to be 0.91, which is close to unity, reflecting that the carrier trap states between the conduction band edge and the fermi level are very low. [190] Moreover, to test the reversibility of the detectors, the time-correlated transient photoresponse of the fabricated GaN-based UV-PD has been analysed. The rise time (as measured from 10% to 90%) and decay time (from 90% to 10%) under UV on/off condition was measured to be ~0.433ms and ~0.434ms, respectively as shown in Figure 5.6(d). Table 5.1 revealed a rapid rise and decay time from the fabricated GaN-NTs based UV PD on Si as compared to other reported values for bare GaN-based PDs.

Table 5.1: Comparison of performance parameters of GaN-based UV-PDs.

Sample	R (mA/W)at 0V	R (mA/W) @ applied bias	Rise / Decay time	EQE%	Ref.
GaN-NT/Si(111) PD Device [D1]	2.47×10^{3}	3.54×10^{4}@ -3V	0.433ms/0.434ms	1.35×10^{4}	**This work**
GaN-NW/n-Si(111)	----	19@ 5V	2.8s/3.7s	6.7	[139]
GaN/Si(111)	----	282@ 15V	----	96.71	[187]
GaN-NW/n-Si(100)	----	68@ 5V	2.4s/3.1s	24.4	[139]
GaN-MWA/p-Si	131	----	2ms / 2ms	49.98	[37]
GaN/Al2O3	104	----		36	[191]
GaN/Al2O3	147	----	0.11ms/0.12ms	50.7	[192]
GaN p-i-n/Al_2O_3	190	210@ -5V	----	65	[193]
GaN/Al_2O_3	300	----	<0.1s	----	[194]

5.3.2.2 Photodetector Performance at Photoconductive mode

The performance of fabricated GaN-NTs UV-PDs (D1 and D2) hasalso been investigated at the photoconductive mode of operation. Figure 5.8 displays the stable time-correlated transient response of the detector (D1) at a fixed optical power of 3mW and variable bias voltage. The results demonstrate increment in photocurrent values with increasing applied bias,*i.e.*, 66.6µA (0V), -0.35mA (-1V), -1.025mA (-2V) and -1.73mA (-3V) which is attributed to increased thermionic field emissions.

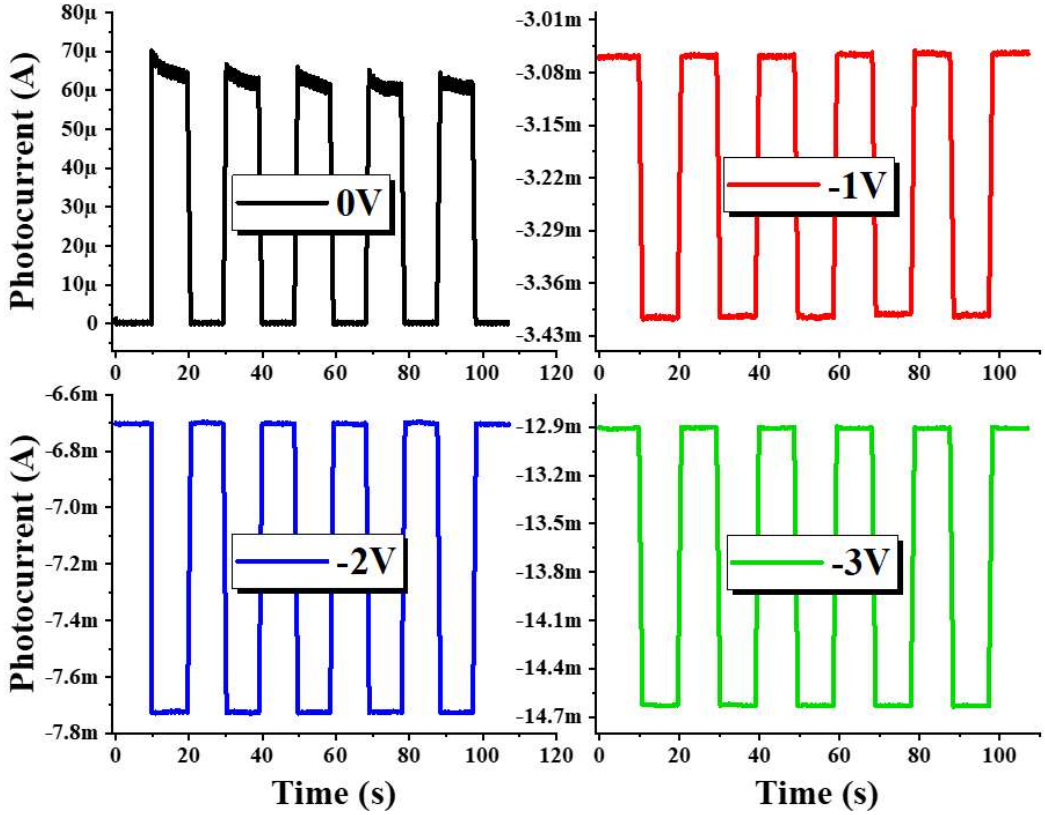

Figure 5.8: Bias dependent time-correlated transient photoresponse of GaN-NTs UV-PD (D1) at 3mW optical power illumination

Moreover, Figure 5.9(a) displays the schematic diagram of another fabricated UV-PD (D2) and Figure 5.9(b) demonstrates the RT I-V characteristics under the dark condition as well as UV-illumination at different optical power density (varying from 3.2 mW/cm^2 to 184 mW/cm^2) with applied bias voltage sweep of ±6V. The left inset of Figure 5.9(b) displays the difference in dark and light current values of bare GaN-NT based UV-PD at higher bias voltages. Thus, the fabricated detector demonstrates a

stable performance even at significantly high operating voltages (up to ±6V) with higher current carrying capacity (as compared to D1) which could be associated with thicker AlN buffer (655nm) and GaN (4.62μm) epitaxial growth (as compared to S1). The observation from the photoconductive mode of operation at varied incident optical power density (Figure 5.9(b)) revealed better device performance by increasing the incident optical power from 3.2 mW/cm^2 to 184 mW/cm^2, the light current value increased from -24.7mA to -36.12mA at -6V applied bias. The applied reverse bias in both the detectors increases the width of the depletion region, which further reduced the junction's capacitance. Thereby, the increased potential region with an electric field allows a quick collection of the generated electrons. Besides, the reverse bias also found advantageous by maintaining lower dark current values without much affecting the photocurrent. Therefore, the device performance in negative bias exhibits better performance as compared to positive bias. Furthermore, to explore the UV photodetection ability of the fabricated device, photoresponse measurements were carried out at a fixed incident optical power density of 3mW or 3.2 mW/cm^2 in the photoconductive mode of operation. The results (shown in Figure 5.9(c)) demonstrate stable time-correlated transient response upon turning "On" and "Off" the UV illumination with a periodic time interval of 20 s. It was observed that the photocurrent rises from -36 μA to -2.05 mA upon increasing the bias from -1V to -6V, which is also attributed to increased thermionic field emissions facilitated the large collection of photogenerated charge carriers.

This increment in the photocurrent with applied bias voltage is reflected in the performance parameters of the fabricated PDs. Figure 5.10(a) displays a significant enhancement in the responsivity (using equation 3.8) of the detector D1 with an applied bias voltage from 0V to -3V, where its value increases from 1.79 A/W (at 0V) to 35.4 A/W (at -3V). Likewise, the responsivity values of detector D2 were also increased from 15.64 A/W (at -1V) to 484.77 A/W (at -6V) as shown in Figure 5.10 (b). Noticeably, the responsivity value of D2,*i.e.*, 88.61 A/W at -3V is found to be the highest as compared to D1 (35.4 A/W, -3V) as well as other bare GaN-NS based UV

photodetectors (Table 5.1). Consequently, the achieved responsivity value of 484.77 A/W by D2 is the highest obtained value as of now as far as bare GaN-based UV-PDs are concerned as tabulated in Table 5.2. On the contrary, the detectivity (using equation 3.9) of detector D1 is calculated to be decreasing from 1.41×10^{11} jones at 0V to 0.183×10^{11} jones at -3V due to the higher dark current values with varying applied bias as shown in Figure 5.10(a).

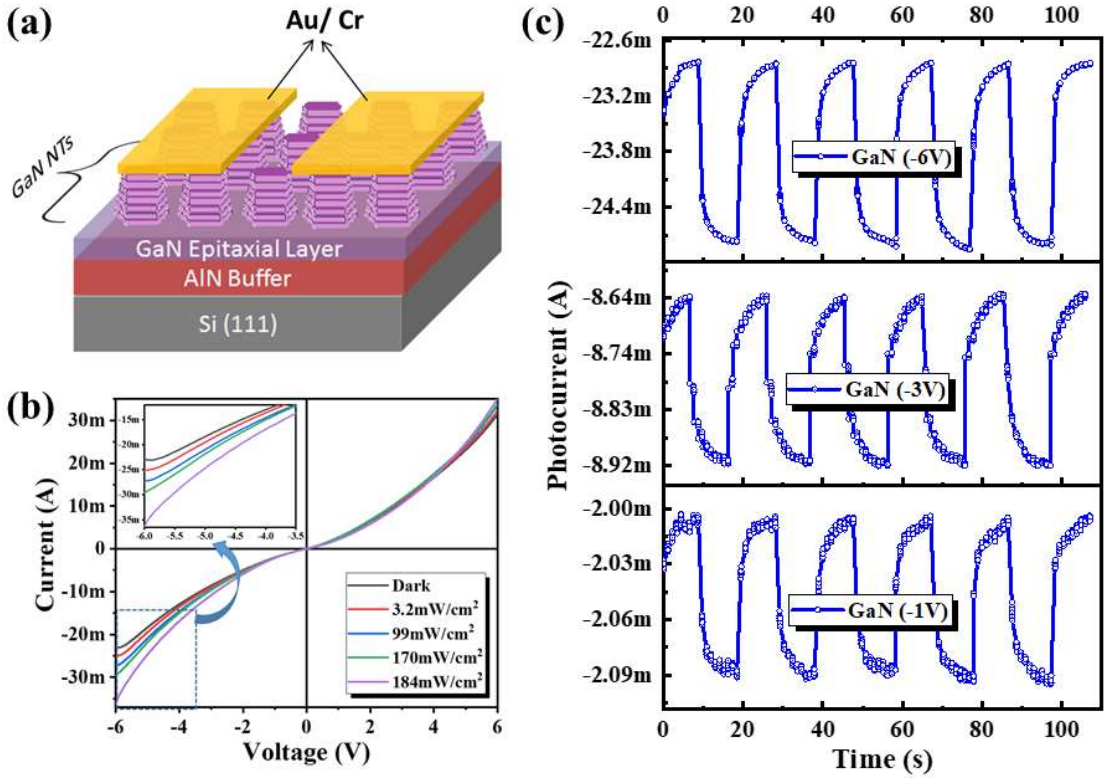

Figure 5.9: (a) A schematic representation of fabricated GaN NTs- based detector (D2); (b) RT I-V curve plotted for dark condition and UV illumination at varied optical power density (inset shows the magnified data at higher bias); (c) Time-correlated UV response under the applied bias of -1, -3 and -6 V.

Besides, unlike D1, the detector D2 taken advantage of thicker AlN buffer layer as well as higher GaN-NTs height which helps in overcome the adverse effect of dark or leakage current in the device. Consequently, by increasing the applied bias voltage, the detector D2 demonstrated the increasing trend of detectivity values from 2.14×10^{10} jones (at -1V) to 1.96×10^{11} jones (-6V) as shown in Figure 5.10(b). The enhanced performance of fabricated UV-PD in this study corresponds to the unique

nanotower morphology of epitaxial GaN, which increases the photon absorption and fast carrier collection. In addition, other important performance parameters such as noise equivalent power (NEP) and external quantum efficiency (EQE %) of the devices are also determined (using equation 3.10 and 4.1)and shown in Figure 5.10(c, d). Both NEP and EQE are related to sensitivity, where NEP basically measures the level of sensitivity of the detector and EQE defined as the conversion rate of incident photons to generate charge carriers that contribute in current conduction. As per the definition, due to the direct proportional relation of NEP with the dark current and inversely with responsivity, smaller NEP values indicate that the detector has a high level of sensitivity. Thus, the Figure 5.10(c) demonstrates the reducing NEP of D1 detector from 3.8×10^{-12} $WHz^{-1/2}$ (0V) to 1.89×10^{-12} $WHz^{-1/2}$ (-3V) and for D2 detector its values starts decreasing from 1.62×10^{-12} $WHz^{-1/2}$ (-1V) to 1.76×10^{-13} $WHz^{-1/2}$ (-6V) as shown in Figure 5.10(d). The determined NEP value of D2 detector,*i.e.*, 1.76×10^{-13} $WHz^{-1/2}$ (at 3.2 mW/cm^2, -6V) elucidates that the fabricated GaN-NTs based UV-PD with thicker AlN buffer layer and higher GaN-NTs structure can detect a signal of power as low as ~0.17 pW as compared to ~0.19 pW (in case of D1) with a signal-to-noise ratio of one after the one-half second of averaging. Similarly, increasing EQE of D1 from 8.6×10^2 % to 1.35×10^4 % [Figure 5.10(c)] and in case of detector D2, this value inverse from 0.6×10^4 % to 1.85×10^5 % [Figure 5.10(d)] with increasing bias also determined as a Figure of merit of the photodetection device. As per the results, the achieved EQE value is 1.85×10^5 % at -6V which is found to be highest among available bare GaN-based detectors (as tabulated in Table 5.2) and reveals the existence of photoconductive gain greater than unity. [195]

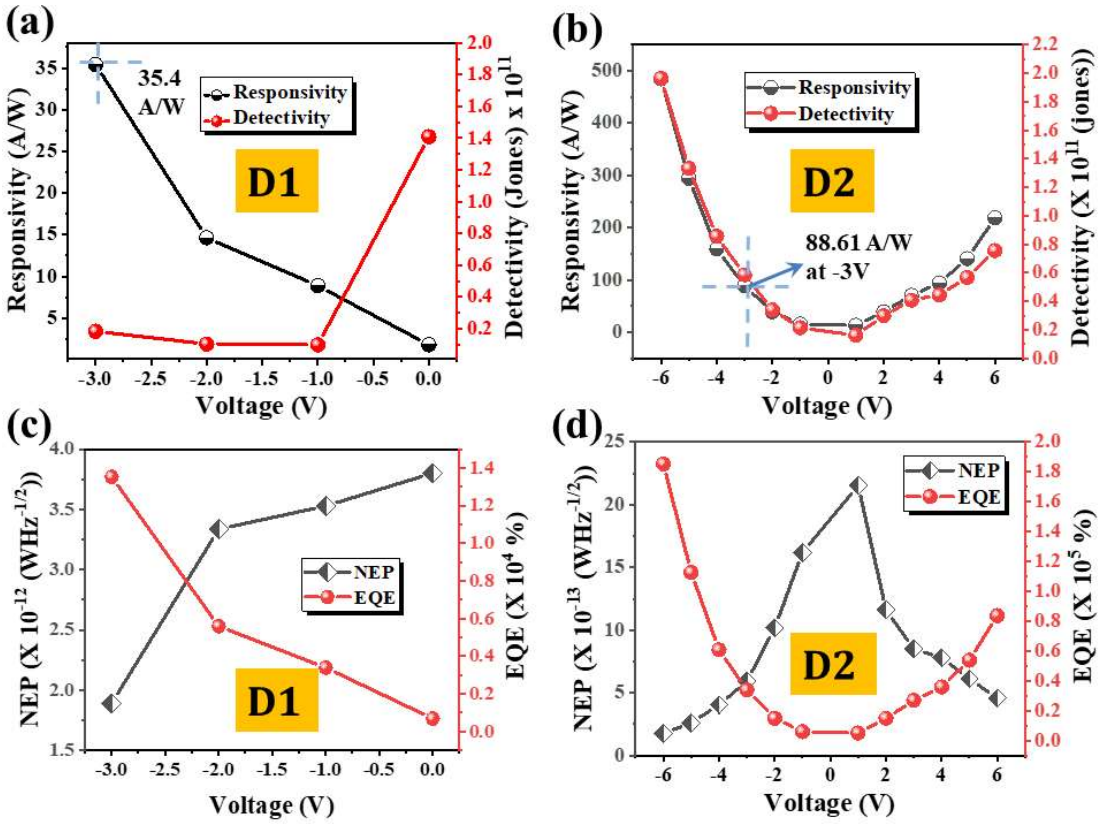

Figure 5.10: (a, b) Responsivity and detectivity graph w.r.t applied bias voltage; (c, d) Noise equivalent power (NEP) and External quantum efficiency (EQE) of fabricated GaN-NTs UV-PDs (D1 and D2) w.r.t applied bias voltage and fixed optical power density 3.2mW/cm^2.

Table 5.2: Comparison of performance parameters of GaN-based UV-PDs

Sample	R (A/W), applied bias	Wavelength/ Opt. Power	Rise / Decay time	EQE%	Ref.
GaN-NT/Si(111) PD Device [D2]	**484.77, -6V**	**325nm/3.2mWcm^{-2}**	**1.16s/1.01s**	**1.85×10^5**	**This work**
GaN-NF/Si(111)	10.5, 1V	325nm/1mW	63ms/27ms	----	[74]
GaN-NT/Al_2O_3/Si	0.122, 3V	365nm/2.4mWcm^{-2}	82ms/164ms		[101]
GaN-NW/n-Si(111)	0.019, 5V	365nm/1.8mW	2.8s/3.7s	6.7	[139]
GaN/Si(111)	0.282, 15V	362nm/0.8Wm^{-2}	----	96.71	[187]
GaN-NW/n-Si(100)	0.068, 5V	365nm/1.8mW	2.4s/3.1s	24.4	[139]
GaN/Si-NPA	0.029, -3V	305nm/16µWcm^{-2}	39.9ms/40.10s	----	[196]
GaN-MWA/p-Si	0.131, 0V	325nm/ 0.9mWcm^{-2}	2ms / 2ms	49.98	[197]

Moreover, to demonstrate of the spectral selectivity of the device and the UV/visible rejection ratio, the wavelength selectivity of the fabricated GaN-NTs based UVPD was measured in the range of 300nm to 800nm at variable applied bias voltage from -1V to -3V (Figure 5.11). The obtained results demonstrate that the fabricated detector exhibits noteworthy UV to visible rejection which is also enhanced by the applied bias voltage.

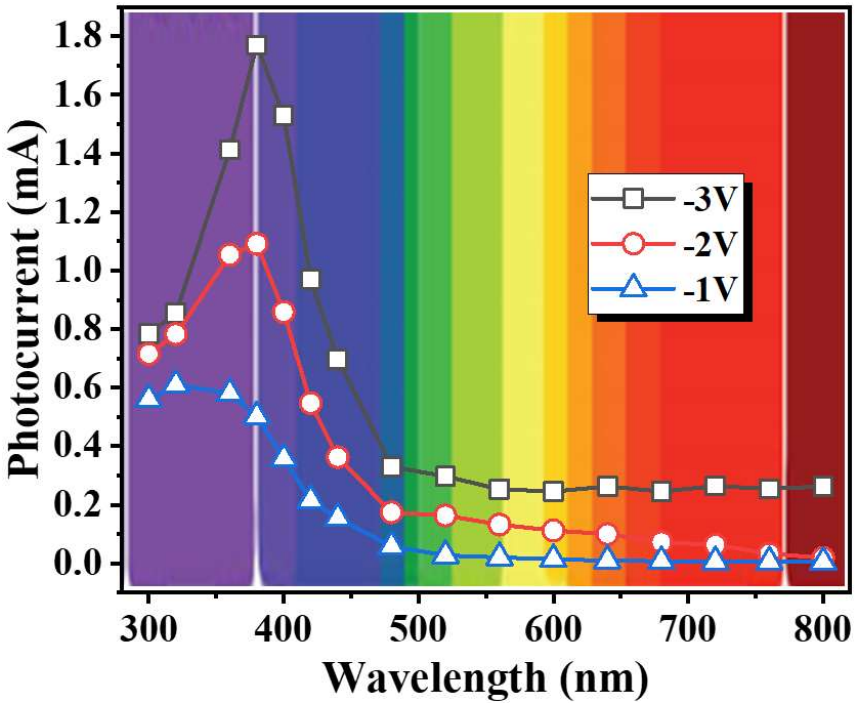

Figure 5.11: Spectral response characteristic of GaN-NTs based UV-PD from 300 to 800 nm under applied bias.

5.4 Summery

In summary, unique tapered ended-nanotower morphology of epitaxially grown hexagonal stacked nanocolumnar GaN structures with different heights and different AlN buffer layers thickness were utilized to fabricate high-performance UV-PDs operable in photovoltaic as well as a photoconductive mode of operation. The fabricated UV-PD with lesser AlN thickness and GaN-NTs demonstrates significantly enhanced performance parameters including very high I_{Light} /I_{Dark} ratio (>10^4) along with high responsivity of 35.4 A/W at -3V and 2.57 A/W at 0V. Moreover, the device displays high EQE ~10^4 % and lower NEP (~10^{-13} $WHz^{-1/2}$) which elucidates the

detection of a signal as low as ~0.19 pW. Besides, particularly at the photovoltaic mode of operation, the time-correlated transient response of the detector demonstrated very high switching speed (~0.433 ms). On the other side, the UV-PD with thicker AlN buffer layer and higher GaN-NTs height display highest ever reported responsivity value of 784.77 A/W, EQE ~10^5 % and very low NEP (~10^{-13} $WHz^{-1/2}$) at a fixed bias voltage of -6V, which elucidates the detection of a signal as low as ~0.17 pW. The spectral selectivity of the device demonstrates noteworthy UV to visible rejection ratio. The low dimensionality of the device with high bias operation for fast transit of charge carriers can be effectively utilized for future nano-optoelectronic devices.

6.1 Introduction

Ultraviolet (UV) photodetectors (PDs) reserve their utmost place in the ubiquitous class of technology due to its applicability in a wide range of application such as environmental monitoring, space to space secure communication, military applications, flame detection, and in medical diagnostics *etc*. [14, 198, 199]. For UV PDs fabrication, sensing materials (semiconductors) with heterojunctions have been utilized with a common strategic approach of utilizing semiconductors having comparable bandgap energies, lesser lattice mismatch and suppressing the interfacial photo carriers' recombination [23]. The heterojunctions with lesser lattice mismatch can achieve high photo-induced charge carrier separation efficiency as well as their efficient opto-electrical transport [24]. The impact of these heterojunction structures has been realized as increased photodetection, higher responsivity, as well as external quantum efficiency [25-27]. So far, numerous heterojunction based UV PDs such as p-NiO/n-ZnO [28], TiO_2/SnO_2[29], TiO_2/NiO [30], Se/ZnO [31], ZnO/SnO_2[32] and ZnO/GaN [33-43]*etc*. have been fabricated. Among them, ZnO/GaN heterojunction based UV PDs have attracted considerable attention due to their similar properties as of the epilayer (*i.e.* GaN) such as analogous crystalline wurtzite structure, better interface [minimum lattice mismatch (1.8%)], wide and direct bandgap [E_{gGaN} (3.4eV), E_{gZnO} (3.3eV)], high thermal coefficient, high carrier mobility, high chemical stability and higher resistance towards electric breakdown field, *etc*. [44]. Su *et al.*[35] and Huang *et al.*[38] demonstrated n-ZnO film /p-GaN film heterojunction UV PDs and display responsivity of 0.68 mA/W and1.5 mA/W, respectively. Recently, nanostructured (ZnO-nanostructures/GaN-film) UV PDs has received considerable attention due to their high surface to volume ratio which leads to higher photon absorption and correspondingly higher photo-stimulated charge carriers which enhance photo as well as electrical conductivities in the device. [39-42] Vikas *et al.* have fabricated n-ZnO-NRs/p-GaN heterostructure based UV detector has demonstrated responsivity 11 A/W and response time (< ms) from the device. [42] Consequently, numerous ZnO-NRs/GaN film nanostructures based UV PDs have been fabricated [33-43] as tabulated in Table-5.1, wherein, highest responsivity value of 437A/W has been demonstrated by Chen *et al.*[43] using n-ZnO/i-ZnO-NRs/p-GaN

film heterojunctions based UV PDs. Despite of major enhancement in opto-electrical properties using the ZnO/GaN heterojunction, the device still lacking to achieve low dark current, high switching speed and most importantly peak responsivity in the desired UV detection range. Hence, one-dimensional (1D) ZnO-nanostructures such as nanorods (NRs) and nanowires were explored due to high susceptibility to UV-light, high density of surface trap states and enhanced surface-to-volume ratio. [44, 45] Therefore, this chapter demonstrates a unique geometry strategic model of nanostructure (ZnO-NRs) over nanostructure [GaN-Nanotowers (NTs)], wherein chemically synthesised wurtzite structure hexagonal ZnO-NRs were uniformly drop-casted over the plasma assisted molecular beam epitaxy (PAMBE) grown vertically aligned tapper ended GaN-NTs. Thereafter, the as-grown ZnO-NRs/GaN-NTs based heterostructure has been utilized to fabricate highly responsive UV-PD.

Along with this, the involvement of nanoplasmonics in nitride materials has been gaining substantial attention in the field of PD research due to metal nanoparticle-induced localized surface plasmon resonance (LSPR) effect [46-49]. The LSPR generated from the light-induced collective oscillation of free conduction band electrons at the interface between metal nanoparticles (NPs) and dielectrics [50], leading to strong absorption, scattering and local field enhancement. These LSPR or NP's nanoplasmonic characteristics are very sensitive to size, the shape of NPs, plasmon energy, plasmon mode symmetry, the density of state of material and electronic structure [52]. Thus, these novel metal NP's nanoplasmonic property has been explored for enhancing the PD performance [46, 53]. The reports suggest that the defect emission energy of ZnO, as well as GaN, matches very well with the LSPR excitation energy. Therefore, the NP's LSPR effect excited by these semiconductor defect band emissions generates hot resonance electrons which will be combined with the already existing electrons of the conduction band of ZnO [54] and GaN. [55, 56] This increases the density of carriers in the conduction band of the heterojunction device and reflected as improved photocurrent as well as enhanced performance of the developed UV detection device. Some previous reports also found in coherence with the fact that the use of NP's nanoplasmonics such as platinum (Pt) NPs [47], aluminium (Al) NPs [48], silver (Ag) [46] and gold (Au) NPs [49] have been realized as a solution for the carrier enhancement seeker GaN-based UV-

PDs. Among them, the utilization of Au-NPs has proven to be noteworthy in LSPR due to advantageous inherent physical properties like high physio-chemical stability, non-linear optics, magneto-plasmonic, optically active, [57] and ease of surface functionalization with plasmon oriented multitude of optical properties. [58, 59] Similarly, Au-NPs decorated ZnO nanostructures based UV detectors result in improved performance by reducing the dark current via the LSPR effect. [56, 60] Still, it remains a challenge to design an effective device structure which can decrease the dark current and increase the sensitivity of the device simultaneously. In the present work, at last, we have explored the surface functionalization of the fabricated ZnO-NRs/GaN-NTs heterostructure based MSM UV-PD by chemically synthesis monodispersed ~10nm sized Au-NPs, where functionalized detector exhibits highest responsivity, EQE and very low NEP as compared to its bare counterpart as well as other available PD in the similar domain.

Furthermore, the fabricated ZnO and GaN nanostructure-based UV PDs have shown remarkable enhancement in their performance by integrating with semiconductor quantum dots (CdS, CdSe, PbS, CdTe and graphene quantum dots(GQDs) *etc*.). The presence of these quantum dots in the photodetection devices was appreciated by enhanced photoconductivity and suppressed carrier recombination. [61-66] Among these quantum dots, the latest addition of nanocarbon materials family,*i.e.*, graphene quantum dots (GQDs) are getting more attention due to their unique merits such as excellent dispersibility, better tunability in chemicophysical properties, abundant active sites, catalytic ability and bandgap opening due to quantum confinement. [67] Moreover, GQDs are also known for their semiconductor behaviour, [68] higher mobility at lesser bias voltage [69] and nano-dimensionality (<100 nm) which allow them the ease of settle down on the surface of detector fabrication mother material (ZnO, GaN *etc*.) structure. The impact of GQDs sensitization on GaN-film and ZnO-NRs on UV PD's performance has been realized by Lin *et al.*[64], and Dhar *et al.*[70]and Rahimi *et al.*[65], respectively, wherein, photo-induced extra charge carriers by GQDs has guided towards enhanced photodetection. Moreover, the presence of GQDs also helps in faster collection of the photogenerated charge carrier leading to reduce response time. Lately, Liu *et al.* have reported GQDs sensitized ZnO-NRs/ GaN-film (MOCVD) heterostructure based UV PD, however the reported

responsivity of the detector is very low (~34mA/W) even at very high applied bias voltage of 10V. [66] Therefore, in this chapter, we have also demonstrated the fabrication of high performance UV-PD utilizing the unique ZnO-Nanorods (ZnO-NRs)/GaN-nanotowers (GaN-NTs)/ heterostructure sensitized with graphene quantum dots. The analysis exhibits the cumulative effect of ZnO/GaN hetero-interface junction (their nanostructures implicated higher surface to volume ratio) and extra photo induced charge carriers via GQDs sensitization with efficient transport by metal-semiconductor-metal (MSM) device structure. Consequently, the fabricated GQDs-ZnO-NRs/GaN-NTs MSM UV PD exhibits highest responsivity, external quantum efficiency (EQE) and very low noise equivalent power (NEP) as compared to its bare counterpart as well as other available PD in the similar domain.

6.2 Methods / Experimental

6.2.1 Synthesis of ZnO-Nanorods

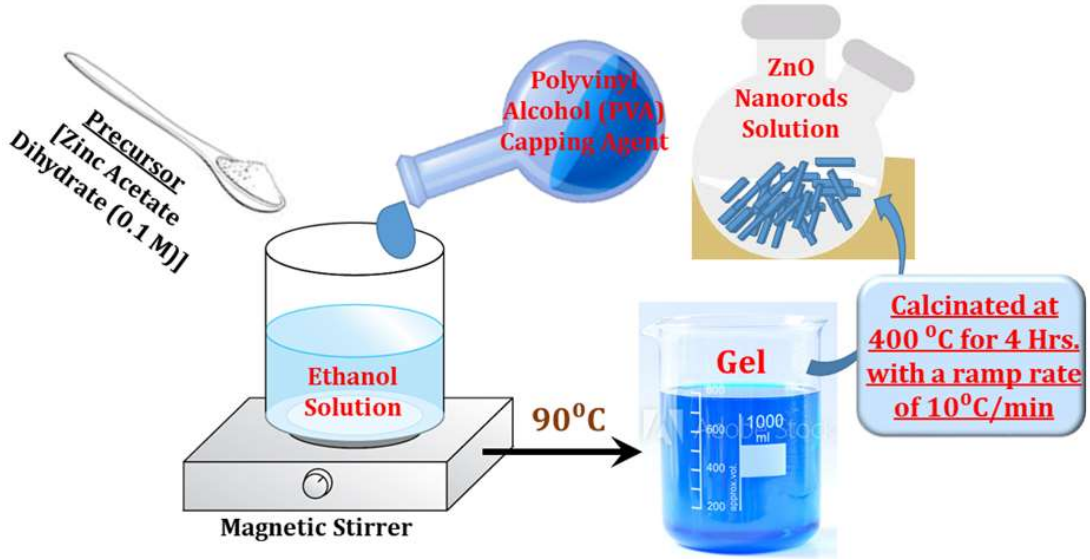

Figure 6.1: Schematics of the chemical synthesis process of ZnO-Nanorods.

ZnO nanorods were synthesized by the sol-gel method [200] followed by calcination (shown in Figure 6.1). Firstly, 0.1 M of precursor (zinc acetate dihydrate) was mixed in ethanol by a magnetic stirrer to get a homogeneous solution (sol). Polyvinyl alcohol (PVA) was then added slowly in the resulting solution that acts as reducing as well as capping agent. The solution was then heated at around 90 °C till it turns into a gel.

Now, the obtained gel was calcined at 400 °C for 4 h at a constant heating rate of 10 °C/min. The resulting product was characterized by various characterization methods.

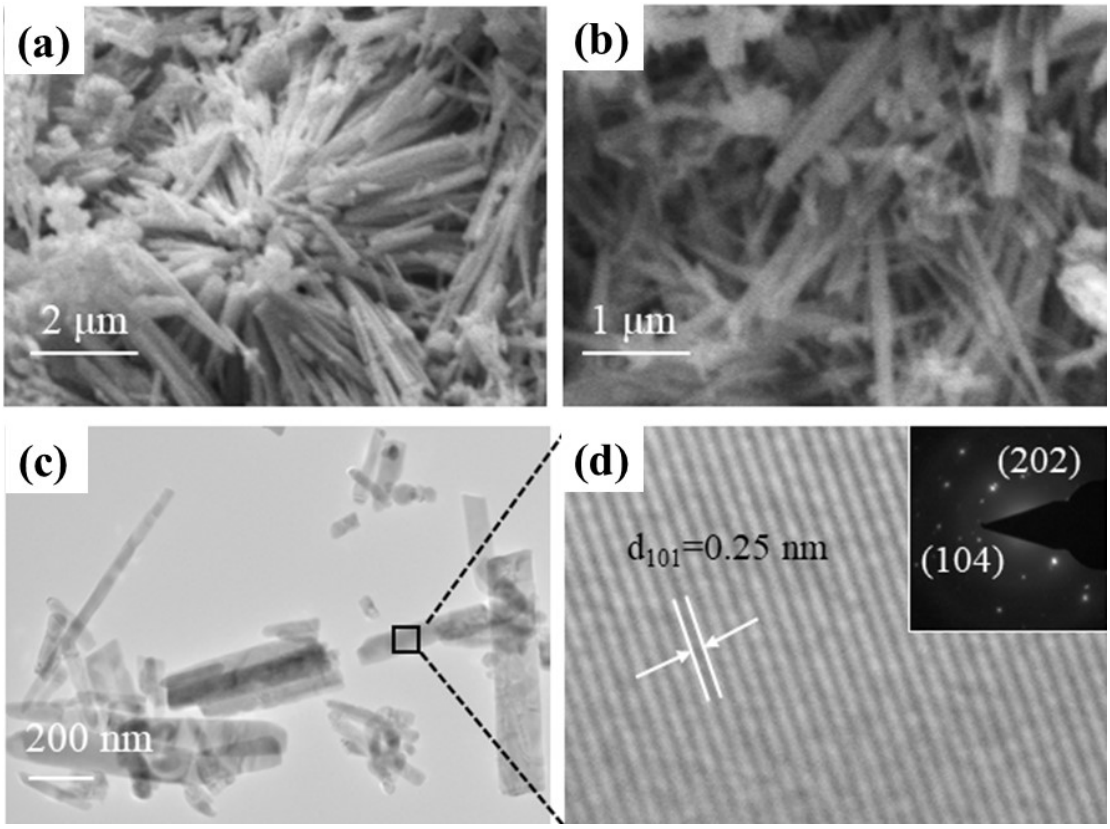

Figure 6.2: (a) Low and (b) High magnification SEM images, (c) Bright-field TEM, (d) HR-TEM image of square portion of ZnO nanorods. Inset in (d) shows a corresponding SAED pattern.

Low and high magnification SEM micrographs clearly depict the rod-like morphology of as-synthesized ZnO nanostructures, as shown in Figure 6.2 (a-b). ZnO nanorods were observed to be agglomerated. For in-depth structural information of obtained nanorods in real and reciprocal space, TEM was performed. Bright-field TEM supports the rod-like structure, as shown in Figure 6.2 (c). HR-TEM image of a small square portion (as indicated in Figure 6.2(c)) reveals well-organized lattice fringes of spacing 0.25 nm representing the d-spacing between (101) planes of wurtzite phase of ZnO nanorods as shown in Figure 6.2 (d). Bright spots in Selected area electron diffraction (SAED) pattern corresponds to the crystalline nature of resulting ZnO nanorods as shown in the inset of Figure 6.2 (d).

6.2.2 Synthesis of Au-Nanoparticles

Gold nanoparticles (Au-NPs) synthesized in the presence of trisodium citrate using Turkevich method [161] with slight modification, has known advantages and applications in multidisciplinary fields. For its synthesis, first 1 mM (20 mL) Gold (III) chloride hydrate ($HAuCl_4.3H_2O$) (M.W. 339.79, Sigma Aldrich, USA (254169), CAS: 27988-77-8) precursor solution is prepared in a flask and reflux at 90 °C along with continuous stirring. Further, 40 mM (2 mL) Tri-sodium citrate ($C_6H_5Na_3O_7.2H_2O$) (M.W. 294.10, Loba Chemie, Mumbai, India, CAS: 6132-04-3) was added to the precursor solution. The colour change from transparent to violet finally to wine red is observed. The wine red colour indicates the formation of colloidal Au-NPs.

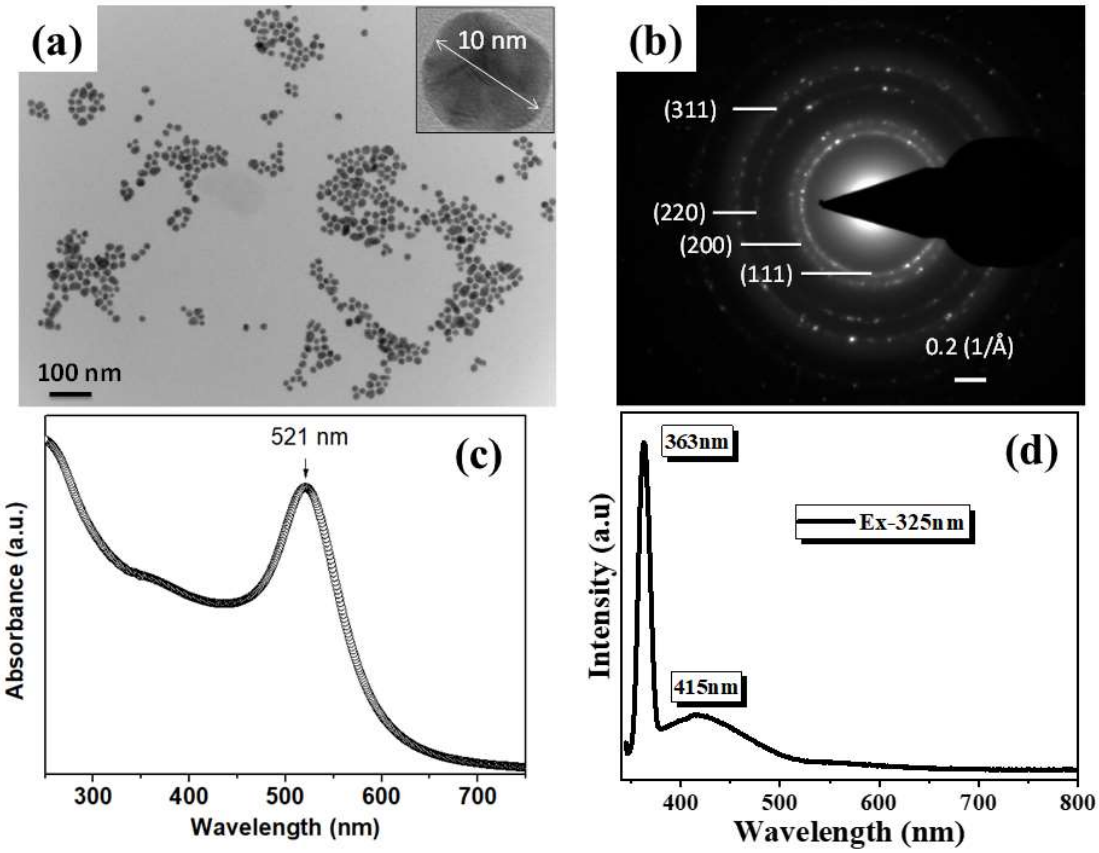

Figure 6.3: (a) shows the HRTEM image of monodispersed Au-NPs and left inset shows higher magnification image of single NP; (b) Selected area electron diffraction pattern of synthesised Au-NPs; (c) The UV-Vis absorbance data of Au-NPs showing surface plasmon resonance (SPR) peak at 520 nm; (d) RT-PL spectra of Au-NPs with 325nm UV laser excitation.

These synthesized Au-NPs have been characterized by high-resolution transmission electron microscopy (HRTEM) (FEI, Tecnai F30 G2 Stwin) and UV-Vis spectroscopy (Agilent, Cary 5000i). Figure 6.3(a) displays, the HRTEM images of monodispersed Au-NPs and left inset of the Figure shows a higher magnification image of single NPs elucidate its spherical shape with an average size ~10 nm. The bright spots in the SAED pattern correspond to planes of the Au-NPs (shown in Figure 6.3 (b)). UV-Visible absorption spectrum shows an LSPR peak position at ~520nm, which also confirm the size of Au-NPs is ~10nm [162] (Figure 6.3(c)). The broadening of UV-Visible absorption spectrum is found directly in correlation with the concentration of Au-NPs, [162] lower the broadening and higher absorption postulates higher concentration of Au-NPs which can contribute more LSPR generated hot carriers into the devices as attributed by room temperature (RT) photoluminescence (PL) measurements of Au-NPs (Figure 6.3 (d)) which was carried out by using FLS980 D2D2 (Edinburg) system with 325nm excitation source (Hd-Cd Kimmon laser).

6.2.3 Synthesis of Graphene Quantum Dots

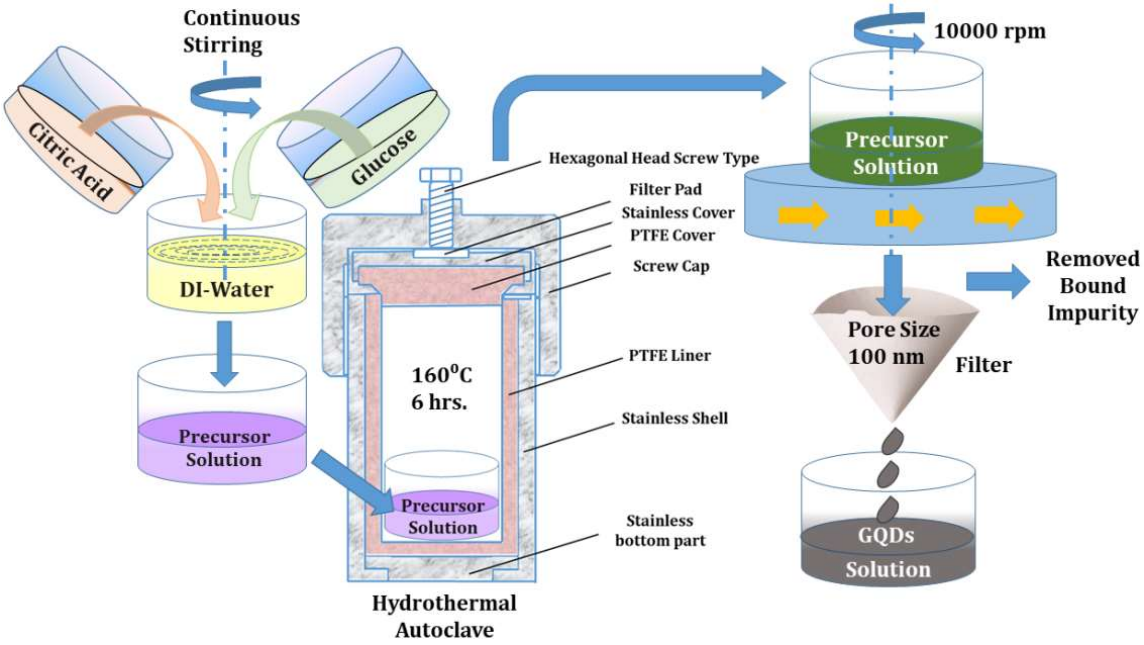

Figure 6.4: Schematic of the chemical synthesis process of GQDs.

Graphene quantum dots were chemically synthesized by a hydrothermal technique where citric acid ($C_6H_8O_7$) and glucose were used as a precursor (in stoichiometric ratios) and mixed with de-ionised (DI) water at room temperature under continuous stirring. (Figure 6.4) The resultant precursor solution was then transferred to Teflon lined stainless-steel autoclave and was kept in a furnace at 160°C for 6 hours and was allowed to cool to the room temperature. Thereafter, the mixture was centrifuged several times using different solvents at 10,000 rpm to remove the bound impurities, and the supernatant was filtered using 100 nm pore size filter. The collected GQDs were sonicated for ~12hr before further characterization. The optical property of synthesised GQDs was investigated by UV-Vis as well as by photoluminescence (PL) techniques at room temperature (RT-PL). Figure 6.5(a) shows the UV-Vis spectrum of the GQDs, where a prominent peak at ~238nm confirms the π–π* transition of aromatic sp^2 clusters and a weaker shoulder peak at ~321nm corresponds to the n–π* transition of C=O bonds. [201, 202] Furthermore, a detailed study was carried out to investigate their photoluminescence properties where GQDs were excited at the wavelength ranging from 325nm to 400nm. The excitation dependent emission spectra demonstrate a red shift from ~500nm to ~540nm, as shown in Figure 6.5(b). It is noteworthy to observe the strongest emission peak of the spectrum at ~510nm with a Stokes shift of ~40nm for an excitation wavelength of 325nm. [202, 203] The photoluminescence emission mechanism of GQDs postulates the presence of quantum size effect, oxygen-containing groups, aromatic conjugated structure and emissive free zigzag sites with carbene alike triplet ground state. [202, 204, 205] Moreover, the size dimensionality of synthesised GQDs has been realized by the high-resolution transmission electron microscopy (HRTEM) techniquewhich displays mono-dispersed sphere-like shaped GQDs with an average size of ~40 nm (shown in Figure 6.6).

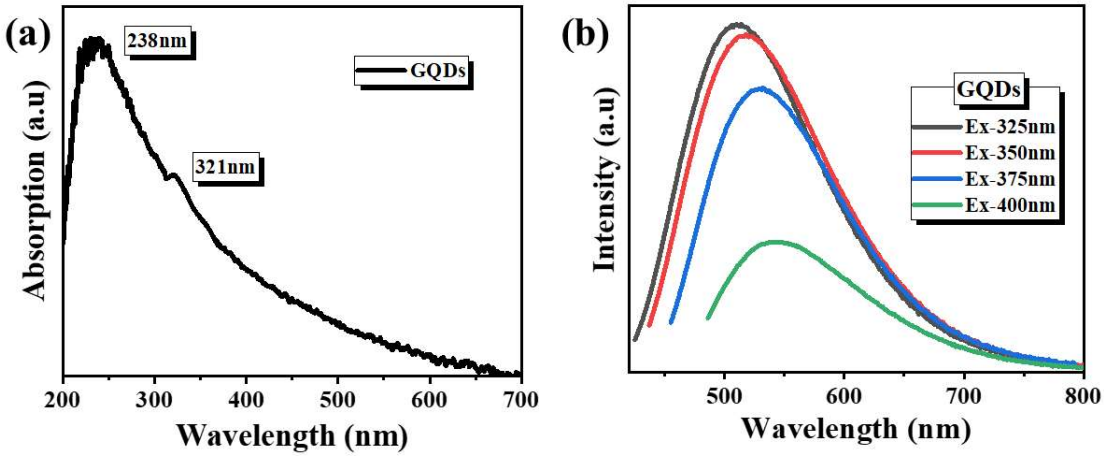

Figure 6.5: (a) UV-Vis spectra of GQDs; (b) RT-PL spectrum of excitation dependent emission spectra.

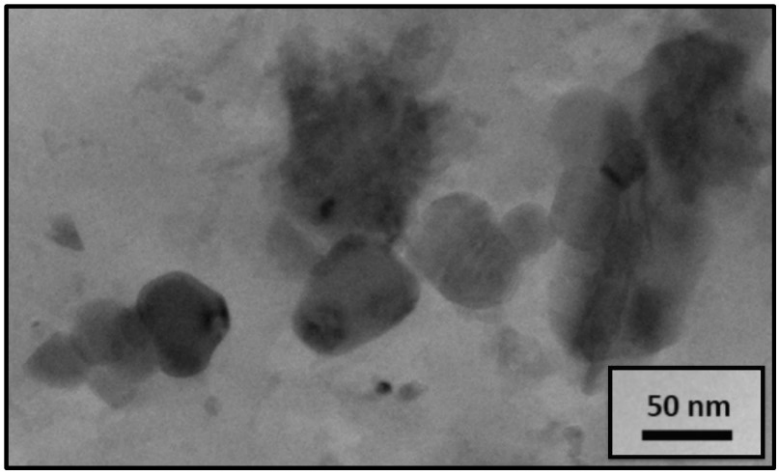

Figure 6.6: HRTEM image of chemically synthesised GQDs.

6.2.4 Characterization

The impact of surface functionalization (by Au-NPs) and sensitization (by GQDs) on the performance of ZnO-NRs/GaN-NTs UV-PDs has been investigated. The structural quality of the grown structures was assessed by High-Resolution X-ray Diffraction (HRXRD) (PANalytical X'Pert PRO MRD System) using CuKα1 radiation (λ= 1.5406 A˚). The morphological and elemental studies of grown GaN-NTs, ZnO-NRs and Au-NPs, have been carried out using field-emission scanning electron microscopy (FESEM), energy-dispersive X-ray spectroscopy (EDS), EDS elemental mapping (ZEISS AURIGA), high-resolution transmission electron microscopy (HRTEM, FEI,

Tecnai F30 G2 S-TWIN) and selected area electron diffraction (SAED) pattern. For analysing the optical properties, UV-Vis spectroscopy (Agilent, Cary 5000i) and room temperature (RT) photoluminescence (PL) measurement were carried out by using FLS980 D2D2 (Edinburg) system with 325nm excitation source (Hd-Cd Kimmon laser) while, Raman spectroscopy was carried out in backscattering configuration, using a 514 nm argon-ion laser.

6.3 Au Nanoparticles Functionalized Hybrid ZnO - NRs / GaN - NTs heterostructured Highly Responsive UV-PD.

6.3.1 ZnO-NRs/GaN-NTs heterostructure formation and their functionalization by Au-NPs

For the formation of ZnO-NRs/GaN-NTs heterostructure, the as-grown (sample S2: chapter 5) longer length GaN-NTs with thicker AlN buffer layer has been utilized as a bottom layer. The epitaxial growth of vertically aligned GaN-NTs array (4.62μm) has been performed on Si (111) substrate with a sandwich buffer layer of AlN (thickness ~650nm±5nm) via plasma-assisted molecular beam epitaxy (Compact-21, Riber, France). For this Gallium, N_2 flow and RF-plasma power have been taken as 666°C, 2.8×10^{-6} torr, 3 sccm and 400 W, respectively and to achieve the unique tapper ended morphology Ga flux was reduced from 2.8×10^{-6}torr to 1.5×10^{-6}torr, details of the growth is discussed in chapter-5 (sample: S2) [27]. The ZnO-NRs were chemically synthesized via sol-gel method followed by calcination. [200] These chemically synthesised ZnO-NRs were drop caste on GaN-NT (Figure 6.7(a)) and spin-coated at 3000 rpm to fabricate the heterostructure [schematics is shown in Figure 6.7(b-c)]. [27] Thereafter, the chemically synthesised monodispersed ~10 nm sized Au-NPs were drop casted over the as-grown ZnO-NRs/GaN-NTs heterostructure and uniformly spin-coated at 4000 rpm followed by 200ºC annealing [shown in Figure 6.7(d-e)].

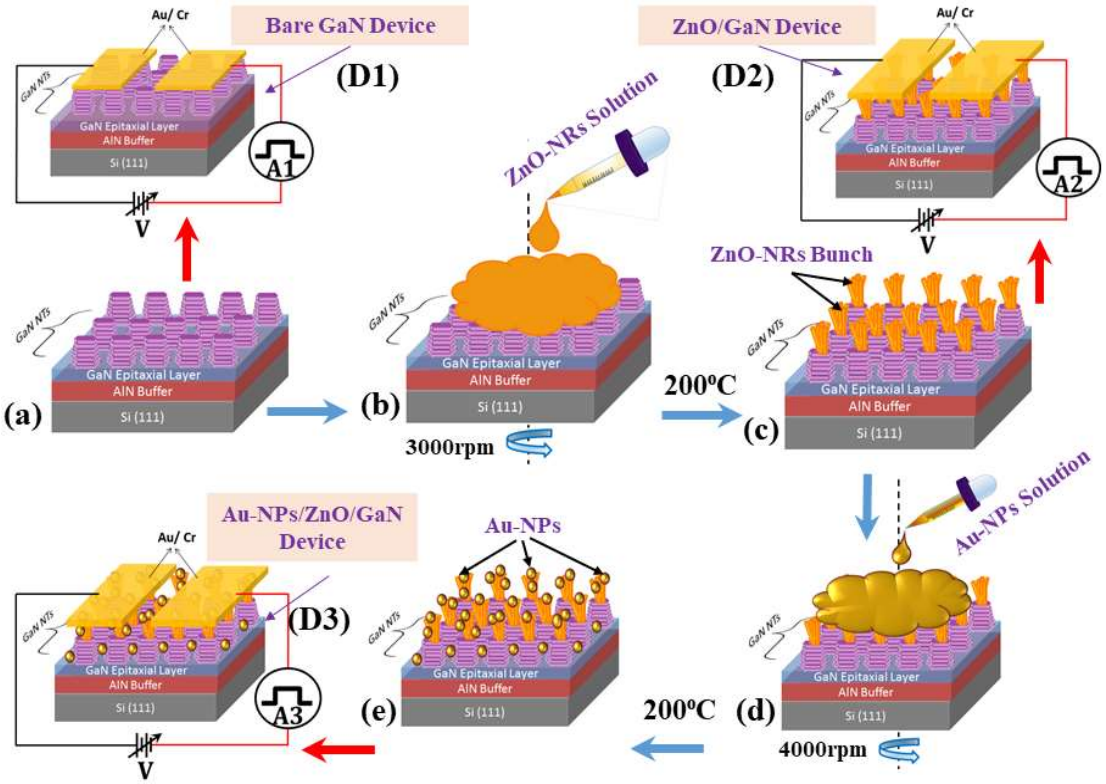

Figure 6.7: Schematic represents the fabrication process of GaN-NTs [D1], ZnO-NRs/GaN-NTs [D2] and Au-NPs/ZnO-NRs/GaN-NTs [D3] based UV-PDs.

6.3.2 UV PD Devices Fabrication

For optoelectronic studies, all three device structures are shown in Figure 6.7,*i.e.* bare GaN-NT array [D1 or D2 (as per chapter-5)], ZnO-NRs/GaN-NTs (D2) and Au-NPs/ZnO-NRs/GaN-NTs (D3) were fabricated by depositing metal electrodes of Au (~200nm)/Cr (~10nm) in MSM geometry by using thermal evaporation system. The active area between the two metal electrodes is 1.18×10^{-3} cm^2. The current-voltage (I-V) and photoresponse measurements were carried out using a probe station setup (S10 Triax probe station with Keithley 2401 acquisition unit). The source unit is equipped with a focused laser source (λ= 325 nm with the variable power density of 3.2 mW/cm^2 to 184 mW/cm^2).

6.3.3 Results and Discussion

(A) Structural, Morphological, Optical and Elemental Analysis after Surface Functionalization of GaN-NTs Array by ZnO-NRs and Au-NPs:

I. Functionalization of as-grown GaN-NTs Array by ZnO-NRs.

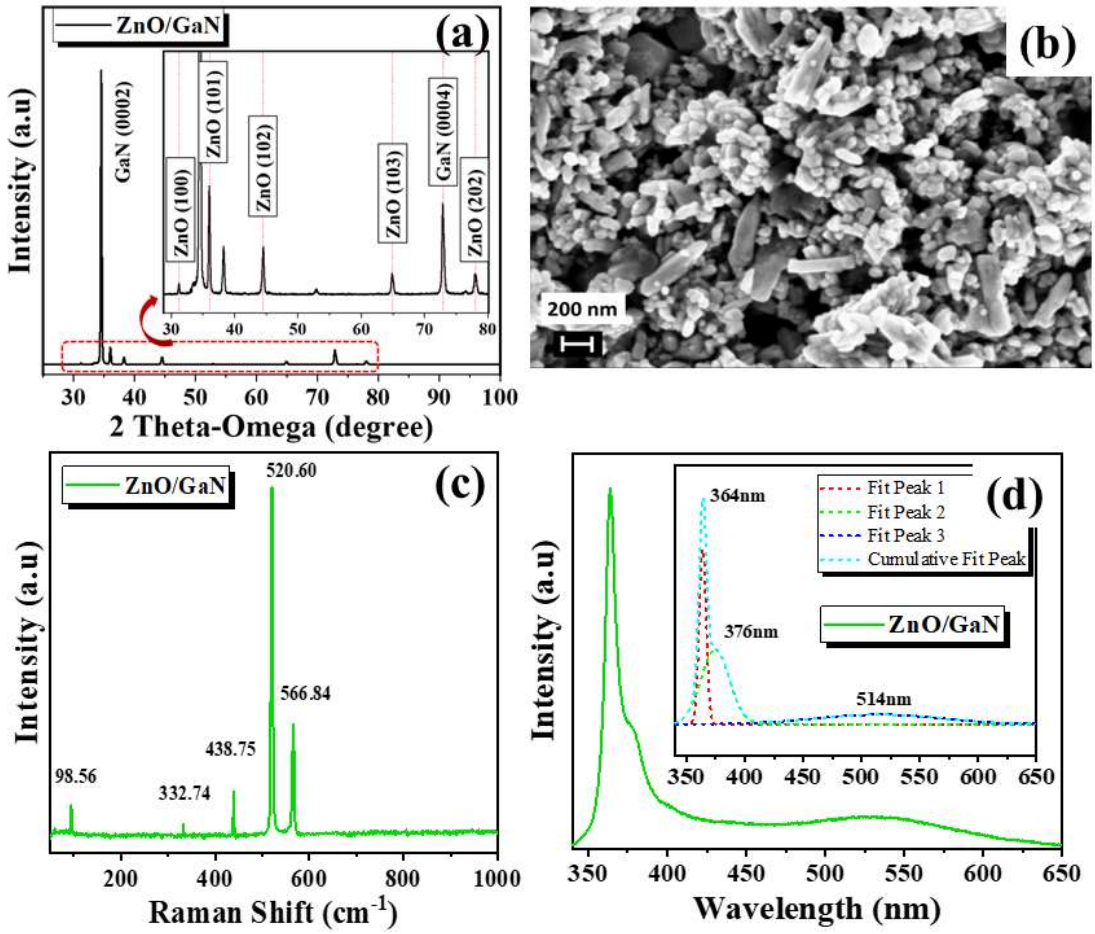

Figure 6.8: (a) HRXRD 2θ-ω scans along (0002) plane of diffraction of ZnO/GaN heterostructure and inset represents the zoom HRXRD spectra; (b) FESEM image of ZnO NRs distributed on GaN NT array. (c) Raman spectra and (d) RT-PL spectra of ZnO/GaN heterostructure.

Now, the surface of the as-grown GaN-NT array has been spin-coated with the chemically synthesised ZnO-NRs. The formed ZnO/GaN hetero-interfaced structure (heterostructure) has been further utilized to see the impact of functionalization on GaN-NT array. Initially, the HRXRD analyses of ZnO NRs/GaN-NT sample has been performed, and 2θ-ω scan is shown in Figure 6.8(a) where the sharp peaks of ZnO along with GaN conclude that the deposited NRs are highly single-crystalline in

nature and having hexagonal wurtzite structure. The inset of Figure 6.8(a) confirms the presence of multiple peaks of ZnO at {31.87 (100), 36.38 (101), 47.64 (102), 63.06 (103)}which are in close agreement with the standard values of ZnO (JCPDS, 36-1451). The morphology of ZnO-NRs functionalized GaN-NTs sample was probed to detect the distributed ZnO-NRs, as shown in Figure 6.8(b). It was found that agglomerated ZnO-NRs were evenly distributed over the GaN-NTs with high distribution density (5.2×10^{10} cm^{-2}) ascribed to 3D nanotower morphology which allows a large number of favourite sites to the ZnO-NRs.

Figure 6.8(c) shows the Raman spectra of developed ZnO-NRs/GaN-NT structure where a sharp and prominent peak at 438.75 cm^{-1} indicates the Raman active optical phonon E_2 mode of ZnO. The appeared E_2 high mode of ZnO confirms the synthesis of ZnO-NRs with wurtzite hexagonal phase. [206] Besides, two weak peaks at 98.56$cm^{-1}$and 332.74 cm^{-1} were also observed which were assigned as E_2 (low) and E_{2H}–E_{2L} (multi-phonon) modes, respectively. The results of Raman scattering analysis were found to be consistent with HRXRD and SAED observations [as shown in the inset of Figure 6.2(d)]. Further to analyse the impact of ZnO-NRs functionalization on the optical states of GaN-NTs, the RT-PL measurements of ZnO/GaN heterostructure sample was carried out [Figure 6.8(d)]. The spectra demonstrate highly intense NBE peak of GaN at ~364 nm along with a shoulder peak at ~ 376 nm which corresponds to the band edge emission of ZnO and a blue shift in the YBE (400nm – 600nm) has also been observed due to ZnO broad YBE.

II. Implementing Nanoplasmonics Effect using Au NPs on ZnO-NRs/GaN-NTs Heterostructure.

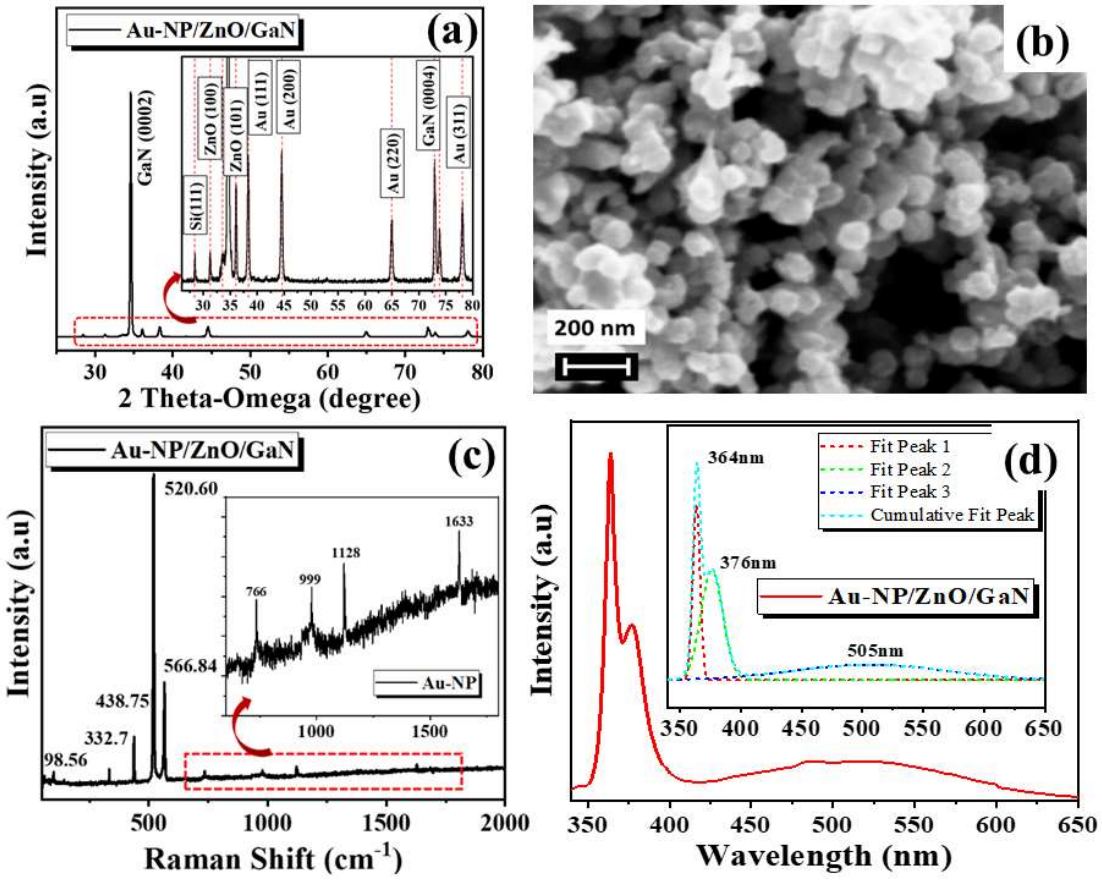

Figure 6.9: (a) HRXRD 2θ-ω scans along (0002) plane of diffraction of Au-NPs/ZnO/GaN heterostructure and inset represents the zoomed HRXRD spectra; (b) FESEM image of Au-NPs/ZnO NRs distributed on GaN NT array. (c) Raman spectra and (d) RT-PL spectra including deconvoluted PL peaks involved in Au-NPS/ZnO-NR/GaN-NT heterostructure.

The grown structure (ZnO-NRs/GaN-NTs) has been functionalized by Au-NPs which are chemically synthesised, monodispersed and pertain an optimized size of ~10 nm. The sharp peaks (Figure 6.9(a)) located at ~38° for (111), ~44.7° for (200), ~64.8° for (220), and 77.5° for (311) in HRXRD 2θ-ω scan shown in the inset of Figure 6.9 (a) indicated the face-centred cubic structure of Au-NPs [207]. Besides, the morphological information of synthesised Au-NPs (Figure 6.3) as well Au-NPs/ZnO-NRs functionalized GaN-NT array structure is shown in Figure 6.9(b), where agglomerated Au-NPs can be observed as shining round particles distributed all over the ZnO-NRs and GaN-NTs. Besides, elemental mapping and EDS analysis of the

nano-plasmon incorporated ZnO/GaN structure were also performed (shown in Figures 6.10 and Figure 6.11), which demonstrate the elemental distribution of Au, Zn and O on GaN-NTs surface and assures the absence of any external impurity element in the grown heterostructure, respectively.

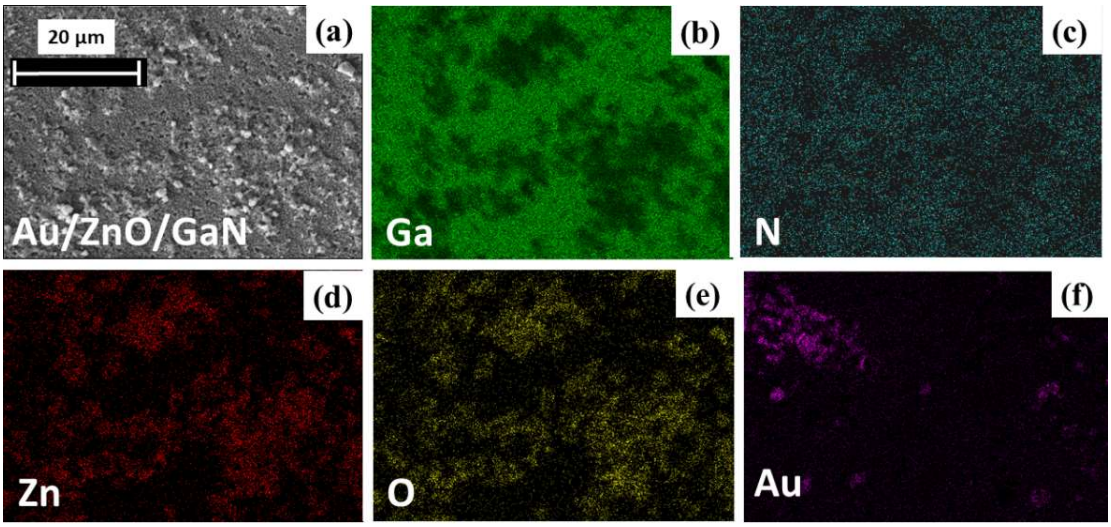

Figure 6.10: Elemental mapping of Au-NPs/ZnO-NRs/GaN-NTs sample.

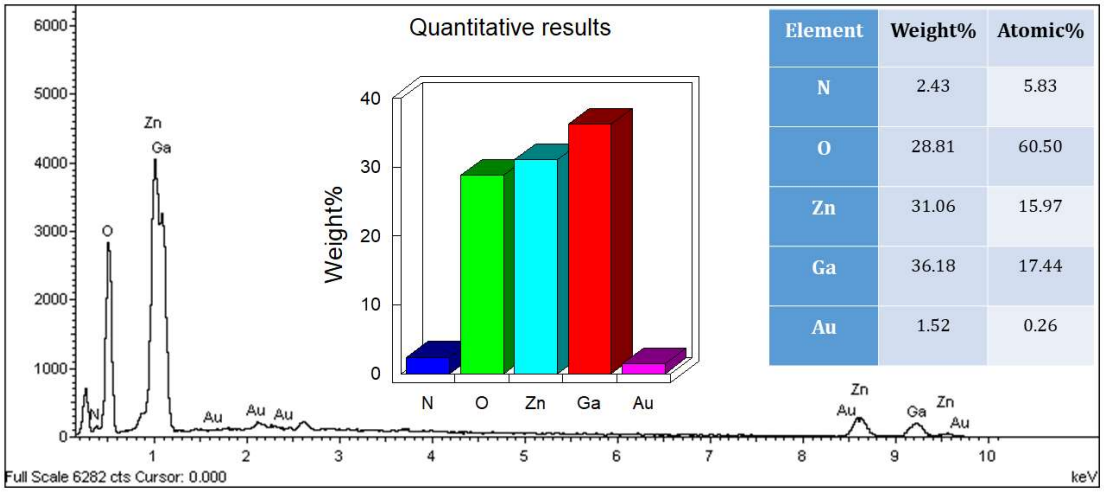

Element	Weight%	Atomic%
N	2.43	5.83
O	28.81	60.50
Zn	31.06	15.97
Ga	36.18	17.44
Au	1.52	0.26

Figure 6.11: EDS analysis of as grown Au-NPs/ZnO-NRs/GaN-NTs sample.

Besides, the analysis of Raman spectra shown in Figure 6.9(c), also confirms the presence of Au-NPs on ZnO-NRs/GaN-NTs sample, where the peak positions (inset of Figure 6.9(c)) 766 cm^{-1}, 1128 cm^{-1} and 1633 cm^{-1} are attributed to the reported Au-NP's Raman peak values. [208] Subsequently, the impact of Au-NP's stimulated

functionalization on the optical states of as-synthesised heterostructure has been analysed through RT-PL measurement, as shown inFigure 6.9(d). The PL spectra demonstrate enhanced intensity NBE peak at ~364nm as a cumulative effect of GaN-NTs as well as Au-NPs [Figure 6.3 (d)] when excited by 325nm UV excitation source. [209, 210] Moreover, the spectra also provide enhanced shoulder peak of ZnO-NRs at ~376nm as compared to without Au-NP based heterostructure. Further, on the addition of Au-NPs on its surface, a clear enhancement in the band edge emission of ZnO has been perceived in the PL spectra along with a broad emission at ~ 505 nm (green emission) which belongs to the Au NPs. Since, the Au-NP's surface plasmon emission is very close to the defect band emission energy of GaN as well as ZnO,*i.e.*, 500nm – 600nm. Therefore, during the UV interaction with GaN, ZnO and Au-NPs, the Au-NPs absorb the emission energy from GaN and ZnO defect band, wherein because of resonant excitation, the Au-NPs produce energetic hot resonant electrons. Some of these hot resonant electrons were further transferred into the conduction band of GaN and ZnO while remaining can recombine with holes in the valence band which contribute to Au NPs' green emission as well as further increasing the intensity of band edge emission of ZnO and GaN [54, 55]. Besides, Au-NPs also contribute extra carriers to ZnO/GaN, which is revealed by a high-intensity emission peak at ~364nm with excitation wavelength 325nm (Figure 6.3 (d)). Therefore, Au-NP's NBE provided carriers generated by 325nm direct excitation as well as carriers provided by NP's absorption from defect emission of GaN as well as ZnO which collectively enhanced the density of generated EHPs when the surface is functionalized by Au NPs.

(B) Impact of Surface Functionalization on GaN-NT Array-based UV-PDs

I. Device characteristics from surface-functionalized (ZnO-NRs and Au-NPs) GaN-NTs

The surface of highly responsive GaN-NTs based UV-PD has been functionalized with chemically synthesized ZnO-NRs and Au-NPs as functionalizing agents. Figure 6.12 displays the rectifying behaviour in RT I-V characteristics of all the devices owing to the work function difference between the Au electrode and GaN semiconductor. Initially, variation in the dark current is closely investigated, where

electrical properties were found to be affected by surface functionalization as the incorporation of ZnO-NRs and further involvement of Au-NPs on the surface of device structure causes the variations in ideality factors as well as barrier heights of the device. Figure 6.12(a) demonstrates that, the dark current increases upon the incorporation of ZnO NRs on GaN-NT surface which could be associated with small Schottky barrier in Au/ZnO compared to Au/GaN metal-semiconductor interface. This is due to the slightly higher work function of ZnO than GaN, which resulted in increased carrier transport concluding an increase in the dark current in ZnO NRs/GaN-NTs based heterojunction device. As an extension to this device design, the light-matter interaction is enhanced by using Au-NPs on the surface of ZnO NRs/GaN NTs heterostructure. The RT I-V characteristics in dark condition reveal that the Au-NPs/ZnO-NRs/GaN-NTs hetero-interface device witnesses a prominent reduction in dark current value (21.6nA) which is even lesser than bare GaN-NT based device. As the metal nanoparticles have the tendency to couple with incident light and generate strong scattering and absorption of the incident light resulting in a localized Schottky junction formation. This develops a charge depletion region in the vicinity of the metal-semiconductor interface, which will promote the reduction in dark current and enhancement in sensing ability of the devices. [211] Upon UV illumination, an incident optical power-dependent study has been performed on both the heterojunction devices with optical power density varied from 3.2 mW/cm^2 to 184 mW/cm^2. The surface-functionalized devices demonstrate UV photodetection as pragmatic by a change in the acquired dark and light currents from RT I-V characteristics shown in Figure 6.12(b) and (c). It can be observed that with increasing optical power density, the light current values of functionalized UV-PDs (ZnO NRs/GaN-NTs and Au NPs/ZnO NRs/GaN-NTs) gradually increases the photocurrent values and even achieved higher values than the bare GaN-NTs based UV detector (see device D2 chapter 5). The increment in photocurrent is attributed to increased photon absorption with the increasing optical power density and enhanced light-matter interaction due to surface functionalization. Quantitatively, it was observed that the photocurrent value of the ZnO NRs/GaN-NTs based UV detector increases from -4.62 mA to -26.3 mA as optical power density increases from 3.2 mW/cm^2 to 184 mW/cm^2 under -6V applied bias as shown in Figure 6.12(b).

Likewise, after ZnO NRs/GaN-NTs is coupled with Au-NPs, the fabricated device demonstrates augmented photocurrent value from -27.43 mA to -51.05 mA (Figure 6.12(c)). The time-correlated photoresponse of these functionalized devices was investigated under periodic switching of UV illumination where a stable transient response has been recorded at fixed incident optical power density of 3.2 mW/cm^2 but varied applied bias from -1 V to -6 V (shown in Figure 6.13). The results demonstrate an increasing trend of photocurrent values,*i.e.*, -0.28 mA, -1.26 mA and -4.62 mA for ZnO NRs based device and -1.92 mA, -9.35 mA and -27.43 mA after Au NPs involvement under the applied bias of -1V, -3V and -6V, respectively. A series of schematic band diagram illustrating the detailed mechanism for enhanced current conduction in the fabricated novel bare as well as functionalized UV PD devices structures were demonstrated in Figure 6.14.

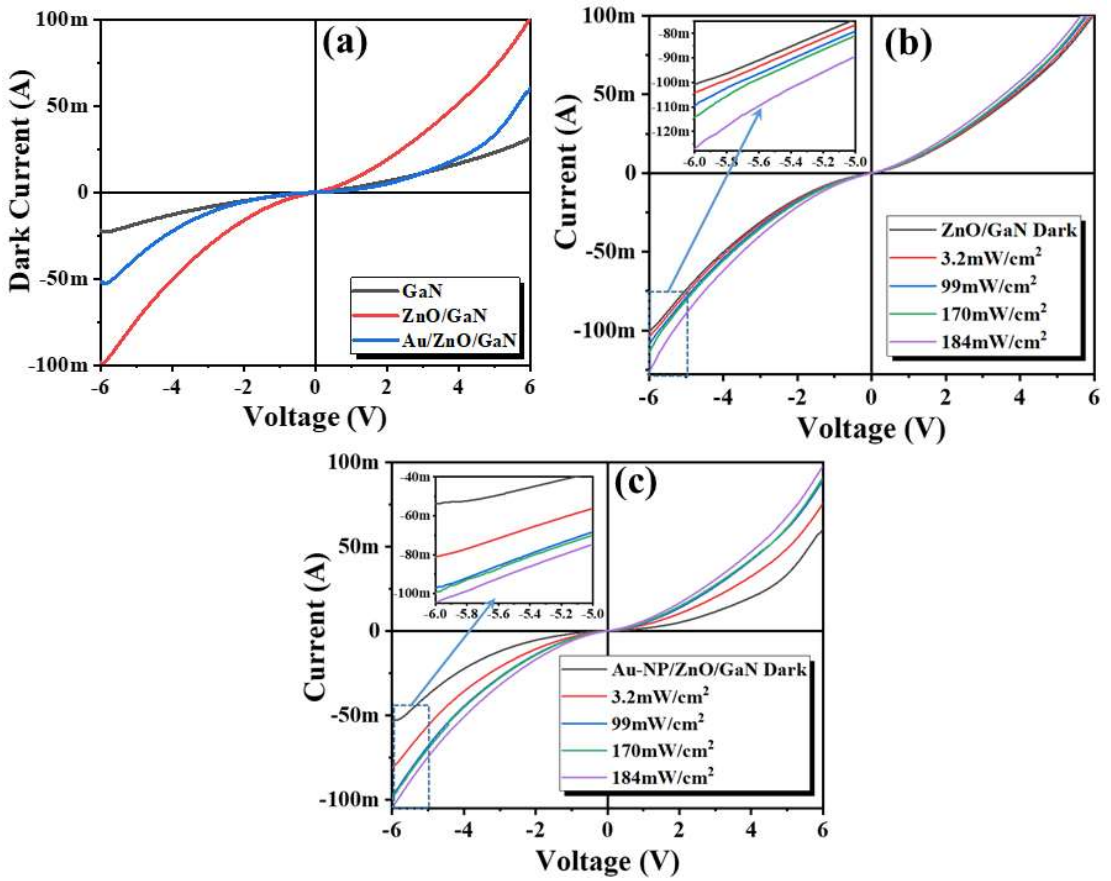

Figure6.12: (a) The I-V plot compares dark current of the bare device with surface functionalized counterparts; The RT-I-V curves plotted for dark condition and UV illumination at varied optical power density (inset shows the magnified data at higher bias) from (b) ZnO NRs/GaN-NTs and (c) Au NPs/ZnO NRs/GaN-NTs device structures.

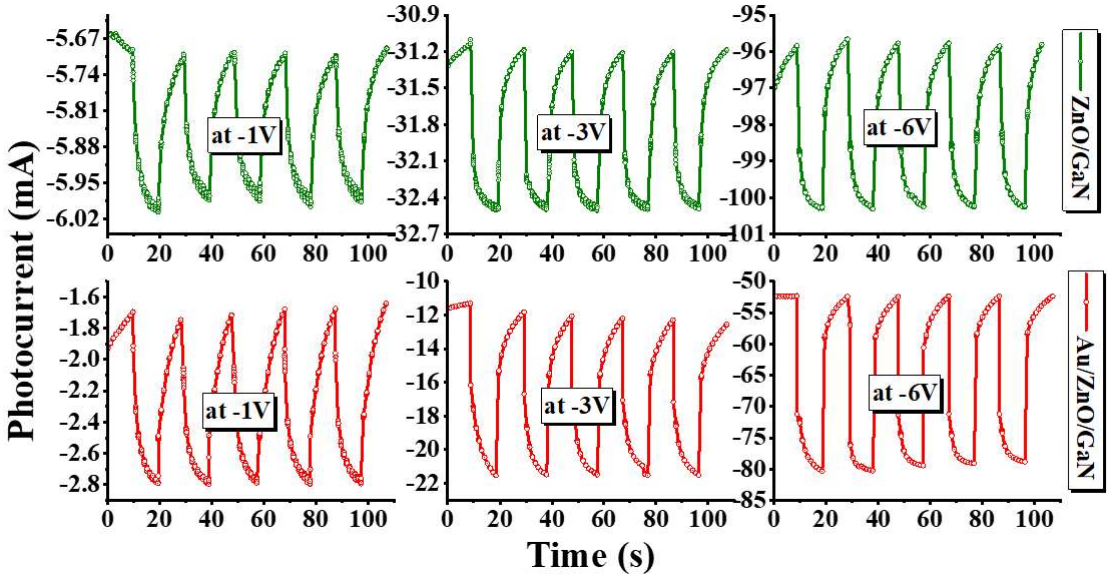

Figure6.13: Time-correlated UV response under the varied applied bias of -1, -3 and -6 V for both the fabricated UV photodetection device structures at a constant optical power density of 3.2 mW/cm^2.

II. Opto-Electrical Transport and its Enhancement Mechanism

To understand the opto-electrical transport in the developed devices, the energy band diagram of fabricated bare GaN-NTs based UV-PD under thermal equilibrium (dark condition) is demonstrated (Figure 6.14(a)). The higher work function of Au-metal electrode (~5.1 eV) as compared to a lower electron affinity ($q\chi$) of GaN (~4.2eV) creates a ~0.9 eV barrier at the metal-semiconductor interface. Under the photoconductive mode of operation, with UV illumination, the photo-generated charge carriers are separated and drifted by the applied electric field (Figure 6.14(b)). Furthermore, the current transport in a device developed upon functionalizing the surface of GaN NTs with ZnO NRs is explained via Figure 6.14 (c) – (e). Under a dark condition in the ambient environment, ZnO-NR's surface adsorbs the oxygen molecules by gathering free electrons to forms ionized oxygen, thereby, develops a depletion layer near the surface of NR (shown in Figure 6.14(c)). [212, 213]

Consequently, the generated electron-hole pairs [$h\nu \rightarrow h^+ + e^-$] further modify the electrical conductivity of the ZnO NRs/GaN-NT device. During UV-photon interaction, generated holes were migrated to ZnO-NRs and discharge the negatively charged oxygen ions by using the energy from electron-hole recombination [$h^+ + O_2^-$

$\rightarrow O_2$] [211]. Therefore, upon UV illumination, the discharged oxygen ions liberated electrons (which were captured by absorbed oxygen on ZnO NR's surface in the dark) along with electrons generated by ZnO NRs as well as GaN-NTs together contribute in increasing the overall photocurrent of the fabricated device (ZnO NRs/GaN-NTs) (as shown in Figure 6.12(b)). Figure 6.14(f) demonstrates the energy band diagram of ZnO/GaN heterojunction by using Anderson model [214], wherein, the electron affinity for ZnO is assumed to be 4.35eV. [215, 216] Depending upon the electron affinity of ZnO and work function of Au, the Schottky barrier at this metal-semiconductor junction (Au/ZnO NR) is reduced compared to Au/GaN-NT junction that resulted in increased current transport due to ZnO NRs functionalization.

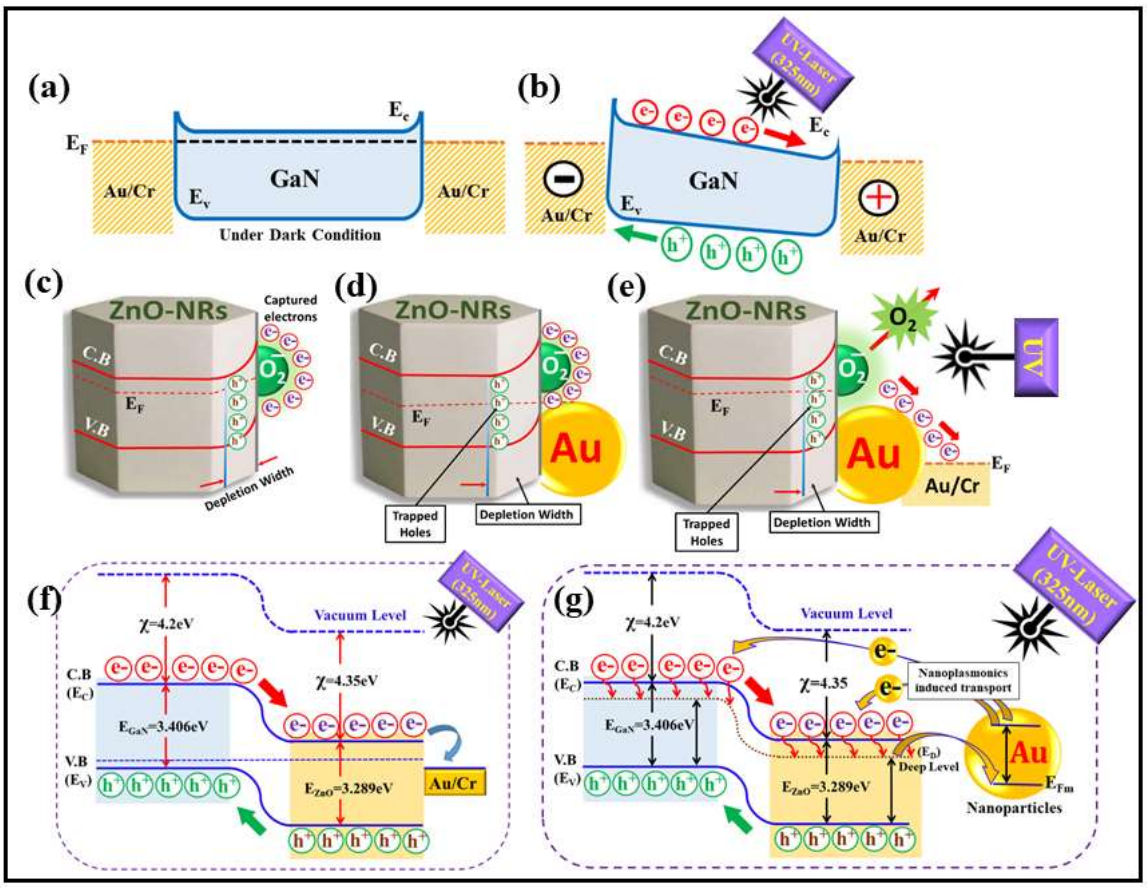

Figure 6.14: (a, b) The schematic energy band diagrams of bare GaN-NTs based device without and with UV illumination, (c-e) The schematic diagram of the ZnO NRs/GaN-NTs UV PD decorated without and with Au-NPs composite and its carrier transport mechanism in the interfacial region when irradiated by UV-light (f, g) Energy band diagrams of the ZnO-NRs/GaN-NTs UV PD without and with Au-NPs.

Moreover, when these ZnO NRs coupled with novel Au NPs, the developed barrier height is found directly in correlation with depletion layer width near the Au NPs/ZnO NRs interface. Thereby, the depletion region is larger as compared to solely ZnO NRs (shown in Figure 6.14(d)). [211] Thus, metal NPs induced larger depletion region produces a low conductive path which cumulatively decreases the dark current of the device (plotted in Figure 6.12(a)). After the device is illuminated by a UV laser of 325 nm, a gradual increment in the light current have been observed due to the incident photon energy (325 nm, 3.815 eV) which is larger than the bandgap (E_g) of GaN (3.406 eV) as well as ZnO (~3.289 eV).

Therefore, Au-NPs decorated ZnO-NRs oriented Au/ZnO interface and related Schottky barrier plays a very significant role in current conduction enhancement, wherein, generated holes drift towards Au NP due to the interactive Coulomb forces [211]. Though, some of the holes were remained trapped at the Au-ZnO interface while others crossed through the Schottky barrier at the interface, resulting in recombination. These trapped holes were restricted from recombination and thereby, allowed more electrons to be collected by the respective electrode (shown in Figure 6.14(e)). Now unlike Au/ZnO interfaces, solely nanoplasmonics stimulated local surface plasmon of Au-NPs to contribute supplementary resonant hot electrons by absorbing the emitted energy from defect bands of the ZnO as well as GaN. Figure 6.14(g) shows the mechanism of sequential energy transfers in this device structure. Conceptually, when GaN and ZnO were simultaneously excited by incident UV-photons, some of the electrons gain enough energy to jump into the respective conduction bands while few electrons could end up being trapped in their respective defect levels. These trapped electrons recombine in the valence band resulting in defect energy emissions. Since the energy between the semiconductors (GaN as well as ZnO) defect emissions and Au-NP's surface plasmon is perfectly matched. Therefore, the defect emission energy has been absorbed and used to stimulate the Au-NPs, which further liberates resonant hot electrons that can be easily transferred into conduction bands of GaN and ZnO [54] simultaneously as shown in Figure 6.14(g). Moreover, it is also experimentally realized (RT-PL of Au-NPs Figure 6.3 (d)) that by directly exciting Au-NPs using 325 nm UV-laser source, these NPs emit

majorly in the same UV region as contributed by GaN and ZnO. Conclusively, the charge carriers transported by the Au/ZnO interfaces, GaN/ZnO UV triggered electrons, and Au-NPs stimulated resonant hot electrons cumulatively facilitate the enhanced performance from the fabricated novel detection device structure (Au NPs/ZnO NRs/GaN NTs).

Next, a comparative evaluation of all three fabricated detectors is compiled where the role of surface functionalization for enhancing the device performance has been realized. Figure 6.15(a) reveals a highly prominent photocurrent enhancement from fabricated detectors before and after functionalization w.r.t. incident optical power density under a constant applied bias of -6 V. As an ideal PD should yield maximum photocurrent at a lowest optical power of incident illumination, thus, the minimum incident optical power density of 3.2 mW/cm^2 is utilized to closely determine the performance parameters of the developed detectors. Henceforth, the devices demonstrate significant enhancement in photocurrent under varied applied bias conditions (Figure 6.15 (b)). Specifically, at an applied bias of -6V, the photocurrent value is increased from -1.86 mA (bare GaN) to -4.62 mA (ZnO NRs/GaN-NTs) and finally to -27.43 mA (Au NPs/ZnO NRs/GaN-NTs), which is attributed to ~ 2.5 fold and ~ 15 fold enhancement by ZnO and Au-NPs functionalization, respectively (shown in Figure6.15(b).

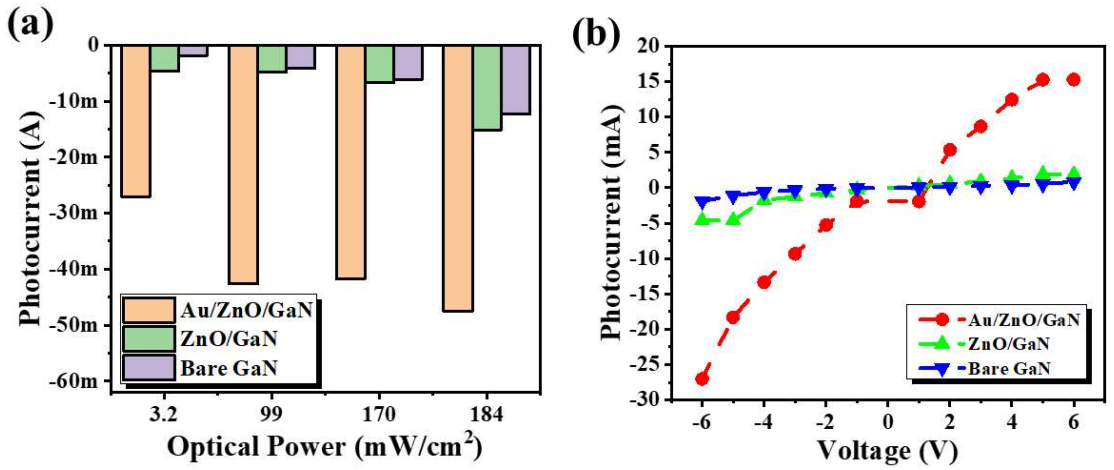

Figure 6.15 Demonstrates the enhancement in performance parameters of functionalized UV-PDs as compared to bare device (a) Power dependent photocurrent enhancement at a fixed applied bias of -6V; (b) The bias dependent photocurrent study at fixed incident optical power density of 3.2 mW/cm^2.

Figure 6.16(a) display responsivity variation with applied bias where the responsivity value with increasing applied bias from -1 V to -6 V was found to be increased from ~16 A/W to ~485 A/W for bare GaN-NT device, ~73 A/W to ~1204 A/W for ZnO NRs functionalized GaN-NT device and ~500 A/W to ~7042 A/W for Au NPs coupled ZnO NRs/GaN-NTs device structure. The obtained results suggest that the responsivity value of 7042 A/W (Au NPs/ZnO NRs/GaN-NTs) achieved at -6V is remarkably very high as compared to available UV detectors (Table 6.1).

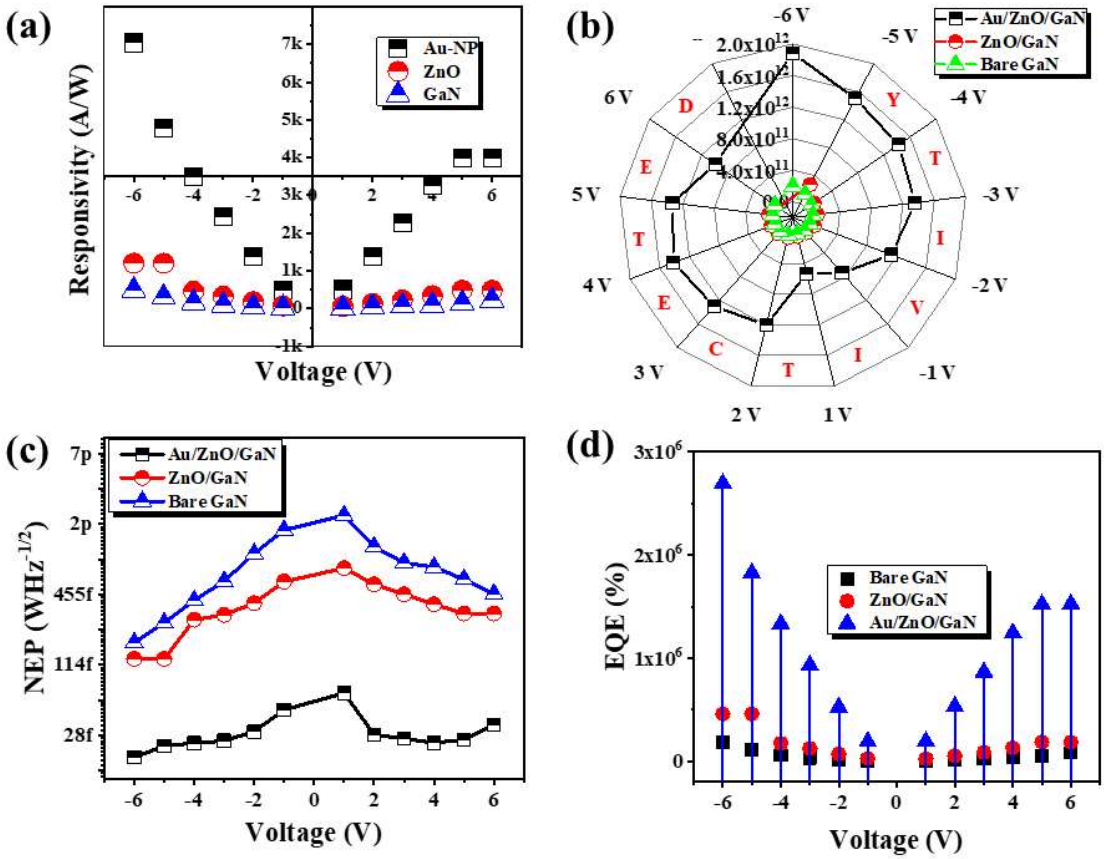

Figure 6.16: Demonstrates the enhancement in performance parameters of functionalized UV-PDs as compared to bare device (a) Responsivity, (b) Detectivity, (c) NEP and (d) EQE.

Correspondingly, other essential performance parameters such as detectivity, NEP and EQE were also determined at variable bias conditions, where gradual enhancement is obtained in either direction of bias as shown in Figure 6.16 (b-d) and tabularized in Table-6.1. Particularly at -6 V applied bias, the device structure coupled with Au NPs demonstrated the maximum detectivity, NEP and EQE value estimated

as 1.88× 10^{12} jones, 1.84× 10^{-14} $WHz^{-1/2}$ and 2.7× 10^{6} %, respectively. The lower NEP value is attributed to the capability of Au-NPs coupled ZnO-NRs/GaN-NTs UV-PD to detect a signal of power as low as ~ 0.18 femto watt with a signal-to-noise ratio of one after the one-half second of averaging. As EQE is directly proportional to responsivity and defined as the probability of creating an electron-hole pair out of one absorbed photon, therefore, the highest responsivity value of 7042 A/W projected the increased EQE value of 2.7× 10^{6} %.

Table 6.1: Comparison of performance parameters of various surface-functionalized UV-PDs.

Materials	**Wavelength/ Opt. Power**	**R(A/W)**	**D (jones)**	**EQE(%)**	**NEP($WHz^{-1/2}$)**	**Ref.**
ZnO-NRs/i-ZnO/GaN	365nm	0.139	--	--	--	[40]
ZnO-NRs/Cds/p-GaN	300nm/3.2μWcm^{-2}	0.176	2.5×10^{12}	--	--	[41]
ZnO-NRs/GaN	360nm	11	--	--	--	[42]
Zn-TPPOH/GaN	365nm/5μWcm^{-2}	220				[217]
i-ZnO/n-ZnO/GaN	360nm/10mWcm^{-2}	437	--	1.6×10^{3}	--	[43]
ZnO-NRs/GaN-NTs	**325nm/3.2mWcm^{-2}**	**1204**	**2.7×10^{11}**	**4.6×10^{5}**	**1.3×10^{-13}**	**This work**
Ag-NP/GaN	360nm	2.45				[46]
Annealed Ag-NP/GaN	360nm	4				[46]
Au-NP/Ga_2O_3/GaN	350nm	1000				[218]
Au-NPs/ZnO/GaN-NT	**325nm/3.2mWcm^{-2}**	**7042**	**1.88× 10^{12}**	**2.7×10^{6}**	**1.84× 10^{-14}**	**This work**

Moreover, to evaluate the switching speed [rise (response) and decay (recovery) time] of the detectors, the time-correlated transient photoresponse of the fabricated devices have been analysed, and experimental data were fitted by following equations. [15]

$$\boldsymbol{I = I_0\left(1 - e^{\frac{-t}{t_r}}\right)} \tag{6.1}$$

$$\boldsymbol{I = I_0\left(e^{\frac{-t}{t_d}}\right)} \tag{6.2}$$

where I_o is the maximum saturation photocurrent value at a particular time t, t_r and t_d stand for the rise and decay time, respectively. The rise time is defined as the time taken by the detector to reach from 10% to 90% of final photocurrent value under UV-illumination and decay time is defined as the time taken by the same detector to reach from 90% to 10% of the final value of photocurrent after switching off UV-illumination. As per the obtained results (shown in Figure 6.17(a-c)) from all three PDs, the observation reveals that, there are two components for rise time 't_r' (τ_{r1} and τ_{r2}) and decay time 't_d' (τ_{d1} and τ_{d2}) whose values are shown in Table-6.2.

Table 6.2: Estimation of rise and decay time by using primary and secondary time constant parameter values obtained after fitting the experimental data.

Fabricated Detectors	**Rise Time (Response)**			**Decay time (Recovery)**		
	τ_{r1}	τ_{r2}	$\mathbf{t_r}$	τ_{d1}	τ_{d2}	$\mathbf{t_d}$
GaN-NTs	0.53s	3.05	**1.16s**	0.46s	3.54s	**1.01s**
ZnO-NRs/GaN-NTs	0.51s	2.64s	**1.12s**	0.53s	4.60s	**1.16s**
Au-NPs/ZnO-NRs/GaN-NTs	0.152s	2.46s	**0.334s**	0.11s	4.9s	**0.241s**

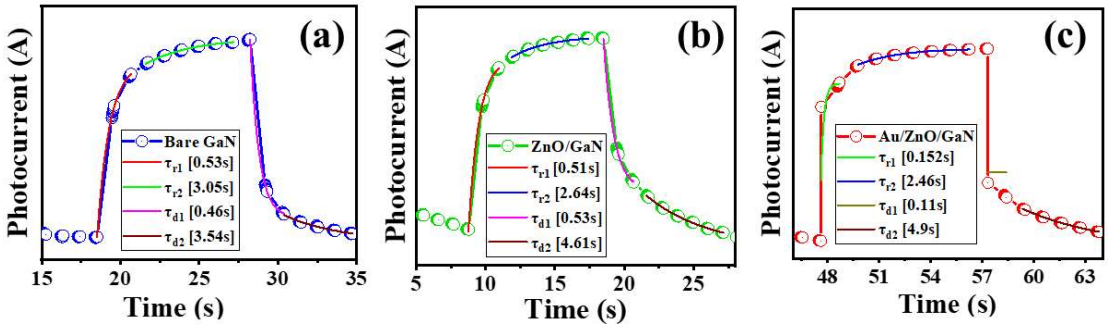

Figure 6.17: The switching speed estimation (rise and decay time) of (a) GaN-NTs , (b) ZnO-NRs/GaN-NTs and (c) Au-NPs/ZnO-NRs/GaN-NTs based UV PD at fixed bias voltage of -6V.

The measured rise and decay time were estimated by multiplying primary time constant components (τ_{r1} and τ_{d1}) with a factor (2.197) as discussed. [219] Therefore, the calculated rise / decay time are found to be ~1.16s / 1.01s (bare GaN-NTs), 1.12s / 1.16s (ZnO NRs/GaN-NTs) and ~334ms / 241ms (Au NPs/ZnO NRs/GaN-NTs). The secondary higher rise/decay time constant values (τ_{r2} and τ_{d2}) attributed to the higher transit time of photo-generated charge carriers as well as persistent photoconductivity

effect. [220] Besides, the obtained values also reveal the significance of Au-NPs decoration of the detector, wherein device display ~350% and 464% improvement in rise and decay time, respectively. Table 6.1 tabularizes the performance parameters of various surface-functionalized UV detectors compared with the novel structures developed in the present work. Till date, unlike other relevant studies, it is the first report where the fabricated UV PD utilizes the cumulative advantages of GaN as well as ZnO nanostructures. Besides, the advancement in novelty of the work is accelerated by the incorporation of resonant hot electrons contributed by LSPR effect of Au-NPs.

6.4 Graphene quantum dots Sensitized ZnO-NRs / GaN-NTs heterostructure based High-Performance UV-PD

6.4.1 GQDs sensitization of ZnO-NRs / GaN-NTs heterostructure

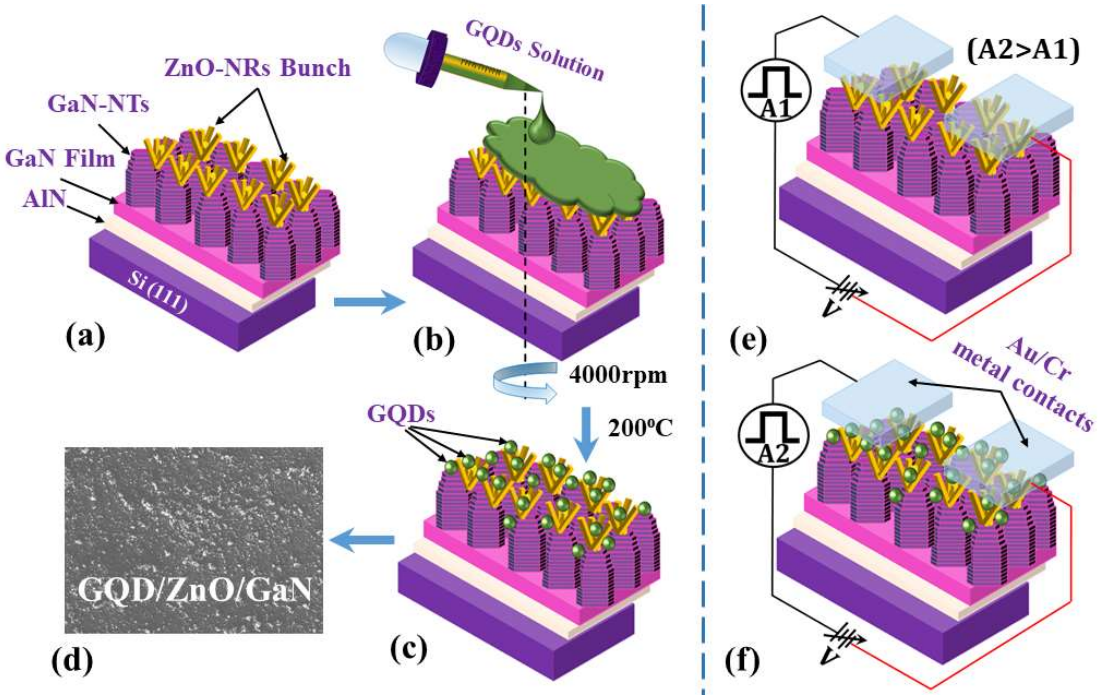

Figure 6.18: Schematic diagram of (a-c) fabrication process of GQDs sensitized ZnO-NRs/GaN-NTs heterostructure, (d) SEM image of GQDs/ZnO-NRs/GaN-NTs heterostructure and (e, f) bare and GQDs sensitized ZnO/GaN based UV PD where A1 and A2 stand for symbols of generated photocurrents from the devices.

Figure 6.18 (a-c) shows a schematic diagram representing the sensitization of ZnO-NRs/GaN-NTs heterostructure by chemically synthesized GQDs. The chemically

synthesized monodispersed GQDs were deposited on ZnO-NRs/GaN-NTs heterostructure by drop caste process which is further followed by spin coating (at 4000 rpm) and thermal annealing up to 200ºC as shown in Figure 6.18.

6.4.2 UV PD Device Fabrication

GQDs sensitized ZnO-NRs/GaN-NTs UV PD was fabricated along with bare ZnO-NRs/GaN-NTs device, as shown in Figure 6.18 (e, f). Furthermore, unlike the complexity of pn-junction based device structure, the fabricated devices have been taken advantage of MSM-junction based geometry, [74, 165] wherein the fabricated detectors demonstrated significantly high responsivity with fast transient reversibility. Thus, Au (~200nm)/Cr (~10nm) electrodes in MSM geometry were deposited with an active area of the device~1.18×10^{-3} cm^2.The photoresponse measurements were carried out via a probe station setup (S10 Triax probe station with Keithley 2401). A focused 325nm laser has been deployed as a UV light source with the incident optical power density of 3.2mW/cm^2.

6.4.3 Results and Discussion

(A) Structural, Morphological, Optical and Elemental Analysis after Sensitization of ZnO-NRs / GaN-NTs heterostructure by GQDs

The crystalline quality of stacked layer-by-layer GaN-NTs array structure, as well as ZnO-NRs/GaN-NTs heterostructure, were gauged by HRXRD 2θ-ω scan along (0002) plane, as discussed in chapter 5 (section 5.3.1). [27] The surface morphology of GaN-NTs was probed by FESEM technique where the planar view image displays hexagonal shaped, high density (distribution density of 6.2×10^9 cm^{-2}) and closely packed GaN-NTs with tapered ended geometry (Figure 6.19 (a)). A cross-sectional FESEM image of GaN-NTs is shown in Figure6.19 (b). The surface morphology of ZnO-NRs deposited GaN-NTs is shown in Figure 6.19 (c) which revealed high density and uniformly distributed ZnO-NRs in the agglomerated form on GaN-NTs. The GQDs sensitized ZnO-NRs/GaN-NTs heterojunction displays the presence of GQDs as a sphere like shaped structure on the ZnO-NRs as well as on GaN-NTs, as shown in Figure 6.19 (d). Moreover, EDS analysis, as well as elemental mapping of the GQDs, decorated ZnO/GaN heterostructure was performed which illustrates the

distribution of GQDs,*i.e.*, carbon compound 'C' along with Zn, O, Ga and N (shown in Figures 6.20 and Figure 6.21).

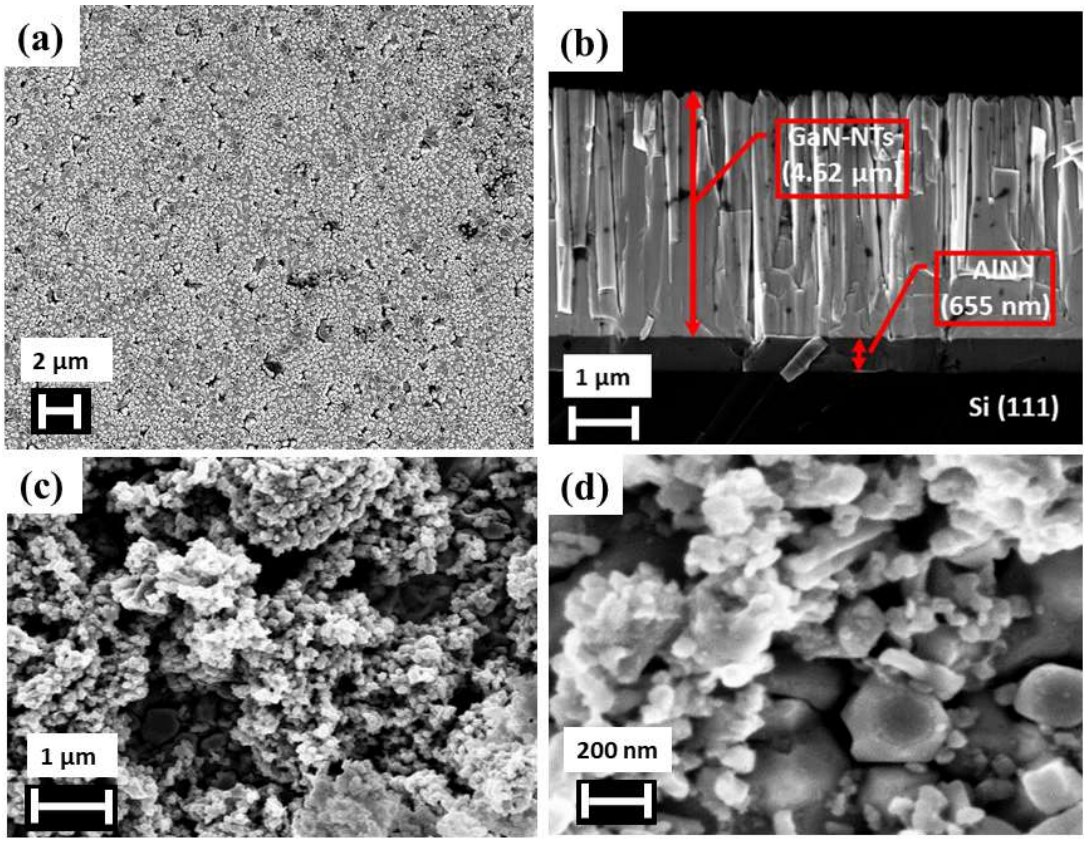

Figure 6.19: (a) Top-view FESEM image of GaN-NTs; (b)cross-sectional-FESEM of GaN-NTs; (c) amalgamated ZnO-NRs on GaN-NTs surface; (d) the magnified image of GQDs sensitized ZnO-NRs/GaN-NTs hetero-structure.

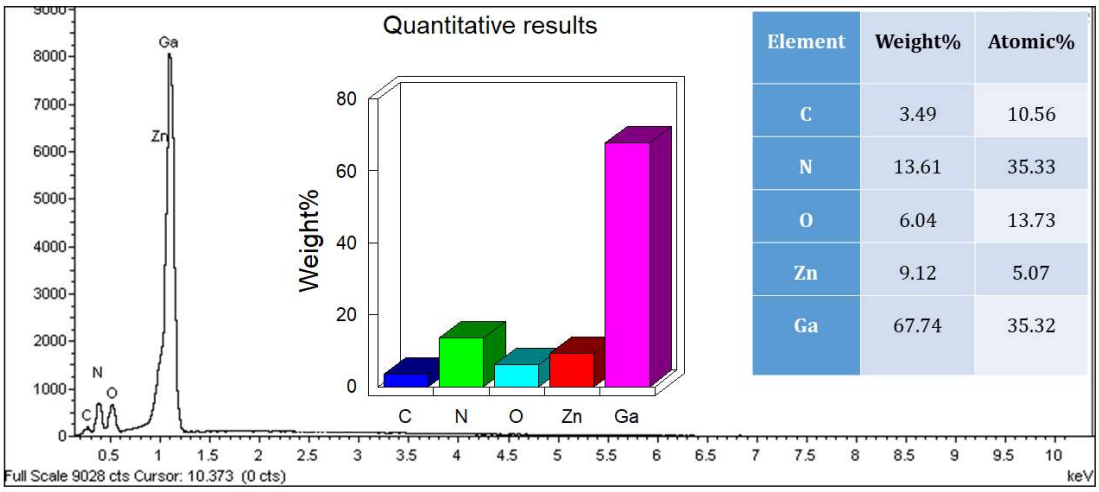

Element	Weight%	Atomic%
C	3.49	10.56
N	13.61	35.33
O	6.04	13.73
Zn	9.12	5.07
Ga	67.74	35.32

Figure 6.20: EDSspectra of as-grown GQDs--ZnO/GaN heterostructure.

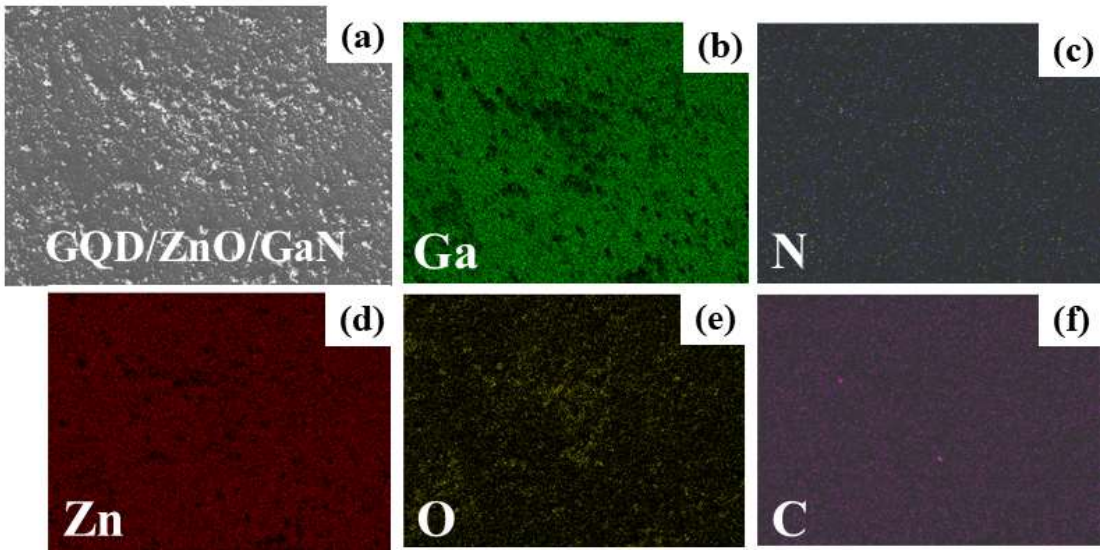

Figure 6.21: Uniform distribution of various elements involved in GQDs--ZnO/GaN heterostructure by elemental mapping technique.

The influence of GQDs sensitization on the optical states of ZnO-NR/GaN-NT heterojunction is determined by RT-PL measurement (shown in Figure 6.22 (a)). The sample display sharp and intense near band edge (NBE) emission peak of GaN at ~364 nm and a prominent shoulder peak for ZnO at ~376nm, which corresponds to their respective bandgap, *i.e.*, 3.40 eV (GaN) and 3.29eV (ZnO), respectively. [132] Moreover, an additional peaks at 425nm and 525nm stands for NBE of GQDs (deconvoluted in the inset of Figure 6.22(a)). Besides NBE, the observed peak at ~ 525 nm is also ascribed to the defect oriented yellow band emission (YBE) of ZnO (Figure 6.22(a)). [206] On addition of GQDs, a reduction in the band edge emission of ZnO followed by its defect band broadening is perceived in the PL spectra (Figure 6.22(a)) which can be attributed to the induction of GQD's optical properties, where GQDs are getting excited from 325nm UV-laser as well as NBE emission of GaN/ZnO and demonstrates its emission spectra in the range of 425nm – 625nm (shown in the inset of Figure 6.22(a)). PL spectrum of bare GQDs obtained separately (Figure 6.5(b)) at variable excitation wavelengths ranging between 325nm – 400nm also confirms the presence of corresponding emission band in the range from 425nm to 625nm.

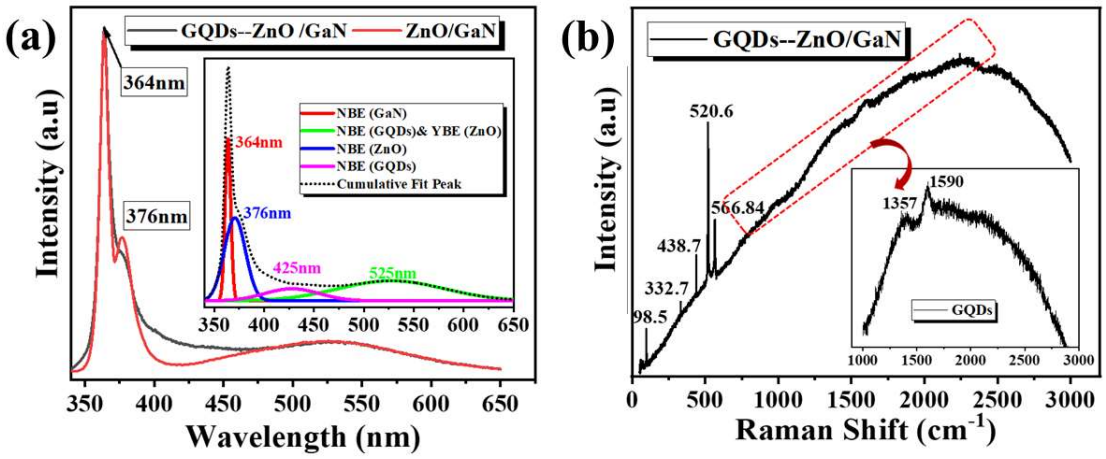

Figure 6.22: (a) RT-PL spectra of GQDs sensitized ZnO/GaN heterostructures; Inset shows the deconvoluted peaks involved in each heterostructure; (b) Raman spectra of GQDs-ZnO/GaN; inset demonstrate GQD's D and G-band.

Raman spectroscopy analysis of the grown heterostructure unveils sharp peaks positioned at 520.6 cm^{-1}, 438.7 cm^{-1} and 566.84 cm^{-1} which were attributed to Si (111) substrate, E_2 (high) mode of ZnO and GaN, respectively (Figure 6.22(b)). The presence of sharp E_2 high mode of ZnO and GaN confirms the synthesis of ZnO/GaN in wurtzite hexagonal phase. [206] Besides, two other peaks at 98.5 cm^{-1} and 332.7 cm^{-1} were also observed which were associated to ZnO E_2 (low) and E_{2H}–E_{2L} (multi-phonon), respectively. The presence of synthesized GQDs was investigated from Raman spectra shown in Figure 6.22(b), wherein the in-plane vibrations of sp^2-hybridized C-C bonds in 2D hexagonal lattice originated G band was observed at 1590 cm^{-1}. Besides, sp^3-hybridized C atoms, defects and disorder related D band was observed at 1357 cm^{-1} (shown in the inset of Figure 6.22(b)). Thus, the integrated intensity ratio (I_D/I_G = 6859/8010 of D-band to G-band peak determine the level of defect in GQD's structure. [221] The estimated value of integrated intensity ratio is found to be 0.86 for synthesised GQDs, which is in close agreement with the earlier reported values. [222]

(B) Impact of GQDs Sensitization on ZnO-NRs / GaN-NTs based UV-PDs

I. Device characteristics from GQDs sensitized ZnO-NRs / GaN-NTs heterostructure

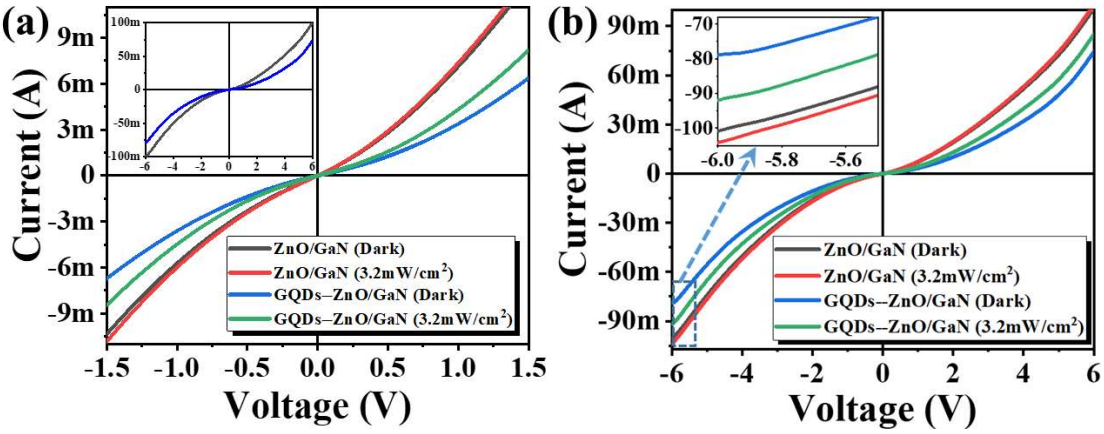

Figure 6.23: RT I-V Characteristics (a) bare and GQDs-ZnO-NR/GaN-NT UV PD at a lower bias of ± 1.5V and optical power density of 3.2mW/cm^2, inset shows the expanded I-V plot till ±6 V to observe the variation in dark current due to GQDs sensitization, (b) RT-I V of bare as well as GQDs sensitized UV PD at higher bias (±6V), inset shows the magnified data at higher bias.

The impact of GQDs sensitization on the opto-electrical characteristics of the fabricated UV PD under the photoconductive mode of operation is analyzed, wherein device exhibit a significant reduction in the dark current and enhancement in UV generated charge carriers. Figure 6.23(a) displays, RT Current-Voltage (I-V) characteristics curve of bare and GQDs decorated ZnO-NRs/GaN-NTs UV-PDs under dark and UV illumination (excitation wavelength λ=325nm, the incident optical power density, P_{opt}=3.2mW/cm^2). The observations reveal that the fabricated devices represent sublinear characteristics on either direction of the polarity with increment in photocurrent (I_{ph} = I_{Light} - I_{dark}) on increasing the applied bias voltages (Figure 6.23(a)). Further, under dark condition, the device with GQDs exhibits significantly reduced dark current I_{dark} as compared to the bare device as shown in the inset of Figure 6.23(a). The dark current values for bare and GQDs sensitized devices are found to be 97.3mA and 79mA, respectively at an applied bias of -6V. Under UV-illumination, the GQDs sensitized device demonstrates >390% enhancement in photocurrent,*i.e.* it increases from 440µA (for bare device) to 1730µA (for GQD

functionalized) at an applied bias of 1.5V. Further, the photocurrent value gradually increases as a function of applied bias and exhibits >287% enhancement (13.14mA for GQD functionalized in comparison to 4.6mA for bare device) at an applied bias of -6V (as shown in Figure 6.23(b)). The enhancement in the photocurrent of GQDs sensitized device attributed to the high density of photo generated charge carriers by directly exciting GQDs through UV-325nm illumination as well as ZnO/GaN defect band emission.

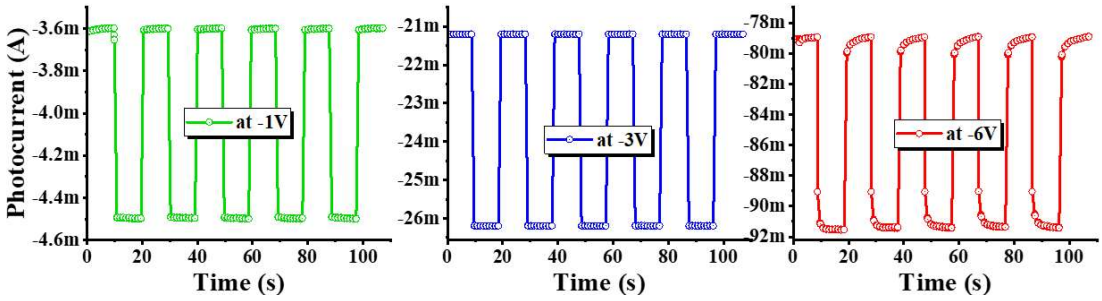

Figure 6.24: Time-correlated transient response of GQDs sensitized UV detector.

Further, the impact of GQD sensitization on time-correlated transient photoresponse of the devices has also been investigated with variable applied bias voltage (-1V to -6V) under periodical switching (10s - On/Off cycles) of UV illumination (325nm with an optical power density of 3.2mW/cm^2). The GQDs sensitized detector demonstrates a stable time-correlated transient response with the increasing trend of photocurrent values,*i.e.*, 0.9mA, 5mA and 13.14mA as compared to its bare counterpart,*i.e.*, 0.3mA, 1.25mA and 4.62mA w.r.t. applied bias of -1V, -3V and -6V, respectively (Figure6.24). Thereby, the sensitized device exhibits significant enhancement in the photocurrent due to extra charge carriers injected by GQDs as compared to its bare counterpart, as shown in Figure 6.25.

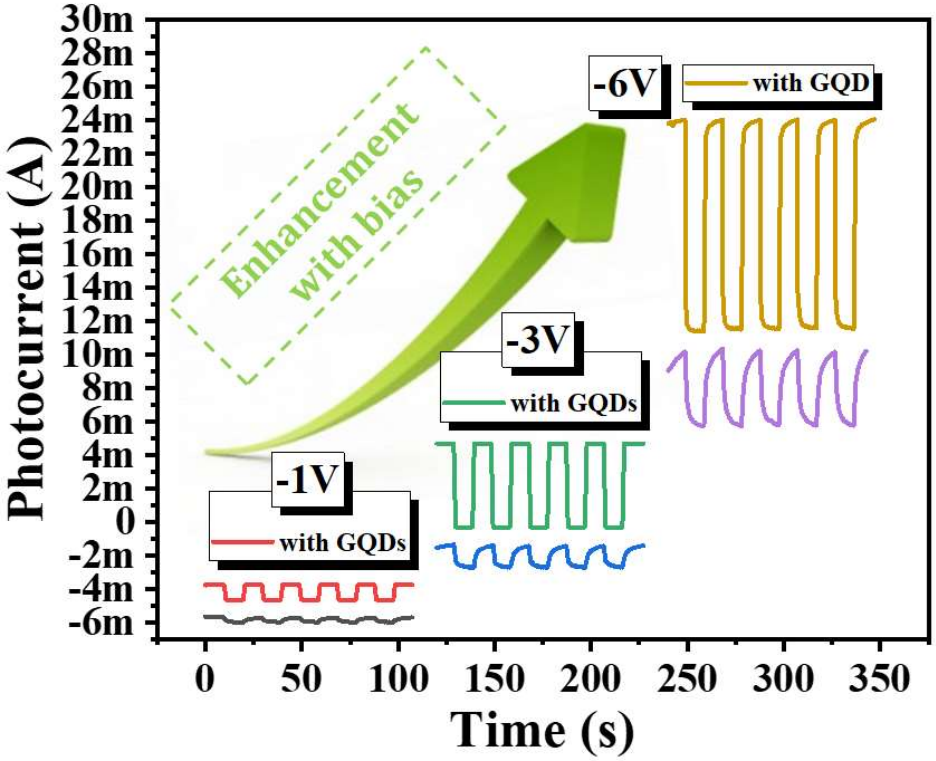

Figure 6.25: GQDs induced transient response as compared to bare UV PD at P_{opt}= 3.2mW/cm^2 and different applied bias voltages.

The time-resolved photocurrent revealed that the switching speed,*i.e.*, the response time (rise time 't_r': as measured from 10% to 90% of the final value of photocurrent) and recovery time (decay time 't_d': from 90% to 10% final value of saturated dark current) of GQDs sensitized ZnO/GaN UV-PD is faster as compared to its bare heterostructure device. Therefore, the switching speed of the GQDs sensitized detector has been evaluated by fitting the experimental data (using the equations 6.1and 6.2) of time-correlated transient photoresponse at a fixed bias voltage of -6V and 3.2mW/cm^2 optical power density (shown in Figure 6.26). The calculated rise time of GQDs sensitized UV PD was 159 ms which is 7 times faster than bare ZnO/GaN heterostructure based detector (t_r = 1.12 s) and the decay time is found to be 68.7 ms which is 17 times faster (ZnO/GaN's t_d = 1.16 s). The measured rise and decay time were estimated by multiplying time constant components (τ_r and τ_d) with a factor (2.197) as discussed. [219] The results indicate that GQDs sensitization in ZnO-NRs/GaN-NTs heterostructure has significantly improved the photocurrent generation as well as the response (rise/decay time) of the fabricated PD.

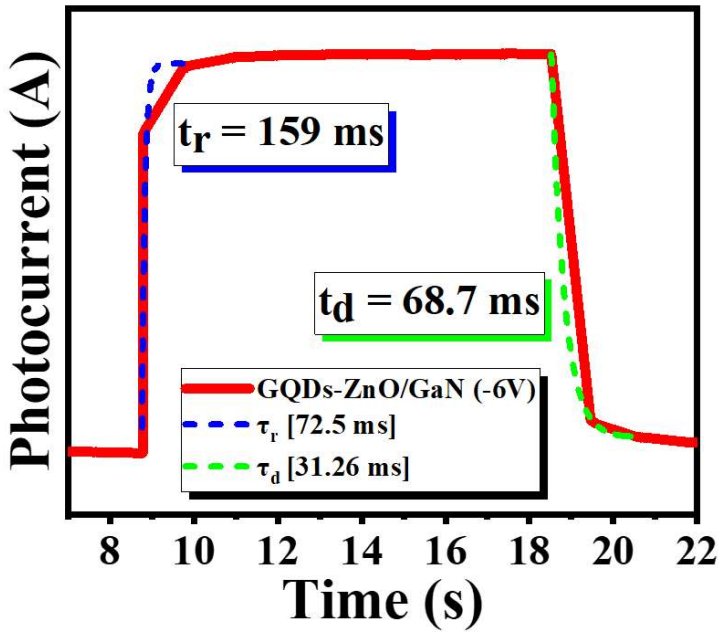

Figure 6.26: The rise and decay (response) time of bare and GQDs sensitized ZnO-NR/GaN-NT UV PD.

To understand the enhanced current transport, the measurement of transient spectra was performed at the emission wavelength of 364 nm for bare and GQDs-ZnO-NRs/GaN-NTs, as shown in Figure 6.27. The fitted experimental data (using 2nd – order exponential decay equation 6.3) yields the lifetime of τ_1 = 0.4 ns, and τ_2 = 25 ns for bare sample while, only a single lifetime, τ_1 = 0.4 ns could be fitted for GQDs sensitized sample (details of the fitting is given in Figure 6.28), where, τ_1 represents the exciton recombination in ZnO/GaN, while τ_2 correspond to the exciton captured by the surface defects. [221, 223]

$$y = y_0 + y_1 \, exp\left(-\frac{t}{\tau_1}\right) + y_2 \, exp\left(-\frac{t}{\tau_2}\right) \tag{6.3}$$

Where y is the emission intensity, y_0, y_1, y_2 are constant, t is the time. Conclusively, the carrier lifetime for the GQDs sensitized sample is distinctively shorter than bare ZnO/GaN, which consolidates that the GQDs almost eliminated the defect oriented extra lifetime and improve the activation as well as retardation time which made the device quicker to respond.

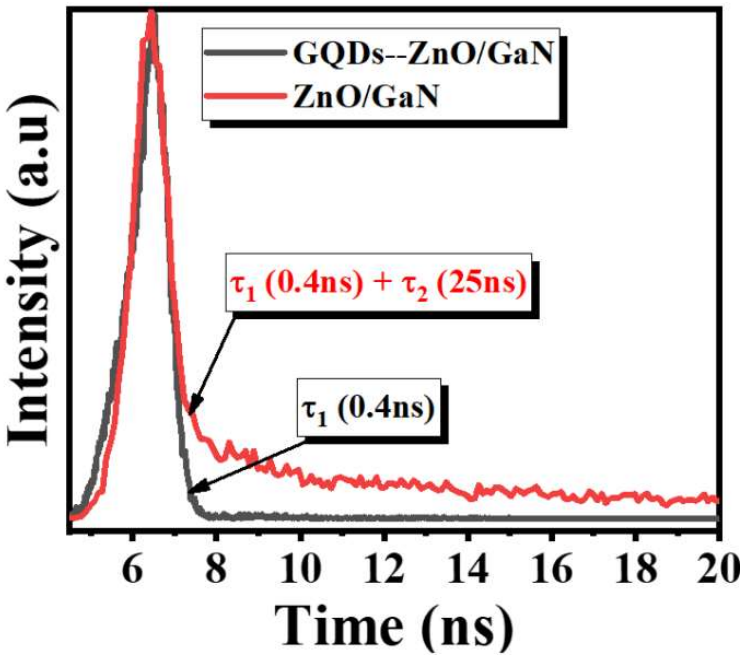

Figure 6.27: Transient spectra of bare and GQDs sensitized ZnO-NRs/GaN-NTs heterostructures.

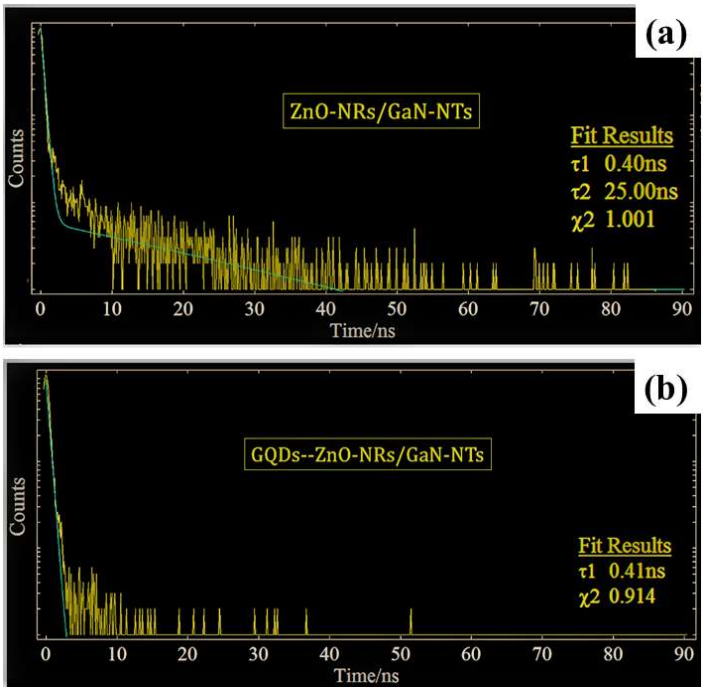

Figure 6.28: Transient spectra show the raw and fitted data of (a) bared ZnO-NRs/GaN-NTs and (b) GQDs—ZnO-NRs/GaN-NTs heterostructures, where sluggish waved signals represent the raw (experimental) data while solid lines are showing fitted data using 2-order exponential decay formula (equation 6.3).

Further, the impact of sensitization on heterojunction based device has been determined in terms of PDs performance parameters such as responsivity, detectivity,

NEP and EQE (using equation 3.8 to 3.10 and 4.1). A change in photocurrent as a function of applied bias voltage (-6V to 6V) at P_{opt} of 3.2mW/cm^2 for both bare as well as sensitized fabricated PDs is shown in Figure 6.29. The histogram demonstrates that the photocurrent achieved its maximum value and sensitized stimulated enhancement at -6V. The impact of enhanced photocurrent in case of sensitized PD is reflected in the performance parameters.

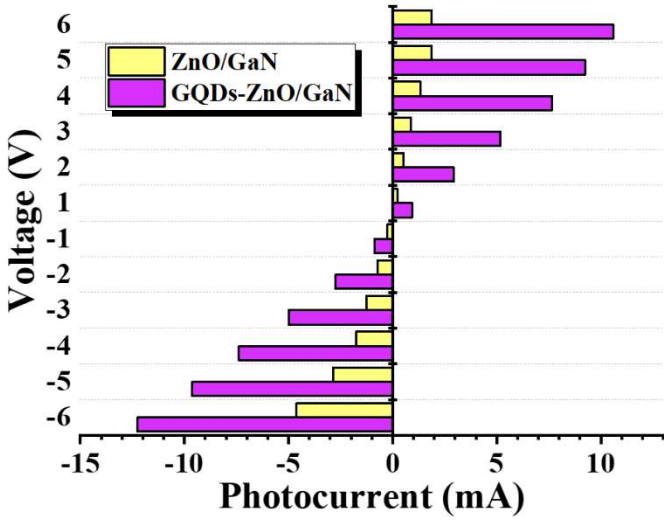

Figure 6.29: Photocurrent w.r.t. applied bias for bare and GQDs sensitized ZnO-NR /GaN-NT UV PD.

Figure 6.30 (a)demonstrates the calculated responsivity values of the fabricated devices in either polarity of the bias voltage. Thereby, in negative bias (-1V to -6V), the responsivity value increases from ~73 A/W to ~1204 A/W for bare ZnO/GaN heterojunction PD while the value of responsivity is enhanced from ~227 A/W to ~3200 A/W for GQDs sensitized detector. Similarly, the calculated responsivity value increases from ~62 A/W to ~487 A/W for bare and from ~220 A/W to ~2760 A/W for GQD sensitized device for applied positive bias (+1V to +6V). The difference in the responsivity for forward (+ve) and reverse (–ve) bias can be understood as sensitized in the reverse bias condition the width (d) of the depletion region (undoped ZnO-NRs and unintentional n-doped GaN-NTs) increases with bias which further reduced the junction's capacitance (C α 1/d). Thereby, the increased potential region with applied electric field allows faster collection of the generated carriers. Moreover, the reverse bias originated increased depletion region also assist in reducing dark current without much affecting the photocurrent. Therefore, the device performance in -ve bias

exhibits better performance as compared to +ve applied bias. It is noteworthy that the responsivity value of ~3200 A/W for GQDs sensitized ZnO/GaN heterostructure is the highest reported value and also showing ~265% higher value than bare ZnO/GaN PDs. A comparison of responsivity and other performance parameters of the GQDs sensitized detector with other available UV-detectors is tabulated in Table-6.3.

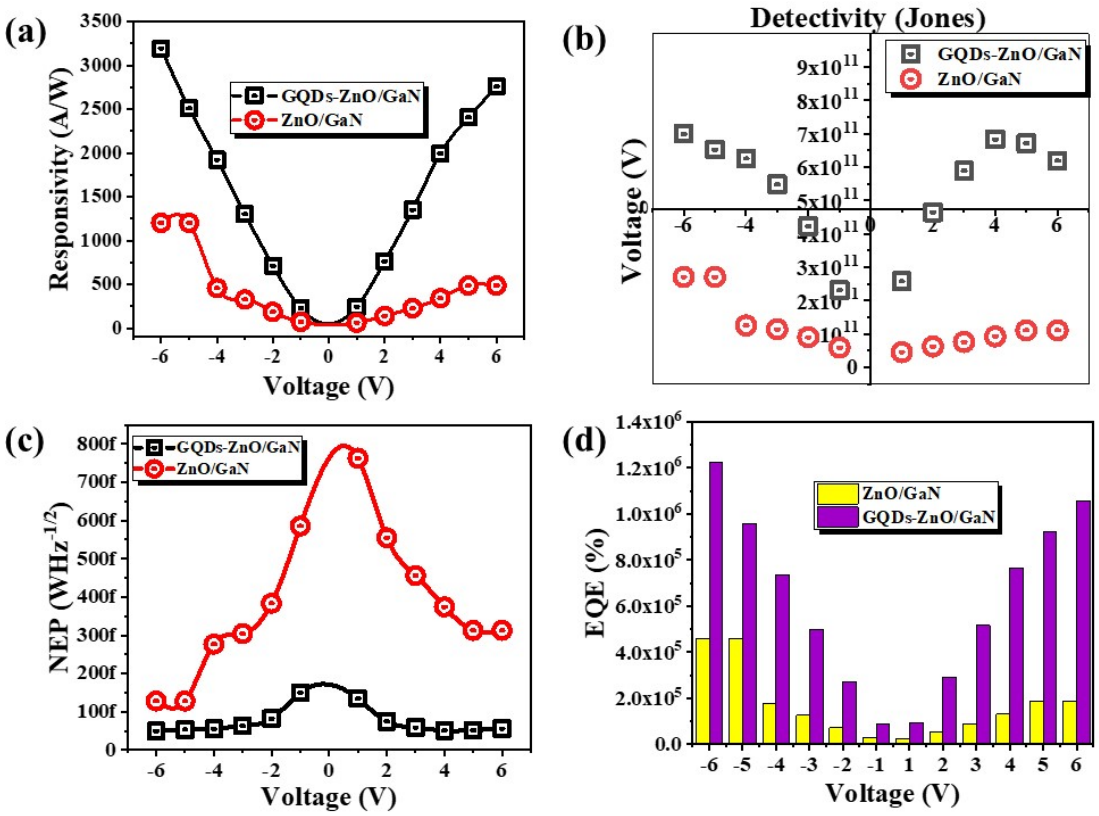

Figure 6.30: Plot of (a) Responsivity, (b) Detectivity, (c) NEP and (d) EQE w.r.t. applied bias for bare and GQDs sensitized ZnO-NR /GaN-NT UV PD.

Other performance parameters such as detectivity, NEP and EQE were also determined, where gradual increment is persisting in either direction of the applied bias, as shown in Figure 6.30 (b-d). The detector with GQDs sensitization demonstrates higher detectivity, NEP and EQE values and achieved its maximum values of 7× 10^{11} jones, 5× 10^{-14} $WHz^{-1/2}$ and 1.2×10^{6}%, respectively at an applied bias of -6V. While the bare device exhibits comparatively lower corresponding values such as 2.7× 10^{11} jones, 1.28× 10^{-13} $WHz^{-1/2}$, 4.6×10^{5}%, respectively. The calculated value of NEP attributed that, the GQDs sensitized detector having the potential to detect a signal of power as low as ~ 50 fW with a signal-to-noise ratio of one after the

one-half second of averaging. Besides, the impact of GQDs sensitization of the detector can also be realized by 1.2×10^6 % EQE, which elucidates the enhanced generation of 12000 as compared to 4600 (bare ZnO/GaN) charge carriers per absorption of photon.

Table 6.3: Comparison of performance parameters of bare ZnO/GaN and GQDs sensitized UV-PDs.

Materials	R(mA/W)	D(jones)	EQE(%)	Ref.
n-ZnO films/p-GaN	0.001	1.41×10^8	--	[33]
n-ZnO films/p-GaN	0.4	3.5×10^{10}	--	[34]
n-ZnO films/p-GaN	0.68	--	--	[35]
ZnO-NRAs/CuOCLNs/p-GaN	1.144	--	--	[36]
ZnO h-balls/p-GaN	1.44	9.47×10^{10}	--	[37]
n-ZnO films/p-GaN	1.51	1.14×10^{10}	--	[38]
n-ZnO-NRs/p-GaN	30		--	[39]
n-ZnO films/CsPbBr3/p-GaN	44.53	2.03×10^{12}	--	[38]
ZnO/GaN pn-junction	132	--	--	[44]
n-ZnO-NRs/i-ZnO/p-GaN	138.9	--	--	[40]
ZnO-NRs/Cds/p-GaN	176	--	--	[41]
ZnO h-balls/CsPbBr3/p-GaN	230.94	2.4×10^{13}	--	[37]
n-ZnO NRs/i-MgO/p-GaN	320	8.0×10^{12}	--	[39]
n-ZnO-NRs/p-GaN	1.1×10^4	--	--	[42]
i-ZnO/n-ZnO/p-GaN	4.37×10^5	--	1.6×10^3	[43]
ZnO-NRs/GaN-NTs	**1.2×10^6**	**2.7×10^{11}**	**4.6×10^5**	**This work**
GQDs/ZnO-NRs/PEDOT:PSS	3.6×10^4	1.3×10^{12}	1.3×10^4	[224]
NGQDs/ ZnO-NRs/PEDOT:PSS	1.6×10^5	8.7×10^{12}	5.7×10^4	[70]
NGQDs/ ZnO-NRs/DMSO-PEDOT:PSS	2.5×10^5	2.4×10^{11}	9.0×10^4	[225]
GQDs/ZnO-NRs Array	$\sim1\times10^3$	--	--	[226]
GQDs/ZnO-NRs/GaN	34	1.15×10^{12}	--	[65]
GQDs/ZnO-NRs/GaN-NTs	**3.2×10^6**	**7.0×10^{11}**	**1.2×10^6**	**This work**

II. Opto-Electrical Transport Enhancement Mechanism

To understand the opto-electrical transport mechanism of fabricated GQDs-ZnO/GaN heterojunction based UV-PD under thermal equilibrium, a scheme is proposed, and a related energy band diagram is described in Figure 6.31. An electron injection barrier (~0.8eV) is created due to the difference in the work function of Au-contact (~5.1eV) as compared to the electron affinity ($q\chi$) of ZnO/GaN (~4.3eV) [211], which helps in the channelization of existing charge carriers even under dark condition. It is reported that the surface of ZnO-NRs has the tendency to absorb oxygen molecules from its surroundings. [211] These oxygen molecule's negatively charge oxygen ions capture the available free electrons on the ZnO surface, which reduces the overall electrical conductivity of the device (ZnO/GaN). After UV illumination, the generated electron-hole pair [$h\nu \rightarrow h^+ + e^-$] increases the density of free electrons, which further enhanced the electrical conductivity of the device. Besides, the incident UV-photons and ZnO-NRs originated holes recombined [$h^+ + O_2^- \rightarrow O_2$] with few ZnO-NRs oxygens trapped electrons and release energy. This energy played a significant role in electronic transport by discharging the negatively charge oxygen ions. [211] From here, due to neutralizing the oxygen ions, the remaining trapped electrons are getting released and increase the density of the mainstream flow of electrons (electrons generated by ZnO as wellas GaN) as shown in Figure 6.31(a). Thereby, under the UV illumination, the cumulatively generated charge carriers by ZnO-NRs as well as GaN-NTs were drifted with the variable applied electric field as shown in Figure 6.31(a). However, the photoresponse mechanism of ZnO-NR/GaN-NT UV-PD found to be similar with GQDs sensitized detector except more flow of electron due to GQDs involvement as shown in Figure 6.31(b). Figure 6.31(c, d) demonstrates the energy band diagram of GQDs-ZnO/GaN heterojunction by using Anderson model. [214, 215] When the heterojunction between ZnO-NR and GaN-NT is formed a charge depletion region is created at the hetero-interface. Accordingly, the generated electrons drift into the ZnO, and respective holes are accelerated towards GaN (shown in Figure 6.31(c)). Besides that, the sensitization material,*i.e.*, GQD's conduction band (3.5~3.7eV) and valence band (5.1~5.4eV) with respect to the vacuum level have been realized to estimate its bandgap up to ~1.5eV. [227, 228] Hence, it will be well understood that the location of GQD's conduction band is higher than GaN's as well as ZnO's

conduction band. This variation in band level of GQDs, GaN, and ZnO, allows band bending near the interface accordingly, as shown in the band diagram (Figure 6.31(d)). Subsequently, when the GQDs-ZnO/GaN heterostructure is UV-illuminated, the transportation of photo-generated electrons took place from higher to lower concentration,*i.e.* from GQDs to ZnO/GaN. [64, 226] Moreover, the band diagram schematic also illustrates that, as compared to majority carriers (electrons), the holes in the valence band of both the semiconductors are very low due to their (holes) involvement in recombination with trapped electrons of oxygen ions.

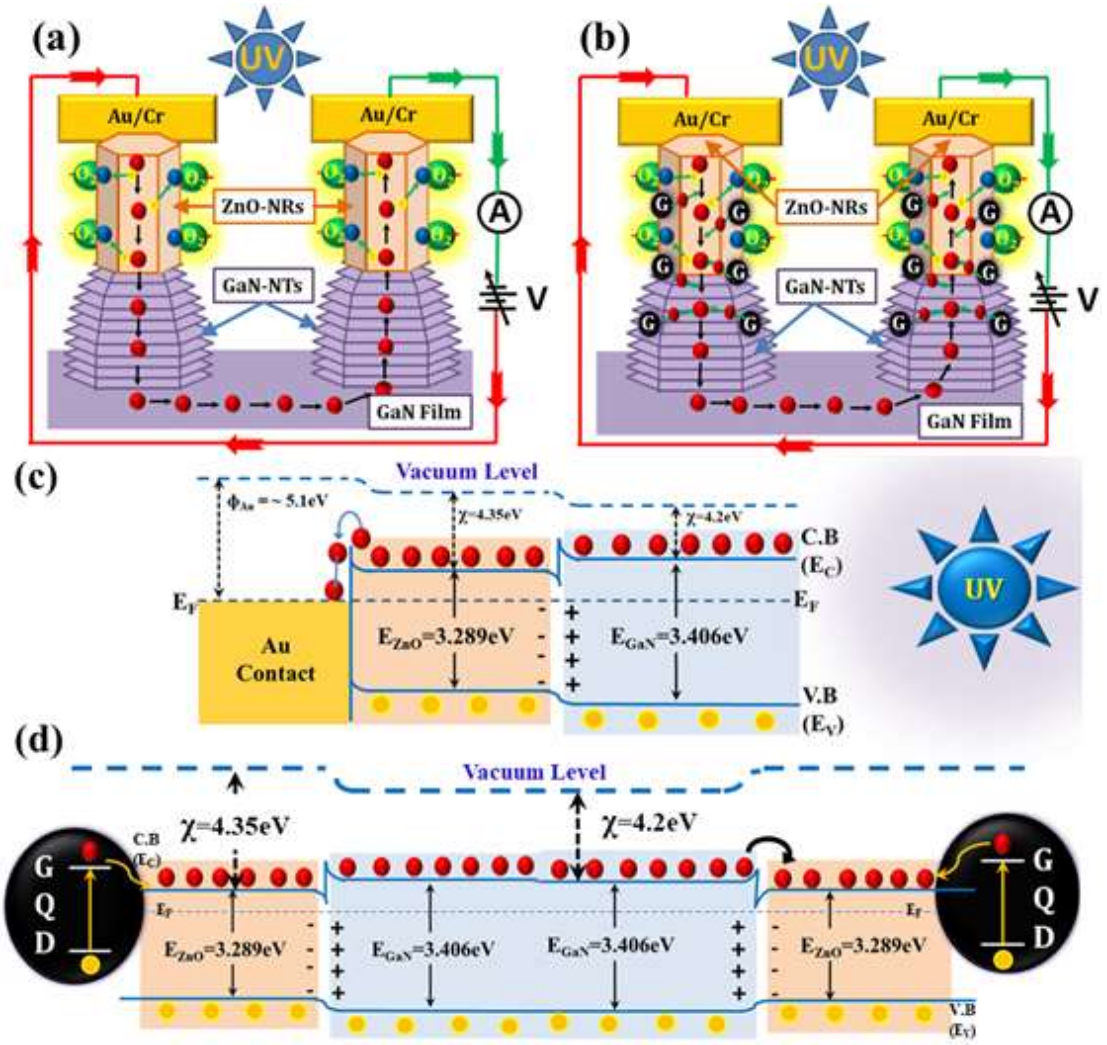

Figure 6.31: (a, b) Schematic band diagrams of the bare and GQDs sensitized UV photodetector illustrating the charge transport, (c, d) Energy band diagram demonstrating the opto-electrical transport of the bare ZnO/GaN and GQDs sensitized UV photodetector.

Thus, under UV illumination, the higher roughness, lower stress - strain and lower optical defects with high surface to volume ratio oriented unique geometry novel GaN-NTs with ZnO-NRs (under UV illumination, the negatively charged electron trapper oxygen ions get neutralized) capable to establish efficient opto-electrical transport due to majority carriers (electrons). Furthermore, the performance of the fabricated PD with efficient opto-electrical transport has been further accelerated by GQDs injected extra charge carriers [generated by directly excited UV 325 nm (as shown in Figure 6.5(b)) and ZnO-NRs defect band range from 380 nm to 475 nm (shown in Figure 6.22 (a))] to the existing mainstream flow of electrons (enhanced photocurrent) and their quick collection at the electrodes due tohighly conductive nature of GQDs.

Besides, to understand the current trajectory through various semiconductor interfaces (*i.e.*, ZnO/GaN, GQD/GaN and GQDs/ZnO/GaN) inside the fabricated photodetectors has been realized with the help of Figure6.32 and 6.33. As per the top view FESEM image of as-grown bare ZnO-NRs/GaN-NTs heterostructure and GQDs sensitized ZnO-NRs /GaN-NTs (Figure6.19 (c and d)), the GaN-NTs, ZnO-NRs as well as GQDs were simultaneously available and directly exposed to the deposited Au/Cr metal contacts. Therefore, as far as opto-electrical transport of the fabricated photodetector devices is concerned, there are multiple parallel current conduction channels offered by multiple interfaces (ZnO/GaN, GQDs/GaN and GQDs/ZnO/GaN) were available to summarised the photocurrent of both the devices such as I_A and I_B. As per the schematic diagram shown in Figure 6.32 (a,b), the flow of current in the device can be well understood, wherein, the bare ZnO/GaN heterojunction based UV photodetector's photocurrent (I_A) found to be lesser as compared to GQDs sensitization injected extra charge carrier enhanced photocurrent (I_B).

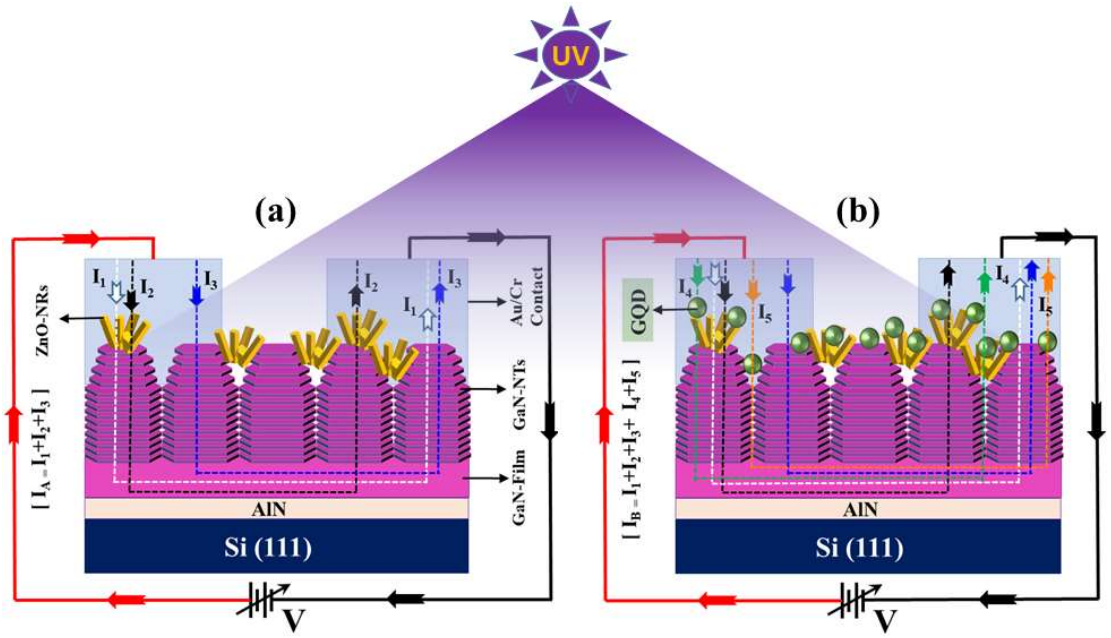

Figure 6.32: Schematic diagram of opto-electrical transport taken place in fabricated (a) bare ZnO/GaN and (b) GQDs sensitized UV photodetectors.

Moreover, another schematic (Figure 6.33) has been visualized to understand the circuitry involved to deliver the photocurrent. Thereby, parallel and series combination of optically sensitive resistance offered by the various semiconductors and their heterojunctions is represented in the best possible way. Besides, the role of the AlN buffer layer in optoelectronic transport is limited to eliminate leakage current due to the higher bandgap of ~6.2 eV.

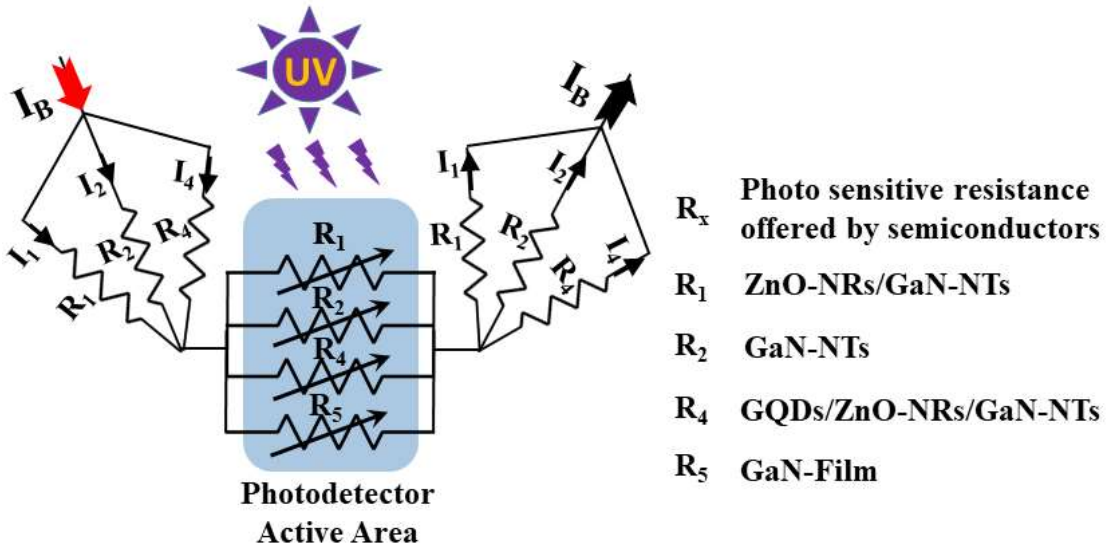

Figure 6.33: Schematics of circuitry involved to deliver the photocurrent.

In addition, the sensitivity of the fabricated GQDs sensitized UV photodetector has also been investigated at a range (from UV to Vis) of wavelengths, as shown in Figure 6.34. The obtained spectral response not only demonstrates excellent UV-Vis rejection ratio but also widen its detection range from UV to Vis due to GQDs incorporation. Therefore, it is noteworthy that, the GQD's involvement not only increase the sensitivity of the fabricated detector but also broaden its detection limit. Moreover, the sensitivity of the fabricated detector specifically in the UV range is also analysed, wherein highest sensitivity is found to be in UV-A (320 nm – 400 nm) region as compared to other [UV-B (280 nm – 320nm) and C (200 nm – 280 nm)].

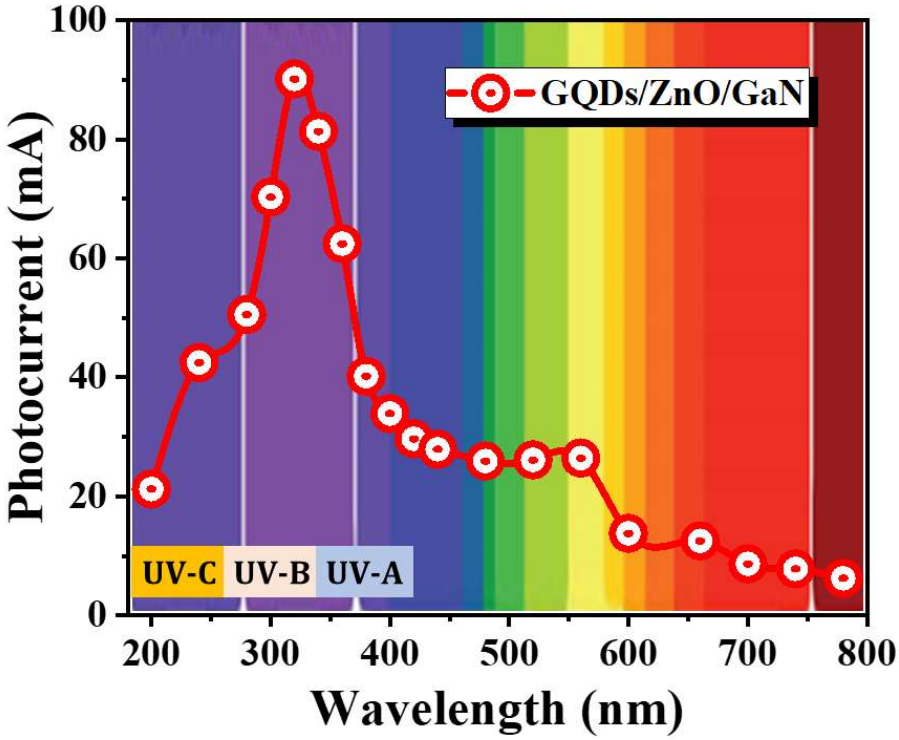

Figure 6.34: Spectral response of the GQDs sensitized ZnO/GaNbased broadband UV photodetector.

6.5 Summary

In summary, we have functionalized the as-grown [sample S2 (with thicker AlN buffer layer and higher GaN-NTs)] vertically-aligned, wurtzite structured, hexagonal shaped, layer by layer stacked crystal, and closely-packed tapered ended unique GaN-Nanotowers geometry-based high-performance UV PD by chemically synthesized hexagonal-shaped ZnO-nanorods. This is the first report where the nanostructures of GaN, as well as ZnO, were effectively utilized for fabricating a UV detection device.

The cumulative advantages of high surface-to-volume ratio, higher light absorption, and the combined contribution of their photocurrents have been discussed. Further, the detailed mechanism for enhancement in the device performance is explained using schematic energy band diagrams. Under the photoconductive mode of operation, the ZnO nanorods equipped GaN-Nanotower based device exhibited augmented responsivity of the detector from 484.77 A/W (bare GaN-NTs) to 1204 A/W (ZnO-NRs/GaN-NTs) at -6V and incident optical power density of 3.2 mW/cm^2. Moreover, the novelty of the study is str*etc*hed to another level by coupling the heterojunction device with Au nanoparticles. The nanoplasmonics induced resonant hot electrons to increase the light-matter interaction, which resulted in enhanced responsivity value from 1204 A/W (ZnO-NRs/GaN-NTs) to the gigantic value of 7042 A/W (Au-NPs/ZnO-NRs/GaN-NTs). Consequently, the fabricated novel detection device structure demonstrated very high external quantum efficiency (2.7×10^6 %) and estimated capability to detect a signal of power as low as ~ 0.18 fW. Furthermore, the study also demonstrated the impact of the sensitization of chemically synthesized novel graphene quantum dots (GQDs) on ZnO-NRs/ GaN-NTs heterostructure based UV PD. The analysis exhibits the remarkable enhancement in the performance of the fabricated UV PD by introducing GQD's electrical as well as optical properties. Thereby, the efficient immobilization of GQDs on ZnO as well as on GaN works as the incident UV light absorbers and electron-holes generator (as observed by excitation wavelength-dependent RT-photoluminescence emission spectrum of bare GQDs). These GQDs injected extra carriers overall increases the existing ZnO/GaN channelized mainstream flow of electrons. The sensitization of ZnO/GaN heterostructure by GQDs decoration also leads to appropriate energy band alignment for better electrical transport. Thus, the formulated GQDs—ZnO-NRs/GaN-NTs MSM UV PD demonstrated as device of advantages, wherein the impression of GQDs has been reflected as enhanced performance UV PD, such as highest responsivity (3200A/W) and very high external quantum efficiency (1.2×10^6 %). Moreover, the calculated very low noise equivalent power (5×10^{-14} $WHz^{-1/2}$) also displays the capability of the fabricated detector to detect a signal of power as low as ~50femtowatt. Herein, the studies in this chapter provide a new perspective towards energy-efficient, tunable broadband opto-electrical device fabrication by utilizing the cumulative, synergistic effect of Au-NP's nanoplasmonics, GQD's capability of sensitization, and compatible ZnO/GaN-based materials heterojunction.

7.1 Conclusion

A systematic study on the growth of III-Nitride semiconductor's nanostructures and their implementation in the fabrication of energy-efficient ultraviolet PD has been presented in this thesis. The study concludes the growth of ultra-thin (~30 nm) GaN-nanoisland to high surface to volume ratio oriented (~4 μm) GaN-nanotowers on Si (111) substrates via PAMBE system. These low as well as high aspect ratio oriented GaN nanostructures were proficiently utilized for the efficient photosensing at photovoltaic as well as photoconductive mode of operation. Moreover, it is also important to note that the novelty of the study,*i.e.*, augmentation of fabricated (GaN-based) PD performance, is accelerated by the synergetic impact of compatible ZnO/GaN heterojunction, unique geometry (nanostructure over nanostructure model), metal nanoparticles LSPR stimulated hot resonant stream of electrons and GQDs sensitization. The major conclusions made from the thesis are presented below, in brief:

- Initially, the epitaxial growth of self-assembled GaN-NIs on Si (111) substrate with an intermediate inhomogeneous layer of Si_3N_4 has been performed via the PAMBE system. The localized compressive strains fields due to bond length variation between Si-Si and Si-N, are relaxed by inhomogeneously oriented, low dimension GaN-NIs with high distribution density (2×10^{10} cm^{-2}) and average surface roughness of 5.80 nm. These tiny dimensional nano-island shaped lower stress and strain facilitated GaN-NIs of just ~30nm height and 50nm diameter showing its dominance to detect the UV rays in MSM structure format as compared to conventionally available 100's of micron thin-film based detector. The non-homogeneous GaN NS and Au contacts material offered asymmetric interfaces leading to distinctive SBHs revealing self-powered operation of the device under photovoltaic mode. Thereby, at 0V, such low dimension ultra-thin GaN-NIs confirmed their potency as UV PD, which exhibited a detectivity, responsivity, and noise equivalent power of 2.34×10^{9} jones, 1.76 mA/W and 3.52×10^{-11} $WHz^{-1/2}$, respectively. Also, the time-correlated transient response of the device revealed a rapid switching speed as the quick rise time constant of 18 ms. Besides, the performance of the fabricated detector is also meticulously investigated at the photoconductive mode of operation with the power-

dependent study, wherein an increment in photocurrent is recorded. This increasing trend of photocurrent is further reflected as increased PD performance parameters such as responsivity (1.76 to 40.2 mA/W) and maximum achieved detectivity (5.3×10^{10} Jones), where a 23 fold and ~1000 fold increment was observed, respectively. Thus, this section of the thesis revealed a new area of research where, unlike the conventional approach of high aspect ratio,*i.e.*, nanorods, nanoribbons, nanobelts, nanopillar, nanotower, and nanoflower structures based PD, very thin layered GaN UV PD found advantageous with ease of fabrication included very low material and processing time. As far as real applications are concerned and the retrieved sensing data from the fabricated detector, the proposed detector found useful for all possible practical applications.

- In the next phase of work, the study corroborates a significant impact of chemically synthesized, monodispersed Au-NPs (~10nm) on the performance of GaN-NIs based UV PD with reduced active area geometry. Thereby, the already fabricated ultra-thin GaN-NIs PD with Au-NPs prominently respond towards UV in both photovoltaic (self-powered) as well as photoconductive mode of operation and display fast and stable time-correlated transient photoresponse with significant enhancement in the performance parameters. The enhanced performance of the fabricated devices is due to nanoplasmonics induced LSPR stimulated stream of hot resonant carriers. Moreover, the electronic transport properties affirmed the influence of Au-NPs in lowering the ideality factor and SBH at the Au/GaN interfaces due to which channel resistance of the fabricated detector is reduced. These distinctive barrier heights stimulated self-powered UV PDs have been shown fast switching speed (response time 40 ms), maximum enhanced responsivity [(~151mA/W) → (~216mA/W), detectivity (7.1×10^{8} jones → 1.2×10^{9} jones), quantum efficiency (58.7% → 82.4%) and reduced NEP [(7.7×10^{-11} $WHz^{-1/2}$)→ (4.5×10^{-11} $WHz^{-1/2}$)] as compared to its bare counterpart. Thus, this section of the thesis provides a new insight understanding, where (firstly reported) the decoration of low dimensional chemically originated Au-NP's nanoplasmonics behaviour on GaN-NIs act as a

detection enhancer with fast recovery time paves the way towards the realization of energy-efficient optoelectronic device applications.

- In this phase of the work, unlike low dimension GaN-NSs based UV PDs, the study has been progressed to the next level of having a higher surface to volume ratio oriented GaN-NSs based UV PDs. Thereby, a unique tapered ended-nanotower morphology of epitaxially grown hexagonal stacked nanocolumnar GaN structures with different heights and different AlN buffer layers thickness were utilized to fabricate high-performance UV-PDs operable in photovoltaic as well as a photoconductive mode of operation. The study also illustrates that the performance of fabricated PD devices majorly depends upon the AlN buffer layer thickness and GaN-NTs heights. Thus, the fabricated UV PD with lesser AlN thickness and GaN-NTs demonstrates significantly enhanced performance parameters particularly at lower bias, including a very high I_{Light} /I_{Dark} ratio (>10^4) along with high responsivity of 35.4 A/W at -3V and 2.57 A/W at 0V. Moreover, the device displays high EQE ~10^4 % and lower NEP (~10^{-13} $WHz^{-1/2}$), which elucidates the detection of a signal as low as ~0.19 pW. Besides, particularly at the photovoltaic mode of operation, the time-correlated transient response of the detector demonstrated very high switching speed (~0.433 ms). On the other side, the UV-PD with thicker AlN buffer layer and higher GaN-NTs height display the highest ever reported responsivity value of 484.77 A/W, EQE ~10^5 %, and very low NEP (~10^{-13} $WHz^{-1/2}$) at a fixed bias voltage of -6V, which elucidates the detection of a signal as low as ~0.17 pico watt. The spectral selectivity of the device demonstrates a noteworthy UV to visible rejection ratio. The low dimensionality of the device with high bias operation for fast transit of charge carriers can be effectively utilized for future nano-optoelectronic devices.

- In the final phase of the work, the study meticulously emphasized three aspects to enhance the existing III-Nitride based UV detection technology such as hybridization, functionalization, and sensitization. Initially, for the execution of these three state of the art detection enhancer tools, the as-grown (higher thickness AlN buffer layer and longer GaN-NTs sample) vertically-aligned,

wurtzite structured, hexagonal shaped, layer by layer stacked nanocrystal, and tapered ended unique GaN-Nanotowers geometry-based high-performance UV PD has been hybridized by chemically synthesised hexagonal-shaped ZnO-nanorods. This is the first report where the nanostructures of GaN, as well as ZnO, were effectively utilized for fabricating a UV detection device. The cumulative advantages of high surface-to-volume ratio, higher light absorption, and the combined contribution of their photocurrents have been discussed. Further, the detailed mechanism for enhancement in the device performance is explained using schematic energy band diagrams. Under the photoconductive mode of operation, the ZnO nanorods equipped GaN-Nanotower based device exhibited augmented responsivity of the detector from 484.77 A/W (bare GaN-NTs) to 1204 A/W (ZnO-NRs/GaN-NTs) at -6V and incident optical power density of 3.2 mW/cm^2. Afterwards, the novelty of the study is str*etc*hed to another level by coupling the heterojunction device with Au nanoparticles. The nanoplasmonics induced resonant hot electrons increase the light-matter interaction, which resulted in enhanced responsivity value from 1204 A/W (ZnO-NRs/GaN-NTs) to the gigantic value of 7042 A/W (Au-NPs/ZnO-NRs/GaN-NTs). Consequently, the fabricated novel detection device structure demonstrated very high external quantum efficiency (2.7×10^6 %) and estimated capability to detect a signal of power as low as ~ 0.18 femto watt. Furthermore, the study also demonstrated the impact of the sensitization of chemically synthesized novel graphene quantum dots (GQDs) on ZnO-NRs/ GaN-NTs heterostructure based UV PD. The analysis exhibits the remarkable enhancement in the performance of the fabricated UV PD by introducing GQD's electrical as well as optical properties. Thereby, the efficient immobilization of GQDs on ZnO as well as on GaN works as the incident UV light absorbers and electron-holes generator (as observed by excitation wavelength-dependent RT-photoluminescence emission spectrum of bare GQDs). These GQDs injected extra carriers overall increases the existing ZnO/GaN channelized mainstream flow of electrons. The sensitization of ZnO/GaN heterostructure by GQDs decoration also leads to appropriate energy band alignment for better electrical transport. Thus, the formulated GQDs—ZnO-NRs/GaN-NTs MSM UV PD

demonstrated as device of advantages, wherein the impression of GQDs has been reflected as enhanced performance UV PD, such as highest responsivity (3200A/W) and very high external quantum efficiency (1.2×10^6 %). Moreover, the calculated very low noise equivalent power (5×10^{-14} $WHz^{-1/2}$) also displays the capability of the fabricated detector to detect a signal of power as low as ~50fW. Conclusively, this portion of the thesis provides a new perspective towards energy-efficient, tunable broad-band opto-electrical device fabrication by utilizing the cumulative synergistic effect of Au-NP's nanoplasmonics, GQD's capability of sensitization, and compatible ZnO/GaN-based materials.

❖ Figure 7.1 demonstrate augmented responsivity values achieved at a glance throughout the thesis work.

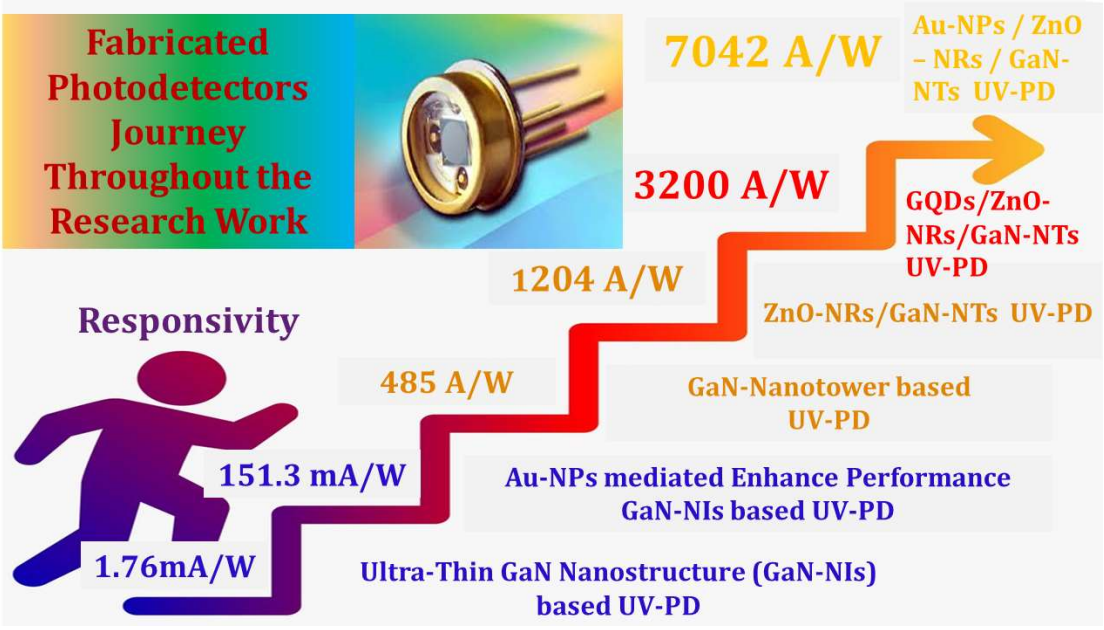

Figure 7.1: Fabricated photodetectors showing increasing trend of achieved Responsivity at a glance.

7.2 Scope of Future Work

As per the famous quote, "the biggest room in the world is the room for improvement," therefore the scope of future work projecting the scope of improvement in the existing PD's technology for the next generation smart sensors development. Currently, III-Nitride nanostructures are interestingly becoming the

smart choice for efficient optoelectronic devices fabrication. Primarily, as far as efficient photodetection is concerned, all the performance parameters are derived on the basis of dark device current as well as photocurrent level. The detection ability of a PD is governed by the dark or leakage current. The importance of dark current can be well understood by the fact that the dark current in a device leads to thermionic emission, heat generation and reduce the signal to noise ratio, which not only degrades the detection capability but also reduce the PD lifetime. Therefore, reduction in dark current is the prime objective as well as a never-ending challenge in front of the researchers. For this, till now, numerous attempts have been made to lowering the dark current, reduces the noise level, and improves the sensitivity of the devices, thereby enabling effective detection of low power optical signals. In the case of III-Nitride based PDs, the detectivity is restricted by the existence of structural defects in the hetero-epitaxially grown layers, particularly high screw components of threading dislocation density, which act as a conduction path for reverse leakage currents. As the work presented in this study provide solutions for growing the high quality low and high surface to volume ratio oriented GaN nanostructures and enhancing the performance from a photodetection device. In the present scenario, some of the major extensions of the work carried out in this study towards developing next-generation optoelectronic devices are suggested below:

- The crystallinity of epitaxial nitride nanostructures can be achieved by growing the GaN thicker films on the various lesser lattice-mismatched substrate like sapphire, GaN epilayer, thicker AlN buffer layer, and SiC,*etc*. These epitaxially grown highly crystalline thicker GaN films can be further converted to desire nanostructures by using a different patterned *etc*hing process such as chemical *etc*hing, laser *etc*hing, and lithography,*etc*. Also, by employing thicker and highly crystalline nanostructures, the structural defects can be minimized, whose impact can be realized in future work as enabling the detection of low power optical signals by means of reduced dark current. On the other side, due to the formation of well-aligned, desired shaped, high density, and higher surface to volume ratio based nanostructures provide more photon absorption active sites, which lead to more photo generated charge carriers.

- A detailed study of the gain mechanism, which has been widely observed in GaN-based Schottky and MSM PDs, will be an interesting topic to be explored. Thereby, two different metal contacts can be used to develop a difference in the ideality factor followed by variation in SBHs, which leads to generating inbuilt potential difference. This inbuilt potential difference not only works as the extra potential to drag the generated charge carriers at the photoconductive mode of operation but also provides the photovoltaic (self-powered) capability to the PD.

- Implementing electrode engineering as a scrutinized solution towards the enhancement of the sensitivity of fabricated detectors. The electrode engineering deals with a reduction in the effective active area by reducing space between the electrodes, reduce channel length, the realization of low resistance contacts, and effective charge collection.

- Narrowing and broadening of photodetection range by fabricating from dedicated solar blind to multipurpose broadband UV PDs. For this, alteration at the PDs fabrication level can be accomplished by incorporating ternary alloy by controlling the Al content in the AlGaN based heterostructures. Besides, various similar domain and III-Nitride compatible semiconductors such as ZnO/GaN, TiO_2/GaN, and SnO_2/GaN NS based heterojunctions can be opened new scope for more efficient and advanced photodetection devices.

- The functionality and performance of the existing III-Nitride UV PDs can be increased by the integration with nanoplasmonic effect and non-plasmonic effect. The nanoplasmonic effect can be produced by metal NPs (Au, Ag, Al, and Pt), which contribute UV photon excited extra hot resonant electron to the existing mother structured (GaN) electron channel. Unlike metal NPs, an interesting approach of the non-plasmonics effect to develop the enhanced performance next-generation UV PDs can be adopted. For this, quantum dots (CdS, CdSe, PbS, CdTe and GQDs,*etc*.) and semiconductor NPs (ZnO-NPs, TiO_2-NPs, and SnO_2-NPs) can be explored as the integrating, sensitizing as well as detection enhancing agent for GaN-based UV PDs. Moreover, 2D nanomaterials such as $MoSe_2$, WSe_2, and MoS_2,*etc*. can also be explored for boosting futuristic photodetection technology.

UV PDs reserve their utmost place in the ubiquitous class of technology due to its applicability in a wide range of applications such as environmental monitoring, space to space secure communication, military applications, flame detection, and medical diagnostics,*etc*. Therefore to understand the critical applicability and big UV PDs market size, the quality of the product is a matter of serious concern. Henceforth, III-Nitride semiconductors as recognized as fabrication materials for next-generation UV PDs. The GaN material is chemically and mechanically stable, having direct bandgap, high thermal conductivity, high mobility as well as high thermal stability. Thus, the III-Nitride energy-efficient PD technology has a long history, interesting present, and exciting future to reveals new materials integration ability, new dimensions, a new approach, next threshold level of performance parameters, and phenomenal capability.

REFERENCES

[1] B. L. Diffey, "Sources and measurement of ultraviolet radiation," *Methods,* vol. 28, pp. 4-13, 2002.

[2] J. Kolnik, İ. H. Oğuzman, K. F. Brennan, R. Wang, P. P. Ruden, and Y. Wang, "Electronic transport studies of bulk zincblende and wurtzite phases of GaN based on an ensemble Monte Carlo calculation including a full zone band structure," *Journal of Applied Physics,* vol. 78, pp. 1033-1038, 1995.

[3] P. Dennis, *Photodetectors: an introduction to current technology*: Springer Science and Business Media, 2012.

[4] M. Brendel, M. Helbling, A. Knigge, F. Brunner, and M. Weyers, "Solar-blind AlGaN MSM photodetectors with 24% external quantum efficiency at 0 V," *Electronics Letters,* vol. 51, pp. 1598-1600, 2015.

[5] M. Razeghi and A. Rogalski, "Semiconductor ultraviolet detectors," *Journal of Applied Physics,* vol. 79, pp. 7433-7473, 1996.

[6] R. Korde and J. Geist, "Quantum efficiency stability of silicon photodiodes," *Applied Optics,* vol. 26, pp. 5284-5290, 1987.

[7] M. Caria, L. Barberini, S. Cadeddu, A. Giannattasio, A. Lai, A. Rusani, and A. Sesselego, "Far UV responsivity of commercial silicon photodetectors," *Nuclear Instruments and Methods in Physics Research Section A: Accelerators, Spectrometers, Detectors and Associated Equipment,* vol. 466, pp. 115-118, 2001.

[8] L. Liu and J. H. Edgar, "Substrates for gallium nitride epitaxy," *Materials Science and Engineering: R: Reports,* vol. 37, pp. 61-127, 2002.

[9] S. Jain, M. Willander, J. Narayan, and R. V. Overstraeten, "III–nitrides: Growth, characterization, and properties," *Journal of Applied Physics,* vol. 87, pp. 965-1006, 2000.

[10] Y. Nanishi, Y. Saito, and T. Yamaguchi, "RF-molecular beam epitaxy growth and properties of InN and related alloys," *Japanese journal of applied physics,* vol. 42, p. 2549, 2003.

[11] J. Wu, W. Walukiewicz, K. Yu, J. Ager Iii, E. Haller, H. Lu, W. J. Schaff, Y. Saito, and Y. Nanishi, "Unusual properties of the fundamental band gap of InN," *Applied Physics Letters,* vol. 80, pp. 3967-3969, 2002.

[12] J. Pankove and J. Berkeyheiser, "Properties of Zn-doped GaN. II. Photoconductivity," *Journal of Applied Physics,* vol. 45, pp. 3892-3895, 1974.

[13] M. A. Khan, J. Kuznia, D. Olson, J. Van Hove, M. Blasingame, and L. Reitz, "High-responsivity photoconductive ultraviolet sensors based on insulating single-crystal GaN epilayers," *Applied Physics Letters,* vol. 60, pp. 2917-2919, 1992.

[14] N. Aggarwal and G. Gupta, "Enlightening Gallium Nitride based UV Photodetectors," *Journal of Materials Chemistry C,* 2020.

[15] A. Gundimeda, S. Krishna, N. Aggarwal, A. Sharma, N. D. Sharma, K. Maurya, S. Husale, and G. Gupta, "Fabrication of non-polar GaN based highly responsive and fast UV photodetector," *Applied Physics Letters,* vol. 110, p. 103507, 2017.

[16] F. Qian, H. Wang, Y. Ling, G. Wang, M. P. Thelen, and Y. Li, "Photoenhanced electrochemical interaction between Shewanella and a hematite nanowire photoanode," *Nano letters,* vol. 14, pp. 3688-3693, 2014.

[17] P. Tchoulfian, F. Donatini, F. Levy, A. Dussaigne, P. Ferret, and J. Pernot, "Direct imaging of p–n junction in core–shell GaN wires," *Nano letters,* vol. 14, pp. 3491-3498, 2014.

[18] B. Deka Boruah and A. Misra, "Energy-efficient hydrogenated zinc oxide nanoflakes for high-performance self-powered ultraviolet photodetector," *ACS applied materials and interfaces,* vol. 8, pp. 18182-18188, 2016.

[19] L. Sang, M. Liao, and M. Sumiya, "A comprehensive review of semiconductor ultraviolet photodetectors: from thin film to one-dimensional nanostructures," *Sensors,* vol. 13, pp. 10482-10518, Aug 13 2013.

[20] M. Yoshizawa, A. Kikuchi, M. Mori, N. Fujita, and K. Kishino, "Growth of self-organized GaN nanostructures on Al2O3 (0001) by RF-radical source molecular beam epitaxy," *Japanese journal of applied physics,* vol. 36, p. L459, 1997.

[21] A. L. Mulyo, Y. Konno, J. S. Nilsen, A. T. van Helvoort, B.-O. Fimland, H. Weman, and K. Kishino, "Growth study of self-assembled GaN nanocolumns on silica glass by plasma assisted molecular beam epitaxy," *Journal of crystal growth,* vol. 480, pp. 67-73, 2017.

[22] K. Kishino and S. Ishizawa, "Selective-area growth of GaN nanocolumns on Si (111) substrates for application to nanocolumn emitters with systematic analysis of dislocation filtering effect of nanocolumns," *Nanotechnology,* vol. 26, p. 225602, 2015.

[23] M. Mishra, A. Gundimeda, T. Garg, A. Dash, S. Das, and G. Gupta, "ZnO/GaN heterojunction based self-powered photodetectors: Influence of interfacial states on UV sensing," *Applied Surface Science,* vol. 478, pp. 1081-1089, 2019.

[24] J. Chen, W. Ouyang, W. Yang, J. H. He, and X. Fang, "Recent progress of heterojunction ultraviolet photodetectors: materials, integrations, and applications," *Advanced Functional Materials,* vol. 30, p. 1909909, 2020.

[25] S. J. Moniz, S. A. Shevlin, D. J. Martin, Z.-X. Guo, and J. Tang, "Visible-light driven heterojunction photocatalysts for water splitting–a critical review," *Energy and Environmental Science,* vol. 8, pp. 731-759, 2015.

[26] G. Konstantatos and E. H. Sargent, "Nanostructured materials for photon detection," *Nature nanotechnology,* vol. 5, pp. 391-400, 2010.

[27] L. Goswami, N. Aggarwal, M. Singh, R. Verma, P. Vashishtha, S. K. Jain, J. Tawale, R. Pandey, and G. Gupta, "GaN Nanotowers Grown on Si (111) and Functionalized with Au Nanoparticles and ZnO Nanorods for Highly Responsive UV Photodetectors," *ACS Applied Nano Materials,* 2020.

[28] A. Echresh, C. O. Chey, M. Z. Shoushtari, V. Khranovskyy, O. Nur, and M. Willander, "UV photo-detector based on p-NiO thin film/n-ZnO nanorods heterojunction prepared by a simple process," *Journal of Alloys and Compounds,* vol. 632, pp. 165-171, 2015.

[29] X. Li, C. Gao, H. Duan, B. Lu, Y. Wang, L. Chen, Z. Zhang, X. Pan, and E. Xie, "High-performance photoelectrochemical-type self-powered UV photodetector using epitaxial TiO2/SnO2 branched heterojunction nanostructure," *Small,* vol. 9, pp. 2005-2011, 2013.

[30] Y. Gao, J. Xu, S. Shi, H. Dong, Y. Cheng, C. Wei, X. Zhang, S. Yin, and L. Li, "TiO2 nanorod arrays based self-powered UV photodetector: heterojunction with NiO nanoflakes and enhanced UV photoresponse," *ACS applied materials and interfaces,* vol. 10, pp. 11269-11279, 2018.

[31] K. Hu, F. Teng, L. Zheng, P. Yu, Z. Zhang, H. Chen, and X. Fang, "Binary response Se/ZnO p-n heterojunction UV photodetector with high on/off ratio and fast speed," *Laser and Photonics Reviews,* vol. 11, p. 1600257, 2017.

[32] W. Tian, T. Zhai, C. Zhang, S. L. Li, X. Wang, F. Liu, D. Liu, X. Cai, K. Tsukagoshi, and D. Golberg, "Low-cost fully transparent ultraviolet photodetectors based on electrospun ZnO-SnO2 heterojunction nanofibers," *Advanced Materials,* vol. 25, pp. 4625-4630, 2013.

[33] H. Zhu, C. Shan, B. Yao, B. Li, J. Zhang, D. Zhao, D. Shen, and X. Fan, "High spectrum selectivity ultraviolet photodetector fabricated from an n-ZnO/p-GaN heterojunction," *The Journal of Physical Chemistry C,* vol. 112, pp. 20546-20548, 2008.

[34] R. K. Saroj, S. Deb, and S. Dhar, "n-ZnO/p-GaN heterojunction ultraviolet (UV) photo detectors with high responsivity and fast response time grown by chemical vapor deposition technique," *Semiconductor Science and Technology,* vol. 33, p. 125012, 2018.

[35] L. Su, Q. Zhang, T. Wu, M. Chen, Y. Su, Y. Zhu, R. Xiang, X. Gui, and Z. Tang, "High-performance zero-bias ultraviolet photodetector based on p-GaN/n-ZnO heterojunction," *Applied Physics Letters,* vol. 105, p. 072106, 2014.

[36] Q.-M. Fu, Z.-C. Yao, J.-L. Peng, H.-Y. Zhao, Z.-B. Ma, H. Tao, Y.-F. Tu, D. Zhou, and Y. Tian, "Enhanced photoresponse in ZnO nanorod array/p-GaN self-powered ultraviolet photodetectors via coupling with CuO nanostructures," *Materials Research Express,* vol. 7, p. 015063, 2020.

[37] Z. Song, H. Zhou, P. Gui, X. Yang, R. Liu, G. Ma, H. Wang, and G. Fang, "All-inorganic perovskite CsPbBr 3-based self-powered light-emitting photodetectors with ZnO hollow balls as an ultraviolet response center," *Journal of Materials Chemistry C,* vol. 6, pp. 5113-5121, 2018.

[38] Y. Huang, L. Zhang, J. Wang, X. Chu, D. Zhang, X. Zhao, X. Li, L. Xin, Y. Zhao, and F. Zhao, "Enhanced photoresponse of n-ZnO/p-GaN heterojunction ultraviolet photodetector with high-quality CsPbBr3 films grown by pulse laser deposition," *Journal of Alloys and Compounds,* vol. 802, pp. 70-75, 2019.

[39] H. Zhou, P. Gui, Q. Yu, J. Mei, H. Wang, and G. Fang, "Self-powered, visible-blind ultraviolet photodetector based on n-ZnO nanorods/i-MgO/p-GaN structure light-emitting diodes," *Journal of Materials Chemistry C,* vol. 3, pp. 990-994, 2015.

[40] L. Zhang, F. Zhao, C. Wang, F. Wang, R. Huang, and Q. Li, "Optoelectronic characteristics of UV photodetector based on GaN/ZnO nanorods p-i-n heterostructures," *Electronic Materials Letters,* vol. 11, pp. 682-686, 2015.

[41] H. Zhou, P. Gui, L. Yang, C. Ye, M. Xue, J. Mei, Z. Song, and H. Wang, "High performance, self-powered ultraviolet photodetector based on a ZnO nanoarrays/GaN structure with a CdS insert layer," *New Journal of Chemistry,* vol. 41, pp. 4901-4907, 2017.

[42] L. Vikas, K. Vanaja, P. Subha, and M. Jayaraj, "Fast UV sensing properties of n-ZnO nanorods/p-GaN heterojunction," *Sensors and Actuators A: Physical,* vol. 242, pp. 116-122, 2016.

[43] C.-H. Chen and C.-T. Lee, "Enhancing the performance of ZnO nanorod/p-GaN heterostructured photodetectors using the photoelectrochemical oxidation passivation method," *IEEE transactions on nanotechnology,* vol. 12, pp. 578-582, 2013.

[44] Y. Q. Bie, Z. M. Liao, H. Z. Zhang, G. R. Li, Y. Ye, Y. B. Zhou, J. Xu, Z. X. Qin, L. Dai, and D. P. Yu, "Self-powered, ultrafast, visible-blind UV detection and optical logical operation based on ZnO/GaN nanoscale p-n junctions," *Advanced Materials,* vol. 23, pp. 649-653, 2011.

[45] Y.-J. Lee, Z.-P. Yang, F.-Y. Lo, J.-J. Siao, Z.-H. Xie, Y.-L. Chuang, T.-Y. Lin, and J.-K. Sheu, "Slanted n-ZnO/p-GaN nanorod arrays light-emitting diodes grown by oblique-angle deposition," *Apl Materials,* vol. 2, p. 056101, 2014.

[46] D. Li, X. Sun, H. Song, Z. Li, Y. Chen, H. Jiang, and G. Miao, "Realization of a high-performance GaN UV detector by nanoplasmonic enhancement," *Advanced Materials,* vol. 24, pp. 845-849, 2012.

[47] X. Zhang, Q. Liu, B. Liu, W. Yang, J. Li, P. Niu, and X. Jiang, "Giant UV photoresponse of a GaN nanowire photodetector through effective Pt nanoparticle coupling," *Journal of Materials Chemistry C,* vol. 5, pp. 4319-4326, 2017.

[48] R. Khan, P. Uthirakumar, K.-B. Bae, S.-J. Leem, and I.-H. Lee, "Localized surface plasmon enhanced photoluminescence of ZnO nanosheets by Au nanoparticles," *Materials Letters,* vol. 163, pp. 8-11, 2016.

[49] A. Shetty, K. J. Sundar, B. Roul, S. Mukundan, G. Chandan, L. Mohan, A. Ghosh, K. Vinoy, and S. Krupanidhi, "Plasmonic enhancement of photocurrent in GaN based UV photodetectors," in *2014 IEEE 2nd International Conference on Emerging Electronics (ICEE)*, 2014, pp. 1-4.

[50] X. Zhou, G. Liu, J. Yu, and W. Fan, "Surface plasmon resonance-mediated photocatalysis by noble metal-based composites under visible light," *Journal of Materials Chemistry,* vol. 22, pp. 21337-21354, 2012.

[51] M. L. Brongersma, N. J. Halas, and P. Nordlander, "Plasmon-induced hot carrier science and technology," *Nature nanotechnology,* vol. 10, pp. 25-34, 2015.

[52] A. Manjavacas, J. G. Liu, V. Kulkarni, and P. Nordlander, "Plasmon-induced hot carriers in metallic nanoparticles," *ACS nano,* vol. 8, pp. 7630-7638, 2014.

[53] L. Goswami, N. Aggarwal, S. Krishna, M. Singh, P. Vashishtha, S. P. Singh, S. Husale, R. Pandey, and G. Gupta, "Au-Nanoplasmonics-Mediated Surface Plasmon-Enhanced GaN Nanostructured UV Photodetectors," *ACS Omega,* 2020.

[54] Z. Yi, J. Chen, J. Luo, Y. Yi, X. Kang, X. Ye, P. Bi, X. Gao, Y. Yi, and Y. Tang, "Surface-plasmon-enhanced band emission and enhanced photocatalytic activity of Au nanoparticles-decorated ZnO nanorods," *Plasmonics,* vol. 10, pp. 1373-1380, 2015.

[55] F. Qin, N. Chang, C. Xu, Q. Zhu, M. Wei, Z. Zhu, F. Chen, and J. Lu, "Underlying mechanism of blue emission enhancement in Au decorated p-GaN film," *RSC advances,* vol. 7, pp. 15071-15076, 2017.

[56] K. Saron, M. Hashim, K. M. Suleiman, and K. Al-Heuseen, "Enhanced ultraviolet emission in photoluminescence of GaN film covered by ZnO nanoflakes," *Journal of luminescence,* vol. 134, pp. 266-271, 2013.

[57] V. Amendola, R. Pilot, M. Frasconi, O. M. Maragò, and M. A. Iatì, "Surface plasmon resonance in gold nanoparticles: a review," *Journal of Physics: Condensed Matter,* vol. 29, p. 203002, 2017.

[58] V. Amendola and M. Meneghetti, "Laser ablation synthesis in solution and size manipulation of noble metal nanoparticles," *Physical chemistry chemical physics,* vol. 11, pp. 3805-3821, 2009.

[59] M.-C. Daniel and D. Astruc, "Gold nanoparticles: assembly, supramolecular chemistry, quantum-size-related properties, and applications toward biology, catalysis, and nanotechnology," *Chemical reviews,* vol. 104, pp. 293-346, 2004.

[60] J. Hwang, F. Wang, C. Kung, and M. Chan, "Using the surface plasmon resonance of Au nanoparticles to enhance ultraviolet response of ZnO nanorods-based Schottky-barrier photodetectors," *IEEE transactions on nanotechnology,* vol. 14, pp. 318-321, 2015.

[61] S. Sarkar and D. Basak, "Self Powered Highly Enhanced Dual Wavelength ZnO@ CdS Core–Shell Nanorod Arrays Photodetector: An Intelligent Pair," *ACS applied materials and interfaces,* vol. 7, pp. 16322-16329, 2015.

[62] R. Dong, C. Bi, Q. Dong, F. Guo, Y. Yuan, Y. Fang, Z. Xiao, and J. Huang, "An ultraviolet-to-NIR broad spectral nanocomposite photodetector with gain," *Advanced Optical Materials,* vol. 2, pp. 549-554, 2014.

[63] Z. Zou, C. Xie, S. Zhang, C. Yang, G. Zhang, and L. Yang, "CdS/ZnO nanocomposite film and its enhanced photoelectric response to UV and visible lights at low bias," *Sensors and Actuators B: Chemical,* vol. 188, pp. 1158-1166, 2013.

[64] T. Lin, M. Inciong, S. Santiago, T. Yeh, W. Yang, C. Yuan, J. Shen, H.-C. Kuo, and C. Chiu, "Photo-induced doping in GaN epilayers with graphene quantum dots," *Scientific reports,* vol. 6, p. 23260, 2016.

[65] K. Rahimi, A. Yazdani, and M. Ahmadirad, "Facile preparation of zinc oxide nanorods surrounded by graphene quantum dots both synthesized via separate pyrolysis procedures for photocatalyst application," *Materials Research Bulletin,* vol. 98, pp. 148-154, 2018.

[66] D. Liu, H.-J. Li, J. Gao, S. Zhao, Y. Zhu, P. Wang, D. Wang, A. Chen, X. Wang, and J. Yang, "High-performance ultraviolet photodetector based on graphene quantum dots decorated ZnO nanorods/GaN film isotype heterojunctions," *Nanoscale research letters,* vol. 13, p. 261, 2018.

[67] Y. Yan, J. Gong, J. Chen, Z. Zeng, W. Huang, K. Pu, J. Liu, and P. Chen, "Recent advances on graphene quantum dots: from chemistry and physics to applications," *Advanced Materials,* vol. 31, p. 1808283, 2019.

[68] M. V. Rama Krishna and R. Friesner, "Quantum confinement effects in semiconductor clusters," *The Journal of Chemical Physics,* vol. 95, pp. 8309-8322, 1991.

[69] A. K. Geim and K. S. Novoselov, "The rise of graphene," in *Nanoscience and technology: a collection of reviews from nature journals*, ed: World Scientific, 2010, pp. 11-19.

[70] S. Dhar, T. Majumder, and S. P. Mondal, "Graphene quantum dot-sensitized ZnO nanorod/polymer Schottky junction UV detector with superior external quantum efficiency, detectivity, and responsivity," *ACS applied materials and interfaces,* vol. 8, pp. 31822-31831, 2016.

[71] J. Millán, P. Godignon, X. Perpiñà, A. Pérez-Tomás, and J. Rebollo, "A survey of wide bandgap power semiconductor devices," *IEEE transactions on Power Electronics,* vol. 29, pp. 2155-2163, 2013.

[72] T. Doi, "Current status and future prospects of GaN substrates for green devices," *Sensors and Materials,* vol. 25, pp. 141-154, 2013.

[73] A. K. Pantazis, G. Konstantinidis, and E. Gizeli, "Characterization of a GaN lamb-wave sensor for liquid-based mass sensing applications," *IEEE sensors journal,* vol. 14, pp. 908-911, 2013.

[74] N. Aggarwal, S. Krishna, A. Sharma, L. Goswami, D. Kumar, S. Husale, and G. Gupta, "A highly responsive self-driven UV photodetector using GaN nanoflowers," *Advanced Electronic Materials,* vol. 3, p. 1700036, 2017.

[75] S. Krishna, A. Sharma, N. Aggarwal, S. Husale, and G. Gupta, "Ultrafast photoresponse and enhanced photoresponsivity of Indium Nitride based broad band photodetector," *Solar Energy Materials and Solar Cells,* vol. 172, pp. 376-383, 2017.

[76] K. Chung, C.-H. Lee, and G.-C. Yi, "Transferable GaN layers grown on ZnO-coated graphene layers for optoelectronic devices," *Science,* vol. 330, pp. 655-657, 2010.

[77] C. Hong, D. Pavlidis, S. Brown, and S. Rand, "Photoluminescence investigation of GaN films grown by metalorganic chemical vapor deposition on (100) GaAs," *Journal of Applied Physics,* vol. 77, pp. 1705-1709, 1995.

[78] B. Mazumder, S. W. Kaun, J. Lu, S. Keller, U. K. Mishra, and J. S. Speck, "Atom probe analysis of AlN interlayers in AlGaN/AlN/GaN heterostructures," *Applied Physics Letters,* vol. 102, p. 111603, 2013/03/18 2013.

[79] G. Antczak and G. Ehrlich, "Jump processes in surface diffusion," *Surface science reports,* vol. 62, pp. 39-61, 2007.

[80] T. Chu, "Gallium nitride films," *Journal of The Electrochemical Society,* vol. 118, p. 1200, 1971.

[81] H. Grimmeiss and B. Monemar, "Low-Temperature Luminescence of GaN," *Journal of Applied Physics,* vol. 41, pp. 4054-4058, 1970.

[82] X. Wang and A. Yoshikawa, "Molecular beam epitaxy growth of GaN, AlN and InN," *Progress in crystal growth and characterization of materials,* vol. 48, pp. 42-103, 2004.

[83] B. Heying, R. Averbeck, L. Chen, E. Haus, H. Riechert, and J. Speck, "Control of GaN surface morphologies using plasma-assisted molecular beam epitaxy," *Journal of Applied Physics,* vol. 88, pp. 1855-1860, 2000.

[84] G. Koblmüller, S. Fernández-Garrido, E. Calleja, and J. Speck, "In situ investigation of growth modes during plasma-assisted molecular beam epitaxy of (0001) GaN," *Applied Physics Letters,* vol. 91, p. 161904, 2007.

[85] G. Koblmüller, F. Wu, T. Mates, J. Speck, S. Fernández-Garrido, and E. Calleja, "High electron mobility GaN grown under N-rich conditions by plasma-assisted molecular beam epitaxy," *Applied Physics Letters,* vol. 91, p. 221905, 2007.

[86] A. Cho, "Epitaxy by periodic annealing," *SurSc,* vol. 17, pp. 494-503, 1969.

[87] J. Müßener, J. r. Teubert, P. Hille, M. Schäfer, J. r. Schörmann, M. de la Mata, J. Arbiol, and M. Eickhoff, "Probing the internal electric field in GaN/AlGaN nanowire heterostructures," *Nano letters,* vol. 14, pp. 5118-5122, 2014.

[88] L. Goswami, R. Pandey, and G. Gupta, "Epitaxial growth of GaN nanostructure by PAMBE for UV detection application," *Applied Surface Science,* vol. 449, pp. 186-192, 2018.

[89] M. Mishra, A. Gundimeda, S. Krishna, N. Aggarwal, L. Goswami, B. Gahtori, B. Bhattacharyya, S. Husale, and G. Gupta, "Surface-engineered nanostructure-based efficient nonpolar GaN ultraviolet photodetectors," *ACS Omega,* vol. 3, pp. 2304-2311, 2018.

[90] S. Krishna, N. Aggarwal, M. Mishra, K. Maurya, M. Kaur, G. Sehgal, S. Singh, N. Dilawar, B. K. Gupta, and G. Gupta, "Epitaxial growth of high In-content In0. 41Ga0. 59N/GaN heterostructure on (11–20) Al2O3 substrate," *Journal of Alloys and Compounds,* vol. 658, pp. 470-475, 2016.

[91] E. Matioli, C. Neufeld, M. Iza, S. C. Cruz, A. A. Al-Heji, X. Chen, R. M. Farrell, S. Keller, S. DenBaars, and U. Mishra, "High internal and external quantum efficiency InGaN/GaN solar cells," *Applied Physics Letters,* vol. 98, p. 021102, 2011.

[92] J. Wu, "When group-III nitrides go infrared: New properties and perspectives," *Journal of Applied Physics,* vol. 106, p. 5, 2009.

[93] M. Martens, J. Schlegel, P. Vogt, F. Brunner, R. Lossy, J. Würfl, M. Weyers, and M. Kneissl, "High gain ultraviolet photodetectors based on AlGaN/GaN heterostructures for optical switching," *Applied Physics Letters,* vol. 98, p. 211114, 2011.

[94] E. Cicek, R. McClintock, C. Cho, B. Rahnema, and M. Razeghi, "AlxGa1-xN-based back-illuminated solar-blind photodetectors with external quantum efficiency of 89%," *Applied Physics Letters,* vol. 103, p. 191108, 2013.

[95] P. Sahoo, S. Dhara, S. Dash, and A. K Tyagi, "One dimensional GaN nanostructures: growth kinetics and applications," *Nanoscience and Nanotechnology-Asia,* vol. 1, pp. 140-170, 2011.

[96] C. Adelmann, N. Gogneau, E. Sarigiannidou, J.-L. Rouviere, and B. Daudin, "GaN islanding by spontaneous rearrangement of a strained two-dimensional layer on (0001) AlN," *Applied Physics Letters,* vol. 81, pp. 3064-3066, 2002.

[97] M. Kumar, T. Bhat, M. Rajpalke, B. Roul, P. Misra, L. Kukreja, N. Sinha, A. Kalghatgi, and S. Krupanidhi, "Self-assembled flower-like nanostructures of InN and GaN grown by plasma-assisted molecular beam epitaxy," *Bulletin of Materials Science,* vol. 33, pp. 221-226, 2010.

[98] S. Dhamodaran, D. S. Chander, and J. Ramkumar, "Anti-reflective and hydrophobic surface of self-organized GaN nano-flowers," *Applied Surface Science,* vol. 257, pp. 9612-9615, 2011.

[99] M. J. Shin, M. J. Kim, H. S. Jeon, H. S. Ahn, S. N. Yi, D. H. Ha, Y. Huh, B. H. Kim, and S. H. Park, "Evolution of GaN nanoflowers from AlN–SiO2 grains on a silicon substrate by chemical vapor reaction," *Vacuum,* vol. 86, pp. 201-205, 2011.

[100] S. Fernández-Garrido, J. Grandal, E. Calleja, M. Sánchez-García, and D. López-Romero, "A growth diagram for plasma-assisted molecular beam epitaxy of GaN nanocolumns on Si (111)," ed: American Institute of Physics, 2009.

[101] T. Wang, F. Cao, X. Ji, and Q. Zhang, "Study on tower-like GaN nanostructure: Growth, optical and fast UV sensing properties," *Superlattices and Microstructures,* vol. 134, p. 106233, 2019.

[102] R. Debnath, R. Meijers, T. Richter, T. Stoica, R. Calarco, and H. Lüth, "Mechanism of molecular beam epitaxy growth of GaN nanowires on Si (111)," *Applied Physics Letters,* vol. 90, p. 123117, 2007.

[103] R. Köster, J.-S. Hwang, C. Durand, D. L. S. Dang, and J. Eymery, "Self-assembled growth of catalyst-free GaN wires by metal–organic vapour phase epitaxy," *Nanotechnology,* vol. 21, p. 015602, 2009.

[104] M.-C. Lu, Y. Chueh, L. Chen, L. Chou, H. Hsiao, and A.-B. Yang, "Synthesis and formation mechanism of gallium nitride nanotubular structure," *Electrochemical and Solid State Letters,* vol. 8, p. G153, 2005.

[105] E. Monroy, F. Omnès, and F. Calle, "Wide-bandgap semiconductor ultraviolet photodetectors," *Semiconductor Science and Technology,* vol. 18, p. R33, 2003.

[106] N. Fu, E. Li, Z. Cui, D. Ma, W. Wang, Y. Zhang, S. Song, and J. Lin, "The electronic properties of phosphorus-doped GaN nanowires from first-principle calculations," *Journal of Alloys and Compounds,* vol. 596, pp. 92-97, 2014.

[107] M. Sanchez-Garcia, E. Calleja, E. Monroy, F. Sanchez, F. Calle, E. Munoz, and R. Beresford, "The effect of the III/V ratio and substrate temperature on the morphology and properties of GaN-and AlN-layers grown by molecular beam epitaxy on Si (1 1 1)," *Journal of crystal growth,* vol. 183, pp. 23-30, 1998.

[108] L. Cerutti, J. Ristić, S. Fernández-Garrido, E. Calleja, A. Trampert, K. Ploog, S. Lazic, and J. Calleja, "Wurtzite GaN nanocolumns grown on Si (001) by molecular beam epitaxy," *Applied Physics Letters,* vol. 88, p. 213114, 2006.

[109] A. Trampert, J. u. Jahn, E. Calleja, and K. Ploog, "TEM study of(Ga, Al) N nanocolumns and embedded GaN nanodiscs," *Microscopy of Semiconducting Materials 2003,* pp. 167-170, 2003.

[110] S. Kukushkin, A. Osipov, V. Bessolov, B. Medvedev, V. Nevolin, and K. Tcarik, "Substrates for epitaxy of gallium nitride: new materials and techniques," *Rev. Adv. Mater. Sci,* vol. 17, pp. 1-32, 2008.

[111] S. Haffouz, V. Kirilyuk, P. Hageman, L. Macht, J. Weyher, and P. Larsen, "Improvement of the optical properties of metalorganic chemical vapor deposition grown GaN on sapphire by an in situ SiN treatment," *Applied Physics Letters,* vol. 79, pp. 2390-2392, 2001.

[112] T. Paskova, V. Darakchieva, E. Valcheva, P. Paskov, I. G. Ivanov, B. Monemar, T. Böttcher, C. Roder, and D. Hommel, "Hydride vapor-phase epitaxial GaN thick films for quasi-substrate applications: Strain distribution and wafer bending," *Journal of electronic materials,* vol. 33, pp. 389-394, 2004.

[113] F. K. Yam, L. L. Low, S. A. Oh, and Z. Hassan, "Gallium nitride: an overview of structural defects," *Optoelectronics-Materials and Techniques,* pp. 99-136, 2011.

[114] R. Calarco, R. J. Meijers, R. K. Debnath, T. Stoica, E. Sutter, and H. Lüth, "Nucleation and growth of GaN nanowires on Si (111) performed by molecular beam epitaxy," *Nano letters,* vol. 7, pp. 2248-2251, 2007.

[115] C. Foxon, S. Novikov, J. Hall, R. Campion, D. Cherns, I. Griffiths, and S. Khongphetsak, "A complementary geometric model for the growth of GaN nanocolumns prepared by plasma-assisted molecular beam epitaxy," *Journal of crystal growth,* vol. 311, pp. 3423-3427, 2009.

[116] J. Carrano, P. Grudowski, C. Eiting, R. Dupuis, and J. Campbell, "Very low dark current metal–semiconductor–metal ultraviolet photodetectors fabricated on single-crystal GaN epitaxial layers," *Applied Physics Letters,* vol. 70, pp. 1992-1994, 1997.

[117] D. Walker, E. Monroy, P. Kung, J. Wu, M. Hamilton, F. Sanchez, J. Diaz, and M. Razeghi, "High-speed, low-noise metal–semiconductor–metal ultraviolet photodetectors based on GaN," *Applied Physics Letters,* vol. 74, pp. 762-764, 1999.

[118] H.-Y. Chen, K.-W. Liu, X. Chen, Z.-Z. Zhang, M.-M. Fan, M.-M. Jiang, X.-H. Xie, H.-F. Zhao, and D.-Z. Shen, "Realization of a self-powered ZnO MSM UV photodetector with high responsivity using an asymmetric pair of Au electrodes," *Journal of Materials Chemistry C,* vol. 2, pp. 9689-9694, 2014.

[119] Z. L. Wang, "Self-powered nanosensors and nanosystems," *Advanced Materials,* vol. 24, pp. 280-285, 2012.

[120] X. Hou, B. Liu, X. Wang, Z. Wang, Q. Wang, D. Chen, and G. Shen, "SnO 2-microtube-assembled cloth for fully flexible self-powered photodetector nanosystems," *Nanoscale,* vol. 5, pp. 7831-7837, 2013.

[121] J. Ding, H. Fang, Z. Lian, J. Li, Q. Lv, L. Wang, J.-L. Sun, and Q. Yan, "A self-powered photodetector based on a CH 3 NH 3 PbI 3 single crystal with asymmetric electrodes," *CrystEngComm,* vol. 18, pp. 4405-4411, 2016.

[122] N. Yamabe, Y. Yamamoto, and T. Ohachi, "Epitaxial growth of β-Si3N4 by the nitridation of Si with adsorbed N atoms for interface reaction epitaxy of double buffer AlN (0001)/β-Si3N4/Si (111)," *physica status solidi c,* vol. 8, pp. 1552-1555, 2011.

[123] R. Calarco and M. Marso, "GaN and InN nanowires grown by MBE: A comparison," *Applied Physics A,* vol. 87, pp. 499-503, 2007.

[124] A. Urbańczyk, F. W. van Otten, and R. Nötzel, "Self-aligned epitaxial metal-semiconductor hybrid nanostructures for plasmonics," *Applied Physics Letters,* vol. 98, p. 243110, 2011.

[125] T. Stoica, E. Sutter, R. J. Meijers, R. K. Debnath, R. Calarco, H. Lüth, and D. Grützmacher, "Interface and wetting layer effect on the catalyst-free nucleation and growth of GaN nanowires," *Small,* vol. 4, pp. 751-754, 2008.

[126] H. D. Batha and E. D. Whitney, "Kinetics and mechanism of the thermal decomposition of Si3N4," *Journal of the American Ceramic Society,* vol. 56, pp. 365-369, 1973.

[127] R. Groh, G. Gerey, L. Bartha, and J. Pankove, "On the thermal decomposition of GaN in vacuum," *physica status solidi (a),* vol. 26, pp. 353-357, 1974.

[128] T. Markurt, L. Lymperakis, J. Neugebauer, P. Drechsel, P. Stauss, T. Schulz, T. Remmele, V. Grillo, E. Rotunno, and M. Albrecht, "Blocking growth by an electrically active subsurface layer: the effect of Si as an antisurfactant in the growth of GaN," *Physical review letters,* vol. 110, p. 036103, 2013.

[129] M. Forsberg, A. Serban, I. Poenaru, C.-L. Hsiao, M. Junaid, J. Birch, and G. Pozina, "Stacking fault related luminescence in GaN nanorods," *Nanotechnology,* vol. 26, p. 355203, 2015.

[130] W. Wang, H. Wang, W. Yang, Y. Zhu, and G. Li, "A new approach to epitaxially grow high-quality GaN films on Si substrates: the combination of MBE and PLD," *Scientific reports,* vol. 6, p. 24448, 2016.

[131] N. Aggarwal, S. T. Krishna, L. Goswami, M. Mishra, G. Gupta, K. Maurya, S. Singh, N. Dilawar, and M. Kaur, "Extenuation of stress and defects in GaN films grown on a metal–organic chemical vapor deposition-GaN/c-sapphire substrate by plasma-assisted molecular beam epitaxy," *Crystal Growth and Design,* vol. 15, pp. 2144-2150, 2015.

[132] A. Denis, G. Goglio, and G. Demazeau, "Gallium nitride bulk crystal growth processes: A review," *Materials Science and Engineering: R: Reports,* vol. 50, pp. 167-194, 2006.

[133] K. Jeganathan, R. Debnath, R. Meijers, T. Stoica, R. Calarco, D. Grützmacher, and H. Lüth, "Raman scattering of phonon-plasmon coupled modes in self-assembled GaN nanowires," *Journal of Applied Physics,* vol. 105, p. 123707, 2009.

[134] L. Zhang, K. Cheng, S. Degroote, M. Leys, M. Germain, and G. Borghs, "Strain effects in GaN epilayers grown on different substrates by metal organic vapor phase epitaxy," *Journal of Applied Physics,* vol. 108, p. 073522, 2010.

[135] W. J. Salcedo, F. J. Ramirez Fernandez, and J. C. Rubimc, "Influence of laser excitation on raman and photoluminescence spectra and FTIR study of porous silicon layers," *Brazilian Journal of Physics,* vol. 29, pp. 751-755, 1999.

[136] R. Velazquez, A. Aldalbahi, M. Rivera, and P. Feng, "Fabrications and application of single crystalline GaN for high-performance deep UV photodetectors," *AIP Advances,* vol. 6, p. 085117, 2016.

[137] D. Zhao, S. Xu, M. Xie, S. Tong, and H. Yang, "Stress and its effect on optical properties of GaN epilayers grown on Si (111), 6H-SiC (0001), and c-plane sapphire," *Applied Physics Letters,* vol. 83, pp. 677-679, 2003.

[138] X. Gao, J. Li, G. Sun, N. Zhang, L. Wang, W. Zhao, and Y. Zeng, "Molecular beam epitaxial growth of GaN on 3C-SiC/Si (111) substrates using a thick AlN buffer layer," in *13th International Conference on Semiconducting and Insulating Materials, 2004. SIMC-XIII-2004.*, 2004, pp. 49-52.

[139] K. Saron, M. Hashim, N. Naderi, and N. K. Allam, "Enhanced light sensing characteristics of nanostructured gallium nitride/silicon heterojunctions: Interface matters," *Journal of Applied Physics,* vol. 114, p. 134510, 2013.

[140] H. Seo, Q. Chen, M. Iliev, L. Tu, C. Hsiao, J. K. Mean, and W.-K. Chu, "Epitaxial GaN nanorods free from strain and luminescent defects," *Applied Physics Letters,* vol. 88, p. 153124, 2006.

[141] K.-W. Liu, S.-J. Young, S.-J. Chang, T.-H. Hsueh, H. Hung, S.-X. Chen, and Y.-Z. Chen, "Growth of gallium nitride on silicon by molecular beam epitaxy incorporating a chromium nitride interlayer," *Journal of Alloys and Compounds,* vol. 511, pp. 1-4, 2012.

[142] Y. Inoue, T. Hoshino, S. Takeda, K. Ishino, A. Ishida, H. Fujiyasu, H. Kominami, H. Mimura, Y. Nakanishi, and S. Sakakibara, "Strong luminescence from dislocation-free GaN nanopillars," *Applied Physics Letters,* vol. 85, pp. 2340-2342, 2004.

[143] S. Liu, J. Ye, Y. Cao, Q. Shen, Z. Liu, L. Qi, and X. Guo, "A flexible and transparent ceramic nanobelt network for soft electronics," *Small,* vol. 4, pp. 2371-2376, 2009.

[144] S. Noh and P. Bhattacharya, "Determination of intrinsic barrier height in the Au/n-GaN contact system," *Applied Physics Letters,* vol. 78, pp. 3642-3644, 2001.

[145] O. Katz, V. Garber, B. Meyler, G. Bahir, and J. Salzman, "Gain mechanism in GaN Schottky ultraviolet detectors," *Applied Physics Letters,* vol. 79, pp. 1417-1419, 2001.

[146] J. Freeouf, T. Jackson, S. Laux, and J. Woodall, "Effective barrier heights of mixed phase contacts: Size effects," *Applied Physics Letters,* vol. 40, pp. 634-636, 1982.

[147] A. G. Reddy, N. Aggarwal, S. Krishna TC, M. Singh, R. Rakshit, and G. Gupta, "Correlation of current–voltage–temperature analysis with deep level defects in epitaxial GaN films," *Applied Physics Letters,* vol. 106, p. 233501, 2015.

[148] Z. L. Wang, "Progress in piezotronics and piezo-phototronics," *Advanced Materials,* vol. 24, pp. 4632-4646, 2012.

[149] H. Chen, H. Liu, Z. Zhang, K. Hu, and X. Fang, "Nanostructured photodetectors: from ultraviolet to terahertz," *Advanced Materials,* vol. 28, pp. 403-433, 2016.

[150] G. Tabares, A. Hierro, J. Ulloa, A. Guzman, E. Munoz, A. Nakamura, T. Hayashi, and J. Temmyo, "High responsivity and internal gain mechanisms in Au-ZnMgO Schottky photodiodes," *Applied Physics Letters,* vol. 96, p. 101112, 2010.

[151] M. Hanzaz, A. Bouhdada, P. Gibart, and F. Omnes, "Impact of the defects on the electrical and optical properties of AlGaN ultraviolet photodetectors," *Journal of Applied Physics,* vol. 92, pp. 13-18, 2002.

[152] X. Zhang, B. Liu, Q. Liu, W. Yang, C. Xiong, J. Li, and X. Jiang, "Ultrasensitive and highly selective photodetections of UV-A rays based on individual bicrystalline GaN nanowire," *ACS applied materials and interfaces,* vol. 9, pp. 2669-2677, 2017.

[153] R. Jia, D. Zhao, N. Gao, and D. Liu, "Polarization enhanced charge transfer: dual-band GaN-based plasmonic photodetector," *Scientific reports,* vol. 7, pp. 1-8, 2017.

[154] L. Liu, C. Yang, A. Patanè, Z. Yu, F. Yan, K. Wang, H. Lu, J. Li, and L. Zhao, "High-detectivity ultraviolet photodetectors based on laterally mesoporous GaN," *Nanoscale,* vol. 9, pp. 8142-8148, 2017.

[155] C. Soci, A. Zhang, X.-Y. Bao, H. Kim, Y. Lo, and D. Wang, "Nanowire photodetectors," *Journal of nanoscience and nanotechnology,* vol. 10, pp. 1430-1449, 2010.

[156] N. Liu, W. Tian, X. Zhang, J. Su, Q. Zhang, and Y. Gao, "Enhancement of ultraviolet detecting by coupling the photoconductive behavior of GaN nanowires and pn junction," *Optics express,* vol. 20, pp. 20748-20753, 2012.

[157] S. Chang, M. Chang, and Y. Yang, "Enhanced responsivity of GaN metal–semiconductor–metal (MSM) photodetectors on GaN substrate," *IEEE Photonics Journal,* vol. 9, pp. 1-7, 2017.

[158] L. Su and N. Qin, "A facile method for fabricating Au-nanoparticles-decorated ZnO nanorods with greatly enhanced near-band-edge emission," *Ceramics International,* vol. 41, pp. 2673-2679, 2015.

[159] L. A. Austin, B. Kang, and M. A. El-Sayed, "Probing molecular cell event dynamics at the single-cell level with targeted plasmonic gold nanoparticles: A review," *Nano Today,* vol. 10, pp. 542-558, 2015.

[160] C. F. Bohren and D. R. Huffman, *Absorption and scattering of light by small particles*: John Wiley and Sons, 2008.

[161] J. Turkevich, P. C. Stevenson, and J. Hillier, "A study of the nucleation and growth processes in the synthesis of colloidal gold," *Discussions of the Faraday Society,* vol. 11, pp. 55-75, 1951.

[162] S. Zeng, X. Yu, W.-C. Law, Y. Zhang, R. Hu, X.-Q. Dinh, H.-P. Ho, and K.-T. Yong, "Size dependence of Au NP-enhanced surface plasmon resonance based on differential phase measurement," *Sensors and Actuators B: Chemical,* vol. 176, pp. 1128-1133, 2013.

[163] A. Khan, W. M. Jadwisienczak, and M. E. Kordesch, "From Zn microspheres to hollow ZnO microspheres: A simple route to the growth of large scale metallic Zn microspheres and hollow ZnO microspheres," *Physica E: Low-dimensional Systems and Nanostructures,* vol. 33, pp. 331-335, 2006.

[164] Q. Wan, T. Wang, and J. Zhao, "Enhanced photocatalytic activity of ZnO nanotetrapods," *Applied Physics Letters,* vol. 87, p. 083105, 2005.

[165] L. Goswami, R. Pandey, and G. Gupta, "Ultra-thin GaN nanostructures based self-powered ultraviolet photodetector via non-homogeneous Au-GaN interfaces," *Optical Materials,* vol. 102, p. 109820, 2020.

[166] Z. Jin, L. Gao, Q. Zhou, and J. Wang, "High-performance flexible ultraviolet photoconductors based on solution-processed ultrathin ZnO/Au nanoparticle composite films," *Scientific reports,* vol. 4, pp. 1-8, 2014.

[167] Y. Liu, X. Zhang, J. Su, H. Li, Q. Zhang, and Y. Gao, "Ag nanoparticles@ ZnO nanowire composite arrays: an absorption enhanced UV photodetector," *Optics express,* vol. 22, pp. 30148-30155, 2014.

[168] L. Qin, C. Shing, and S. Sawyer, "Metal–semiconductor–metal ultraviolet photodetectors based on zinc-oxide colloidal nanoparticles," *IEEE electron device letters,* vol. 32, pp. 51-53, 2010.

[169] S. SAWYER, L. QIN, and C. SHING, "Zinc oxide nanoparticles for ultraviolet photodetection," *International Journal of High Speed Electronics and Systems,* vol. 20, pp. 183-194, 2011.

[170] R. Khokhra, B. Bharti, H.-N. Lee, and R. Kumar, "Visible and UV photo-detection in ZnO nanostructured thin films via simple tuning of solution method," *Scientific reports,* vol. 7, pp. 1-14, 2017.

[171] S. Chakrabartty, A. Mondal, M. B. Sarkar, B. Choudhuri, A. K. Saha, and A. Bhattacharyya, "${\rm TiO} _ {2} $ Nanoparticles Arrays Ultraviolet-A Detector With Au Schottky Contact," *IEEE Photonics Technology Letters,* vol. 26, pp. 1065-1068, 2014.

[172] A. J. Molina-Mendoza, A. Moya, R. Frisenda, S. A. Svatek, P. Gant, S. Gonzalez-Abad, E. Antolin, N. Agraït, G. Rubio-Bollinger, and D. P. de Lara, "Highly responsive UV-photodetectors based on single electrospun TiO 2 nanofibres," *Journal of Materials Chemistry C,* vol. 4, pp. 10707-10714, 2016.

[173] J. Hofmann and W. Steinmann, "Plasma resonance in the photoemission of silver," *physica status solidi (b),* vol. 30, pp. K53-K56, 1968.

[174] J. Sipe and J. Becher, "Surface-plasmon-assisted photoemission," *JOSA,* vol. 71, pp. 1286-1288, 1981.

[175] S. A. Maier, *Plasmonics: fundamentals and applications*: Springer Science and Business Media, 2007.

[176] U. Kreibig and M. Vollmer, "Springer Series in Material Science," *Optical properties of metal clusters, Springer Verlag, Berlin,* 1995.

[177] P. Bharadwaj, B. Deutsch, and L. Novotny, "Optical antennas. Adv. Opt. Photon. 1, 438–483," ed, 2009.

[178] X. Li, D. Xiao, and Z. Zhang, "Landau damping of quantum plasmons in metal nanostructures," *New Journal of Physics,* vol. 15, p. 023011, 2013.

[179] K. Watanabe, D. Menzel, N. Nilius, and H.-J. Freund, "Photochemistry on metal nanoparticles," *Chemical reviews,* vol. 106, pp. 4301-4320, 2006.

[180] T.-C. Chiang, C.-Y. Chiu, T.-F. Dai, Y.-J. Hung, and H.-C. Hsu, "Surface-plasmon-enhanced band-edge emission and lasing behaviors of Au-decorated ZnO microstructures," *Optical Materials Express,* vol. 7, pp. 313-319, 2017.

[181] X. Duan and C. M. Lieber, "Laser-assisted catalytic growth of single crystal GaN nanowires," *Journal of the American Chemical Society,* vol. 122, pp. 188-189, 2000.

[182] W. Han, P. Redlich, F. Ernst, and M. Rühle, "Synthesis of GaN–carbon composite nanotubes and GaN nanorods by arc discharge in nitrogen atmosphere," *Applied Physics Letters,* vol. 76, pp. 652-654, 2000.

[183] W. Han, S. Fan, Q. Li, and Y. Hu, "Synthesis of gallium nitride nanorods through a carbon nanotube-confined reaction," *Science,* vol. 277, pp. 1287-1289, 1997.

[184] Y. Liu, X. Wang, L. Fu, and D. Zhu, "Tower-like structure of ZnO nanocolumns," *Chemical communications,* pp. 1304-1305, 2003.

[185] J. Hsu, F. F. Schrey, and H. Ng, "Spatial distribution of yellow luminescence related deep levels in GaN," *Applied Physics Letters,* vol. 83, pp. 4172-4174, 2003.

[186] G. You, W. Guo, C. Zhang, P. Bhattacharya, R. Henderson, and J. Xu, "Excitation dependent two-component spontaneous emission and ultrafast amplified spontaneous emission in dislocation-free InGaN nanowires," *Applied Physics Letters,* vol. 102, p. 091105, 2013.

[187] L. Ravikiran, K. Radhakrishnan, N. Dharmarasu, M. Agrawal, Z. Wang, A. Bruno, C. Soci, T. Lihuang, and A. K. Siong, "Responsivity drop due to conductance modulation in GaN metal-semiconductor-metal Schottky based UV photodetectors on Si (111)," *Semiconductor Science and Technology,* vol. 31, p. 095003, 2016.

[188] T.-H. Chou, "GaN Thin Films Deposited on n-Si (111) Substrate with a Metal Organic Chemical Vapor Deposition System for Sensing Ultraviolet Light," *Sensors and Materials,* vol. 28, pp. 689-694, 2016.

[189] Z. Alaie, S. M. Nejad, and M. Yousefi, "Recent advances in ultraviolet photodetectors," *Materials Science in Semiconductor Processing,* vol. 29, pp. 16-55, 2015.

[190] S.-C. Kung, W. E. van der Veer, F. Yang, K. C. Donavan, and R. M. Penner, "20 μs photocurrent response from lithographically patterned nanocrystalline cadmium selenide nanowires," *Nano letters,* vol. 10, pp. 1481-1485, 2010.

[191] X. Sun, D. Li, Z. Li, H. Song, H. Jiang, Y. Chen, G. Miao, and Z. Zhang, "High spectral response of self-driven GaN-based detectors by controlling the contact barrier height," *Scientific reports,* vol. 5, p. 16819, 2015.

[192] W. Mou, L. Zhao, L. Chen, D. Yan, H. Ma, G. Yang, and X. Gu, "GaN-based schottky barrier ultraviolet photodetectors with graded doping on patterned sapphire substrates," *Solid-State Electronics,* vol. 133, pp. 78-82, 2017.

[193] G. Wang, H. Lu, D. Chen, F. Ren, R. Zhang, and Y. Zheng, "High quantum efficiency GaN-based pin ultraviolet photodetectors prepared on patterned sapphire substrates," *IEEE Photonics Technology Letters,* vol. 25, pp. 652-654, 2013.

[194] M. Peng, Y. Liu, A. Yu, Y. Zhang, C. Liu, J. Liu, W. Wu, K. Zhang, X. Shi, and J. Kou, "Flexible self-powered GaN ultraviolet photoswitch with piezo-phototronic effect enhanced on/off ratio," *ACS nano,* vol. 10, pp. 1572-1579, 2016.

[195] S. Rathkanthiwar, A. Kalra, S. V. Solanke, N. Mohta, R. Muralidharan, S. Raghavan, and D. N. Nath, "Gain mechanism and carrier transport in high responsivity AlGaN-based solar blind metal semiconductor metal photodetectors," *Journal of Applied Physics,* vol. 121, p. 164502, 2017.

[196] X.-X. Chen, X.-H. Xiao, Z.-F. Shi, R. Du, and X.-J. Li, "Self-powered ultraviolet photodetection realized by GaN/Si nanoheterostructure based on silicon nanoporous pillar array," *Journal of Alloys and Compounds,* vol. 767, pp. 368-373, 2018.

[197] W. Song, X. Wang, H. Chen, D. Guo, M. Qi, H. Wang, X. Luo, X. Luo, G. Li, and S. Li, "High-performance self-powered UV-Vis-NIR photodetectors based on horizontally aligned GaN microwire array/Si heterojunctions," *Journal of Materials Chemistry C,* vol. 5, pp. 11551-11558, 2017.

[198] L. Peng, L. Hu, and X. Fang, "Low-dimensional nanostructure ultraviolet photodetectors," *Advanced Materials,* vol. 25, pp. 5321-5328, 2013.

[199] L. Rigutti, M. Tchernycheva, A. De Luna Bugallo, G. Jacopin, F. Julien, L. F. Zagonel, K. March, O. Stephan, M. Kociak, and R. Songmuang, "Ultraviolet photodetector based on GaN/AlN quantum disks in a single nanowire," *Nano letters,* vol. 10, pp. 2939-2943, 2010.

[200] H. Karami and E. Fakoori, "Synthesis and characterization of ZnO nanorods based on a new gel pyrolysis method," *Journal of Nanomaterials,* vol. 2011, 2011.

[201] D. Pan, J. Zhang, Z. Li, and M. Wu, "Hydrothermal route for cutting graphene sheets into blue-luminescent graphene quantum dots," *Advanced Materials,* vol. 22, pp. 734-738, 2010.

[202] Y. Li, Y. Hu, Y. Zhao, G. Shi, L. Deng, Y. Hou, and L. Qu, "An electrochemical avenue to green-luminescent graphene quantum dots as potential electron-acceptors for photovoltaics," *Advanced Materials,* vol. 23, pp. 776-780, 2011.

[203] D. Jiang, Y. Chen, N. Li, W. Li, Z. Wang, J. Zhu, H. Zhang, B. Liu, and S. Xu, "Synthesis of luminescent graphene quantum dots with high quantum yield and their toxicity study," *PLoS One,* vol. 10, p. e0144906, 2015.

[204] L. Lin and S. Zhang, "Creating high yield water soluble luminescent graphene quantum dots via exfoliating and disintegrating carbon nanotubes and graphite flakes," *Chemical communications,* vol. 48, pp. 10177-10179, 2012.

[205] P. Routh, S. Das, A. Shit, P. Bairi, P. Das, and A. K. Nandi, "Graphene quantum dots from a facile sono-fenton reaction and its hybrid with a polythiophene graft copolymer toward photovoltaic application," *ACS applied materials and interfaces,* vol. 5, pp. 12672-12680, 2013.

[206] Y. Xing, Z. Xi, Z. Xue, X. Zhang, J. Song, R. Wang, J. Xu, Y. Song, S.-L. Zhang, and D. Yu, "Optical properties of the ZnO nanotubes synthesized via vapor phase growth," *Applied Physics Letters,* vol. 83, pp. 1689-1691, 2003.

[207] Y. J. Lee, K. Song, S.-H. Cha, S. Cho, Y. S. Kim, and Y. Park, "Sesquiterpenoids from Tussilago farfara flower bud extract for the eco-friendly synthesis of silver and gold nanoparticles possessing antibacterial and anticancer activities," *Nanomaterials,* vol. 9, p. 819, 2019.

[208] T. K. T. Vu, Q. D. Nguyen, T. D. Nguyen, and T. H. Trinh, "Preparation of metal nanoparticles for surface enhanced Raman scattering by laser ablation method," *Advances in Natural Sciences: Nanoscience and Nanotechnology,* vol. 3, p. 025016, 2012.

[209] S. T. Kochuveedu, J. H. Oh, Y. R. Do, and D. H. Kim, "Surface-Plasmon-Enhanced Band Emission of ZnO Nanoflowers Decorated with Au Nanoparticles," *Chemistry–A European Journal,* vol. 18, pp. 7467-7472, 2012.

[210] J. Im, J. Singh, J. W. Soares, D. M. Steeves, and J. E. Whitten, "Synthesis and optical properties of dithiol-linked ZnO/gold nanoparticle composites," *The Journal of Physical Chemistry C,* vol. 115, pp. 10518-10523, 2011.

[211] K. Liu, M. Sakurai, M. Liao, and M. Aono, "Giant improvement of the performance of ZnO nanowire photodetectors by Au nanoparticles," *The Journal of Physical Chemistry C,* vol. 114, pp. 19835-19839, 2010.

[212] N. Hsu, W. Hung, and Y. Chen, "Origin of defect emission identified by polarized luminescence from aligned ZnO nanorods," ed: American Institute of Physics, 2004.

[213] J. M. Lin, H. Y. Lin, C. L. Cheng, and Y. F. Chen, "Giant enhancement of bandgap emission of ZnO nanorods by platinum nanoparticles," *Nanotechnology,* vol. 17, p. 4391, 2006.

[214] A. Milnes, "Feucht," *DL Heterojunctions and Metal-Semiconductor Junctions Academic Press, New York, USA,* 1972.

[215] J. A. Aranovich, D. Golmayo, A. L. Fahrenbruch, and R. H. Bube, "Photovoltaic properties of ZnO/CdTe heterojunctions prepared by spray pyrolysis," *Journal of Applied Physics,* vol. 51, pp. 4260-4268, 1980.

[216] L. Zhang, Q. Li, L. Shang, F. Wang, C. Qu, and F. Zhao, "Improvement of UV electroluminescence of n-ZnO/p-GaN heterojunction LED by ZnS interlayer," *Optics express,* vol. 21, pp. 16578-16583, 2013.

[217] M. Garg, B. R. Tak, V. R. Rao, and R. Singh, "Giant UV photoresponse of GaN-based photodetectors by surface modification using phenol-functionalized porphyrin organic molecules," *ACS applied materials and interfaces,* vol. 11, pp. 12017-12026, 2019.

[218] Z.-D. Huang, W.-Y. Weng, S.-J. Chang, Y.-F. Hua, C.-J. Chiu, and T.-Y. Tsai, "${\rm Ga} _ {2}{\rm O} _ {3} $/GaN-Based Metal-Semiconductor-Metal Photodetectors Covered With Au Nanoparticles," *IEEE Photonics Technology Letters,* vol. 25, pp. 1809-1811, 2013.

[219] S. K. Jain, N. Aggarwal, S. Krishna, R. Kumar, S. Husale, V. Gupta, and G. Gupta, "GaN-UV photodetector integrated with asymmetric metal semiconductor metal structure for enhanced responsivity," *Journal of Materials Science: Materials in Electronics,* vol. 29, pp. 8958-8963, 2018.

[220] A. O. Goushcha and B. Tabbert, "On response time of semiconductor photodiodes," *Optical Engineering,* vol. 56, p. 097101, 2017.

[221] F. Li, D. I. Son, S. H. Cho, W. T. Kim, and T. W. Kim, "Flexible photovoltaic cells fabricated utilizing ZnO quantum dot/carbon nanotube heterojunctions," *Nanotechnology,* vol. 20, p. 155202, 2009.

[222] W.-S. Kuo, C.-L. L. Hsu, H.-H. Chen, C.-Y. Chang, H.-F. Kao, L. C.-S. Chou, Y.-C. Chen, S.-J. Chen, W.-T. Chang, and S.-W. Tseng, "Graphene quantum dots conjugated with polymers for two-photon properties under two-photon excitation," *Nanoscale,* vol. 8, pp. 16874-16880, 2016.

[223] D. Ick Son, H. Yeon Yang, T. Whan Kim, and W. Il Park, "Photoresponse mechanisms of ultraviolet photodetectors based on colloidal ZnO quantum dot-graphene nanocomposites," *Applied Physics Letters,* vol. 102, p. 021105, 2013.

[224] J. Li and J.-J. Zhu, "Quantum dots for fluorescent biosensing and bio-imaging applications," *Analyst,* vol. 138, pp. 2506-2515, 2013.

[225] S. Dhar, T. Majumder, and S. P. Mondal, "Phenomenal improvement of external quantum efficiency, detectivity and responsivity of nitrogen doped graphene quantum dot decorated zinc oxide nanorod/polymer schottky junction UV detector," *Materials Research Bulletin,* vol. 95, pp. 198-203, 2017.

[226] S. Dhar, T. Majumder, P. Chakraborty, and S. P. Mondal, "DMSO modified PEDOT: PSS polymer/ZnO nanorods Schottky junction ultraviolet photodetector: Photoresponse, external quantum efficiency, detectivity, and responsivity augmentation using N doped graphene quantum dots," *Organic Electronics,* vol. 53, pp. 101-110, 2018.

[227] X. Yan, B. Li, X. Cui, Q. Wei, K. Tajima, and L.-s. Li, "Independent tuning of the band gap and redox potential of graphene quantum dots," *The journal of physical chemistry letters,* vol. 2, pp. 1119-1124, 2011.

[228] X. Yan, X. Cui, B. Li, and L.-s. Li, "Large, solution-processable graphene quantum dots as light absorbers for photovoltaics," *Nano letters,* vol. 10, pp. 1869-1873, 2010.